



UNIVERSITÀ DELLA CALABRIA



Department of Physics

Bernardino Telesio – Doctorate School of Science and Technique

**Thesis submitted for the degree of Doctor of Philosophy in Science and
Technology of Mesophases and Molecular Materials**

M³ – XXVIII Cycle

FIS/07

**Advanced Materials (Ceramics in particular) for
Structural Applications**

**School Director
Prof. Roberto Bartolino**

**Supervisor
Prof. Nicola Scaramuzza**

**Curriculum Coordinator
Prof. Carlo Versace**

**Candidate
Hari Krishna Koduru**

Academic Year : 2012 – 2015

Contents

Acknowledgements	i
Abstract	ii
Preface	iii
List of Figures	iv
List of Tables	ix

Part - I. Polymer Thin films for Soft Matter Applications

Section	Description	Page No.
1.0	Chapter – I Introduction	1
1.1	Versatile properties of the polymers	3
1.2	Classification of polymers	4
1.3	Mechanism of polymerization in polymers	7
1.4	Introduction to Conducting Polymers	8
1.5	Conjugated Polymers	9
1.6	Introduction Polypyrrole (PPy)	10
1.7	Poly(vinyl alcohol) (PVA)	12
2.0	Chapter – II Polymer thin film deposition techniques	15
2.1	Spin Coating technique	16
2.2	Dip coating technique	16
2.3	Solution casting technique	16
2.4	<i>Electrochemical polymerization</i>	18
2.5	Spray – coating technique	18
2.6	Thermal Evaporation technique	19
2.7	Sputtering technique	20
2.8	Chemical Vapor Deposition technique	21
2.9	Pulsed laser deposition (PLD) technique	23
2.10	History of Plasma	23
2.11	The plasma approximation	26

2.12	Types of Plasmas	28
2.13	Plasma polymerization	29
2.14	Criteria of Monomer Choice	33
2.15	Plasma Reactors types	33
2.16	System Pressure	35
2.17	Cold Plasma Polymerization (CPP)	39
2.18	CPP Experimental Set-up for the Growth of Polymer Thin Films	40
2.19	Characterization Techniques – Polymer Thin films	41
2.19.1	Structure	41
2.19.2	Atomic Force Microscopy (AFM)	43
2.19.3	Optical properties	45
2.19.4	Theory for Optical absorption	46
2.20	Fourier-Transform Infrared Spectroscopy	46
2.21	Dielectric Spectroscopy	47
2.22	Surface wetting properties	54
3.0	Literature Survey	55
3.1	Scope of the work	67
3.2	Objectives of the work	68
	References	69
4.1	Chapter – III Cold plasma polymerization and characterization of Polypyrrole thin films.	78
4.1.1	Introduction	78
4.1.2	Experimental Section	79
4.1.3	Results and Discussion	81
4.1.4	Conclusions	92
	References	94
4.2	Chapter – IV Influence of Silver nanoparticles Inter layer on Optical and Dielectric Properties of PVA Thin films	97
4.2.1	Introduction	97
4.2.2	Experimental	98
4.2.3	Results and Discussion	99

4.2.4	Conclusions	110
	References	111

Part - II. Hyperbolic Metamaterials for Spontaneous Emission enhancement.

Section	Description	Page No:
5.0	Chapter – V Introduction to Hyperbolic Metamaterials	114
5.1	Radiative and nonradiative decay: the quantum efficiency	116
5.2	Purcell Effect	116
5.3	Optical Microcavities	118
5.4	Photonic Crystals	119
5.5	Metamaterials	121
5.5.1	About discovery of “Metamaterials”	122
5.5.2	Theory of Metamaterials	123
5.6	Hyperbolic Metamaterials	125
5.6.1	Surface Plasmons (SPs) and Surface plasmon polaritons (SPPs)	125
5.6.2	EMT for Multilayer system	133
5.6.3	Origin of the high-k modes in HMMs	135
5.6.4	Applications of HMMs	136
5.6.5	Literature Survey	137
5.6.6	Scope of the work	148

5.6.7	Objectivities of the present work	149
	References	150
6.0	Chapter – VI Thin films growth and characterization techniques	156
6.1	Thermal evaporation	156
6.2	Electron beam evaporation	157
6.3	Electron beam lithography	158
6.4	Ellipsometry	160
6.5	Stylus Profilometry	162
6.6	Photoluminescence Spectroscopy	163
6.7	Time-Correlated Single Photon Counting Technique	166
7.0	Chapter – VII Spontaneous Emission rate enhancement using Hyperbolic metamaterials	170
7.1	Introduction	170
7.2	Designing and fabrication of Hyperbolic Metamaterials	172
7.3	Prism Coupling technique	178
7.4	Grating Coupling technique	180
8.0	Chapter – VIII Augmentation of Spontaneous emission in dye embedded hyperbolic metamaterial associated with grating coupled technique.	191
8.1	Introduction	191
8.2	Results and Discussion	193

	References	199
--	------------	-----

Published papers

Contributions to International Conferences

ACKNOWLEDGEMENTS

It is my with extreme pleasure I express my sincere gratitude to my Respected Supervisor Professor Nicola Scaramuzza, with whose benevolent guidance, constant encouragement, timely and cheerful cooperation, the present work would take this form. I also want to acknowledge Professors, Roberto Bartolino, Carlo Versace, Andrei Ionescu and Doctors: Lucia Marino, Salvatore marino, Emanuela Bruno, Caterina Maria Tone and Giovanni Desiderio.

My earnest thanks to Prof. Giuseppe Strangi, Nano Plasm Laboratory, Department of Physics, Case Western Reserve University, Ohio, USA, for his generous help to get an opportunity to continue my research work in Nano Plasm Laboratory for the period of 1 – 1 – 2014 to 31 – 12 – 2014 and guided me to work in the advanced fields such as Metamaterials.

I owe my sincere thanks to Dr. K.V. Sreekanth and Prof. Antonio de Luca, for their goodwill, cheerful assistance, incessant help, inspiring discussions, conscientious labour, friendly cooperation, best wishes and advice.

Special thanks to all my friends and my well-wisher Ciccio Scommarella for his kindness and sympathy.

I avail this opportunity to express my sincere, high debt and deep sense of gratitude to all my beloved Teachers. Due to their motivation and blessings, I got this opportunity to continue my carrier in research filed. This work of thesis is dedicated to all of my Respected Teachers.

Hari Krishna Koduru

Rende, November 30, 2015.

ABSTRACT

The study of ‘Intrinsic and Metal nano particles doped polymer thin films for soft matter applications and nanostructured Hyperbolic metamaterials’ is an challenging and dynamic field of research with significant implications in the development of novel technologies, like gas sensors, bio-medical application and engineering of spontaneous emission of florescent molecules. In the present investigation, we presented research work in two directions. We prepared Polymer thin films by homemade Cold Plasma Polymerization technique and studied their Microstructural, Optical and dielectric responses as a function of thin film growth parameters, in view of gas sensor applications. In other direction, we fabricated lamellar structured Hyperbolic Metamaterials by employing physical and chemical vapour thin film deposition techniques and employed them as effective substrates to engineer the life time of florescent dye molecules.

The first part of this thesis is devoted to preparing Polypyrrole (PPy) thin films of nano sized thickness, by Cold plasma polymerization technique and analyzing the influence of Plasma power on Microstructural, Optical, wetting and dielectric properties of grown PPy films. Fabricating layered structures of “PVA/AgNPs/PVA” thin films to investigate the influence of rate of distribution of AgNPs on dielectric responses of PVA matrix to employ them as a gas sensor applications, whose study is still open and is getting substantial interest in industrial and academic environments.

Enhancement of spontaneous emission is a dynamic and challenging fundamental quantum phenomenon in optics and in nutshell it opens new avenues for spectrum of futuristic applications. Metamaterials are artificially designed nanocomposite materials, in which bulk electromagnetic properties arise due to underlying structural resonances and near field coupling between the designed sub-wavelength building blocks. Metamaterials promise to alleviate the classical limitations of optics and led to exotic applications such as negative refraction, sub-wavelength resolution imaging, invisibility devices and perfect absorbers. In the second part of this thesis, we fabricated Hyperbolic metamaterials and proposed new grating coupled hyperbolic metamaterial (GCHMM) configuration for the enhancement of spontaneous emission rate of dye molecules by exploiting the unique property of a hypergrating to outcouple and extract the non-radiative plasmonic modes.

PREFACE

This thesis contains work carried out in the Licryl Laboratory, University of Calabria and Nano Plasm Laboratory, Department of Physics, Case Western Reserve University, Ohio, USA during the period 2012 – 2015 under the supervision of **Prof. Nicola Scaramuzza**. During the Ph.D course one paper has been published, which is listed below with other three papers are in progress.

1. K.V. Sreekanth, **K. Hari Krishna**, Antonio De Luca and Giuseppe Strangi, “Large spontaneous emission rate enhancement in grating coupled hyperbolic metamaterials” Scientific Reports (Nature) 2014 11;4:6340.
2. **K. Hari Krishna**, K. V. Sreekanth and Giuseppe Strangi, “Dye embedded and nanopatterned hyperbolic metamaterials for spontaneous emission rate enhancement”. (In preparation).
3. **K. Hari Krishna**, Lucia Marino, Janardhanam Vallivedu, Chel-Jong Choi, and Nicola Scaramuzza, “Cold plasma polymerization and characterization of polypyrrole thin films”. (Submitted to Plasma Process and Polymers, **Under Review**).
4. **K. Hari Krishna**, Lucia Marino, and Nicola Scaramuzza, “Influence of Silver nanoparticles Inter layer on Optical and Dielectric Properties of PVA Thin films”. (Inpreparation).

List of Figures

Fig. No	Title	Page No:
1.1	Polymers and their applications in multi-fields	
1.2	The structure of pyrrole	
1.3	Oxidative polymerization of pyrrole to polypyrrole proceeds via a one electron oxidation of pyrrole to a radical cation, which subsequently couples with another radical cation to form the 2,2'-bipyrrole. This process is then repeated to form longer chains.	
1.4	Chemical structures of polypyrrole In neutral aromatic and quinoid forms and in oxidized polaron and bipolaron forms.	
1.5	Structural unit of PVA	
2.1	Elemental process in a plasma	
2.2	Diagram of plasma polymerization	
2.3	Commonly used gases for plasma surface deposition and plasma treatment	
2.4	Diagram of a DC Plasma Reactor	
2.5	Diagram of a RF plasma reactor	
2.6	Schematic representation for cold plasma polymerization thin film deposition setup.	
2.7	The Grazing incidence X-ray diffraction block diagram	
2.8	Basic block diagram of an AFM	
2.9	The Debye relaxation function. The full line is the real part ϵ' and the dashed line is the imaginary part ϵ'' . Plotted for ϵ_α , ϵ_s and $\tau = 10^{-4}$ s.	
2.10	The Cole–Cole relaxation function. The full lines are the real parts and the dashed lines are the imaginary parts. Curves are plotted for $\alpha = 1$, $\alpha = 0.8$, $\alpha = 0.6$, $\alpha = 0.4$ and $\alpha = 0.2$.	
2.11	The Cole–Davidson relaxation function. The full lines are the real parts and the dashed lines are the imaginary parts. Curves are plotted for $\beta = 1$, $\beta = 0.8$, $\beta = 0.6$, $\beta = 0.4$ and $\beta = 0.2$.	
4.1	X-ray diffraction patterns of cold plasma polymerized PPy thin films grown at various plasma powers.	
4.2	FTIR spectra of cold plasma polymerized PPy thin films at different plasma powers.	
4.3	AFM images corresponding to PPy thin films prepared at plasma powers (a) 10 W (b) 30 W and (c) 50 W.	

4.4	UV – visible absorption spectra for plasma polymerized PPy films at various plasma powers	
4.5	Impedance measurements for PPy thin films as a function of plasma powers (a). The variation real impedances as a function of applied frequency in the range 10 mHz – 100 KHz. (b). Nyquist plots (Z'' versus Z') for grown films at various growth conditions.	
4.6	Behavior of estimated dielectric constants of grown films as a function of frequency (solid black line represents the fit).	
4.7	Cole – Cole plots for plasma polymerized PPy films	
4.8	Atomic force micrographs for ‘PVA/AgNPs’ thin films various temperatures (a) T = 20 °C (b) T = 100 °C (c) T = 200 °C (d) variation of rms roughness.	
4.9	Optical absorption spectra for ‘PVA/AgNPs’ thin films at various temperatures in the range 20 °C – 200 °C.	
4.10	Plots of the dielectric permittivity vs. log of frequency (log f) as a function of temperatures for ‘PVA/AgNPs/PVA’ thin films (MLTs).	
4.11	Fitting results for dielectric spectrum of ‘PVA/AgNPs/PVA’ thin films (MLTs) at T = 100 °C: (a) real part, (b) imaginary part.	
4.12	Fitting results for dielectric spectrum of ‘PVA/AgNPs/PVA’ thin films (MLTs) at T = 150 °C: (a) real part, (b) imaginary part.	
4.13	The Variation of the loss tangent ($\tan \delta$) with frequency at different temperatures for ‘PVA/AgNPs/PVA’ thin films (MLTs).	
4.14	The frequency variation of (a) real (M') and (b) imaginary (M'') parts of electric modulus at different measuring temperatures.	
5.1	Interaction of a photon with two energy levels of an atom. Left: Absorption moves the atom from the ground state to the excited state. Middle: Spontaneous emission moves the atom from the excited to the ground state. Right: Induced emission of a photon, by a photon interfering with an atom in the excited state.	
5.2	The microcavities according to the confinement method and by according to high Q and ultrahigh Q.	
5.3	Photonic crystal structures in various directions.	
5.4	Typical transmission spectra $T(\lambda)$ of a one-dimensional PBG structure.	
5.5	The pointing Vectors representation of EM waves in left handed and right handed materials.	
5.6	Schematic representation of the possible domains of electromagnetic materials.	

5.7	Surface plasmons at interface of Metal and Dielectric films.	
5.8	The confined motion of SPPs along metal-dielectric interface.	
5.9	(a) A one-dimensional array of grooves of width a , depth h , and periodicity d . (b) An $a \times a$ square holes arranged on a $d \times d$ lattice are cut into the surface of a perfect conductor, in which localized surface plasmon modes can be induced by the structure. (c) The dispersion relation $[\omega(k_x)]$ of the surface bound states supported by the one-dimensional array of grooves [Fig. 5.9 (a)], with geometrical parameters $a/d=0.2$ and $h/d=1$.	
5.10	k-space topology: The isofrequency contour for (a) an isotropic dielectric is a sphere, (b) extraordinary waves in a uniaxial medium with extreme anisotropy ($\epsilon_{xx} = \epsilon_{yy} > 0$) and $\epsilon_{zz} < 0$, it is a hyperboloid (type I HMM). (c) Hyperboloid of a type II metamaterial when two components of the dielectric tensor are negative ($\epsilon_{xx} = \epsilon_{yy} < 0$) and $\epsilon_{zz} > 0$.	
5.11	Schematic of anisotropic multilayer composite. The perpendicular direction is defined as parallel to the normal vector from the surface of the metamaterial and the parallel direction is defined as the plane parallel to the metamaterial interface.	
5.12	EMT predicts that a metal dielectric composite can behave as an effective dielectric, effective metal, Type I HMM or Type II HMM depending on the wavelength and fill fraction of the metal. Optical phase diagrams for (a) Ag=Al ₂ O ₃ multilayer system (b) Ag=TiO ₂ multilayer system.	
5.13	Schematic of an anisotropic nanowire composite. The perpendicular direction is defined along the long axis of the nanowire and the parallel direction is defined as the plane along the short axis of the nanowire.	
5.14	(a) Dispersion of the dielectric constants in a practical multilayer semiconductor realization of the HMM. Note the broadband region in which Type I HMM response is achieved (b) Exact numerical calculation (neglecting loss) in the multilayer structure showing the bloch high-k mode and coupled surface plasmons at the interfaces (c) Evanescent wave incident on an effective medium slab couples to the high-k mode and is transmitted. In contrast, the evanescent wave decays away in vacuum.	
6.3.1	E resist cross-section: The electron beam causes chemical changes in the exposed areas.	
6.3.2	E resist cross-section: Only the chemically changed e resist can be dissolved in a specific solvent (positive lithography).	

6.3.3	E resist cross-section after metal deposition	
6.4.1	The general principle in ellipsometry.	
6.4.2	Illustration of a thin film on top of a substrate.	
6.6.1	Electron configurations for (a) a singlet ground state; (b) a singlet excited state; and (c) a triplet excited state.	
6.6.2	Energy level diagram for a molecule showing pathways for the deactivation of an excited state: vr is vibrational relaxation; ic is internal conversion; ec is external conversion; and isc is an intersystem crossing. The lowest vibrational energy for each electronic state is indicated by the thicker line. The electronic ground state is shown in black and the three electronic excited states are shown in green. The absorption, fluorescence, and phosphorescence of photons also are shown.	
6.6.3	Absorbance spectrum and fluorescence emission spectrum for tyrosine in a p ^H 7, 0.1 M phosphate buffer.	
6.6.4	FluoroLog3-2iHR1-TCSPC-IGA, optical configuration.	
6.7.1	Experimental set up used for the lifetime photoluminescence measurements.	
7.2.1	Schematic representation of fabricating steps for HMM structure: (a) Control sample composed of single period of 'Ag/Al ₂ O ₃ ' layers (b) Three periods of 'Ag/Al ₂ O ₃ ' layers (c) Six periods of 'Ag/Al ₂ O ₃ ' layers.	
7.2.2	Characterization of HMM: (a) Experimentally determined permittivity values of Ag and Al ₂ O ₃ thin films. The red and blue lines represent the real and imaginary permittivity values of Ag, respectively and black line represents the permittivity values of Al ₂ O ₃ . (b) Real parts of effective permittivity of Ag/Al ₂ O ₃ HMM determined with effective media theory. The Ag/Al ₂ O ₃ HMM shows hyperbolic dispersion at $\lambda \geq 430$ nm.	
7.2.3	(a) Reference sample and (b) dye doped PMMA layer deposited over fabricated HMM structures.	
7.2.4	(a) Absorption spectrum of dye dissolved PMMA (for reference sample). (b) Steady-state photoluminescence measurements of dye on reference sample.	
7.2.5	Time-resolved photoluminescence measurements of Coumarin dye on Ref and HMM samples. (a) in elliptical region ($\lambda_c=420$ nm), (b) at critical wavelength ($\lambda_c=430$ nm), and (c) in hyperbolic region ($\lambda_c=450$ nm).	
7.2.6	Variation of spontaneous emission lifetimes of the Coumarin dye on Ref and HMM samples, as a function of emission wavelength. (a) first decay time and (b) second decay time.	

7.3.1	Two methods of prism-coupling radiation to SPPs; (a) Otto configuration, and (b) Kretschmann-Raether configuration.	
7.3.2	Dispersion of a SPP at a metal-dielectric interface (schematic). Lines (a) and (b) illustrate the dispersion of plane waves in the spacer layer (S) and the high index prism (P) respectively where n is the refractive index of the medium. Only photons (polaritons) with momenta that lie between lines (a) and (b) may couple to SPPs.	
7.4.1	Grating geometry and coordinate system used throughout this thesis. The direction of the electric field vector (E) is illustrated for the situation when p-polarised (TM) radiation is incident.	
7.4.2	Fabrication steps for GCHMM: (a) SEM image of designed 2D grating structure over PMMA substrates (b) Dye deposited over HMM (c) Electron beam exposed PMMA layer over dye posited HMM (d) Ag layer (20 nm) deposited over Electron beam exposed PMMA layer over dye posited HMM (e) Ag grating over HMM structure.	
7.4.3	Reflectance spectra as a function of excitation wavelength: (a) Reflectance spectrum of various samples obtained at incident grazing angle of 50° . The studied samples are shown in Figs. (b) to (e). The GCHMM sample (iv) shows four prominent reflectance dips corresponding to the excited plasmonic modes (both surface and bulk plasmon polaritons) from the geometry.	
7.4.4	Transmittance spectrum of GCHMM at normal incidence. The obtained four prominent transmission maximum correspond to the excitation of plasmonic modes from GCHMM	
7.4.5	Reflectance spectra of GCHMM as a function of incident angle. (a) 430 nm, (b) 450 nm and (c) 480 nm.	
7.4.6	Time-resolved photoluminescence measurements of Coumarin dye on various samples, Ref (pink), HMM (red), HMM with Ag (black), and GCHMM (blue)) with emission wavelength: (a) in elliptical region ($\lambda_e = 420$ nm), (b) at critical wavelength ($\lambda_c = 430$ nm), and (c) in hyperbolic region (le ($\lambda_e = 450$ nm).	
7.4.7	Time-resolved photoluminescence measurements of Coumarin dye on HMM with Ag and GCHMM samples. (a) in elliptical region ($\lambda_e=420$ nm), (b) at critical wavelength ($\lambda_c=430$ nm), and (c) in hyperbolic region ($\lambda_e=450$ nm). Red lines represent the corresponding fit.	
7.4.8	Lifetimes of dye on GCHMM and Ag film deposited HMM normalized with respect to HMM sample: for (a) first decay time (t_1) and (b) second decay time (t_2). The	

	solid lines are for eye guide. Enlarged plot of normalized decay time of GCHMM is shown in the inset of (a) and (b). Normalized lifetime is studied as a function of emission wavelength from elliptical to hyperbolic dispersion. In the case of GCHMM, a maximum decay rate is observed at 510 nm for both decay times.	
8.1.1	Designed two different HMM structures: (a) 5 stacks of Pure PMMA (25 nm) and Ag (12 nm) multilayered HMM structure (b) 5 stacks of “SiO ₂ /DCM dye doped PMMA/SiO ₂ ”(25 nm) and Ag (12 nm) lamellar DEHMM structure (c) Reference sample.	
8.2.2	Real parts of permittivity tensor components HMM evaluated in accordance with effective medium theory.	
8.2.3	Steady – state photoluminescence measurements for reference, dye on top HMM and DEHMM samples.	
8.2.4	Emission kinetics of dye molecules on various samples as a function of emission wavelength at 580 nm.	
8.2.5	Variation of (a) first decay time (τ_1) and (b) second decay times (τ_2) for reference, dye placed on top of HMM and DEHMM samples, as a function of emission wavelengths.	
8.2.6	Grating coupled DEHMM (GCDEHMM) sample structure	
8.2.7	Variation of first decay time (τ_1) as a function of emission wavelengths, for reference, DEHMM and GCDEHMM samples.	

List of Tables

Table No.	Title	Page. No
4.1	Fitting parameters for PPy films deposited at various plasma powers	
4.2	Fitting parameters for relaxation process for 'PVA/AgNPs/PVA' structured cell at different temperatures.	
4.3	Fitting parameters for DC conductivity of 'PVA/AgNPs/PVA' structured cell at different temperatures.	
5.1	Selection of Metal and dielectric layers for the abrication of HMM structures in various Electromagnetic regions	

**Part – I. Polymer thin films for
Soft matter applications**

1.0 Introduction

The field of ‘Polymer Science and Thin films technology’ is a vibrant contributor to cutting edge advances in the current Science & Technology, not only in its own right, but also due to wide array of industries and technologies made possible by the use of polymer materials. Polymers have unique, molecularly definable properties and process advantages unattainable in any other kind of material. Their attractiveness comes, in part, from the wide varieties of structures, molecular weights and functionalities available via rational synthesis of polymers and their characteristically broad range of possible processing modes. Polymers are the light and flexible materials in nature and human society. Compared with most inorganic structural materials, they are of low density ($\approx 1\text{ g cm}^{-3}$).

Polymers form a very significant class of materials without which the life seems very difficult. In everyday human life, they are all around us in different forms such as rubber, in plastic, in resins, and in adhesives and adhesives tapes. The word *polymer* is derived from Greek words, poly = many and mers = parts or units of high molecular mass each molecule of which consist of a very large number of single structural units joined together in a regular manner. In other words, polymers are giant molecules of high molecular weight, called macromolecules, which are build up by linking together of a large number of small molecules, known as monomers. The chemical reaction process, in which the monomers combine to form polymer is known as *polymerization* [1]. Polymers have existed in natural form since life began and those such as DNA, RNA, proteins and polysaccharides play crucial roles in plant and animal life. However, it was not until the middle of the 20th century that we began to understand the true nature of polymers. The utilization of polymeric materials has permeated every facet of our lives and it is hard to visualize today’s world with all its luxury and comfort without man-made polymeric materials. The first generation of man-made polymers was the result of empirical activities and main focus was on chemical composition with virtually no attention paid to the structure. In the first half of 20th century, extensive organic and physical developments had let to the first understanding of the structural concepts of polymers, i.e long chains (or) a network of covalently bonded molecules. In this regard, German chemist H. Standinger studied

systematically about the polymers and stated that these polymer were composed of giant molecules known as *macromolecules* [2, 3]. Later, the discovery of nylon by Carothers and his fundamental research work contributed to the elucidation of the nature of polymers. The impetus quest for novel polymer materials to aid in the defense effort during World war II resulted for the discovery of plastics (such as Polyethylene, polyester resins, acrylonitrile-butadiene-styrene etc.,) which were used to design and fabricate radar cable, telephone handsets, luggage, and safety helmets etc., for military use. The Nobel-prize-winning research work contributions in the field of stereo-specific catalysts led to the ability of polymer chemists to control the properties of polymers, which can be tailor-made for specific applications. Currently, with the existing of advanced technologies it is possible to prepare smart polymers provided with exceptional properties for futuristic applications as represented in the following Figure – 1.1.

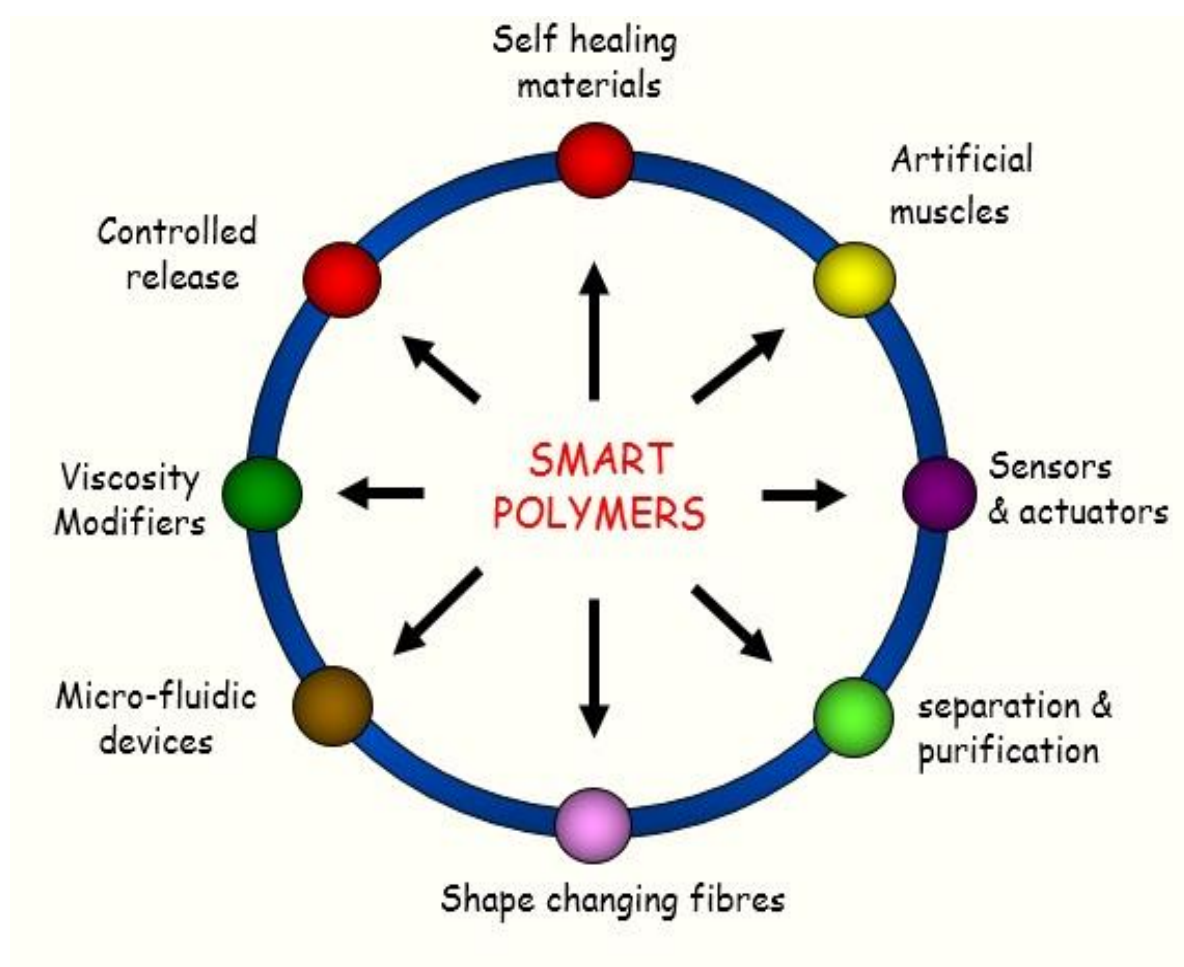


Figure – 1.1. Polymers and their applications in multi-fields.

1.1 Versatile properties of the polymers

It is worth to mention that, polymers consist exceptional structural features like (i) Intra-molecular features and (ii) Intermolecular features, which make them as versatile.

1.1.1 Intra-molecular features

Generally, polymers consist of characteristic chain-like molecules (i.e monomers), which linked covalently together to form macromolecules. Hence rotation is possible with respect to covalent bonds and this leads to the rotational isomerism (i.e *conformations*) and irregularly entangled rather than straight molecules.

1.1.1 (a) Conformations

The conformation of a polymer is the arrangement of the bond orientations both within the backbones, and array side-groups and branches. Basically three specific orientations are there, known as *trans*, *+gauche* and *-gauche*.

1.1.1 (b) Configurations

It explains about the spatial arrangement of the side chemical elements (or) groups of elements about the backbone molecular chains. These configurations establishes during polymerization of the polymers and they cannot be changed by rotations. Configurations provide the information about the arrangements (such as *cis* and *trans*) of identical atoms (or) groups of atoms around a double bond in monomer.

1.1.1 (c) Stereo regularity

The arrangement of side elements/groups around the asymmetric segment of vinyl-type repeating units. Resultantly, three different forms (*atactic*, *isotactic* and *syndiotactic*) of polymer chain results from head-to-tail addition of the monomers. Both stereo regularity and configurations provide the information about crystallization and the extent of crystallinity in polymers.

1.1.1 (d) Conjugated chains

The unsaturated alternating single and double bonds are known as conjugated chains. Generally, conjugated polymers demonstrate considerable electrical conductivity.

1.1.1. (e) Branched chains

In this type chains, linear back bone chain coexist with pendant side chains. It occurs during the polymerization of monomers (> 2). The presence of branched chains impedes the ability of polymers to crystallize.

1.1.1.(f) Molecular mass

It represents the number of repeating units in a polymer molecule and it must have a threshold value for the development of polymer properties. Therefore above described characteristic intra-molecular properties influence the glass transition and melting temperatures, crystallinity (or) amorphousness nature, the functionality and frequency of the reactive sites along the backbone chains of polymers.

1.1.2 Intermolecular features

Intermolecular features explains about the bulk properties of polymer.

1.2 Classification of polymers

Polymers can be classified in many different ways based on their source, structure of polymer, mode of polymerization and molecular forces.

1.2.1 Based on source, polymers are classified as follows

(i) Natural polymers:

The polymers which obtain by nature (or) natural resources like plants and animals. These are of considerable importance because they are generally bio-compatible, bio-degradable, non-toxic and non-immunogenic. Due to their exceptional qualities, they can use in Nano drug delivery, pharmaceutical and bio-medical applications, etc., [4 – 7],

Eg. Proteins, Cellulose, starch, rubber etc.,

(ii) Synthetic polymer:

The polymers which have been synthesized in the laboratory are known as synthetic polymers and are also known as manmade polymers [8, 9].

Eg: Polyvinyl alcohol, polyethylene, polystyrene, polysulfone, etc.

(iii) Semi synthetic polymers:

Chemically modified natural polymers are known as semi synthetic polymer. Hydrogenated natural rubber, cellulose, cellulose nitrate, emthyl cellulose, etc., [10 - 12].

1.2.2 Based on structure polymers are classified as linear, branched and cross linked polymers.

Linear polymers:

These polymers consist of long and straight chains. When monomers are joined end-to-end like links along a chain, a polymer with a simple linear structure is formed. In some polymers shorter chains grow off the long chain at certain intervals, so that a branched structure is formed [13]. The examples are high density polythene, polyvinyl chloride, etc. These are represented as follows:

Branched chain polymers:

A polymer chain having branch points that connect three or more chain segments; examples include graft copolymers, star polymers, comb polymers, and dendritic polymers [14].

Cross linked or Network polymers:

A cross-link is a bond that links one polymer chain to another. They can be covalent bonds or ionic bonds. "Polymer chains" can refer to synthetic polymers or natural polymers (such as proteins). When polymer chains are linked together by cross-links, they lose some of their ability to move as individual polymer chains. Cross-links can be formed by chemical reactions that are initiated by heat, pressure, change in pH, or radiation [15].

1.2.3 Based on Polymerization:

Polymers can also be classified on the basis of mode of polymerization into two sub groups.

Additive polymers:

The polymers, which are formed by the repeated addition of monomer molecules possessing double or triple bonds are known as additive polymers, e.g., the formation of polythene from ethane and polypropene from propene. If the addition polymers formed by the polymerization of a single monomeric species are known as homo-polymers, e.g., polythene. The polymers made by addition of polymerization from two different monomers are termed as copolymers, e.g., Buna-S, Buna-N, etc.

Condensation Polymers:

The polymers formed via repeated condensation reactions between two different bi-functional or tri-functional monomeric units, are known as condensation polymers. In these polymerization reactions, the elimination of small molecules such as water, alcohol, hydrogen chloride, etc. take place. The examples are terylene (dacron), nylon 6, 6, nylon 6, etc. For example, nylon 6, 6 is formed by the condensation of hexamethylene diamine with adipic acid.

Based on molecular forces:

The unique mechanical properties of polymers like tensile strength, elasticity, toughness, etc., are significantly governed by intermolecular forces. For example, van der Waals forces and hydrogen bonds present in the polymers [16, 17]. These forces also bind the polymer chains to make the polymers strong and utilize them in various fields. By considering the magnitude of intermolecular forces present in the polymers, they are classified into four groups as follows:

Elastomers:

The polymer, which exhibit “rubber-like” behavior provided with elastic properties are known as elastomers. In these, polymer chains are bonded by weakest intermolecular forces and make the polymers to stretch by the application of external forces. Due to the presence of few “cross-links” in the polymers, these elastomers can regain their shape after removal of external forces.

Eg: Buna-S Buna-N, neoprene, etc.,

Fibers: If the strength of the inter molecular forces are strong (like hydrogen bonds) and responsible for thread forming solids, are known as fibers. Due to the presence of characteristic hydrogen bonds, they exhibit high tensile strength and high modulus.

Thermoplastic polymers:

The polymers in which strength of intermolecular forces of attraction lies between elastomer and fibers, are known as thermoplastic polymers. These polymers possess linear (or) strong branched type of chain molecules capable of repeatedly softening on heating and hardening on cooling.

Eg: Polythene, polystyrene, polyvinyls, etc.,

Thermosetting plastics:

These polymers are cross linked or heavily branched molecules, which on heating undergo extensive cross linking in moulds and again become infusible. These cannot be reused. Eg: Bakelite, Urea-formaldelyde resins, etc.

1.3 Mechanism of polymerization in polymers

The linking together of a large number of monomers with each other to form a macromolecule (or) polymer molecule through chemical reactions is termed as polymerization. It can also be defined as the fundamental process by which low molecular weight compounds are converted into high molecular weight compounds. Currently, polymerization process is classified into (i) Step growth polymerization and (ii) Chain growth polymerization [18]. The degree of polymerization is related to the molecular mass (M) of the polymer and is given by the equation,

$$D_p = \frac{M}{m} \dots\dots\dots (1.1)$$

1.3.1 Condensation Polymerization (or) Step growth Polymerization

Condensation polymerization is a chemical reaction in which polymer is formed and a small molecule of by-product with a lower molecular weight is released. The eliminated by-product is called condensate. The reaction can take place between two similar (or) different monomer, which is also known as step growth polymerization [19, 20].

1.3.2 Addition Polymerization (or) Chain Polymerization

In this polymerization, two (or) more molecules of monomers attach together to form a polymer. In this polymerization, there is no elimination of any molecule. It is a chain reaction and no by product is released. It is obtained by linking together the monomer molecules by a chain reaction to give a polymer whose molecular weight is exactly an integral multiple of that of the monomer as in the case of polyethylene obtained by polymerization of ethylene. Only a single monomer is involved in addition polymerization and hence the polymer is homopolymer and contains the same monomer units, heat (or) a catalyst for opening the double bond of the monomer and creating the reactive sites [above third reference].

1.4 Introduction to Conducting Polymers

The conducting polymers attract attention of researchers and engineers from a variety of fields in science and technology as promising electrode materials for energy storage devices (electro-chemical batteries and capacitors), electro catalysts and biosensors based thereon, photo luminescent and electroluminescent materials, artificial muscles, gas separating membranes, anticorrosive coatings, electromagnetic shields, materials for microlithography, etc. [21]. In addition, the possibilities to produce conducting polymers electrochemically and to control their properties by electrochemical means are of interest on their own. Polymers have long been used as insulating materials. For example, metal cables are coated in plastic to insulate them. However, there are at least four major classes of semiconducting polymers that have been developed so far. They include conjugated conducting polymers, charge transfer polymers, ionically conducting polymers and conductively filled polymers. The conductively filled conducting polymers were first made in 1930 for the prevention of corona discharge. The potential uses for conductively filled polymers have since been multiplied due to their ease of processing, good environmental stability and wide range of electrical properties. The report of electrical conductivity in ionic polymers attracted considerable interest [22]. Since then, various ionically conducting polymers or polymer electrolytes have been prepared for a wide range of applications ranging from rechargeable batteries to smart windows.

The discovery of electrical conductivity in molecular charge transfer (CT) complexes in the 1950s [23] promoted the development of conducting CT polymers,

and led to subsequent findings of superconductivity with molecular CT complexes in 1980 [24] and with fullerene in 1986 [25]. The conductivity in CT complexes arises from the formation of appropriate segregated stacks of electron donor and acceptor molecules and a certain degree of charge transfer between the stacks. In addition, Along with all of the activities described above, various conjugated polymers have been synthesized, which show excellent electrical properties [26]. Owing to the delocalization of electrons in a continuously overlapped $\pi - \pi^*$ orbital along the polymer backbone, certain conjugated polymers also possess interesting optical and magnetic properties. These unusual optoelectronic properties allow conjugated polymers to be used for a large number of applications, including protecting metals from corrosion, sensing devices, artificial actuators, all-plastic transistors, non-linear optical devices and light emitting displays. Due to the backbone rigidity intrinsically associated with the delocalized conjugated structure, however, most *unfunctionalized* conjugated polymers are intractable (*i.e.* insoluble, infusible and brittle). Some of them are even unstable in air.

1.5 Conjugated Polymers

Conjugated polymers are organic macromolecules which consist at least of one backbone chain of alternating double- and single-bonds. Due to the fact that the p_z -orbitals of the carbon atoms which forms the π -orbitals of the alternating double-and single-bonds mesomerize more or less, *i.e.* the single and double bonds becomes similar, double-bonds overlaps also over the single bonds. Furthermore, the π -electrons can be easier moved from one bond to the other, what makes conjugated polymers to be one-dimensional semiconductors. Conjugated polymers have a framework of alternating single and double C-C, C-S or C-N bonds. The characteristics of the π -bonds are the source of the semiconducting properties of these materials. The difference in energy between the π orbital and an anti-bonding π^* orbital produces the band gap that determines the electrical and optical properties of the material [27]. Like inorganic semiconductors they can be doped, to increase their conductivity extremely. For the discovery and development of such conductive polymers Alan J. Heeger, Alan G. MacDiarmid, Hideki Shirakawa received the Nobel prize in chemistry 2000. The most simple conjugated polymer is polyacetylene, which consist only of a single chain of alternating single- and double-bonds.

The conductivity of such polymers is the result of several processes. For example, in traditional polymers such as polyethylenes, the valence electrons are bound in sp^3 hybridized covalent bonds. Such "sigma-bonding electrons" have low mobility and do not contribute to the electrical conductivity of the material. However, in conjugated materials, the situation is completely different. Conducting polymers have backbones of contiguous sp^2 hybridized carbon centers. One valence electron on each center resides in a p_z - orbital, which is orthogonal to the other three sigma-bonds. All the p_z orbitals combine with each other to a molecule wide delocalized set of orbitals. The electrons in these delocalized orbitals have high mobility when the material is "doped" by oxidation, which removes some of these delocalized electrons. Thus, the conjugated p-orbitals form a one-dimensional electronic band, and the electrons within this band become mobile when it is partially emptied. The band structures of conductive polymers can easily be calculated with a tight binding model. In principle, these same materials can be doped by reduction, which adds electrons to an otherwise unfilled band. In practice, most organic conductors are doped oxidatively to give p-type materials. The redox doping of organic conductors is analogous to the doping of silicon semiconductors, whereby a small fraction silicon atoms are replaced by electron-rich, *e.g.*, phosphorus, or electron-poor, *e.g.*, boron, atoms to create n-type and p-type semiconductors, respectively. Due to its simple conjugated molecular structure and fascinating electronic properties, polyacetylene has been widely studied as a prototype for other electronically conducting polymers [28].

1.6 Introduction Polypyrrole (PPy)

Organic polymers which are π – conjugated and having hetrocyclic structures have received great attention because of their potential applications. Among the conducting polymers known to date, ones based upon PPy have attracted special interest because of their high conductivity, their ease and high flexibility in preparation, their stability and good mechanical properties. Polypyrrole (ppy) is mostly concentrated due to simple oxidation and easy water solubility of monomer (pyrrole). In addition ppy possesses high conductivity, fast electrochemical switching and high specific capacitance values and environmental stability [29]. Depending on type of preparation routes, PPy can change the electrical and optical properties with size and shape of

nanostructures, which is an important goal in state-of-the-art of material designing [30 – 32]. PPy in thin film form can be used in potential technological applications such as in electronic and electrochromic devices [33 – 35], counter electrode in electrolytic capacitors [36] sensors [37 – 39], chromatographic stationary phases [40], light-weight batteries [41], membrane separation [42] consequently, have attracted a great deal of attentions in recent years and this is currently one of the most active areas of research in polymer science and engineering at present.

Polypyrrole is amorphous and usually gives only a diffuse halo in X-ray diffraction patterns [43, 44]. The electron diffraction showed that there are up 15% (of total volume) of crystalline domains in the bulk of amorphous PPy [45] The experimental data indicate that the crystalline regions have a monoclinic lattice; the pyrrole rings are oriented so that nitrogens of neighboring rings are oriented in opposite directions as show in the following Figure – 1.2.

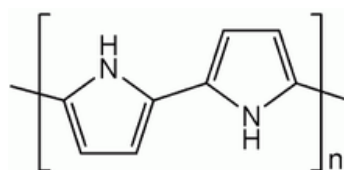


Figure - 1.2 The structure of pyrrole.

Polypyrrole (PPy) can be formed chemically or electrochemically through oxidative polymerization of pyrrole monomer, Figure – 1.3.

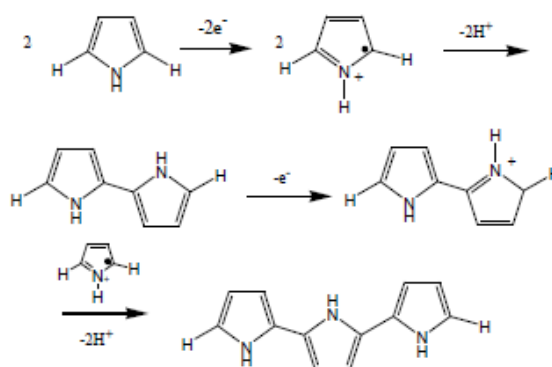


Figure – 1.3: Oxidative polymerization of pyrrole to polypyrrole proceeds via a one electron oxidation of pyrrole to a radical cation, which subsequently couples with another radical cation to form the 2,2'-bipyrrole. This process is then repeated to form longer chains.

The final form of polypyrrole is that of a long conjugated backbone as seen in Figure – 1.4. The polymer has resonance structures that resemble the aromatic or quinoid forms. In this neutral state the polymer is not conducting and only becomes conducting when it is oxidized. The charge associated with the oxidized state is typically delocalized over several pyrrole units and can form a radical cation (polaron) or a dication (bipolaron). The physical form of polypyrrole is usually an intractable powder resulting from chemical polymerization and an insoluble film resulting from electro polymerization.

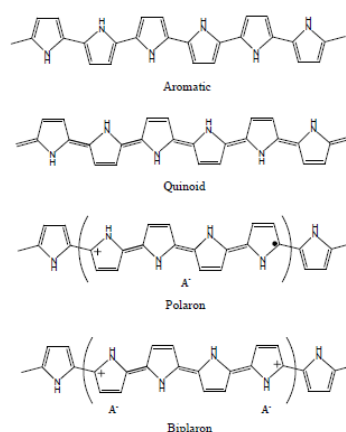


Figure – 1.4: Chemical structures of polypyrrole In neutral aromatic and quinoid forms and in oxidized polaron and bipolaron forms.

1.7 Poly(vinyl alcohol) (PVA)

In recent years energy conversion devices based on organic semiconductors are an emerging research field with substantial future prospects and it has attracted great attention due to the advantages of light weight, flexibility, and low cost of production with the possibility of fabricating large area devices based on solution processing. Polymeric materials have been the subject of intense scientific and technological research because of their potential applications. In particular, conducting polymers have been extensively investigated in the area of electronics and optoelectronics due to their attractive properties [46, 47]. Polymeric dielectric materials have been preferred because of their dielectric and physical properties over a wide range of temperatures and frequencies. Over the years, among various polymers, poly(vinyl alcohol) (PVA), as one of the most important polymers, has recently received considerable interest, owing to its numerous potential applications in electronic components. It has different internal structure that may be considered as

amorphous or semicrystalline. The semicrystalline structure of PVA showed an important feature rather than of amorphous one. This is because semicrystalline PVA leads to formation of both crystalline and amorphous regions [48 – 50]. PVA polymer is soluble in water and other solvents and is widely used in synthetic fiber, paper, contact lens, textile, coating, and binder industries, due to its excellent chemical and physical properties, nontoxicity, processability, good chemical resistance, high dielectric strength, good charge storage capacity, wide range of crystallinity, good film formation capacity, complete biodegradability, and high crystal modulus dopant-dependent electrical and optical properties [51 – 54]. PVA is comprised of carbon chain backbone with hydroxyl groups attached to methane carbons; these OH groups can be a source of hydrogen bonding and hence assist in the formation of polymer composite. Interestingly, semicrystalline materials have exhibited improvement in certain physical properties due to crystal-amorphous interfacial effect.

PVA is unique among polymers (chemical compounds made up of large, multiple-unit molecules) in that it is not built up in polymerization reactions from single-unit precursor molecules known as monomers. Instead, PVA is made by dissolving another polymer, polyvinyl acetate (PVAc), in an alcohol such as methanol and treating it with an alkaline catalyst such as sodium hydroxide. The resulting hydrolysis, or “alcoholysis,” reaction removes the acetate groups from the PVAc molecules without disrupting their long-chain structure. When the reaction is allowed to proceed to completion, the product is highly soluble in water and insoluble in practically all organic solvents. Incomplete removal of the acetate groups yields resins less soluble in water and more soluble in certain organic liquids. PVA is used in sizing agents that give greater strength to textile yarns and make paper more resistant to oils and greases. It is also employed as a component of adhesives and emulsifiers, as a water-soluble protective film, and as a starting material for the preparation of other resins. The chemical structure of the resulting vinyl alcohol repeating units is shown in the Figure – 1.5.

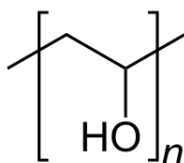


Figure – 1.5. Structural unit of PVA

Experimental
&
Characterization techniques

2.0 Polymer thin film deposition techniques

In recent years, polymer thin film science has grown worldwide into a major research area. The significance of thin film coatings and the synthesis of new materials for industry have resulted in a tremendous increase of innovative thin film processing technologies. The major exploitation of thin film science is still in development state and goes hand – in – hand with the explosion of scientific and technological breakthrough in microelectronics, optics and nanotechnology. Currently, rapidly changing needs for thin film materials characterization and fabrication of devices are creating new opportunities for the development of new processes, materials and technologies. Therefore, basic research activities will be necessary to improve knowledge, understanding and to develop predictive capabilities for relating fundamental physical and chemical properties to the microstructure and performance of polymer thin films in various applications. Results of combined experimental and theoretical investigations are prerequisite for the development of new thin film systems and the tailoring of their microstructure and performance.

The thin film technology activity is represented by a relatively new research area, called “SURFACE ENGINEERING”. Surface Engineering has been one of the most expanding scientific areas includes the design and processing of surface layers and coatings, internal interfaces and their characterization. This Surface Engineering is directed by the demands of thin film and surface characteristics of materials. These thin film systems necessitate direct control of materials on the molecular and atomic scale, including surface modifications, deposition and structuring. Many these techniques were accountable for remarkable advances in the fundamental understanding of the physics and chemistry of thin films, their microstructural evolution and their properties. This progress has led to the development of novel materials, expanded applications and new designs of devices and functional thin film systems. It is noteworthy that, the quality of thin films, their microstructural and basic characteristics in a device level mainly depend upon type of thin film deposition techniques. There exists a variety of several physical/chemical vapor thin film deposition techniques/technologies originate from purely physical or purely chemical processes. In this regard various thin film deposition techniques were illustrated and discussed about their respective working principles and limitations in comparison to the other film processing techniques.

2.1 Spin Coating technique

Spin coating is a simple process for rapidly depositing thin coatings onto relatively flat substrates. The substrate to be covered is held by some rotatable fixture (using vacuum to clamp the substrates in place) and the coating solution to spread out and leave behind a very uniform coating of the chosen material on the surface of the substrate. The advantage of spin coating is its ability to quickly and easily produce very uniform films from a few nanometers to a few microns in thickness. The use of spin coating in organic electronics and nanotechnology is widespread and has built upon many of the techniques used in other semiconductor industries but also has some differences due to the relatively thin films, and high uniformity that are required for effective device preparation, as well as the need for self-assembly and organization to occur during the casting process [55, 56].

2.2 Dip coating technique

Dip coating is the precision controlled immersion and withdrawal of any substrate into a reservoir of liquid for the purpose of depositing a layer of material. Many chemical and nanomaterial engineering research projects in academia and industry make use of the dip coating technique. Many factors contribute to determining the final state of the dip coating of a thin film. A large variety of repeatable dip coated film structures and thicknesses can be fabricated by controlling many factors: functionality of the initial substrate surface, submersion time, withdrawal speed, number of dipping cycles, solution composition, concentration and temperature, number of solutions in each dipping sequence, and environment humidity. The dip coating technique can give uniform, high quality films even on bulky, complex shapes. The dip coating technique is used to make thin films by self-assembly and with the sol-gel technique. Self-assembly can give film thicknesses of exactly one monolayer. The sol-gel technique creates films of increased, precisely controlled thickness that are mainly determined by the deposition speed and solution viscosity [57 – 59].

2.3 Solution casting technique

Polymer films can be prepared by two distinct casting techniques, which are

- (i) Free casting technique and
- (ii) Blade casting technique.

(i) Free casting technique:

In free casting (FC) technique, pre-prepared polymer solution at optimized conditions, is poured onto a flat-bottomed glass cup without imposing hydrodynamic stress on the liquid. The solvent is allowed to evaporate under ambient conditions until the film hardens. The hardened film is then removed from the cup by washing it off with distilled water and placed in a vacuum oven at 100 °C for 12 h for final drying. DSC and gas chromatography data indicated that this procedure was effective in removing residual solvent and moisture from the film. The thickness of films produced by this method is dependent in a straightforward way on concentration and the volume of liquid in the cup. In this study, the concentration was varied in the range 1-8 (wt/wt) % and the liquid volumes ranged from 5 to 20 mL yielding film thicknesses of 12- 200 pm. The lower limit is due to difficulties in producing self-supporting films with uniform thickness while attempts to produce films thicker than 200 pm usually led to various gross defects, such as "orange peel", on the film surface [60].

(ii) Blade casting technique:

In blade casting (BC) technique, pre-prepared polymer solution is poured onto surface of a substrate and a knife blade uses to spread the liquid over a flat glass substrate. In this process, considerable hydrodynamic stresses are generated during the coating step. Since the liquid films produced are relatively thin, initial solvent removal from the cast layer was relatively fast under ambient conditions-the films were hard to the touch within minutes. The coatings are left at ambient for ca. 12 h, and final solvent is removed by placing the coated substrates in a vacuum oven at 25°C for few hours. After removal from the oven the coatings are soaked in distilled water, peeled off the substrate, and dried again in vacuum for 2 h at 60 °C. It is important to note that the order of peeling the film from the substrate, i.e., before or after drying in the oven, has a significant effect on the properties of the film. The final film thickness was dictated by the blade height and the concentration. The effect of blade height on the thickness of the deposited film can be estimated from the coating dynamics of a slot coater, and the effect of concentration derives from a simple mass balance. The blade height is varied in the range 120 - 760 µm and the concentrations used were 5-20 (wt/wt) %, producing thicknesses in the range 12 - 114 µm [61].

In this technique, the limitations are dictated by difficulties in controlling thickness uniformity (for the thin films) and various surface defects (for the thick films). In both methods, but especially in the BC process, air currents above the drying layers and exceedingly fast drying produced “orange peel” defects on the dried films. To circumvent this problem, the BC films were enclosed in a glass box and a lid was placed on the FC cups while the films were drying at ambient. This slowed down the evaporation rate yielding films with good clarity. Some of the films became opaque due to spontaneous crystallization during the initial drying step. This is prevalent in the thick polycarbonate films. When the enclosing box was gradually removed, the drying rate was increased and the crystallization process could be effectively suppressed.

2.4 Electrochemical polymerization

In polymers thin films technology, the emergence of advancements made in electrochemical polymerization (ECP) technique which is a fast developing field interfacing polymer science and electrochemistry. It provides a novel approach to the synthesis of conducting polymers. ECP is normally carried out in a single compartment electrochemical cell by adopting a standard three electrodes configuration and typically electrochemical bath consists of a monomer and a supporting electrolyte dissolved in appropriate solvent. ECP can be carried out either potentiostatically (i.e. constant voltage condition) or galvanostatically (i.e. constant current condition) by using a suitable power supply. Potentiostatic conditions are recommended to obtain thin films while galvanostatic conditions are recommended to obtain thick films [62, 63].

2.5 Spray – coating technique

Spray coating in general includes the formation of fine droplets of a coating solution and their deposition and coalescence on a substrate. The liquid to be used for coating breaks up into small droplets by atomization in the spray nozzle. The generated droplets are then deposited on a substrate kept below the spray nozzle where they coalesce to form a coating. Conventionally, air pressure is used for the atomization where the liquid coming through the nozzle is broken down into tiny droplets upon passage through a narrow orifice [64]. Alternatively, the ultrasonic atomization technique, in which high frequency sound vibration generates a fine mist of solution, is used for spray coating and often preferred over pneumatic atomization [65].

Overall, the advantages of ultrasonic spray coating are as follows: simplicity, good transfer efficiency, economical, precise conformal coating on planar and nonplanar surfaces, generation of small droplets in the micrometer range, and good reproducibility [66, 67]. Spray coating is associated with many material and process parameters which must be controlled in order to obtain a uniform film. The concentration of the polymer solution, the solvent used, the substrate on which the solution is sprayed, the number of spray passes, the flow rate of the polymer solution, the temperature of the substrate, the distance between the spray nozzle and the substrate, the speed of the moving nozzle during spraying, and the air pressure which transports the sprayed droplets to the substrate are all to be taken into consideration.

2.6 Thermal Evaporation technique

Thermal evaporation technique is one of the widely used deposition technique for the preparation of polymer thin films. The physical stages of film formation consists of several distinguishable steps of film as (1) sublimation of the material to be deposited to the vapor phase, (2) transfer of vapors from the evaporant to the substrate, (3) condensation of vapors upon arrival on the substrate and their rearrangement or modifications of their building on the substrate surface. In this method, materials sublime at lower temperature under vacuum and mean free path of the vapor atoms is considerably large at lower pressure and hence a sharp pattern of the film is obtained. The characteristics of the films are influenced by rate of evaporation, pressure during deposition, thickness of the film, angle of evaporation, temperature of the substrate and residual atmosphere. All these parameters can be controlled in the thermal evaporation technique [68, 69].

Resistive heating is one of the simple and versatile physical vapor deposition techniques, using which a large variety of materials can be evaporated onto different substrates. In this method, the material to be deposited is heated resistively or radiative to a very high temperature in a very low pressure ($< 10^{-6}$ Torr) till it vaporizes. The vapor species thus created in extremely clean ambient are transported through vacuum to condense on the substrates placed above the source to form a pure

film. A variety of heating sources are used to evaporate materials depending on the form of availability such as wire, powder, foil, solid etc., of the evaporate material.

2.7 Sputtering technique

(a) DC sputtering:

When the surface of a material is bombarded with high velocity positive ions, the atoms of the surface will be ejected, this phenomenon is known as sputtering. The atoms ejected from the surface can be condensed on a substrate to form a thin film. The energetic particles, which cause sputtering, may be ions, neutral atoms, neutrons, electrons or protons. Most sputtering applications are performed by the bombardment with ions. The sputtering yield is the most important parameter for characterizing the sputtering process. The sputtering yield depends on the bombarded material, its structure, composition, the characteristics of the incident ion and also the experimental geometry. Now a day the sputtering has become one of the most versatile techniques in thin film technology for preparing the thin films of almost all the material [70].

(b) RF sputtering:

It is difficult to sputter the insulating target by DC sputtering. If an insulator target is substituted for metal target, a surface positive charge built upon the front surface of the insulator during ion bombardment. This charge build up can be prevented by simultaneous bombardment of the insulator with ion beam and electron beam particles. Alternatively, applying a RF potential to the metal electrode placed behind the dielectric plate target can prevent the charge accumulation on the surface. At RF potential, the electrons oscillating in the alternating field have sufficient energies to cause ionizing collisions and the discharge will be self-sustained. The high voltage at the cathode, which is essential in a DC glow discharge for the generation of secondary electrons, is no longer required here for the discharge to maintain itself. Since the electrons have much higher mobility than ions, many more electrons will reach the dielectric target surface during the positive half-cycle than ions during the negative half – cycle, and the target will become self – biased negatively. The negative DC potential on the insulating target surface repels electrons from the vicinity of this surface, creating an enriched sheath.

The ions in front of the target bombard the target and process the sputtering. It should be noted that since the applied RF field appears between the two electrodes, an electron escaping from the inter electrode space as result of random collision will no longer oscillate in the RF field. Therefore, these electrons will not get sufficient energy to cause ionization hence will be lost from the glow. But if magnetic field is applied parallel to the RF field, it will constrain the electrons without being lost to the flow, thus improving the efficiency of the RF discharge. So a magnetic field is more important in RF sputtering than in the DC case. A grounded metal is placed close to the other side of the metal electrode to extinguish the glow on the electrode side and to prevent sputtering of the metal electrode. Thin films of quartz, aluminum oxide, boron nitride and various glasses have been prepared using RF sputtering. Although good quality films have been prepared by sputtering, this technique has the disadvantage of being a low deposition rate process. Moreover, the films produced by sputtering require a post-deposition heat treatment in appropriate ambient conditions [71, 72].

2.8 Chemical Vapor Deposition technique

The CVD technique has been the most commonly employed thin-film deposition technique in the industry for the deposition of inorganic thin films, due to the robustness and the low cost of the process [73]. CVD of inorganic films requires high substrate temperatures and high powers which would damage the functional groups of the polymer and lead to undesirable crosslinking, therefore, CVD is traditionally not compatible with polymer thin-film deposition. However, through modifications of the CVD reactants or reactor designs, polymer depositions at low temperatures and low-energy inputs can be achieved, making CVD a widely used technique for polymer deposition [74]. Deposition of highly cross-linked, insoluble polymers, copolymers of incompatible monomers (organic networks) or conducting polymers can easily be achieved using CVD. The CVD also allows the application-specific tuning of the chemical compositions of the copolymers to achieve the desired response. The polymer CVD techniques can be categorized according to the polymerization mechanism, such as chain-growth and step-growth of polymers.

(i) Chain-growth CVD polymers:

Free-radical polymerization is one of the most common polymerization methods in which chains with free-radical species are successively added to form the polymer. Almost any chemical with a vinyl group can be polymerized using this method. The first step of the polymerization is the initiation step which involves creation of free radicals that are highly reactive due to their unpaired electron. Free radicals can be created using an initiator; light, heat or redox reaction. These radicals then react with the monomers creating free-radical active sites. The second step is the propagation step where the polymer chains grow by the addition of monomer molecules to the free-radical active sites. The active site is then transferred to the end of the newly added chain. The third and the final step is the termination step which can occur via several mechanisms. The active sites of two chains or the active site of a chain and a free radical can meet and react which terminates the chain propagation. Another possibility is that the active chain site can react with a non-radical molecule which may not transfer the active site further and thus, terminates the chain.

(ii) Step-growth CVD Polymers:

Step-growth polymerization proceeds by the reaction of functional groups rather than of a free-radical chain end. In step growth, increases in chain length are achieved sequentially through pairwise reactions between monomers, dimers and higher oligomers. Step-growth polymerization is further categorized as either addition or condensation polymerization. For addition polymers, such as polyurethane, the only product is the polymer chain itself. In contrast, condensation polymerization also results in the release of small molecules, such as water. Common condensation polymers are polyamides, polyesters and polyacetals. One process that utilizes step polymerization as a vapor-phase deposition technique is the vapor deposition polymerization (VDP) method which involves the condensation polymerization of two vapor-phase monomers on a surface without the use of initiator species or initiating plasma or hot filaments. Instead, the monomers are evaporated inside the crucibles and are directly sent to the cooled sample surface enabling the deposition of monomers with low volatility. Poly(amides), poly(amino acids) and poly(imides) are some of the polymers that have been deposited using VDP.

2.9 Pulsed laser deposition (PLD) technique

Pulsed laser deposition (PLD) is a thin film growth technique in which the photon energy of a laser characterized by pulse duration and laser frequency interacts with a bulk material. As a result, material is removed from the bulk depending on the absorption properties of the target materials. A laser pulse is focused onto the surface of a target (solid or liquid) in a vacuum chamber and thereby removes material. A significant removal of materials occurs above a certain threshold power density, and the ejected, partially ionized material forms a luminous ablation plume. Polymers are a class of materials which require low threshold fluencies for a gentle processing (reduced energy and heat transfer). This makes them suitable candidates for low power laser ablation. The ablation of polymers developed a variety of applications, ranging from drilling to ophthalmology. For ablation, the UV region of the spectrum is of interest, because it allows involving photochemical degradation which is intrinsically more precise than thermal decomposition. The short wavelength is also advantageous for a precision processing operating at the diffraction limit. Most commercial polymers absorb below $\lambda = 250$ nm and these polymers can be ablated with the corresponding excimer or Nd:YAG lasers. By applying shorter wave length chemical bonds like C-bonds can be broken leading to a carbonization of the surface of these polymers [75, 76].

2.10 History of Plasma

It well acquaint that, in the Universe, matter exists in four different states from the molecular interrelations point of view, namely: solid, liquid, gas and plasma. Simply speaking, plasma is a kind of ionized gas, into which sufficient energy is provided to free electrons from atoms or molecules and to allow both species, ions and electrons, to coexist. Generally, the plasma state can be divided into two main types;

(i). Low-temperature plasma: The state in which only a part of gas molecules is ionized and the gas is a mixture of electrons, ions, free radicals, excited and neutral molecules.

(ii). high-temperature plasma: The state in which all atoms are fully ionized. This type of plasma can be found, for example, in the Sun or in laboratories involved in nuclear fusion research, but this type of plasma is rather not interesting as a technology for the preparation of new materials.

The low-temperature plasma can be divided, in turn, into two further types, such as equilibrium and non-equilibrium plasmas. In the equilibrium plasma, often called the thermal plasma, electrons and the rest of plasma species have nearly the same temperature ($T_e \approx T_{\text{gas}}$), much higher than the room temperature. Such plasma can be generate in plasma jets and torches. On the other hand, the non-equilibrium plasma, called sometimes the cold plasma, is characterized by the lack of thermal equilibrium between electrons and the rest of plasma species. In this case the electron temperature is in the range of 10^4 – 10^5 K, whereas the rest of the species are at temperature close to the room temperature. Under such conditions, chemical processes (e.g. chemical synthesis of new materials) can be performed at the room temperature using energetic electrons to cleavage covalent bonds in the gas molecules. By contrast, very high temperature of all the species in the thermal plasma considerably limits its application for the chemical syntheses and the surface modifications of thermal-degradable materials.

As one can see, among the various types of plasmas, the cold plasma is especially recognized as a promising tool on the road towards the search for new materials. The creation of such materials by the cold plasma technology can be carried out in two ways; the first one is the deposition of completely new materials in the form of thin films, which is mainly accomplished by plasma polymerization processes (sometimes not quite correctly called plasma-enhanced chemical vapor deposition (PECVD)), and also, but relatively more rarely, by reactive sputtering processes. Thin-film materials with unusual chemical constitution, molecular construction and nanostructure can be obtained in this way. The second way consists in the modification of conventional materials, performed by their cold plasma treatment. Generally, such a treatment triggers three basic processes occurring mainly on the surface. It can create new functional groups by implantation of atoms present in the plasma, it can generate free radicals that then react with atmospheric oxygen and water molecules giving additional functional groups or can be used in

grafting processes, and finally it can modify the microporous structure by the etching and degradation effects.

The development of the physics and technology of polymer thin films has significantly been stimulated by their utilization in Opto-electronic industry, sensors and for numerous conventional and high-tech applications. In this direction, plasma deposition, treatment, and etching of polymers is an important branch of plasma-materials interactions involving technologies that are progressively replacing the standard one in many fields of materials and surface science. It is well acknowledged that, plasma assisted thin film deposition methods have been distinguished as industrially viable and pioneered to grow 'uniform and less concentration of structural defective' thin films at lower substrate temperatures. The plasma polymerization is one of the plasma assisted polymerization technique and relatively simple single-step technique to deposit pinhole free, uniform and conformal organic thin films of conducting polymers consisting novel surface properties with wide functionalities. Plasma polymers are deposited on surfaces contacting a glow discharge of organic (or) organometallic feed gases in the form of a thin film and/on as a powder [77]. Plasma polymerization is a specific type of plasma chemistry, which involves reactions between plasma species, between plasma and surface species, and between surface species [78, 79].

In the cases of a free-radical mechanism, two types of reactions may be postulated: (i) *Plasma-induced polymerization*, and (ii) *Plasma-state polymerization*. Plasma-induced polymerization is the conventional free-radical induced polymerization of molecules containing unsaturated carbon-carbon bonds; the plasma-state polymerization depends on the presence of electrons and other energetic species in plasma to break any bond. Unlike conventional polymer, plasma polymers do not consist of chains with regular repeat unit, but tend to form an irregular three-dimensional cross-linked network. The chemical structure and physical properties may be quite different from the conventional polymer which is derived from the same starting materials. Plasma-polymerized films are generally chemically inert, insoluble, mechanically tough, thermally stable, and have been used in wide variety of applications [80, 81]. In this method, established plasma discharge initiates and dissociates the monomer molecules I into neutral particles and reactant fragments in

the form of electrons, ions and free radicals. The product of recombination of these fragments on over surface of substrates is a highly branched and cross linked by three dimensional network of a plasma polymer. The plasma polymerization process offers several advantages over conventional polymer synthesis;

1. The starting fee gases used may not contain the type of functional groups normally associated with conventional polymerization;
2. Plasma polymerization is essentially an atomic process and in most cases plasma polymers are highly branched & highly cross-linked;
3. Such films are often highly coherent and adherent to a variety of substrates, including conventional polymers, glasses, and metals;
4. Polymerization may be achieved without the use of solvents and a wide range of compounds can be preferred as a monomer and even saturated hydrocarbons.
5. Plasma polymer films can be easily produced with thickness of 500 Å to 1 μm;
6. Ultrathin, “pin-hole” free films may be prepared;
7. Through careful control of the polymerization parameters, it is possible to tailor the films with respect to specific chemical functionality, thickness and other chemical and physical properties by controlling the growth parameter like monomer flow, substrate temperature and plasma power.

2.11 The plasma approximation

Charged particles must be close enough together that each particle influences many nearby charged particles, rather than just the interacting with the closest particle (these collective effects are a distinguishing feature of plasma). The plasma approximation is valid when the number of electrons within the sphere of influence (called the Debye sphere whose radius is the Debye screening length) of a particular particle is large. The average number of particles in the Debye sphere is given by the plasma parameter Λ .

When speaking about the plasma parameter one considers the bulk plasma. The plasma parameter is number, usually denoted by a capital Λ , which measures the average number of electrons contained with Debye sphere (a sphere of radius the Debye length) in plasma. It is defined as $\Lambda = (4\pi n \lambda_D^3)/3$, where n is the number of density of particles, and λ_D is the Debye length. In plasma physics, the Debye length

(named after the Dutch physical chemist Peter Debye) is the scale over which mobile charge carriers (i.e electrons) screen out electric fields in plasmas and other conductors.

$$\lambda_D = \sqrt{\frac{\epsilon_0 k / q_e^2}{\frac{n_e}{T_e} + \sum_{ij} j^2 n_{ij} / T_i}} \dots\dots\dots (2.1)$$

Where, $\lambda_D, \epsilon_0, k, q_e, T_e, T_i, n_e, n_{ij}$ represent Debye length, permittivity of the free space, Boltzman constant, electron charge, temperatures of the electrons and ions, density of electrons and density of atomic species i, respectively and with positive ionic charge $j q_e$. The ion term is often dropped, the resulting formula for the Debye length being,

$$\lambda_D = \sqrt{\frac{\epsilon_0 k T_e}{n_e q_e^2}} \dots\dots\dots (2.2)$$

Although this is only valid when the ions are much colder than the electrons. In other words, the Debye length is the distance over which significant charge separation can occur. In space plasmas, where the electrons density is relatively low, the Debye length may reach macroscopic values, such as in the Magnetosphere, Solar wind, Interstellar medium and Intergalactic medium. Taking into account a Maxwell-Boltzmann distribution with three degrees of freedom, $\langle E \rangle = \left(\frac{3}{2}\right) (k_B T)$, 1 degree Kelvin corresponds to 8.6×10^{-5} eV.

2.11.1 Bulk interactions:

The Debye screening length is short compared to the physical size of the plasma. This criterion means that interactions in the bulk of the plasma are more important than those at its edges, where boundary effects may take place.

2.11.2 Plasma frequency:

The electron plasma frequency (measuring plasma oscillations of the electrons) is large compared to the electron-neutral collision frequency (measuring frequency of collisions between electron and neutral particles). When this condition is

valid, plasmas act to shield charges very rapidly – quasi neutrality is another defining property of plasmas. If we consider a neutral plasma, consisting of a gas of positively charged ions and negatively charged electrons, then, if there is displacement by a tiny amount of all the electrons with respect to the ions, the Coulomb force pulls back, acting as a restoring force. If the electrons are cold, then the charge density oscillates at the plasma frequency:

$$\omega_{pe} = \sqrt{\frac{ne^2}{m\epsilon_0}} \dots\dots\dots (2.3)$$

Where n is the density of electrons, e is the electric charge, m is the mass of the electron, and ϵ_0 is the permittivity of free space. The formula is derived under the approximating that the ion mass is infinite. This is generally a good approximating, as the electrons are so much lighter than ions.

2.12 Types of Plasmas

Temperature is one way of classifying plasmas [82]. The ,most important temperatures that characterize plasma are:

1. The gas temperature, which characterizes the translational energy of the gas;
2. The excitation temperature, which characterizes the energy of the excited particles in the plasma;
3. The ionization temperature, which characterizes the ionization energy;
4. The dissociation temperature, which characterizes the dissociation energy;
5. The radiation temperature, which characterizes the radiation energy.

Complete thermodynamic equilibrium cannot be achieved in the plasma as the radiation temperature cannot equal the temperature in the plasma bulk. However, local thermodynamic equilibrium (LTE) can be reached in laboratory environment. Based on the presence or absence of this local thermodynamic equilibrium, laboratory and industrial plasmas are two types.

2.12.1 Thermal Plasma:

When there is existence of LTE, the plasma is called thermal plasma. LTE can exist when the heavy particles are very energetic, at temperatures of the order of $10^6 - 10^8$ K.

2.12.2 Cold Plasma:

In low-pressure discharges, LTE is not achieved. In the case, the electron temperature is much higher than that of the heavy particles. The electron temperatures can reach values as high as $10^4 - 10^5$ K, while the gas temperature can be as low as room temperature. This non equilibrium characteristic allows the cold plasma to have physical and chemical reactions at relatively low temperatures. Cold plasmas are generated by means of radio Frequency (RF), DC and microwave excitation.

2.12.3 The advantages of Plasma processing:

- (a). Environmentally benign process, as it does not have any residues;
- (b). It is room temperature process;
- (c). Plasma polymers can be deposited on a wide variety of substrates;
- (d). Uniform pinhole free films can be deposited;
- (e). Films have excellent adherence to the substrate.

2.12.4 Disadvantages of Plasma processing:

- (a). The deposited films have low abrasion resistance;
- (b). Owing to very low deposition rates, only thin films can be deposited economically on high production items;
- (c). All the surfaces “seen” by the plasma are coated. This makes reactor cleaning essential for consistent results;
- (d). Retrofitting equipment is expensive.

2.13 Plasma polymerization

Plasma polymerization is the deposition of thin films on substrate surfaces from organic monomers by means of plasma. Plasma polymers have been observed since the early 19th century in the form of oily products on electrode surfaces and walls of reactors, when working with electric discharges in a glass reactor [83 – 86].

However these were through of as annoying by-products of electric discharge process. It was not until the late 20th century that the specific characteristics of these films were studied and their reaction mechanisms elucidated [87 – 91].

Plasma polymerization is different from conventional polymerization in the fact that it may be characterized as elemental or atomic polymerization [92]. This is because in glow discharge polymerization the monomer structure is not retained, but the original monomer molecules serve as a source of elements for the formation of large molecules. This, plasma polymer is not usually identified from the starting material. The polymerization mechanisms and structure of the plasma polymer is deduced from the breakdown of monomer molecules based on the strength of their chemical bonds.

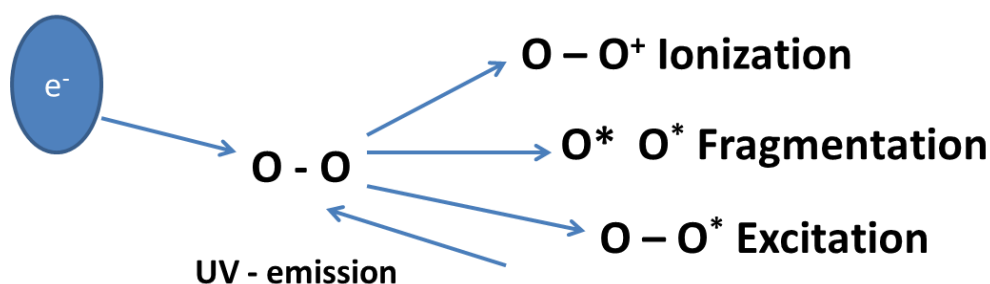


Figure – 2.1. Elemental process in a plasma

Unlike conventional polymerization, most of the reactions in plasma polymerization are one-step reactions between two reactive species. Some other reactions are between activated species and a molecule, which are essentially the same as the propagation reaction of the conventional addition polymerization as represented in Figure – 2.1. Such reactions can proceed in a chain mechanism if the reacting molecules has the appropriate molecular structure. However, even in such cases the formation of polymerization is because of the very low ceiling-temperature of addition polymerization in vacuum.

Plasma polymerization is usually initiated and generated in the vapor phase during the plasma process. As polymerization proceeds, the growing polymer cannot remain in the vapor phase and diffuses to a surface. Reactive species in the gas phase, such as ions and free radicals, may simultaneously interact with surfaces inside the

plasma reactor that have been activated by the impact of the glow discharge to form ions or free radicals from the surface molecules of substrates. As the ions and free radicals do not distinguish between the various substrates, they interact and form polymers on all the substrates, including the walls of the reactor. Plasma polymer film deposition and growth steps on that surface may follow [93].

The homogeneous polymerization in the plasma phase and heterogeneous polymerization at the surface of the growing film can be summarized by the reaction scheme proposed originally by Poll et al. [94]. As shown in this Figure – 2.2, the gaseous precursor monomers can polymerize in the plasma and deposit as film (reaction path 1, characterized by a rate k_1), be converted in the plasma into reactive products (path 2), or be converted in non-reactive products (path 4). The reactive products can convert into depositing polymer film (path 3) or can be converted to non-reactive products (path 5). Degradation of the polymer film can occur to form non-reactive products (path 6).

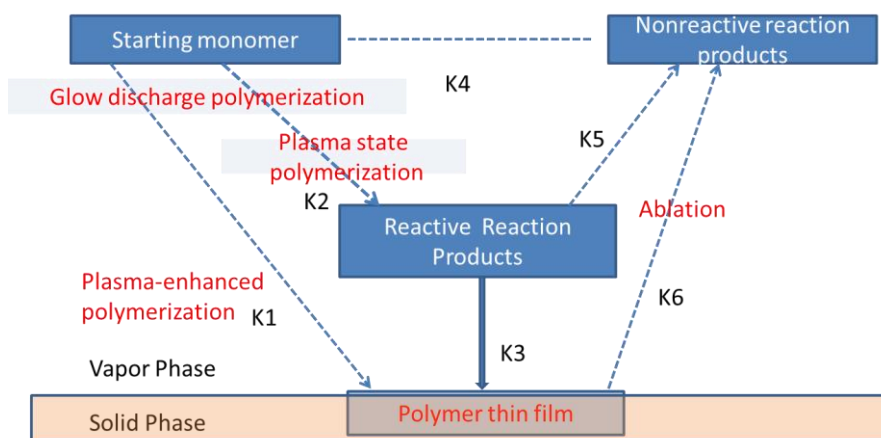


Figure – 2.2 Diagram of plasma polymerization.

path 1, by which the monomer is directly polymerized into the growing film, is also called plasma induced polymerization. This is essentially a conventional molecular polymerization process, triggered in this case by reactive plasma species. Plasma induced polymerization can take place only if the original monomer contains polymerizable functional groups, such as double, triple, or cyclic bonds [95]. Deposition of a polymer film through path 2 and 3 is considered as ageing plasma polymerization. In plasma polymerization, the intermediate reactive products can be

ions, excited molecules, and free radicals not necessarily preserving the original monomer. The monomer does not need to have polymerizable groups in order to undergo plasma polymerization.

As the monomer molecules in plasma, for the most part, become shattered into reactive particles, there remain at most, only partially preserved chemical structures of the output gases in the product, which results in cross-linked and disordered structural preservation and crosslinking gradients can be controlled through process parameters, such as pressure, working gas flow and applied electrical output; so that one can also construct so called gradient layers (i.e with increasing degree of crosslinking over the thickness). The variety of obtainable plasma polymer layers can be increased if we mix the monomer with gases, which are typically used for modification processes (Figure – 2.3). The result will be a modified plasma polymer layer, which combines the principal advantages of the plasma with the functionality of a plasma modified surface [96 – 101].

Oxygen	Modification of polymer, cleaning, degreasing and hydrophilisation	Hydrocarbons Ethylene, Ethane, Acetylene, Methane	polymerization
Hydrogen	Cleaning of meals Reduction of oxidized layers	CF ₄ , SF ₆	Etching
Nobel gases He, Ne Ar	Activation and degreasing	Fluorocarbons C ₂ F ₄ , C ₂ F ₆ , ...	Hydrophobisation Polymerisation
Nitrogen	Activation of polymers	Si-organic reagents HMDSO, TMS, ...	Polymerixation
N ₂ O, CO ₂ , NH ₃ , ...	Modification		

Figure – 2.3: Commonly used gases for plasma surface deposition and plasma treatment.

2.14 Criteria of Monomer Choice

The selection criteria of a suitable chemical precursor for coating applications are that the precursor [102].

- (i). is stable at room temperature;
- (ii). Has low vaporization temperature and high saturation of vapour pressure;
- (iii). Can generate vapour that is stable at low temperature (i.e before decomposing or reacting at higher temperature);
- (iv). Has suitable deposition rate. Low deposition rates for thin film applications (e.g semiconductor industry) and high deposition rates for thick coating applications;
- (v). Undergoes decomposition/chemical reaction at temperature below the melting temperature and phase transformation of the substrate depending on the engineering applications.

2.15 Plasma Reactors types

The main categories of reactor designs (based on the used electrical sources) are presented below [103]. There are three types of plasma reactors for plasma polymerization of organic monomers. Radio frequency (RF) (usually 13.56 Hz) and microwave (MW) (2.45 GHz) are mainly used when the substrates are insulating materials. DC reactors, which have a direct current source, are simpler than the other two categories and are the best ones for electric conductive substrates. The substrates can act as electrodes of the DC reactor. Currently, the RF reactor is the most plasma reactor, because the MW reactor is too complicated and DC has some restrictions about the substrates.

(a) DC plasma Reactor:

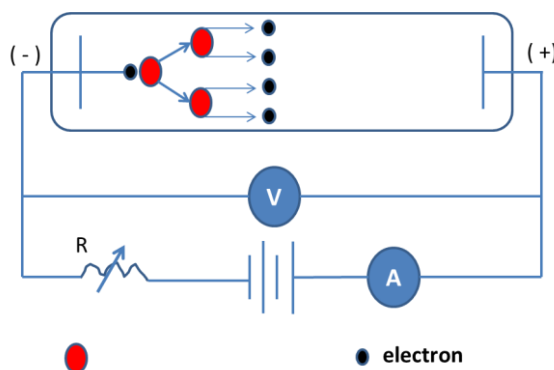


Figure – 2.4: Diagram of a DC Plasma Reactor

In DC plasma reactors, the plasma is sustained between two parallel plate electrodes as shown in Figure – 2.4, and the electric power is supplied to excite the plasma in the abnormal discharge mode. The distances between the electrodes and the pressure in the reactor have to satisfy Paschen's law [104].

$$V_b = \frac{C_1(pd)}{C_2 + \ln(pd)} \dots\dots\dots (2.4)$$

Where, p , d , C_1 & C_2 and V_b are pressure of the gas, distance between electrodes, constants (which depend on the nature of the gas) and breakdown voltage, respectively. The power supplies used to sustain EC plasma can generally be used in a constant voltage, constant current, or constant power mode. The power supplies should be able to control the preset value in each mode. The excitation and sustainment of a DC plasma require the use of electrically conductive electrodes and samples. However, electrically insulating films may deposit locally on the surface of the electrodes or samples due to contaminants formed in the plasma. In such cases, local dielectric breakdown normally occurs, causing arcing that results in spikes of high currents. The power supply must be able to withstand these spikes and return to normal operation with shutting off. Nevertheless, it must also be able to distinguish between the transient currents and shorts that may occur between the electrodes and ground surfaces. This feature, called arc suppression, must be a characteristic of a DC power supply of a plasma reactor.

(b) RF Plasma Reactor

RF discharges have many advantages over DC discharges, which explains the wider use of RF plasma as compared to DC plasma:

1. RF plasma can be excited and sustained using either conductive or nonconductive electrodes, while DC discharges require the electrodes to be conductive throughout the process;
2. RF plasma can be sustained with internal as well as external electrodes, while DC discharges require the electrodes to be inserted inside and reactor and be in direct contact with the plasma. Use of external electrodes is sometimes required when the

gases of the discharge are corrosive or when it is necessary to reduce contamination of the plasma with the material of the electrodes;

3. RF plasmas are characterized by higher ionization efficiencies than the DC plasma;
4. RF plasma can be sustained at lower gas pressures than DC plasma;
5. In RF plasma the energy of the ions bombarding the sample is controlled by the negative bias, which can be adjusted over a wide range of values. Samples placed on the cathode of the DC discharge are exposed to bombardment of high – energy ions that are accelerated at voltages that have to be above the minimal breakdown voltage. This can cause damage to sensitive substrates.

A typical RF-plasma system is shown in Figure – 2.5. These kinds of reactors couple the RF power to two parallel electrodes inserted the reactor. The coupling is done through special RF Vacuum feedthroughs. One electrode is often grounded together with the walls of the reactor. This arrangement is also called a diode or parallel plate reactor. This is the most common approach in the design of industrial RF plasma reactors, but it is not suitable for some specific processes (use of powders etc.)

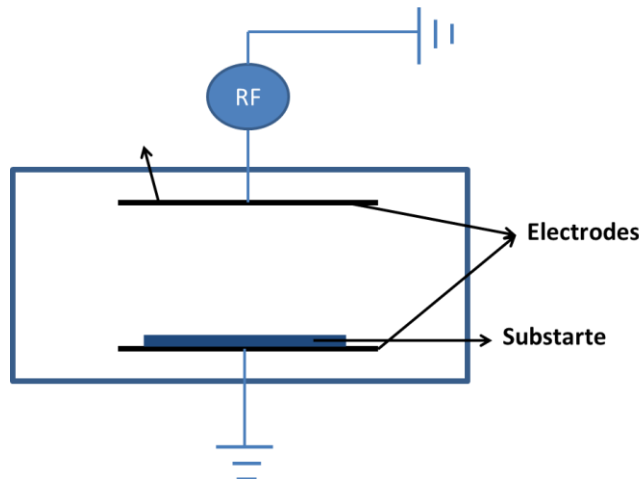


Figure – 2.5 Diagram of a RF plasma reactor

2.16 System Pressure

The system pressure is perhaps the most misunderstood and mistreated parameter regarding the glow discharge polymerization phenomenon. This misunderstanding comes from the lack of distinction between nonpolymer-forming and polymer-forming plasmas. As mentioned earlier, efficient glow discharge polymerization is an excellent pump. Consequently, the polymerization itself changes

the system pressure. Another factor contributing to the misunderstanding is the failure to recognize the effect of product gas. In many cases, the system pressure observed before glow discharge, P_0 , is cited as though it represents the system pressure during glow discharge polymerization, P_g . In some cases P_g can be adjusted with respect to P_0 by controlling the pumping rate. Since P_g is dependent on the production rate of product gas, such an operation is not always possible. Furthermore, in view of the etching effect of the product-gas plasma which is highly dependent on the amount and nature of product gas, such an operation does not seem to have any advantage or significance in controlling the process. The following points clarify the meaning of system pressure in glow discharge polymerization:

1. The system pressure before glow discharge, P_0 , at a given rate is entirely dependent on the pumping rate [105 – 107]. The higher the pumping rate, the lower is the value P_0 .
2. The pumping rate of a system is dependent on the nature of the gas is particularly important when a liquid trap or a turbo molecular pump is employed in a vacuum system,. These are excellent pumps for most organic vapors (starting material of glow discharge polymerization). And some gases; however, they offer virtually no pumping action for H_2 , which is the main product gas when hydrogen-containing compounds are used as the starting material;
3. As far as the gas phase is concerned, glow discharge polymerization acts as an additional pump.
4. Glow discharge polymerization changes the gas from the starting material to the product gas;
5. Consequently, the system pressure with the glow discharge on, P_g , is largely determined by the pumping efficiency of the product gas, the efficiency of the polymerization, and the production rate of the product gas.

6. Therefore, there is no unique relationship between P_g , and P_0 . In a system where the polymerization yield is maintained at nearly 100 %, P_g is determined by the glow rate but not by the value of P_0 .

Since the velocity and the ionization of gas molecules are dependent on pressure [108] the value of P_g (but not P_0) is important in controlling the distribution of polymer deposition and the properties of polymers formed in glow discharge polymerization. Nevertheless, P_g cannot be considered as a manipulate processing factor. The value of P_g can be manipulated to a certain extent, but it is largely determined by the nature of the starting material (i.e gas production rate). A change in pressure also changes the volume and intensity of the plasma, which not only changes the relative position of the polymer-collecting in the plasma but also the ratio of polymer collected on the surface to the total amount of polymers formed. The discussion of polymer deposition rate has a meaning only when the ratio mentioned above is close to unity or at least does not change significantly within the range of experimental conditions.

Therefore, the dependence of polymer de[position rate on the pressure should be interpreted only in the context that the pressure is an empirical controlling factor of plasma reactor.

2.16.1 Flow rate and other factors:

Flow rate determines the amount of gas available for plasma polymerization per unit time and can also be used to determine the deposition rate of plasma polymer [109]. The flow of monomer is generally given by the volume of the gas at standard temperature and pressure per unit time. In the case of low flow rate and low pressure the diffusion of gases is more important than the flow, whereas in the case of higher flow rate and higher pressure the flow plays the more important role. The resident time of monomer molecules in the plasma is dependent on the length of plasma in the direction of displacement (consequently, the volume of plasma) and the mass flow velocity [110].

In the diffusion-dominant case, nearly all monomer molecules coming into the reaction chamber any polymerize; consequently, the apparent rate of polymer

deposition is controlled by the monomer feed-in rate (flow rate). Nevertheless, the deposition rate increases (in the low-flow-rate region) nearly linearly proportionally to the monomer flow rate. As the flow rate increases, the resident time of the monomer in the plasma decreases [111]; as a result the rate of polymer deposition as well as the yield of polymerization both decrease with increasing flow rate. It should be noted here that all these observations were made at a fixed discharge wattage. As mentioned earlier, none of the parameters such as discharge power, flow rate, and system pressure can be treated as an independent parameter. All factors influence the glow discharge polymerization in an interrelated manner, and such a plot merely represents the slicing of a three dimensional profile at a fixed plane. The following aspects should be taken into consideration when one considers the dependence of polymer deposition on operational factors such as pressure, discharge power, and flow rate.

1. The total volume and intensity of plasma changes as the operational factors vary. Therefore, the ratio of plasma volume to the total volume of the system also changes.
2. The surface on which polymer exclusively deposits may change with operational factors. If the polymer deposition rate is measured with a substrate placed on the inside surface of an electrode, it may lead to a dramatic decrease in the polymer deposition rate at lower pressures. However, it may simply be due to the shift of the polymer deposition surface at lower pressure when the polymer starts to deposit more on the other side of the electrode and also on the wall of the chamber.
3. The medium in which glow discharge polymerization occurs is not homogeneous. Therefore, the location of the polymer deposition surface and the type of glow to which the surface is exposed are very important factors.

Other important parameters for a plasma deposition include: the discharge power, geometrical factors of the plasma reactor, nonpolymerizable gas, distribution of polymer deposition etc.

2.17 Cold Plasma Polymerization (CPP)

It is well acknowledged that, plasma assisted thin film deposition methods have been distinguished as industrially viable and pioneered to grow 'uniform and less concentration of structural defective' thin films at lower substrate temperatures [112, 113]. Cold plasma polymerization (CPP) is one of the plasma assisted polymerization technique and relatively simple single-step technique to deposit pinhole free, uniform and conformal organic thin films of conducting polymers consisting novel surface properties with wide functionalities [114, 115]. It refers to the deposition of polymer films through plasma dissociation, in which plasma discharge energizes and dissociates the monomer molecules into neutral particles and reactant fragments in the form of electrons, ions and free radicals. The product of recombination of these fragments on over surface of substrates is a highly branched and cross linked by three dimensional network of a plasma polymer. It evokes that, plasma polymerized polymers are expected to be essentially different in micro-structural and chemical properties from conventional ones, even if the same monomer is utilized for both plasma and conventional polymerizations [116, 117]. The advantages corresponding to cold plasma polymerization can be mentioned as follows;

- (i) Polymer thin films of thicknesses ranging from 1 to 1000 Å can be prepared on variety of substrates;
- (ii) Plasma polymerization is essentially an atomic process and in most cases plasma polymers are highly branched & highly cross-linked;
- (iii) A wide range of compounds can be preferred as a monomer and even saturated hydrocarbons;
- (iv) The monomer used for plasma polymerization does not need to contain a functional group, such as a double bond;
- (v) It is easy to tailor surface morphology and structural properties by controlling the growth parameter like monomer flow, substrate temperature and plasma power. These advantages have resulted in the rapid development of plasma assisted thin film deposition technology during the past decades, for applications ranging from adhesion to composite materials, protective coating, printing, membranes, biomedical etc.

2.18 CPP Experimental Set-up for the Growth of Polymer Thin Films

The home built cold plasma polymerization unit has been adapted to grow PPy thin films of uniform thickness over ITO coated glass substrates and respective schematic representation of the plasma reactor is illustrated in the Figure – 2.6. It consists of a cylindrical shaped glass tube of length 50 cm and diameter around 8 cm, which is clamped between two aluminum metal plates of thickness 1 cm. The bottom aluminum plate is coupled to a vacuum system line and controlled flux of pyrrole monomer (Sigma-Aldrich, MW: 67.09 g/mol) vapor flow is allowed (through inlet provided at top aluminum plate) into the plasma chamber in the proximity of the substrate holder, between the active anode and cathode elements. The whole set up is evacuated to 1×10^{-3} Torr by a rotary pump (EDWARDS, Model: RV 12) and a constant and high density of cylindrical shaped plasma is established between two electrodes by providing electric field between two electrodes using DC source. Electrons emitted by the surface of the cathode are accelerated into the applied electric field of the anode-cathode system and generate excited monomer molecules while en route to the ITO coated glass substrate.

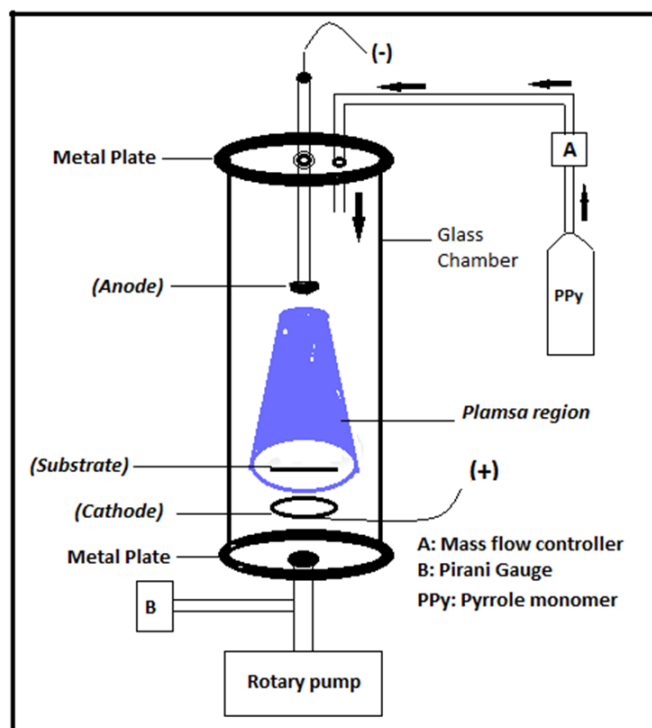


Figure – 2.6 Schematic representation for cold plasma polymerization thin film deposition setup.

Initially, well cleaned ITO coated glass substrates are introduced inside the plasma reactor and placed on top of cathode (which acts as substrate holder). The respective reactor is evacuated to a base pressure of 1×10^{-3} Torr using mechanical pump and followed by a DC voltage is applied across two electrodes to initiate the glow discharge in the reactor chamber. By adjusting the mass flow controller, small amount of PPy vapors are allowed into the reactor chamber for few seconds to strengthen the established glow discharge. In the next step, distance between two electrodes is optimized such that, substrates are in the proximity of dense glow discharge. The DC source voltage is kept constant (at 1 KV) and current value is varied between 10 mA to 50 mA and stabilized the established plasma. PPy vapors are allowed into the chamber at controlled flow rate such that working pressure in the chamber as 1×10^{-1} Torr, so that PPy monomer are entered into the plasma region and interacts with energetic species to polymerize to form uniform and with quality PPy thin films on ITO substrates. PPy monomers are allowed into the chamber for constant deposition time interval of 5 minutes to obtain PPy films of average thickness 250 nm. After the film deposition, the working pressure is bring back to base pressure of 1×10^{-3} Torr

2.19 Characterization Techniques – Polymer Thin Films

In this section, various analytical techniques employed in the characterization of Plasma polymerized thin films are briefly described. The film characterization involves the determination of Micro structure, composition, optical, Surface wetting and dielectric properties.

2.19.1 Structure

Polymer thin film materials are extensively employed in the field of designing and fabrication of various novel devices in the current Science & Technology. In this direction, the peer investigation on the basic structure of used materials and interfaces information in the devices are imperative for the understanding of their properties. Because there is a tendency to investigate how the material properties are modified when they are confined. At present, the study of nano objects becomes very important not only from fundamental point of view to understand, and how the structural confinement influences the physical properties of the materials and also its broad

technological impact. In this respect, X-ray diffraction (XRD) technique has been recognized as a powerful tool to acquaint about structural characterization of the materials. Using this technique unknown phases can be identify by comparing with the ata from known structure, quantify changes in the cell parameters, orientation, crystallite size and other structural parameters. The crystallographic structure, cell parameters, space group and atomic co-ordinates of novel or unknown crystalline materials can be determined using XRD technique.

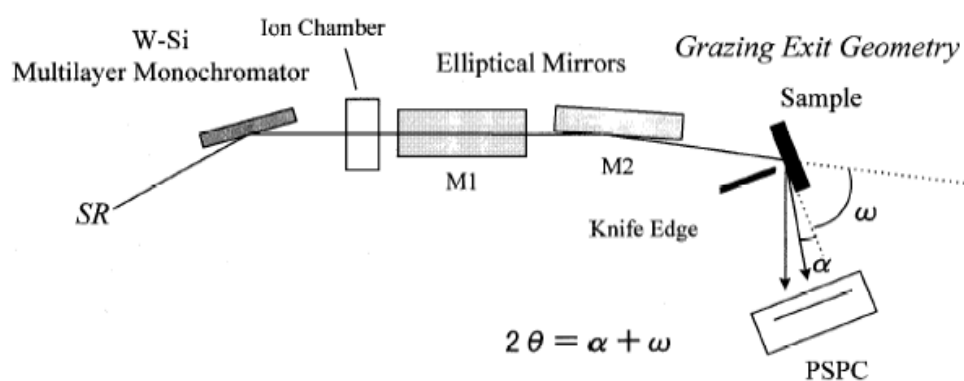


Figure – 2.7 The Grazing incidence X-ray diffraction block diagram

However, in recent years techniques have been devised that in combination with the availability of intense collimated beams from synchrotron sources. These sources can transfer produced X-ray beams into versatile and powerful tool for investigation of surfaces, monolayer and ultra-thin films. Therefore, it is important not only to obtain information about the atomic structure of the material and also about the existence of nano particles in the samples. In this connection Grazing incidence X-ray diffraction technique is acknowledged as efficient tool, which has been commonly employed in surface structure analysis. The basic block diagram is represented in the Figure – 2.7.

In the present investigation, Siefert computerized X-ray diffractometer (model 3003 TT) is employed for the structural analysis of the experimental films. The scanning angle is varied from 15° – 60° and with grazing angle of 3° . The Cu $K\alpha$ target is used as the X-ray source ($\lambda = 1.5418 \text{ \AA}$) and the target is operated at 40 KV

and at 30 mA. From the obtained XRD data the inter planar spacing (d) can be evaluated using the Bragg's relation [118],

$$2d \sin(\theta) = n\lambda \dots\dots\dots (2.5)$$

where „n“ is the order of diffraction ($n > 1$) „ λ “ the wavelength of X-rays and ‘ θ ’ is diffraction angle. Using the estimated ‘d’ values and from the identified set of (h k l) lattice planes, the lattice parameters can be evaluate for the different structures. The crystallite size can be estimated from the obtained GIXRD data by measuring the full width at half maximum (FWHM) values for respective diffraction peaks, which is inversely proportional to the crystallite size L_{hkl} perpendicular to the (h k l) plane.

$$L_{(hkl)} \propto \frac{1}{\beta}$$

$$L_{(hkl)} = \frac{\lambda}{\beta \cos(\theta)} \dots\dots\dots (2.6)$$

This relation is known as Scherrer's Equation.

2.19.2 Atomic Force Microscopy (AFM)

The atomic force microscopy belongs to the family of scanning probe microscopes (SPM), which uses the interaction between a sharp tip and the surface to obtain a topographic representation of the sample. The AFM is being used to investigate the processing and materials problems in a wide range of technologies affecting the electronics, telecommunications, biological, chemical, automotive, aerospace and energy industries. The AFM is being applied to studies such as surface morphology, abrasion, adhesion, cleaning and corrosion. By using AFM one can image surface of the sample in atomic resolution and also measure the force at nano - Newton scale. Unlike traditional microscopes, the AFM does not rely on electromagnetic radiation such as photon or electron beams to create an image [119]. An AFM is a mechanical imaging instrument that measures the three dimensional topography as well as physical properties of a surface with a sharpened cantilever. The sharpened cantilever is positioned close enough to the surface such that it can interact with the

force fields associated with the surface. Then the cantilever is scanned across the surface such that the forces between the cantilevers remain constant. An image of the surface is then reconstructed by monitoring the precise motion of the probe as it is scanned over the surface.

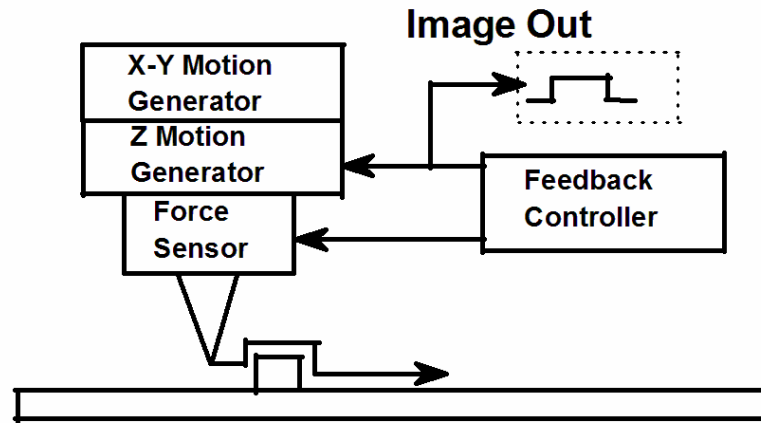


Figure – 2.8 Basic block diagram of an AFM

The significant part of the AFM is the force sensor which transforms the force interaction over the tip-sample junction to an electrical signal that can be handled by the feedback electronics. The cantilevers of AFM are highly flexible, these cantilevers exerts lower downward forces on the sample resulting in less distortion and damage while scanning. For this reason, AFM cantilevers generally have spring constant of about 0.1 N/M. The spring constant of cantilever depends on its shape, its dimensions and the material from which it is fabricated as shown in Figure – 2.8. The resonant frequencies range from few Kilo-hertz to hundred kilo-hertz providing high-speed response. The equation of the resonant frequency of the spring

$$f = \frac{1}{2\pi} \sqrt{\frac{\text{spring constant}}{\text{mass}}} \dots\dots\dots (2.7)$$

The root mean square (rms) surface roughness, defined as the average height deviation from the mean data plane i.e.

$$R_q = \sqrt{\frac{\sum z_i^2}{N}} \dots\dots\dots (2.8)$$

The commercial vendors manufacture almost all AFM cantilevers by micro lithography process similar to those used to make computer chips. The AFM can be compared to traditional microscopes such as the optical or scanning electron microscopes for measuring dimensions in the horizontal axis. However, it can also be compared to profilers for making measurements in the vertical axis to a surface. One of the great advantages of AFM is the ability to magnify the images in three dimensional X, Y and Z axes. The AFM is being used to solve processing and materials problems in a wide range of technologies. The materials being investigated include thin and thick film coatings, ceramics composites, glasses, synthetic and biological membranes, metals, polymers and semiconductors. In the present investigation, Digital Instruments AFM Nanoscope III in a simple contact mode of operation was used for obtaining the AFM images of the grown polymer thin films.

2.19.3 Optical properties

The optical properties like transmittance and reflectance of tungsten trioxide thin films are corded using Hitachi U 3400 UV-Vis-NIR double beam spectrophotometer, with accuracy limits ± 2 nm in the UV-Vis region and ± 1 nm in the NIR region. The optical alignment of the spectrophotometer, the Deuterium (D_2) lamp is used as a radiation source in the UV region and iodine tungsten lamp (W_1) is used in a VIS-NIR region. Light coming from the source is reflected by the concave mirror M_1 which is then chopped in to regular pulses by the chopper CH. This beam passes through the slit S_1 and is directed to the prism (P) by the toroidal mirror M_2 and concave mirror M_3 . The dispersed light beam is focused onto the monochromator (S_2) by the mirrors M_3 , M_4 and M_5 . The light is then reflected onto the gratings G_1 and G_2 with the concave mirror M_6 which again gets reflected by M_6 and M_7 and passes through the rotating mirror M_8 which splits the beam into two paths; one passes through the sample and the other through the reference in the sample compartment. These two beams are directed onto detectors with the help of plane mirrors M_{12} , M_{13} , M_{14} , M_{15} and M_{16} toroidal mirrors. The detectors, photomultiplier tube (R928) [UV-Vis] and Pbs [NIR] are used to measure the difference in the intensities of the sample and the reference beams. The measured optical absorbance/transmittance/reflectance intensity is displayed on the monitor as a function of the wavelength and the spectrum is recorded.

2.19.4 Theory for Optical absorption

According to Beer-Lambert's formula

$$I = I_0 \exp(-\alpha d) \dots\dots\dots (2.9)$$

Here I, I₀, α and 'd' represent Intensity of light after transmission through the sample, intensity of the incident light, optical absorption coefficient and thickness of the film, respectively.

$$\alpha = \frac{2.303 \log\left(\frac{1}{T}\right)}{d} \quad (T = \text{transmittance})$$

$$\alpha = \frac{2.303 * A}{d} \quad (A = \text{absorbance}) \dots\dots\dots (2.10)$$

When the energy of incident photon is greater than that of the band gap ($h\nu > E_g$) the absorption coefficient 'α' can be expressed as follows,

$$\alpha = \frac{A}{h\nu} \left[(h\nu - E_g)^{1/2} + \frac{\pi}{2} \cdot B - B \cdot \text{Sin}^{-1} \left(\frac{h\nu - E_g}{h\nu - E_g + B^2} \right)^{1/2} \right] \dots\dots\dots (2.11)$$

$$\text{Here } B^2 = \frac{(C_c + C_v)^2}{4(b_c + b_v)}, \quad b_c, b_v > 0 \text{ and } C_c, C_v \geq 0$$

$$\text{For } h\nu - E_g \leq B^2 \dots\dots\dots (13)$$

$$\text{Then } \alpha = \frac{A}{h\nu \cdot 3B^2} (h\nu - E_g)^{3/2}$$

$$\text{Therefore } \alpha = \frac{A}{h\nu} (h\nu - E_g)^{1/2} \quad (A = \text{absorption coefficient})$$

2.20 Fourier-Transform Infrared Spectroscopy

The total internal energy of a molecule in a first approximation can be resolved into the sum of rotational, vibrational and electronic energy levels. Infrared spectroscopy is the study of interactions between matter and electromagnetic fields in the IR region. In this spectral region, the EM waves mainly couple with the molecular vibrations. In other words, a molecule can be excited to a higher vibrational state by absorbing IR radiation. The probability of a particular IR frequency being absorbed depends on the actual interaction between this frequency and the molecule. In general, a frequency will be strongly absorbed if its photon energy coincides with the vibrational energy levels of the molecule. IR spectroscopy is therefore a very powerful technique which provides fingerprint information on the chemical composition of the sample.

In the conventional dispersive-type spectrometer, a grating or a prism is used to disperse light into individual frequencies, and a slit placed in front of the detector to determine which frequency to reach the detector. However the FTIR spectrometer operates on a different principle called Fourier transform. The mathematical expression of Fourier transform can be expressed as follows,

$$F(\omega) = \int_{-\alpha}^{+\alpha} f(x) \cdot e^{i\omega x} \cdot dx \dots\dots\dots (2.12)$$

The reverse Fourier transform is, $f(x) = \frac{1}{2\pi} \int_{-\alpha}^{+\alpha} F(\omega) \cdot e^{-i\omega x} \cdot dx$

where ω is angular frequency and x is the optical path difference in our case. $F(\omega)$ is the spectrum and $f(x)$ is called the interferogram. In the present investigation, FTIR studies have been carried out to understand the elemental composition of the films during the growth process. The as prepared plasma polymerized Plasma polymerized films are scarped from ITO coated glass substrates and pelletized by mixing with KBr to record FTIR spectra in the range $4000 - 400 \text{ cm}^{-1}$ by Spectrum One FT-IR Perkin Elmer spectrometer.

2.21 Dielectric Spectroscopy

Dielectric spectroscopy (DS) is a robust and versatile measurement technique with numerous applications in fundamental science and engineering field. The principle which is the basis of this measurement technique (DS) is the correlation between the dielectric behavior of a substance subjected to a time variable electric field, and its microscopic properties. Among its main advantages are its wide frequency range, in fact the modern DS technique may work on frequencies from 10^{-6} to 10^{12} Hz, and the (relative) simplicity of conducting measurements in different conditions of temperature (-170°C to 500°C) and, sometimes, pressure. Dielectric spectroscopy measures the time or frequency dependent response of current and voltage of a sample to a changing electric field. It is especially sensitive to intermolecular interactions and is able to monitor cooperative processes at the molecular level. The outcome of an experiment is typically given in the form of a dimensionless quantity, the complex dielectric permittivity, which depends on parameters like frequency, temperature, and pressure. Experiments can be conducted in the time domain as well as in the frequency domain. In case of a frequency domain experiment a sinusoidal voltage with a fixed angular

frequency is applied and the response for that frequency is obtained, and consequently also Variation of the frequency then gives the full spectrum. Any material can be polarized by an external electric field. Numerous mechanisms can contribute to the polarization, in fact the macroscopic polarization is a result of different microscopic polarization mechanisms (modes) that can be divided in three categories.

2.21.1 Deformation polarization or charge displacement.: The electric field moves the electric charges slightly away from their equilibrium positions, but without causing a real current although. It can be divided into two independent types:

- ✓ **Electron polarization:** This includes the displacement of the electron cloud relative to the core of an atom, movement of the core itself from its equilibrium position in a crystal, and shifts of bonding electron pairs. In this case a dipole moment is induced. Because electrons are very light, they have a rapid response to the field changes; they may even follow the field at optical frequencies.
- ✓ **Atomic polarization:** the displacement of atoms or atom groups in the molecule under the influence of an external electric field.

2.21.2 Orientational polarization: Here dipoles move to new equilibrium orientations. Essentially molecules with an induced or permanent dipole moment, thus caused by some charge distribution in the molecule, reorient themselves to align their dipole moment with the electric field. The rotation is counteracted by the thermal motion of the molecules. Therefore, the orientation polarization is strongly dependent on the frequency of the applied electric field and on the temperature.

2.21.3 Redistribution of free charges or ionic polarization: In a real material, conducting as well as non-conducting, there are always free charges present. These charges will also move through the material under influence of the field and accumulate at the edges of the material, or eventually at internal interfaces in heterogenous systems. This kind of polarization demonstrates only weak temperature dependence and is determined mostly by the nature of the interface where the ions can accumulate. Many cooperative processes in heterogeneous systems are connected with ionic polarization.

Each of these classes has a typical time scale related to it. The larger the unit to be moved and the distance to be bridged, the longer the related time scale. *Charge displacement* takes place at time scales of 10^{-14} s. The displacement of electrons is about one or two orders of magnitude faster than that of the cores of the atoms. Actually, in dielectric experiments it is usually considered an instantaneous process. The electronic polarizability contributes at optical frequencies and is usually considered in terms of the refractive index. The *orientational polarization* covers a broad range of time scales. Factors influencing the speed at which a molecule or a part of it can reorient are, among others, the size of molecule and the intermolecular potentials to overcome. Also the degree of cooperativity is important: some processes involve lots of molecules and thus can be very slow. Typical values are 10^{-9} s for the reorientation of a small molecule to 10^{-2} s for certain cooperative reorientations in liquid crystals or motions in polymers. The redistribution of free charges is generally the slowest process, since it involves the movement of the charge carrier through the material. Thus it will depend on material parameters like the viscosity and on the size of the charge carrier. Thus it will depend on material parameters like the viscosity and on the size of the charge carrier.

In practice the analysis of a dielectric spectrum is based on the determination of the distribution of the relaxation times of the processes that are seen in the spectrum. Although a number of approaches are possible, the presence of computers with some special programs makes it now possible to easily perform non-linear fits to model functions. In the following parts, a number of model functions, will be presented. The collection given here is based on the Debye function, that has been extended empirically to account for certain types of broadening of the spectra.

2.21.4 The Debye relaxation function:

In Figure – 2.9, the Debye function introduced in the previous section, is plotted, splitted in his real and imaginary part. The real part shows a step down, and the half height of this step is found at $\omega = \tau^{-1}$. For the imaginary part, the top of the peak corresponds to this frequency. Here we see that the function is symmetric around $\omega = \tau^{-1}$ and that the half-width is 1.14 decades.

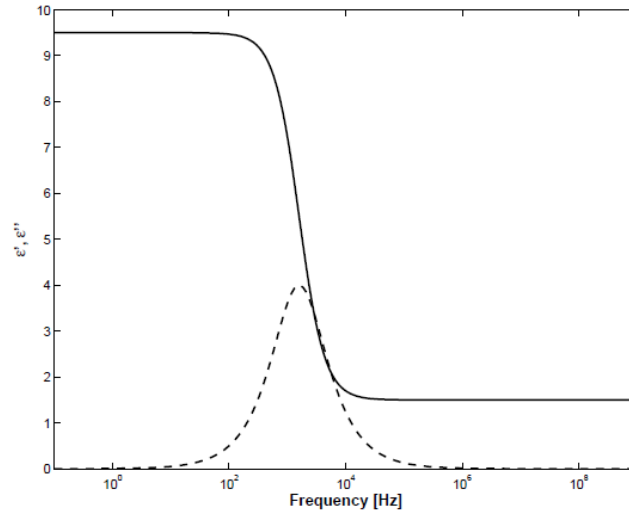


Figure – 2.9 The Debye relaxation function. The full line is the real part ϵ^I and the dashed line is the imaginary part ϵ^{II} . Plotted for ϵ_α , ϵ_s and $\tau = 10^{-4}$ s .

2.21.5 The Cole-Cole relaxation function:

Since in reality a perfect Debye relaxation is rare, some empirical modifications have been made, resulting in broadened peaks in the imaginary parts and smeared out steps in the real part. The Cole–Cole function is aimed at the description of a symmetric broadening of the peak. This is done by expressing the equation as follows,

$$\epsilon^*(\omega) = \epsilon_\infty + \frac{\epsilon_s - \epsilon_\infty}{1 + (i\omega\tau_m)^\alpha} \dots\dots\dots (2.13)$$

The distribution or shape parameter α , which lies between 0 and 1, describes the broadening: $\alpha = 1$ corresponds to the situation of no broadening (the Debye function) and with decreasing α the peak becomes lower and broader. Sometimes one uses $(1 - \alpha)$ instead of α . In Figure – 2.10, real and imaginary part for some values of α are plotted. The maximum of the peak is located at $\omega = \tau^{-1}$.

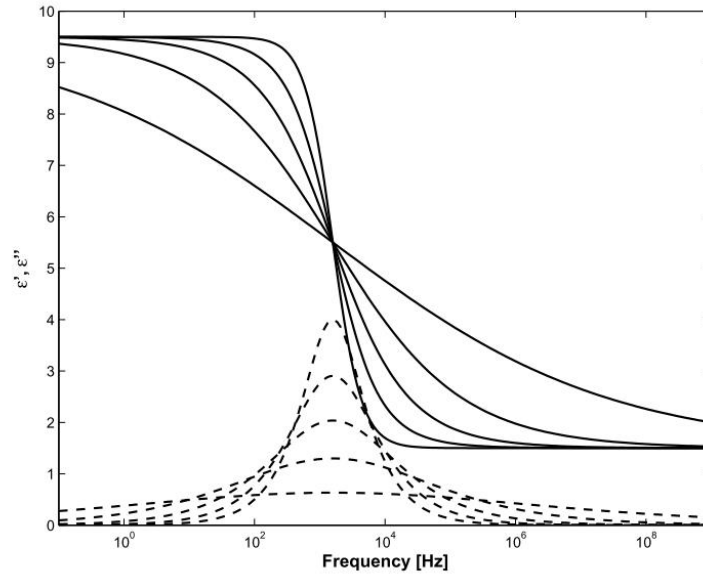


Figure – 2.10 The Cole–Cole relaxation function. The full lines are the real parts and the dashed lines are the imaginary parts. Curves are plotted for $\alpha = 1$, $\alpha = 0.8$, $\alpha = 0.6$, $\alpha = 0.4$ and $\alpha = 0.2$.

2.21.6 The Cole-Davidson relaxation function:

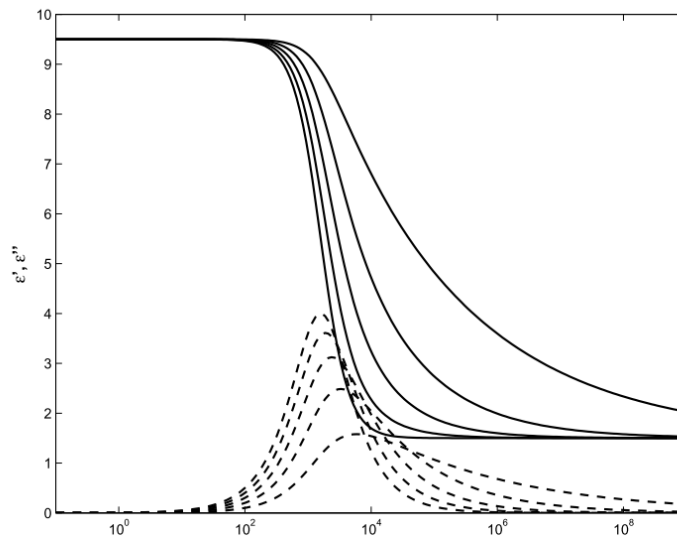


Figure – 2.11 The Cole–Davidson relaxation function. The full lines are the real parts and the dashed lines are the imaginary parts. Curves are plotted for $\beta = 1$, $\beta = 0.8$, $\beta = 0.6$, $\beta = 0.4$ and $\beta = 0.2$.

When the relaxation peak is only broadened at the high frequency side, the Cole–Davidson function can be used. In this case a shape parameter β is introduced, resulting in the expression,

$$\epsilon^*(\omega) = \epsilon_\infty + \frac{\epsilon_s - \epsilon_\infty}{(1 + i\omega\tau_m)^\beta} \dots\dots\dots (2.14)$$

For this expression reduces to the Debye function. β takes values between 0 and 1. Plots of the Cole–Davidson function for some values of β are given in Figure – 2.11.

2.21.7 The Havriliak-Negami relaxation function:

The Havriliak–Negami function is the natural combination of the Cole–Cole and Cole–Davidson functions: it describes the combined symmetric and asymmetric broadening by two shape parameters α and β both between 0 and 1.

$$\varepsilon^*(\omega) = \varepsilon_\infty + \frac{\varepsilon_s - \varepsilon_\infty}{(1 + (i\omega\tau_m)^\alpha)^\beta} \dots\dots\dots(2.15)$$

Additions of other phenomena:

The expressions given in the previous paragraphs describe the orientational polarization. The polarization at high frequencies or short timescales is summarized by a dielectric constant. The only additions to be made are at low frequencies or long timescales. In this regime, the movement of charge carriers through the samples becomes important and it can be observed in the dielectric spectra. The first phenomenon is electrical conduction. This simple movement of charge carriers leads typically to a response that is the same as of an ohmic conductor. It shows only in the imaginary part of the dielectric permittivity. When analyzing a dielectric spectrum, it is accounted for by a term of the form

$$-\frac{i\sigma}{\varepsilon_0\omega^s} \dots\dots\dots(2.16)$$

is the DC electrical conductivity and the exponent ‘s’ is a fitting parameter that has a value of 1 for pure ohmic conduction. Note again that because of its purely imaginary character this term only contributes to imaginary part ε'' . Electrode polarization can be seen as a large rise of ε' for low frequencies. The explanation is that for slowly varying fields, the mobile charge carriers can reach the electrodes. Because they cannot leave the sample they build up a charged layer. This layer masks the electric field in the bulk of the actual sample and gives rise to the increased ε' . Since electrode polarization does not tell much about the sample (actually mainly that it contains free charges), the part with the electrode polarization is often excluded from the analysis. If for some reason it is necessary to include this part, it is fitted with a power law in the real part:

$$A\omega^\lambda \dots\dots\dots(2.17)$$

The exponent n takes values typically in the order of -1.5 to -2. A consequence of electrode polarization is that the power law of the conductivity contribution changes, and that a second power law for the conductivity is necessary. The Maxwell–Wagner effect is equivalent to electrode polarization, but in this case the charges accumulate at the internal boundaries of a heterogeneous sample. In the dielectric spectra this shows up as an ordinary relaxation process. In a formulation with equivalent electrical circuits, it can be shown that a Maxwell–Wagner process appears when a sample consists of two parts with different dielectric permittivity and electrical conductivity.

2.21.8 Basic concepts of measurement technique:

There are a number of possibilities to determine ϵ^* . A first classification to make is between time-domain ($\epsilon^*(t)$) and frequency-domain techniques ($\epsilon^*(f)$). Since in this work time-domain techniques have not been used, all our attention will go to frequency-domain technique. The basis of any measurement of $\epsilon^*(f)$ is essentially a determination of the impedance Z of the sample. It then requires some simple calculation to arrive at a value for ϵ^* . In the simplest case, that of a pure capacitor, the value of the impedance is given by

$$Z_c = \frac{1}{\omega C} \dots\dots\dots (2.18)$$

Where $\omega = 2\pi f$. For the case of a dielectric sample cell, one can use either a measured value of the vacuum capacitance or the equation for the geometrical capacitance, for example equation 2.2 in the case of a parallel plate capacitor. One gets

$$\epsilon = \frac{C}{C_0} \dots\dots\dots (2.19)$$

In reality the impedance is a complex number and the complex form of Z_c is:

$$Z_c^* = \frac{1}{i\omega C} \dots\dots\dots (2.20)$$

This means that also the phase information must be measured, to allow for the determination of both real and imaginary part of ϵ^* . Suppose that a sinusoidal voltage is applied to the sample and the voltage over and current through the sample are determined, including the phase information. This gives:

$$V(t) = V_0 \exp(i\omega t) \dots\dots\dots (2.21)$$

$$I(t) = I_0 \exp(i\omega t + i\phi) \dots\dots\dots (2.22)$$

so the complex impedance becomes

$$Z^* = \frac{V_0}{I_0} \exp(i\phi) \dots\dots\dots (2.23)$$

and the complex permittivity looks like

$$\epsilon^* = \frac{-i}{\omega Z^*} \frac{1}{C_0} \dots\dots\dots (2.24)$$

The value obtained for ϵ^* is that corresponding to the frequency of the applied field.

The present discussion could be considered very short but we can justify it considering that modern dielectric equipment is like a black box that when operated correctly gives the right value of complex permittivity.

2.22 Surface wetting properties

The topic of wetting has received tremendous interest from both fundamental and applied points of view. It plays an important role in many industrial processes, such as oil recovery, lubrication, liquid coating, printing, and spray quenching. In recent years, there has been an increasing interest in the study of superhydrophobic surfaces, due to their potential applications in, for example, self-cleaning, nanofluidics, and electrowetting. Wettability studies usually involve the measurement of contact angles as the primary data, which indicates the degree of wetting when a solid and liquid interact. Small contact angles (90°) correspond to high wettability, while large contact angles (90°) correspond to low wettability.

In the present investigation, CAM 200 Optical Contact Meter (KSV instruments Ltd) is used to study surface hydrophilic nature of grown thin films. KSV's CAM 200 is a fully computer controlled instrument based on video capture of images and automatic image analysis for measuring static or dynamic contact angles, surface or interfacial tensions of liquids, surface free energies, and absorption of liquids into porous materials. CAM 200 uses drop shape analysis for determining static or dynamic contact angles, absorption and surface/interfacial tensions of liquids. A CCD

fiirewire camera with telecentric zoom optics combined with LED based background lighting allows capturing images at frame intervals from 10 ms to 1000s.

3.0 Literature Survey

L. Viau et. al [120] investigated about electrochemically oxidization of Pyrrole in two conventional media (water and acetonitrile) and in three room temperature ionic liquids 1-butyl-3-methylimidazolium hexafluorophosphate, 1-ethyl-3-methylimidazolium bis(trifluoromethanesulfonyl)imide. Infrared and Raman Spectroscopies confirmed the formation of polypyrrole by electro polymerization but were unable to demonstrate the presence of anions in the polymer films. The use of ionic liquids as growth media resulted in polymer films having a good electrochemical activity. The difference of activity from one polymer film to the other was mainly attributed to the difference of viscosity between the solvents used. The morphological features of the polypyrrole films were also fully studied. Profilometric measurements demonstrated that polymer films grown, at the same potential, in ionic liquids were thinner and had a smaller roughness than those grown in other solvents. Atomic Force Microscopy showed that polypyrrole films had nearly similar micrometric modular structure whatever the growth medium even if some differences of porosity and homogeneity were observed using Scanning Electron Microscopy. The incorporation of counter-anions at the top surface of the films was finally evidenced by X-ray Photoelectron Spectroscopy. These anions were also incorporated inside the polymer film with a uniform distribution as shown by Glow Discharge Optical Emission Spectroscopy.

P.Lianoset.al [121] fabricated moderately reduced graphene oxide/polypyrrole/PEDOT composite films via a three-step process. Graphene oxide/polypyrrole composites were first composed by in-situ polymerization. Uniform thin films of graphene oxide/polyrrole were then deposited on transparent conductive electrodes and annealed at 300 °C to produce moderately reduced graphene oxide/polypyrrole composite films. Even though, at this temperature loss of polypyrrole begins due to calcination, the presence of polypyrrole facilitates uniform film formation and prepares it for the next step of conductive polymer deposition. Finally, poly(3,4 ethylenedioxythiophene), PEDOT, was deposited on the reduced graphene

oxide/polypyrrole film by one-step electrodeposition and was employed as electro catalyst on counter electrodes in dye-sensitized solar cells. Cells employing this composite electro catalyst demonstrated power conversion efficiency of 7.1 %, which is comparable to that of Pt-based cells made under similar conditions. These findings support the idea of Pt-free solar cells.

S. S. Shinde et. al [122] reported about the fabrication of three different morphologies such as mud-like, cauliflower and interconnected nanoparticles of polypyrrole (ppy) thin films through oxidant assisted successive ionic layer adsorption and reaction (SILAR) method. The influence of oxidants like ammonium per sulfate (APS), ferric chloride (FC) and potassium dichromate (PDC) on structural, morphological, surface areas and electrochemical properties of ppy thin films is examined. Among three different morphologies, interconnected nanoparticles shaped ppy thin films provide a unique three-dimensional (3D) network, high surface area and meso-porous structure which satisfy the requirements for better super capacitive electrode materials. The electrochemical tests manifest the high specific capacitance of 510 F g^{-1} at a current density of 0.25 mA cm^{-2} with 85% capacitive retention after 1000 cycles. These studies propose that the formation of distinct nanostructures through oxidant dependent chemical polymerization route is a straightforward way for improving the electrochemical properties of PPy based super capacitors.

Y. Qiu et. al [123] proposed a pulse electro-polymerization method in order to synthesize a PPy/GO composite for supercapacitor applications, and for direct incorporate graphene oxide (GO) into polypyrrole (PPy) films without any additional dopants. The PPy/GO prepared by the pulse electro-polymerization (PC PPy/GO) exhibits a higher specific capacitance. A shorter pulse on time (t_{on}) results in higher specific capacitance, but there is an optimum pulse current amplitude (I_A) related to the highest specific capacitance. The PC PPy/GO film ($I_A = 4 \text{ mA cm}^{-2}$, $t_{on} = 50 \text{ ms}$) has a high specific capacitance of 660 F g^{-1} estimated from galvanostatic charge-discharge in 1 M KCl at a current density of 0.5 mA cm^{-2} . Stability tests for the PPy/GO yield long cycling life up to 1000 cycles with 10% decay in specific capacitance at charge-discharge current density of 10 mA cm^{-2} in the potential range of -0.5 to 0.5 V_{SCE} .

C. D. Lokhande et. al [124] presented about the cost-effective, novel and simple chemical synthesis of polypyrrole (PPy) thin films for supercapacitor application. These PPy films are characterized by different techniques such as X-ray diffraction (XRD), Fourier transform infrared spectroscopy (FTIR) and scanning electron microscopy (SEM). The XRD pattern reveals the amorphous nature of PPy thin film, which is highly feasible for super capacitors. Further, FTIR study confirms the formation of PPy. The surface morphological study exhibit the coverage of uniform and smooth morphology on thin film. The electrochemical super capacitive properties of PPy thin films are evaluated using cyclic voltammetry (CV) in 0.5 M H₂SO₄ electrolyte, which exhibits the maximum specific capacitance of 329 Fg⁻¹ at the scan rate of 5 mV s⁻¹. Additionally, an equivalent series resistance (ESR) of PPy thin films is found to be 1.08 Ω using electrochemical impedance measurement.

The electro synthesis of polypyrrole (PPy) thin film on stainless steel electrode was performed by *V. Puri et. al* [125] in presence of P-Tulensulfonic acid. The electromagnetic reflection, shielding effectiveness, permittivity and conductivity in the frequency range 8.2 to 18 GHz were studied and the effect of change in the acid concentration on the properties is reported. The microwave conductivity varies from 16 S/cm to 415 S/cm with frequency. The dielectric constant and dielectric loss factor decreases with increase in frequency.

J.B. Yadav et. al [126] reported about the effect of oxidant to monomer (O/M) ratio on optical and structural properties of Polypyrrole (PPy) thin film deposited by chemical oxidation polymerization technique. Noticeable changes have observed in the properties of PPy thin films with O/M ratio. Cauli flower structure have been observed in FE-SEM images, where in grain size is observed to decrease with increase in O/M ratio. AFM results are in good agreement with FE-SEM results. From FTIR spectra it is found that, PPy is in highly oxidized format low O/M ratio but oxidation decreased with increase in O/M ratio. Also C–C stretching vibrations of PPy ring is decreased whereas C = C stretching is increased with ratio. Absorption peak around 450nm corresponds to π – π^* transition and around 800nm for polarons and bipolarons. The intensity of such peaks confirms the conductivity of PPy, which is observed maximum at low O/M ratio and found to decrease with increase in ratio.

Optical bandgap (BG) is found to increase from 2.07 eV to 2.11 eV with increase in the O/M ratio.

D.K.Y. Wong et. al [127] demonstrated conducting polypyrrole films as a potential green technology for electro-chemical treatment of azo dyes in waste waters using Acid Red1 as a model analyte. These films were synthesized by anodically polymerizing pyrrole in the presence of Acid Red1 as a supporting electrolyte. In this way, the anionic Acid Red 1 is electrostatically attracted to the cationic polypyrrole backbone formed to maintain electro neutrality, and is thus entrapped in the film. These Acid Red 1- entrapped polypyrrole films were characterized by electrochemical, microscopic and spectroscopic techniques. Based on a two-level factorial design, the solution pH, Acid Red 1 concentration and polymerization duration were identified as significant parameters affecting the entrapment efficiency. The entrapment process will potentially aid in decolourising Acid Red1-containing waste waters. Similarly, in a cathodic process, electrons are supplied to neutralize the polypyrrole backbone, liberating Acid Red1 into a solution. In this work, following an entrapment duration of 480 min in 2000 mgL^{-1} Acid Red1, we estimated 21% of the dye was liberated after a reduction period of 240 min. This allows the recovery of Acid Red 1 for recycling purposes. A distinctive advantage of this electrochemical Acid Red 1 treatment, compared to many other techniques, is that no known toxic by-products are generated in the treatment. Therefore, conducting polypyrrole films can potentially be applied as an environmentally friendly treatment method for textile effluents.

In this report, the effect of different dopant anions on deposition and characteristics of polypyrrole (PPy) thin film has been studied by *B. Pourabbas et. al.* [128] Ultra-thin films of conducting PPy were deposited on insulating surfaces of glass and oxidized silicon wafer by in situ chemical polymerization in the presence of different anionic dopants including sodium dodecylbenzenesulfonate, sodium dodecyl sulfate, α -naphthalene sulfonic acid, anthraquinone-2-sulfonic acid sodium salt monohydrate/5-sulfosalicylic acid dehydrate, and camphor sulfonic acid. Hydrophilic/hydrophobic properties and morphology of the self-assembled monolayer of N-(3-trimethoxysilylpropyl)pyrrole, the surface modifying agent in this work, and PPy thin films were characterized before and after deposition by contact angle measurements, field emission scanning electron microscopy, and atomic

force microscopy. Chemical structure, thickness, and conductivity of the thin films were also studied by attenuated total reflectance Fourier transform infrared spectrometer, ellipsometry, and four-point probe measurements. The results showed deposition of thin films of conducting PPy with comparable thickness in the range of 6 – 31 nm and different morphologies, uniformity, and smoothness with average roughness in the range of 0.3 – 6 nm and relatively high range of conductivity on the modified surfaces.

S.A. Gangal et. al [129] synthesized Polypyrrole thin films in situ by chemical polymerization. Fourier transform infrared spectroscopy revealed formation of polypyrrole. The morphological studies by scanning electron microscopy showed formation of uniform granular structure with average grain size of 0.6 μm . The film composition was characterized by X-ray photoelectron spectroscopy for chemical composition in polypyrrole film. These films were investigated for their sensing behavior towards NH_3 and NO at room temperature. It has been observed that these films are selective for NH_3 and the sensitivity exhibited a linear response in range of 4–80 ppm.

V.B. Patil et. al [130] reported about preparation of camphor sulfonic acid doped polypyrrole using different weight percentages of camphor sulfonic acid (10–50%) dispersed in polypyrrole by solid state synthesis method. Films of CSA doped PPy were prepared by spin coating technique on a glass substrate. The effect of varying concentrations of CSA on the structure, morphology, optical and electrical properties of polypyrrole was explored using X-ray diffraction (XRD), Fourier transform infrared (FTIR) spectroscopy, scanning electron microscopy (SEM) atomic force microscopy (AFM), UV–visible spectroscopy and two probe technique respectively. The presence of CSA in PPy matrix and their interaction was confirmed by using XRD and FTIR techniques. The dramatic change in the surface morphology has been observed with increasing content of CSA in PPy matrix. The AFM study shows porous uniform globular morphology. The UV–vis spectra of CSA doped PPy film was found to shift to a lower wavelength side as compared to those of observed in PPy, indicating synergetic interaction between dopant CSA and PPy. CSA doped PPy not only can maintain a good solubility but also enhance the electrical conductivity. The results of dc electrical conductivity shows that, increase

inelectrical conductivity of PPy with increasing content of CSA (10–50%) in PPy matrix.

T. He et. al [131] successfully synthesized porous polypyrrole (PPy) CEs by electrochemical method. Detailed mechanism about the electro-polymerization and film growth has been investigated both experimentally and theoretically. The influence of iodine species pre-stored in the film during polymerization on the properties of resultant PPy CEs (such as porous structure, doping state, and electrocatalytic activity) and, thereby, the device performance has been studied thoroughly. We envision that the results may help to facilitate the research and development of the polymer- based CEs used in DSSCs.

S. Ghani et. al [132] followed a two-step electrochemical polymerization method for the fabrication of polypyrrole (PPY) thin films decorated with copper nanostructures on a stainless steel has been employed. The PPY film thickness affects the size, shape, and the number density of the copper nanostructures and provides an easy approach to control the morphology of these nanostructures. SEM images show nanorod like structures of copper on 200 nm PPY film. By employing this composite film as counter electrode (CE), a dye sensitized solar cell (DSSC) achieves a conversion efficiency of 7.42%, which is greater than Pt CE based DSSC (5.63%). The superior photovoltaic efficiency for the Cu-PPY film is attributed to unique porous PPY thin film and copper nanorods structure that leads to higher cathodic current density (5.38 mA/cm^2), large electro catalytic activity, and small charge transfer resistance ($1.92 \text{ } \Omega \text{ cm}^{-2}$). Therefore, Cu-PPY composite can be considered a competitive and promising CE material with the traditional and expensive Pt CE, for large-scale DSSCs production.

V.B. Patil et. al [133] prepared Polypyrrole (PPy) successfully via chemical oxidation polymerization technique using pyrrole as a monomer and ammonium per sulphate (APS) as oxidant. PPy sensors were fabricated on glass substrates using spin coating technique and characterized using FTIR, SEM, AFM and TEM techniques as well as gas sensing performance of prepared sensors towards various reducing and oxidizing gases were studied. Formation of polypyrrole was confirmed by FTIR spectrum. SEM analysis revealed that, polypyrrole film has highly porous granular

morphology suitable for gas sensing application. The AFM analysis showed interconnected granular, porous morphology. The gas sensing studies demonstrate that, the PPy sensor showed outstanding gas sensing properties towards NO₂ gas operating at room temperature with good selectivity and excellent repeatability. Furthermore, the PPy sensor is able to detect up low concentration of (10 ppm) NO₂ gas with reasonable sensitivity (12%) and can be reliably used to monitor the concentration of NO₂ gas over the range 10–100 ppm. The plausible response mechanism of PPy sensor towards NO₂ gas operating at room temperature is also discussed.

W. Donne et. al [134] via chronoamperometric electrodeposition method and characterized in terms of their physico-chemical and electrochemical properties and performance. Analysis of the chronoamperometric data shows that electrodeposition of the thin film results in a relative increase in electrochemically active surface area of up to 30 times. This finding was supported by transmission electron microscopy (TEM), atomic force microscopy (AFM) and profilometry analysis of the films. Electrochemical quartz crystal microbalance (EQCM) studies have allowed for the direct determination of electrode mass, both during deposition and electrochemical performance evaluation, which has enabled analysis of electrode properties, including film growth (up to 26 $\mu\text{g}/\text{cm}^2$), density ($\sim 2 \text{ g}/\text{cm}^3$), and the charge storage during electrochemical cycling, including the rates of mass uptake/removal with charge. The characteristics of the composite electrodes were compared with PPy-only electrodes throughout.

A novel flexible H₂ gas sensor was fabricated by *Pi-G. Su et. al* [135] by following the layer-by-layer (LBL) self-assembly of a polypyrrole (PPy) thin film on a polyester (PET) substrate. A Pt-based complex was self-assembled in situ on the as-prepared PPy thin film, which was reduced to form a Pt-PPy thin film. Microstructural observations revealed that Pt nanoparticles formed on the surface of the PPy film. The sensitivity of the PPy thin film was improved by the Pt nanoparticles, providing catalytically active sites for H₂ gas molecules. The interfering gas NH₃ affected the limit of detection (LOD) of a targeted H₂ gas in a real-world binary gas mixture. A plausible H₂ gas sensing mechanism involves catalytic effects of Pt particles and the formation of charge carriers in the PPy thin

film. The flexible H₂ gas sensor exhibited a strong sensitivity that was greater than that of sensors that were made of Pd- MWCNTs at room temperature.

Gliclazide sensing was investigated by *N. Adhouma et. al* [136] based on differential pulse voltammetry measurements of an electro polymerized molecularly imprinted polymer (E-MIP) film. The E-MIP polymer was prepared via anodic electro polymerization of pyrrole in the presence of GLZ onto glassy carbon electrodes using cyclic voltammetry (CV). GLZ molecules are successfully trapped into the polypyrrole matrix creating, after their subsequent removal, shape-complementary artificial recognition sites. The effect of several significant operational parameters (monomer and template concentrations, number of CV scans, pH and incubation time) on film analytical performances were investigated and optimized. Under optimized conditions, the sensor response exhibited high sensitivity toward the target template and was linearly proportional to GLZ concentration ($R^2 = 0.998$) over the range 5×10^{-11} to 4×10^{-10} M, with a detection limit ($3 \sigma/m$) of 1.2×10^{-11} M. The precision of the method (R.S.D., $n = 6$) for within and between-days is better than 1.4% and 2.48%, respectively at 10^{-10} M. Moreover, the selectivity of E-MIP sensor, against potentially competing molecules (Imp. B, Imp. E, glipizide, glibenclamide, glimepiride), was demonstrated. The developed E-MIP sensor was successfully applied to the determination of GLZ in three pharmaceutical products and gave results in close agreement with the reference HPLC method with mean recoveries between 95.4 and 98.8%, showing promising potential in practical applications.

Water dispersed polypyrrole was chemically synthesized by *V. Ponnuswamy et. al* [137] by using Dodecylbenzene sulfonic acid (DBSA) as dopant and Poly(4-styrene sulfonic acid (PSS) as co-dopant. The 10 wt % of PSS doped polypyrrole composite shows higher process ability. The prepared composites aqueous solution was deposited to get thin films by spin coating technique at various spin rates of 1000 rpm, 2000 rpm and 3000 rpm. The paper reports on effect of spin coating rate, thickness, surface roughness, and photo luminescence of water dispersed DBSA/PSS /PPY composite thin films. The transmittance is found to be decreased with increasing spin rates. Surface roughness of the films were analyzed by atomic force microscopy. The Root Mean Square (RMS) and Roughness

(Ra) values were found as (22.5 nm, 89 nm), (135 nm and 18 nm), and (70 nm and 113 nm) values. The super hydrophilic nature of the Composite films was studied by water contact angle measurements. The contact angle values were found to be 8.61, 9.41 and 101 for different spin rates. Photoluminescence (PL) of DBSA/PSS/PPY composite films reveals the emission with high intensity at high spin rates. Thickness of the composite films was found as 378 nm, 333 nm and 304 nm at 1000 rpm, 2000 rpm and 3000 rpm.

M. Taunk et. al [138] synthesized Polypyrrole (PPy) by a chemical oxidation method using ammonium Persulfate to obtain a solution processable PPy powder. The resultant PPy powder was then solution processed to deposit flexible thin films of PPy over flexible substrates. PPy film samples were then characterized using UV-vis spectroscopy, FTIR spectroscopy and X-ray diffraction. It was found that conductivity of PPy ($\sigma = 2.4 \times 10^{-2}$ S/cm) reduces by an order of magnitude after solution processing in the form of films. The temperature dependent conductivity of PPy pellet and flexible films of PPy were measured in the temperature range of 80–300K. It was observed that PPy films show stronger temperature dependence than pelletized samples. Charge transport in PPy samples has been investigated using Kivelson's and Mott's variable range hopping models. Mott's parameter such as density of states at the Fermi level $N(E_F)$, average hopping distance (R) and average hopping energy (W) have been estimated for PPy samples. The results showed that at room temperature average hopping distance for PPy film was about 22.3 Å and average hopping energy was 128.6 meV.

A study on the distribution of polarons vs. bipolarons as charge carriers in polypyrrole thin films doped with different dopant anions (chloride, p-toluenesulfonate and anthraquinone-2-sulfonate) is reported by *P-C Wang et. al* [139]. The polypyrrole thin films synthesized by oxidative chemical polymerization have comparable thickness in the range of 80 – 100 nm. However, with the variation of the dopant anion, the conductivity of the polypyrrole thin films can differ by three orders of magnitude. The conductivity of polypyrrole thin films doped with chloride, p-toluenesulfonate and anthraquinone-2-sulfonate is 0.64 S/cm, 7.1 S/cm and 120 S/cm, respectively. The Raman spectroscopy and electron spin resonance (ESR) spectroscopy results show that (i) both polarons and bipolarons are present

in the three types of polypyrrole thin films and (ii) the distribution of polarons vs. bipolarons as charge carriers in polypyrrole varies with the dopant anion used. The overall study reveals that the charge carriers in the anthraquinone-2-sulfonate-doped polypyrrole thin film are mainly spinless bipolarons, whereas the charge carriers in the chloride-doped polypyrrole thin film are dominated by paramagnetic polarons.

N. Alizadeh et. al [140] performed electrochemical polymerization of pyrrole on the surface of FTO electrode in the presence of tiron as doping anion with the aim of producing uniform, adherent, conducting and electroactive films. The use of tiron promoted charge transfer during electro polymerization and allowed reduced electro polymerization potential of polypyrrole (PPy). The resultant polymer was characterized via scanning electron microscopy (SEM), electrochemical and spectro electrochemical methods. SEM study indicates that the PPy-tiron has a spherical morphology with primary particles size of 40–60 nm. The spectro electrochemical analysis revealed the PPy-tiron has distinct electrochromic properties in the presence of different transition metal salts (CoCl_2 , NiCl_2 , CuCl_2 , FeCl_2 , MnCl_2 and ZnCl_2) as supporting electrolyte compared to conventional electrolyte solutions. Results showed that the electrochromic properties of PPy-tiron such as optical contrast, switching time, film stability and coloration efficiency were greatly enhanced in the presence of transition metal cations. PPy-tiron exhibited a switching time of 1.5 s and the maximum transmittance contrast (DT%) and coloration efficiency calculated 62% and $136.7 \text{ cm}^2 \text{ C}^{-1}$ at 800 nm in the presence of Ni^{2+} ion, respectively.

J. V. Thombare et. al [141] prepared Polypyrrole (PPy) thin films on stainless steel and ITO coated glass substrate at a constant deposition potential of 0.8 V versus saturated calomel electrode (SCE) by using the electrochemical polymerization method. The PPy thin films were deposited at room temperature at various monomer concentrations ranging from 0.1 M to 0.3 M pyrrole. The structural and optical properties of the polypyrrole thin films were investigated using an X-ray diffractometer (XRD), FTIR spectroscopy, scanning electron microscopy (SEM), and ultraviolet-visible (UV-vis) spectroscopy. The XRD results show that polypyrrole thin films have a semi crystalline structure. Higher monomer concentration results in

a slight increase of crystallinity. The polypyrrole thin films deposited at higher monomer concentration exhibit high visible absorbance.

Poly(vinyl alcohol)–silver (PVA–Ag) nanocomposite films were prepared by **S. Mahendia et. al** [142] via the soft chemical route. They studied about Effect of concentration of embedded Ag nanoparticles on conductivity and dielectric relaxation behavior of these nanocomposite films has been studied. An increase in dc conductivity from 1.38×10^{-11} to 9.17×10^{-11} S/cm and decrease in frequency dependent dielectric constant (from 1.74 to 1.07 at 75 kHz) are observed with the increase in concentration of Ag nanoparticles in PVA from 0 to 1.32 wt%. The values of ac conductivity and polarization relaxation time, deduced from dielectric data, also corroborate towards the enhanced conducting behaviour of PVA matrix with increase in the concentration of embedded Ag nanoparticles.

M. Zheng et. al [143] prepared Silver-dispersed PVP (Ag/PVP) thin films by spin coating from an alcohol solution of polyvinylpyrrolidone (PVP) in which silver nitrate were dissolved. A peak formed at 430–450 nm in the UV/VIS-spectra resulted from the surface plasma resonance of the silver nanoparticles. With the increase of annealing temperature, the plasma resonance absorption peak was broadened and intensities increased. The peak position of the surface plasma resonance also shifted to a high wavelength. XRD results confirmed the presence of silver particles in thin films. The absorption peak position calculated from the absorption spectrum is in very good agreement with Maxwell-Garnet (MG) theory using the dielectric constant of silver particles to calculate results of the absorption coefficient, a , of the silver particles.

N. Faraji et. al [144] prepared Silver/polyvinyl alcohol (PVA) nanocomposites via quick precipitation method, using hydrazine as a reducing agent. Preparing of silver/PVA nanocomposites by this method is done for the first time. The samples are characterized by Uv-Visible spectroscopy, X-ray diffraction (XRD), transmission electron microscopy (TEM). Nonlinear optical properties are carried out by Z-scan technique using a blue CW laser beam operated at wavelength 405 nm. It is shown that the synthesized samples have negative nonlinear refractive index and the magnitude is in the order of 10^{-8} . The nonlinear refractive index increases as amount of reducing agent increases.

R. Gradess et. al [145] demonstrate the use of nanocomposite thin films of poly(vinyl alcohol) with embedded silver NPs for chemosensing purposes. Silver NPs are in situ synthesized inside polyvinyl alcohol during the bake step of the formation of a nanocomposite thin film. The polymer in the nanocomposite provides an appropriate chemical and electromagnetic environment for metal NPs in order to interact with and hence detect the chemical species. A limit of detection below 20 nM is found when detecting 2-mercaptoethanol as the analyte, when measuring spectral changes (peak wavelength, linewidth and intensity) in the Localized Surface Plasmon Resonance. Potential qualitative and semi-quantitative sensors based on such nanocomposites would be easy-to-prepare, easy-to-use and low-cost, which are the basis of a fully disposable sensing platform technology.

I.O. Ali et. al synthesized Silver nanoparticles using two different reduction methods, namely, chemical reduction using hydrazine hydrate, and UV irradiation in the presence of polyvinyl alcohol (PVA) as a stabilizing agent. The successful incorporation of silver nanoparticles in a PVA matrix was confirmed by UV-vis spectroscopy, X-ray photoelectron spectroscopy (XPS), X-ray diffraction (XRD), transmission electron microscopy (TEM) and Fourier transform infrared (FT-IR) spectroscopy. XPS studies reveal that the Ag3d states convert from Ag₂O to Ag⁰ by reduction with hydrazine and UV irradiation. TEM results indicate that silver nanoparticles of spherical shape were formed following reduction by UV irradiation and yielded an average diameter from 13 to 26 nm. On the other hand, nanorods with an average length of 130 nm and diameter of 25 nm were produced following reduction by hydrazine hydrate. Measurements of optical spectra show that the surface plasmon resonance was localized around 425 nm, and confirmed the growth of Ag nanoclusters when reduced by hydrazine. XRD demonstrated that the colloidal nanoparticles were restricted to only authentic silver.

3.1 Scope of the work

The conducting polymers attract attention of researchers and engineers from a variety of fields in science and technology as promising electrode materials for energy storage devices (electro-chemical batteries and capacitors), electro catalysts and biosensors. Metal – polymer hybrid nanocomposites (MPHNs) have been recognized as potential systems for advanced functional applications. Incorporation of metal nanoparticles in polymer matrices has revolutionized the research effort in the field of composites as they lead to the achievement of synergistic effects from the organic and inorganic components of the system and have led to the expansion of the spectrum of applications. It is well acquaint that, polymer as dielectric materials are promising host matrices for encapsulation of metal nanoparticles such as Gold, Nickel, Silver, Copper, and so forth, as they act both as reducing as well as capping agents and also provide environmental and chemical stability. In parallel, the presence of metal nanoparticles inside the polymer matrix will also affect the properties of host itself.

Among conducting polymers, Polypyrrole (PPy) is one of the promising conducting polymers, owing to its promising electrical, mechanical, unique properties like flexibility, able to tailor made for specific uses and good environmental stability.

Polyvinyl alcohol (PVA) is a promising material by virtue of its high dielectric strength, excellent film forming, adhesive and dopant-dependent electrical and dielectric properties. In addition, PVA is highly soluble in water, biologically friendly and the carbon chain backbone with hydroxyl groups attached to methane carbons has ability to enhance the formation of polymer composite by incorporation of inorganic nanoparticles inside polymer matrix. Coating of particle surfaces with PVA prevents their agglomeration, giving rise to mono-dispersed particles. Silver nanoparticles (AgNPs) are of substantial interest because their characteristic properties (e.g., size and shape depending optical, electrical and magnetic properties) which can be incorporated into antimicrobial applications, biosensor materials and electronic components.

It is well acknowledged that, the quality of grown thin films depends on type of deposition technique and respective film processing parameters. In this direction, cold plasma polymerization (CPP) is single step, low cost and promising plasma assisted polymerization technique to prepare thin films of conducting polymers consisting of novel surface properties with wide functionalities, good adhesion to the substrate and better conductivity. In this technique, a greater uniformity and growth

process in detriment of the nucleation processes can be achieved by controlling the DC power of continues plasma.

3.2 Objectives of the work

- Optimizing the film growth conditions in Cold Plasma Polymerization technique
- Depositing Polyrrole (PPy) thin films on ITO coated glass substrates at ambient conditions.
- Studying the influence of Plasma Power on Microstructural properties of PPy films.
- Investigating the Optical, wetting and Dielectric properties of PPy films as a function of plasma power.
- Preparing “PVA/AgNPs/PVP” multilayered films on ITO glass substrates.
- Investigating the influence of “rate of diffusion of AgNPs in PVA matrix as a function of annealing temperature” on their microstructural and dielectric properties.

References

1. A.D. Jenkins, P. Kratochvíl, R.F. T. Stepto, U.W. Suter, *Pure and Applied Chemistry* 68 (1996) 2287.
2. H. Staudinger, J. Fritsch, *Helvetica Chimica Acta* 5 (1992) 785.
3. L.H. Sperling, L. H. (Leslie Howard) (2006). *Introduction to physical polymer science. Hoboken, N.J.: Wiley. p. 10.*
4. C. W. Vendruscolo, C. Ferrero, E. A. G. Pineda, *Carbohydrate Polymers* 76 (2009) 86.
5. H. E. Huber and G. I. Christenson, *Journal of Pharmaceutical Sciences* 1(1996) 59.
6. T. R. Bhardwaj, M. Kanwar, R. Lal, and A. Gupta, *Drug Development and Industrial Pharmacy* 26 (2000) 1025.
7. J. Varshosaz, N. Tavakoli, and S. A. Eram, *Drug Delivery* 13 (2006) pp. 113.
8. K.A. Athanasiou, C.E. Agrawal, F.A. Barber, S.S. Burkhart, *Journal of Arthroscopy* 14 (1998) 726.
9. E.A. Wang, V. Rosen, J.S. D'Alessandro, M. Bauduy, P. Cordes, T. Harada, *Proc. Natl Acad Sci* 87 (1990) 2220.
10. S. Mima, M. Miya, R. Iwamoto, S. Yoshikawa, *Journal of Applied Polymer Science* 28 (1983) 1909.
11. R. Jayakumar, N. Nwe, S. Tokura and H. Tamura, *International Journal of Biological Macromolecules* 40 (2007) 175.
12. M. Rinaudo, *Polymer International*, 57 (2008) 397.
13. Allcock, Harry R.; Lampe, Frederick W.; Mark, James E. (2003). *Contemporary Polymer Chemistry* (3 ed.). Pearson Education. p. 546.
14. Meyers, M. A.; Chawla, K. K. (1999). *Mechanical Behavior of Materials. Cambridge University Press. p. 41.*
15. Duarte, F. J. , *Applied Optics* 38 (1999) 6347.
16. J.-M. Lehn, *Supramolecular Chemistry — Concepts and Perspectives VCH, Weinheim (1995).*
17. S. Paliwal, S. Geib, C.S. Wilcox, *Journal of American Chemical Society* 116 (1994), p. 4497.
18. Odian George, *Principles of Polymerization, Fourth Edition, Wiley International, Jersey, USA, 2004.*

19. Flory P.J., "Principles of Polymer Chemistry:", Sixteenth Printing, *Cornell University Press, New York, 1995*.
20. Piringer O.G., Baner A.L., "Plastic Packaging: interaction with food and pharmaceutical", 2nd Edition, *Wiley-VCH Verlag GmbH, Weinheim. Futura, M, 1977*.
21. MAldissi (Ed.) *Intrinsically Conducting Polymers: an Emerging Technology (Dordrecht: Kluwer Academic, 1993)*.
22. P.V. Wright, *British Polymer Journal* 7 (1975) 319.
23. H. Akamatu, H. Inokutchi, Y. Matsunaga, *Nature* 173 (1954) 168.
24. D. Jerome, M. Mazaud, M. Ribault, K. Bechgaard, *Journal of Physique Letters* 41 (1980) 95.
25. Z. Iqbal, R.H. Baughman, B.L. Ramakrishna, S. Khare, N.S. Murthy, H.J. Bornemann, D.E. Morris, *Science* 254 (1986) 826.
26. Skotheim, T.A., Elsenbaumer, R.L., Reynolds, J.R. (eds) (1998) *Handbook of Conducting Polymers, Marcel Dekker, New York*.
27. L.T. Brown, E.H. Le May and E.B. Bursten: Chemistry, The Central Science, *Prentice Hall, Englewood Cliffs, New York, 1991*.
28. Chien, J.C.W. (1984) *Polyacetylene, Chemistry, Physics, and Material Science, Academic Press, London*.
29. L. Viaua, J.Y. Hihna, S. Lakarda, V. Moutarlier, V. Flaudb, B. Lakarda *Electrochimica Acta* 137 (2014) 298.
30. A. Davies, P. Audette, B. Farrow, F. Hassan, Z. Chen, J.Y. Choi, A. Yu, *Journal of Phys. Chem. C* 115 (2011) 17612.
31. J. Choi, H. Kim, S. Haam, S.Y. Lee, *J. Dispersion Sci. Technol.* 31 (2010) 743.
32. X. Zhang, J. Zhang, Z. Liu, C. Robinson, *Chem. Commun.* 16 (2004) 1852.
33. Mattan J, Uusimaki A, Torvela H and Leppavuori S, *Makromol. Chem., Macromol. Symp.* 22 (1988) 161.
34. Talaie A, Lee J Y, Lee Y K, Jang J, Romagnoli J A, Taguchi T and Maeder E, *Thin Solid Films* 363 (2000) 163.
35. Natalie M, Rowley and Roger J Mortimer, 2002, *Science progress*, 85 (3) 243.
36. Krings L H M, Havinga E E, Donkers J J M and Vork F T A *Synth. Metals*, 54 (1999) 453.
37. Adeloju S B and Show S J and Wallace G G, *Analitica Chimica Acta*, 1993, 281, 611-620 & 621-627.

38. Slater J M and Watt E J, *Analytical proceeding*, 26 (1989) 397.
39. Sukeerthi S, and Contractor A Q, *Indian J. Chem*, 33A (1994) 565.
40. Ge H, Teasdale P R and Wallace G G, *J. Chromatography* 544 (1991) 305.
41. N. Mermilliod and J. Tanguy, *Journal of Electrochemistry Society* (1986) 1073.
42. Mirmohseni A, Price W E, Wallace G G and Zhao H, *J. Intelligent Material Systems and Structures* 4 (1993) 43.
43. G. B. Street, T. C. Clark, M. T. Krounbi, K. K. Kanazawa, V. Lee, P. Pfluger, J. C. Scott, G. Weiser, *Molecular Crystals and Liquid Crystals* 83 (1982) 253.
44. J. C. Scott, P. Pfluger, T. C. Clark, G. B. Street, *Am. Chem. Soc., Polym. Prepr.* 23 (1982) 119.
45. G K Chandler, D Pletcher, in *Special Reports Electrochemistry Vol. 10 (London: Royal Society Chemistry, 1985)* p. 117.
46. M. Sağlam, M. Biber, A. Türüt, M. S. Ağırtas, and M.C. Akar, *International Journal of Polymeric Materials*, 54 (2005) 805.
47. A. H. Salama, M. Dawy, and A. M. A. Nada, *Polymer-Plastics Technology and Engineering*, 43 (2004) 1067.
48. A. Wnuk, M. Kaczkan, Z. Frukacz et al., *Journal of Alloys and Compounds* 341 (2002) 353.
49. K. Toyoshima, "Acetalization of polyvinyl alcohol," in *Polyvinyl Alcohol Properties and Applications*, C. A. Finch, Ed., chapter 15, pp. 391–411, *John Wiley & Sons, London, UK, 1973*.
50. S. N. Ege, *Organic Chemistry*, The University of Michigan, Ann Arbor, Mich, USA, 1989.
51. F. Billmeyer Jr., *Text Book of Polymer Science*, Wiley, Singapore, 1984.
52. G. Hirankumar, S. Selvasekarapandian, N. Kuwata, J. Kawamura, and T. Hattori, *Journal of Power Sources* 144 (2005) 262.
53. H. Zhang and J. Wang, *Spectrochimica Acta Part A: Molecular and Biomolecular Spectroscopy* 71 (2009) 1927.
54. S.-K. Jeong, Y.-K. Jo, and N.-J. Jo, *Electrochimica Acta* 52 (2006) 1549.
55. B. Chandar Shekar, S. Sathish, R. Sengoden, *Physics Procedia* 49 (2013) 145.
56. Hagen Klauk, Marcus Halik, Ute Zschieschang, Günter Schmid, and Wolfgang Radlik, *Journal of Applied Physics* 92 (2009) 5259 – 5263.

57. Like Huang, Ziyang Hu, Ke Zhang, Peipei Chen, Yuejin Zhu, *Thin Solid Films* 578 (2015) 161.
58. Marco Schott, Wojciech Szczerba, and Dirk G. Kurth, 30 (2014) 10721.
59. Zaher Ihdenea, Ahmed Mekki, Boualem Mettai, Rachid Mahmouda, Boudjema Hamada, Mohamed M. Chehimi, *Sensors and Actuators B: Chemical* 203 (2014) 647.
60. Harshawardhan Pol, Sourya Banik, Lal Busher Azad, Sumeet Thete, Pankaj Doshi and Ashish Lele, *Proceedings of PPS-30 AIP Conf. Proc.* 1664, 080006-1.
61. Xiao Liu, How Yong Ng, *Journal of Membrane Science* 469 (2014) 112.
62. K. Gurunathan, A. Vadivel Murugan, R. Marimuthu, U.P. Mulik, D.P. Amalnerkar, *Materials Chemistry and Physics* 61 (1999) 173.
63. A.F. Diaz, J.F. Bargon, in: T.A. Skotheim (Ed.), *Handbook of Conducting Polymers*, Marcel Dekker, New York, 1986, p. 81.
64. S. Tobiska, P. Kleinebudde, *Pharmaceutical Developing Technology* 8 (2003) 39.
65. R.J. Lang, *Journal of Acoustical Society of America* 34 (1962) 6.
66. N. P Pham, J. N Burghartz and P. M Sarro, *Journal of micro mechanics and microengineering*, 15 (2005) 691.
67. N.P. Pham, E. Boellaard, J.N. Burghartz, P.M. Sarro, *Journal of Microelectromechanical Systems* 13 (2004) 491.
68. P.V. Ashrit, *Thin Solid Films* 385 (2001) 81.
69. D. Manno, A. Serra, M. Di Giulio, *Thin Solid Films* 324 (1998) 44.
70. Amreen A. Hussain, Arup R. Pal, Rajib Kar, Heremba Bailung, Joyanti Chutia, *Materials Chemistry and Physics* 148 (2014) 540.
71. E.N. Bolbasov, M. Rybachuk, A.S. Golovkin, L.V. Antonova, E.V. Shesterikov, *Materials Letters* 132 (2014) 281.
72. Shou Seino, Shunsuke Sasaki, Tatsuki Owashi, Kei Oya, Satoru Iwamori, *Vacuum* 111 (2015) 160.
73. B. Reeja-Jayan, Moni Priya, K. Gleason Karen, *Nano Science and nano Technology* 7 (2015) 33.
74. Aftin Ross, Hakan Durmaz, Kenneth Cheng, Xiaopei Deng, Yuwei Liu, *Langmuir* 31 (2015) 5123.
75. Yuxing Ji, Chuanli Qin, , Haijun Niu, Ligu Sun, Zheng Jin, Xuduo Bai, *Dyes and Pigments* 117 (2015) 72.

76. Catalin Constantinescu, Andrei Rotaru, Anca Nedelcea, Maria Dinescu, *Materials Science in Semiconductor Processing* 30 (2015) 242.
77. N. Morosoff, An introduction to plasma polymerization, in R.d'Agostino (ed.), *Plasma Deposition, Treatment, and Etching of Polymers, Academic Press, 1990.*
78. Y. Takahashi, M. Iijima, K. Inagawa and A. Itoh, *J. Vac. Sci. Technol. A* 5 (1987) 2253.
79. Y. Kagami, T. Yamauchi, Y. Osada and I. Yoshizawa, *Journal Applied Physics* 68 (1990) 610.
80. H. Yasuda, M.O. Bumgarner, *Journal of Polymer Science and Polymer Chemistry*, Ed. 1976, 14, 195.
81. K.J. Rajan, D.S. Kumar, *Journal of Applied Polymer Science* 83 (2002) 1856.
82. A. Grill, *Cold Plasma in Materials Fabrication: from fundamentals to applications, IEEE Press, New Jersey, 1994.*
83. A. Brewer, R. Kveck, *Journal of Physical Chemistry* 35 (1931) 1293.
84. J. Sustin, J. Black, *Journal of American Chemical Society* 4552 (1930) 52.
85. E. Linder, A Davis, *Journal of Physical Chemistry* 35 (1931) 3649.
86. R.L. Stewart, *Physical Review* 35 (1934) 488.
87. J. Goodman, *Journal of Polymer Science* 44 (1960) 551.
88. M. Stuart, *Nature* 199 (1963) 59.
89. A. Bradley J.P. Hammes, *Journal of Electrochemical Society* 110 (1963) 15.
90. A. Bradely, *Transactions of the Faraday Society* 61 (1965) 773.
91. N.M. Bashara, C.T. Day, *Journal of Applied Physics* 35 (1964) 3498.
92. H. Yasuda, *Plasma Polymerization, Academic Press, Orlando (1985).*
93. H. Yasuda, *Plasma Polymerization – Kinetic and Mechanistic Aspects, Academic Press, Orlando, Florida, (1985).*
94. H.U. Poll, M. Artz, K.H. Wickleder, *European Polymer Journal* 12 (1976) 505.
95. H. Yasuda, *Thin Film Processes*, eds. Kern W. and Vossen J.L., *New York, Academic Press, 361, (1978).*
96. Vaitrin-UI C, Boissie-Laporte C, Chausse A, Leprince P, R. Messsina, *Progress in Organic Coatings*, 38 (2000) 9.
97. H. K. Yasuda, Q.S. Yu, C.M. Reddy, C.E. Moffitt, D.M. Wieliczka, *Journal of Applied Polymer Science*, 85 (2002) 1387.
98. W.J. Ooij, N. Zhang, S. Guo, *Fundamentals and Applied Aspects of Chemically Modified Surfaces, The Royal Society of Chemistry, (1999).*

99. M. Zeuner, H. Neumann, J. Meichsner, *Vacuum* 48 (1997) 443.
100. T.F. Wang, T.J. Lin, D.J. Yang, J.A. Antonelli, *Progress in Organic Coatings* 28 (1996).
101. H.K. Yasuda, T.F. Wang, D.L. Cho, T.J. Lin, J.A. Antonelli, *Progress in Organic Coatings* 30 (1996).
102. C. Lili Vescan, Handbook of thin film process technology, Bristol (UK), Institute of Physics, (1995).
103. Y. Lin and H. Yasuda, *Journal of Applied Science*, 60 (1996) 543.
104. J.L. Cecchi, Handbook of Plasma Processing Technology, eds. Stephen M. Rossnagel, Jerome J. Cuomo, and William D. Westwood, Park Ridge, NJ: Noyes publication, (1990).
105. H. Yasuda and T. Hirotsu, *Journal Polymer Science Polymer Chemistry Ed.* 16 (1978) 229.
106. H. Yasuda and T. Hirotsu, *Journal Polymer Science Polymer Chemistry Ed.* 16 (1978) 313.
107. H. Yasuda and T. Hirotsu, *Journal Polymer Science Polymer Chemistry Ed.* 16 (1978) 743.
108. A.T. Bell, *Journal of Macromol. Sci. Chem.* 10 (1976) 309.
109. H. Yasuda and C.E. Lamaze, *Journal of Polymer Science* 17 (1973) 1519.
110. H. Yasuda and C.E. Lamaze, *Journal of Polymer Science* 17 (1973) 1533.
111. H. Kobayashi, A.T. Bell and M. Shen, *Macromolecules* 7 (1974) 277.
112. C.D. Easton, M.V. Jacob, R.A. Shanks, *Polymer* 50 (2009) 3465.
113. W.J. Yoon, D. Bhattacharyya, R.B. Timmons, P.R. Berger, *Organic Electronics*, 11 (2010) 1767.
114. F. Hochart, J. Levalois-Mitjaville, R.D. Jaeger, *Polymer* 41 (2000) 3159.
115. H. Yasuda, "Plasma Polymerization" Academic Press, New York (1985).
116. H. Yasuda, T. Hirotsu, *Journal Polymer Science: Polymer Chemistry Edition*, 16 (1978) 743.
117. C. Zhang, J. Hu, J. Cong, Y. Zhao, W. Shen, H. Toyoda, M. Nagatsu, Y. Meng *Journal of Power Sources* 196 (2011) 5386.
118. B.D. Cullity, „Elements of X-ray Diffraction“, Addison-Wesley Publishing Company, Inc., Reading, Massachusetts (1967).
119. V. Lapshin, Review of Scientific Instruments, 66 (1995) 4718.
120. L. Viau, J.Y. Hihn, S. Lakard, V. Moutarlier, V. Flaud, B. Lakard,

- Electrochimica Acta* 137 (2014) 298.
121. M. S. Ramasamy, A. Nikolakapoulou, D. Raptis, V. Dracopoulos, G. Paterakis, P. Lianos, *Electrochimica Acta* 173 (2015) 276.
122. S. S. Shinde, G. S. Gund, D. P. Dubal, S. B. Jambure, C. D. Lokhande, *Electrochimica Acta* 119 (2014) 1.
123. Kai Qi, Y. Qiu, X. Guo, *Electrochimica Acta* 137 (2014) 685.
124. S. S. Shinde, G. S. Gund, V. S. Kumbhar, B. H. Patil, C. D. Lokhande, *European Polymer Journal* 49 (2013) 3734.
125. S. Jamadade, S. V. Jadhav, V. Puri, *Journal of Non-Crystalline Solids* 357 (2011) 1177.
126. A.A.Jatratkar, J.B. Yadav, S.V. Kamat, V.S. Patil, D.B. Mahadik, H.C. Barshili, V. Puri, R.K. Puri, *Journal of Physics and Chemistry of Solids* 80 (2015) 78.
127. M.M. Haque, W.T. Smith, D.K.Y. Wong, *Journal of Hazardous Materials* 283(2015)164.
128. M. Mahmoodian, B. Pourabbas, S. Mohajerzadeh, *Thin Solid Films* 583 (2015) 255.
129. A. Joshi, S.A. Gangal, S.K. Gupta, *Sensors and Actuators B* 156 (2011) 938.
130. S.T. Navale, A.T. Mane, A.A. Ghanwat, A.R. Mulik, V.B. Patil, *Measurement* 50 (2014) 363.
131. S. Lu, X. Zhang, T. Feng, R. Han, D. Liu, T. He, *Journal of Power Sources* 274 (2015) 1076.
132. S. Ghani, R. Sharif, S. Bashir, A. A. Zaidi, M.S. Rafique, A. Ashraf, S. Shahzadi, S. Rafique, A. H. Kamboh, *Journal of Power Sources* 282 (2015) 416
133. S.T. Navale, A.T. Mane, M.A. Chougule, R.D. Sakhare, S.R. Nalage, V.B. Patil, *Synthetic Metals* 189 (2014) 94–99.
134. P. Ningsih, C. Z. Holdsworth, S. W. Donne, *Synthetic Metals* 196 (2014) 8.
135. Pi-G. Su, C-C. Shiu, *Sensors and Actuators B* 157 (2011) 275.
136. H. Hrichi, M. R. Louhaichi, L. Monser, N. Adhouma, *Sensors and Actuators B* 204 (2014) 42.
137. P. Jayamurugan, V. Ponnuswamy, Y.V. SubbaRao, S. Ashokan, S. Meenakshisundar, *Materials Science in Semiconductor Processing* 39 (2015) 205.

138. M. Taunk, S. Chand, *Materials Science in Semiconductor Processing* 39 (2015) 659.
139. P-C Wang, J-Y Yu, *Reactive & Functional Polymers* 72 (2012) 311.
140. J. V. Thombare, M. C. Rath, S. H. Han, and V. J. Fulari, *Journal of Semiconductor* 34 (2013) 1.
141. J. V. Thombare, S. K. Shinde, G. M. Lohar, U. M. Chougale, S. S. Dhasade, H. D. Dhaygude, B. P. Relekar, and V. J. Fulari, *Journal of Semiconductor* 35 (2014) 1.
142. Suman Mahendia, A.K. Tomar, Shyam Kumar, *Journal of Alloys and Compounds* 508 (2010) 406.
143. M. Zheng, M. Gu, Y. Jin, G. Jin, *Materials Research Bulletin* 36 (2001) 853.
144. N. Faraji, W.M. Mat Yunus, A. Kharazmi, E. Saion, M. Shahmiri, *Journal European optical society Rapid Publication* 7 (2012) 12040 .
145. R. Gradess, R. Abargues, A. Habbou, J. Canet-Ferrer, *Journal of Materials Chemistry* 19 (2009) 9233.
146. I.O. Ali, *Colloids and Surfaces A: Physicochem. Eng. Aspects* 436 (2013) 922.

Results and Discussion

4.1 Cold plasma polymerization and characterization of Polypyrrole thin films

4.1.1 Introduction

In view of the novel characteristics of intrinsically conducting organic polymers have been receiving much attention because of their wide range of applications from insulator to superconductors [1, 2]. Among conducting polymers, Polypyrrole (PPy) is one of the promising conducting polymers, owing to its promising electrical, mechanical, unique properties like flexibility, able to tailor made for specific uses and good environmental stability [3–7]. These innate properties of PPy have been attracted by the community of “soft matter researchers” and inclined their research to adapt PPy as in thin film form to abridge both polymer and optoelectronic industries for innovative applications. Previously, most of the researchers focused on optical absorption, sensing and electrical properties of PPy thin films prepared by various conventional thin film deposition techniques [8–17]. However, the main challenge of the deposition techniques is to control the growth process to obtain highly uniform, pinhole free and desired film structure to have efficient properties.

It is well acknowledged that, plasma assisted thin film deposition methods have been distinguished as pioneered to prepare uniform, less concentration of structural defective, high quality and adherent with a high degree of crosslinking and branching at lower substrate temperatures [18, 19]. The chemical reactions in presence of plasma are very complex and non-specific in nature, which lead to effect on quality and chemical structure of polymer films. Cold plasma polymerization (CPP) is single step, low cost and promising plasma assisted polymerization technique to prepare thin films of conducting polymers consisting of novel surface properties with wide functionalities, good adhesion to the substrate and better conductivity [20, 21]. In this technique, a greater uniformity and growth process in detriment of the nucleation processes can be achieved by controlling the DC power of continues plasma.

In the present study, PPy thin films are synthesized with desired characteristics by using home built DC power induced Cold plasma polymerization technique on ITO coated glass substrates. Different DC powers are applied to investigate the effect of plasma power on growth, nucleation, microstructural, optical and dielectric properties of plasma polymerized PPy films. X-ray diffraction (XRD), FTIR spectroscopy, atomic

force microscopy (AFM), UV-Visible absorption spectroscopy and dielectric spectroscopic measurements have been carried to characterize films. The obtained dielectric responses of PPy films are interpreted in terms of influence of film growth conditions and microstructural properties. In parallel Havriliak-Negami (H-N) equation is adapted to fit the dielectric spectroscopy (DS) data and to understand the frequency dependency of dielectric parameters such as dielectric strength, relaxation time and conductivity values.

4.1.2 Experimental Section

Materials

Pyrrole (98%, Sigma-Aldrich) was used without further purification. Cold plasma polymerization was performed in home-built plasma reactor, which consisted of a discharge glass vessel (8 cm diameter and 50 cm in length) cylindrical shaped reactor and it was clamped between two aluminum metal plates of thickness 1 cm. Two electrodes were arranged inside the reactor and ITO coated glass substrates were placed on top of cathode for polymerization for all the experiments. The DC source was connected across the two electrodes for the generation of plasma in the reactor. The vapor container with the pyrrole monomer was attached to the deposition chamber through standard manifold with flux adjusted with a vacuum cock and needle valve. The reactor chamber pressure was determined by employing a Prani type vacuum meter (vacuum brand GMBH, Germany), positioned between the cold trap and reactor. The mechanical vacuum pump (EDWARDS, Model: RV 12) was connected to plasma reactor and entire reactor was evacuated to base pressure of 1×10^{-3} Torr. At room temperature, Pyrrole monomer was allowed into reactor chamber at controlled flow rate and the resultant pressure in the reactor chamber was maintained 0.4 Torr and then the chamber was filled with monomer vapour until the required pressure attain a desired level. A constant and high density of cylindrical shaped plasma is established between two electrodes by providing electric field between two electrodes using DC source. Electrons emitted by the surface of the cathode were accelerated in the applied electric field of the anode-cathode system and generate excited monomer molecules while en routed to the ITO coated glass substrate. All polymerizations were performed at room temperature for a constant deposition time of 5 min and by varying the plasma powers in the range 10 – 50 W. After the completion of the plasma polymerization process, the

films were stored at ambient conditions in a dry glove box and the characterization, other experiments were carried out as soon as possible.

The structural changes in deposited PPy thin films were investigated using X-ray diffraction (XRD) technique (BRUKER, Germany, Model: D8 Advance, Source : 2.2 KW Cu anode, Ceramic X-ray tube, Detector: Lynx Eye detector, Beta filter: Ni filter) with step width 0.05° and step time of 1.25 sec using $\text{CuK}\alpha$ radiation ($\lambda = 1.5406 \text{ \AA}$). The respective ITO peaks were subtracted from XRD spectra of PPy films prepared at various plasma powers. Fourier transform infrared (FT-IR) measurements were performed on a Spectrum One FT-IR Perkin Elmer spectrometer in normal transmission mode equipped with a mercury cadmium tellurium detector and KBr beam splitter. All samples were scraped from ITO coated glass substrates and pelletized after mixing with KBr; these pellets were used to record IR spectra over the range 400–4000 cm^{-1} . Atomic force microscopy (AFM) images were acquired with a Nano Focus (MOD-1M Plus and Tip size of 10 nm) by non-contact mode. Images were analyzed by WSXM 5.0 and Develop 5.0 software for data acquisition and image processing, respectively. The optical absorption spectra were recorded for all polymerized PPy films using Cary-5E Varian spectrophotometer in the range 250–1200 nm. During absorption measurements bare ITO coated glass substrates were used as reference sample. The polymeric film was sandwiched between two ITO coated glass plates of resistivity $100 \text{ }\Omega/\text{square}$ and dielectric measurements carried out at room temperature using an EG&G 273A galvanostat-potentiostat/impedentiometer controlled by the impedance software M398 in order to acquire the real and imaginary parts of impedance in the frequency range 10 mHz–100 KHz with a maximum applied voltage of 1.4 V (RMS) and in the absence of external bias. The obtained results were fitted with Mathematica curve fitting tool using a self-made software first tested on previously published data and analyzed with commercial software widely used. The use of the self-made software allows us to control, optimally several parameters, which is not possible with the commercial software. The values obtained by means of the fit, allows us to evaluate corresponding dielectric properties such as dielectric strength and conductivity values for the grown films.

4.1.3 Results and Discussion

Cold plasma polymerized PPy thin film thickness has been estimated using Stylus profilometer-Veeco dektak 8 and resultant thicknesses of grown films are found to be in the range 220 – 270 nm. To understand the influence of plasma power on modifications in structural properties, X-ray diffraction patterns are recorded in the 2θ range $10^\circ - 80^\circ$. XRD spectra corresponding to all the films (*Figure 4.1*) prepared at various glow powers are noticed to be smooth, diffused and non-characteristic in nature. A broad headed peak at $2\theta = 23.5^\circ$ indicates the amorphous nature of grown films and it can be attributed to scattering from PPy chains at inter planar spacing with an estimated intermolecular distance of 4.112 Å [22]. With the enhancement of plasma power to the higher values, a slight enhancement in intensity of the amorphous peak is noticed.

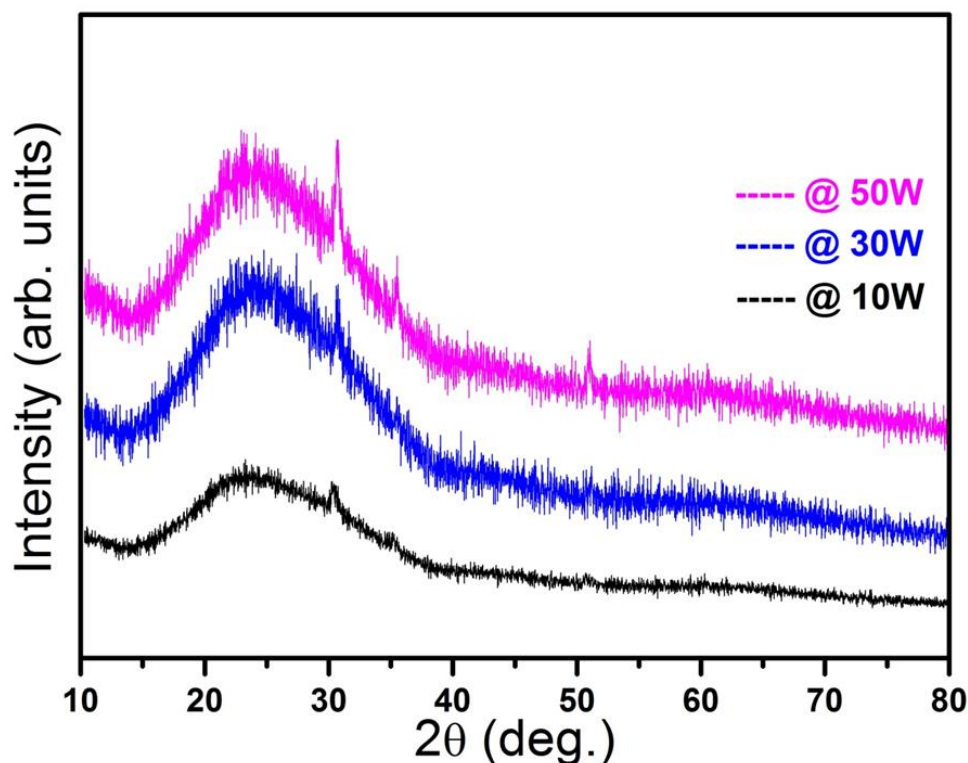


Figure 4.1 X-ray diffraction patterns of cold plasma polymerized PPy thin films grown at various plasma powers.

The FTIR absorption spectra of cold plasma polymerized PPy thin films are recorded (*Figure 4.2*) to understand the influence of plasma power on PPy polymer functionality. In the spectra, all characteristic peaks of polymerized PPy functional

groups can be identified. Significantly, respective FTIR spectra demonstrated two relatively broad and characteristic peaks in the wave number regions 3300–3400 cm^{-1}

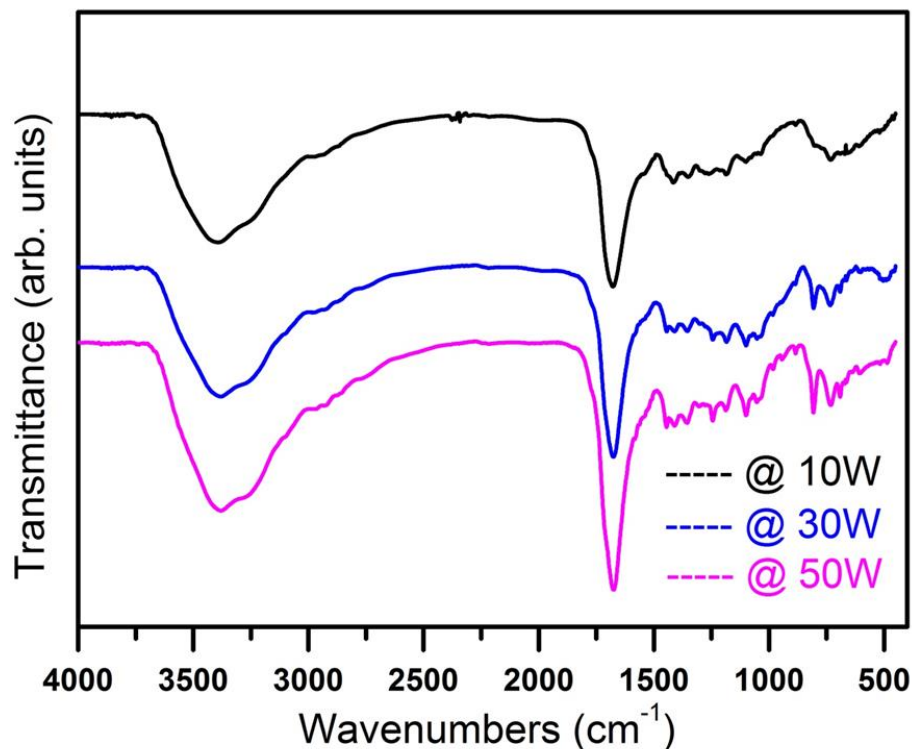


Figure 4.2 FTIR spectra of cold plasma polymerized PPy thin films at different plasma powers.

and 1635 – 1700 cm^{-1} , respectively. The broad and intense peak at around 3380 cm^{-1} is ascribed to the existence of sp^3 C–H stretching together with –NH stretching vibration and correspond to aromatic amines, the contribution of in plane vibrations of C=N and/or C=C and N–H are noticed between 1650–1700 cm^{-1} [23,24]. These presence of band at around 3380 cm^{-1} confirms the retention of opening of aromatic rings and heterocyclic compounds [25–27]. The stretching vibration of C=C and N–H bending between 1440 and 1400 cm^{-1} and bands at 1370 cm^{-1} , 1185 cm^{-1} are assigned to in plane vibration and breathing of the pyrrole rings, respectively [28]. The peaks present at 732 cm^{-1} and 1094 cm^{-1} reveal the C–H out and in plane bending, respectively [29]. Evidently as a function of plasma power, the intensity of the characteristic peaks are observed to be increased slightly and this could be due to improvement in polymerization and the cross-linking of free radicals by the presence of plasma. The FTIR spectra of cold plasma polymerized PPy films demonstrated less intense & closely separated absorption peaks corresponding to alkenes which resulted from broken rings also contribute as peaks at lower wave number region 500–1000 cm^{-1} [30].

Because when the pyrrole rings are broken, branching and crosslinking reactions tend to occur predominantly. Thus, primary, secondary or even tertiary amines may appear in the plasma polymerized PPy samples, which makes the absorption complicated in this wavenumber region. It is worth to mentioned that, in the present study we did not observe the presence of nitrile group, which represents a loss of functionality due to the pyrrole ring opening. This result authenticates that the cold plasma polymerization is promising technique to produce structurally less defective PPy films by controlling high fragmentation effect during the growth process.

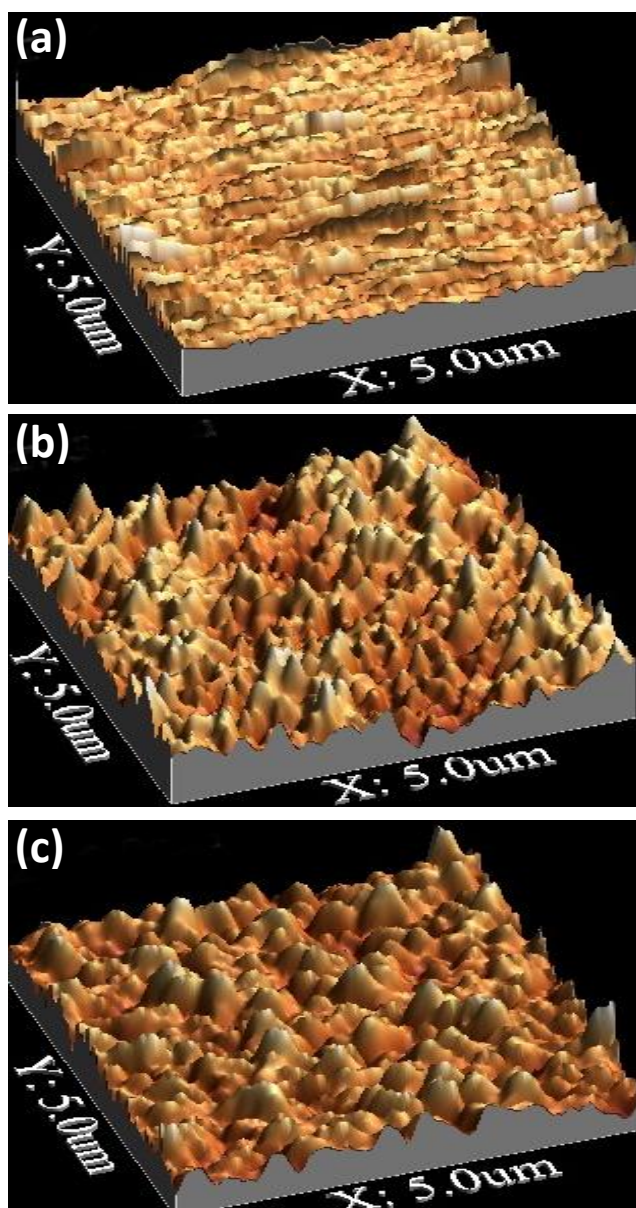


Figure 4.3 AFM images corresponding to PPy thin films prepared at plasma powers (a) 10 W (b) 30 W and (c) 50 W.

The surface morphology of cold plasma polymerized PPy thin films at different plasma powers is investigated using AFM (Figure 4.3) and roughness measurements are performed on several images taken from the same sample in order to estimate uniformity and homogeneity. From Figure 4.3a-c, it is evidenced that the morphology of the polymerized PPy layer is greatly affected by continuous cold plasma power. The morphology of films prepared at lower plasma power of 10 W is observed to be uniform, denser, moderately smooth and entire surface is composed of numerous irregular wrinkles of size 100 – 200 nm (Figure 4.33a). This type of surface morphology could be due to development of internal stresses in the matrix of grown PPy thin film. The enhancement of plasma power to the higher values leads to considerable changes in size, shape, roughness and density of the clusters over surface of films. For the PPy films grown at 50 W, the surface of the films is noticed to be composed of characteristic vertical spike shaped clusters of sizes in the range 400 – 500 nm. The evaluated root mean square (rms) surface roughness of the grown films increased from 0.08 nm to 0.7 nm with the enhancement of plasma power from 10 W to 50 W, respectively. This could be due to higher ratio value of ‘grain growth vs. nuclei formation’ and in cold plasma polymerization process, ionization of pyrrole monomer is not so intense that layer growth overcomes the nuclei formation. With the enhancement of plasma powers, the rate of growth of formation of nucleation sites and their agglomeration over ITO substrate are relatively higher than layer growth process. Therefore the AFM results revealed that, cold plasma polymerized PPy films have better uniformity and promising morphological characteristics.

The obtained results can be interpreted as follows: during the PPy film growth process in cold plasma polymerization technique, the activation of monomers and reactivation of the recombined molecules over surface of the substrates are essentially due to fragmentation by characteristic controlling parameter (W/FM) of established plasma in the plasma reactor [31]. This ‘ W/FM ’ (W = power in J/s, F = monomer flow rate in mol/s and M = molecular weight of monomer in Kg/mol) is an apparent input energy per the unit of monomer molecule in J/Kg and magnitude of ‘ W/FM ’ parameter is considered to be proportional to the concentration of activated species in the plasma region. Obviously for constant monomer flow rate (F) and molecular weight (M) values, the polymer formation rate (i.e polymer deposition rate) is directly proportional to power of the established ‘plasma region’ in the deposition chamber. Therefore at

lower deposition rates (i.e at 10 W) less energetic activated monomer species reach the surface of substrates to form growth centers and later polymerize with each other to form uniform PPy thin films. Hence we can observe irregular wrinkles formation over surface of the substrates and generation of internal stresses in the matrix of polymer thin film during the growth as evidenced from Figure 4.3a. The enhancement of plasma power to the higher values leads to the generation of higher concentration of activated species provided with higher energy. As a result, the as-deposited higher energetic active species can move over surface of the substrate toward active growth centers to agglomerate with each other in vertical direction to the substrate. This might be due to the enhancement of rate of mobility of active species than the rate of formation of growth centers over the surface of substrate provided with increase of micro voids inside the matrix of PPy thin films. Due to this reason, films grown at higher plasma power of 50 W were demonstrated distinguished surface morphology provided with higher root mean square (rms) roughness and composed of vertical spike shaped clusters. Interestingly, we could not observe considerable changes in structural properties in long range as a function of plasma power.

Investigating the optical properties of CPP thin films is prerequisite to understand their functionality as active layers in energy efficient and impending optoelectronic applications. The deposited films are well adherent to substrates and color of the films is noticed to change from golden yellowish to light yellowish color as a function of plasma power. Figure 4.4 shows the UV–visible absorption spectra of CPP PPy thin films in the wavelength range 200 – 1200 nm and the characteristic peak at 280 nm represents the absorption of amine (-NH-) groups [32]. and the absorbance of the films is increased significantly with increasing of plasma power due to slight enhancement in film thicknesses. The fundamental absorption refers to band-to-band or exciton transition, which manifests itself by a rapid rise in absorption (known as absorption edge) and provides the information about optical band gap (E_g). For the films grown at lower plasma power (at 10 W) characteristic optical absorption edge is noticed at around 417 nm, which divulges the significant identity of PPy [33]. As a function of plasma power the respective absorption edge is shifted towards higher wavelength side and found to be at 490 nm for the films grown at higher plasma

powers (at 50 W). The optical band gaps are determined from the absorption spectra of films and by following Tauc's relation[34],

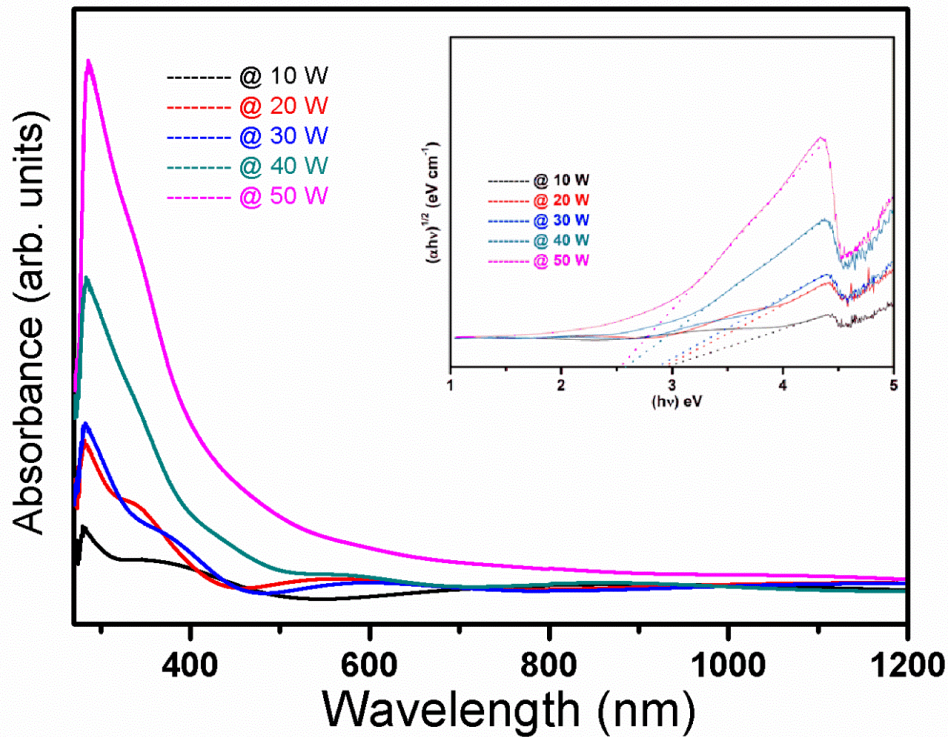


Figure 4.4. UV – visible absorption spectra for plasma polymerized PPy films at various plasma powers.

$$(\alpha hv) \propto (hv - E_g)^n \quad \text{where } n = 1, 2, 3 \quad \dots\dots\dots (4.1.1)$$

where ‘ α ’ is the absorption coefficient, ‘ hv ’ is the energy of the incident photon, E_g the optical band gap and the index ‘ n ’ is connected with the distribution of density of states. The present system obeys the rule of indirect transition with $n = 2$. The absorption coefficient is evaluated using the relation,

$$\alpha = O_d/t \quad \dots\dots\dots (4.1.2)$$

Where O_d is the optical density measured at a given film thickness (t), and the extinction coefficient is expressed as follows,

$$k = \alpha\lambda/4\pi \quad \dots\dots\dots (4.1.3)$$

Where λ is wavelength of incident photon. The value of $(\alpha hv)^{1/2}$ with incident photon energy hv is plotted (inset of Figure 4) and the value of E_g is determined by

extrapolating the linear region of the plot $(\alpha hv)^{1/2}$ versus hv , to zero absorption. The estimated optical band gap values are decreased as a function of plasma power. PPy film polymerized at 10 W, is demonstrated higher bandgap value of 2.97 eV (i.e Q - band) and decreased to 2.53 eV with an increase of plasma power to 50 W. Since plasma polymerized polymers show less conductivity and in this case the absorption process can be explained by exciton absorption. In polymers, $\pi \rightarrow \pi^*$ allowed transition is known as an asymmetric change of the dipole moment. According to Peierls' distribution theory, π band originate from highest occupied molecular orbital HOMO and the π^* band originating from lowest unoccupied molecular orbital LUMO, with energy gap in between them [35–38]. Generally, in polymerization process the rate of branching and cross linking of activated species on surface of substrates is directly proportional to established strength of plasma. The polymer films grown at lower plasma power are not highly branched and cross linked to form three dimensional networks and the enhancement of plasma power leads to branching & cross linking of activated pyrrole monomer species and responsible for micro level modifications in structure of polymer matrix. These micro modifications in PPy polymer matrix are responsible for decrease of optical band gap values as a function of plasma power.

Impedance spectroscopy (IS) is one of the promising analytical tools to analyze linear electrical response of materials of interest (including electrode effects) and the subsequent analysis of the response to yield useful information about physicochemical properties of the systems. In the present study, we recorded IS spectra for all PPy films at room temperature and investigated $Z^*(\omega)$ and $\epsilon^*(\omega)$ parameters to understand electrical and dielectric properties as a function plasma power. Figure 6 shows the dependence of both real (Z^I) and imaginary impedance (Z^{II}) components of polymerized PPy films on applied frequency in the range 10 mHz – 100 KHz. The Z^I values are almost constant at lower and higher frequency regions, and interestingly decreased monotonically in intermediate frequency zone and we noticed same trend for all the PPy films grown at various plasma powers in the range 10 W – 50 W (Figure 4.5a). The peak maximum value of Z^{II} is noticed to be shifted towards higher frequency region with the increase of plasma power (inset of Figure 6a). The Nyquist plots for PPy films (Figure 4.5b) demonstrated characteristic single semicircles close to origin [39]. These semicircles divulge the presence of the parallel combination

of bulk resistance corresponding to migration of ions and bulk capacitance (due to the immobile polymer chains). Therefore, the frequency response for the grown thin films

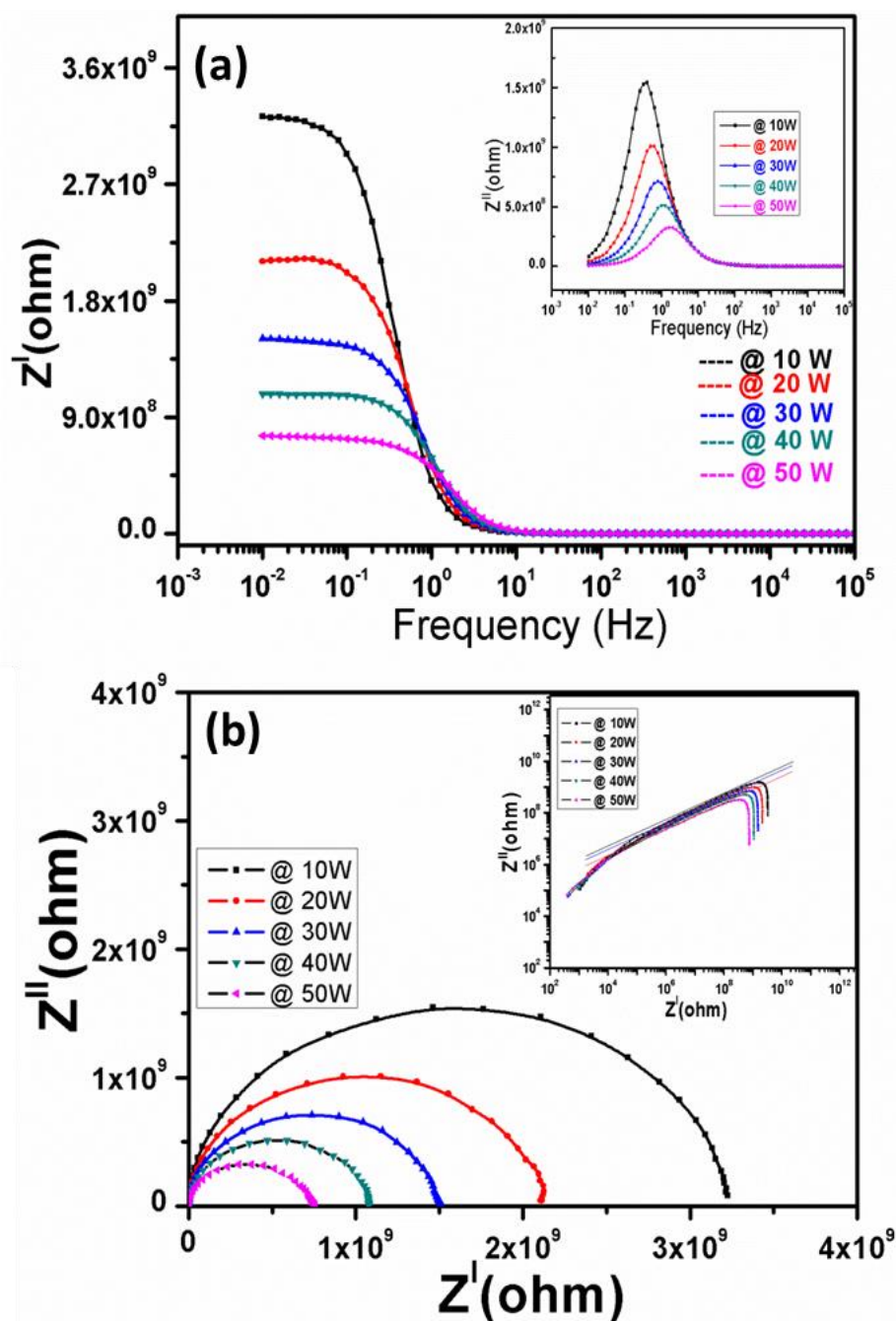


Figure 4.5. Impedance measurements for PPy thin films as a function of plasma powers (a). The variation real impedances as a function of applied frequency in the range 10 mHz – 100 KHz. (b). Nyquist plots (Z'' versus Z') for grown films at various growth conditions.

can be represented by an equivalent electrical circuit consisting of series resistance (R_s) corresponding to contact resistance of the ITO/polymer interface and the bulk

resistance (R_p) in the parallel RC network, bulk capacitance (C_p) associated to layer resistance of the anthracene derivative, geometric capacitance of the polymer layer, respectively. The estimated slope values from Nyquist plots on log – log scale are observed to be nearly equal to 0.5 (inset of Figure 4.5b) and it signifies the single characteristic relaxation time [40]. The bulk resistances of the grown films are evaluated by the intersection of semicircle with the real axis and respective conductivity values are increased considerably with the increase of plasma power to the higher values (Table 4.1).

Plasma power (W)	$\Delta\varepsilon$ (V/M)	ω	α	β	σ_{fit} (S/m) X 10^{-12}	σ_{est} (S/m) X 10^{-12}	ξ
10	0.12	0.001	0.87	0.5	1.35	1.37	0.96
20	0.14	0.005	0.82	0.79	2.11	2.00	0.99
30	0.2	0.009	0.79	0.99	2.97	2.92	0.97
40	0.3	0.009	0.90	0.99	3.97	4.08	0.96
50	0.7	0.01	0.99	0.99	6.00	5.82	0.99

Table 4.1. Fitting parameters for PPy films deposited at various plasma powers.

During dielectric measurements, the resultant complex impedance Z can be expressed in terms of admittance as follows,

$$Y = \frac{1}{Z} = \frac{1}{Z^I + iZ^{II}} = \frac{1}{R + iX} = G + iB = G + i(2\pi f)C \dots\dots\dots (4.1.4)$$

In the expression, Y is the Admittance, R the Resistance (real impedance), X the Reactance, G the Conductance, B the Susceptance, C the Capacitance and C_0 the Empty Capacitance. Therefore, the real and imaginary parts of dielectric constant are,

$$\varepsilon^I = \frac{C}{C_0} \text{ and } \varepsilon^{II} = \frac{G}{\omega C_0} \dots\dots\dots (4.1.5)$$

Experimentally, real and the imaginary parts of dielectric constant have been calculated from impedenziometric data by using following equations,

$$\varepsilon^I = -\frac{X}{(X^2+R^2)} \frac{d}{\varepsilon_0 A} \frac{1}{2\pi f} \dots\dots\dots (4.1.6)$$

$$\varepsilon^{II} = \frac{R}{(X^2+R^2)} \frac{d}{\varepsilon_0 A} \frac{1}{2\pi f} \dots\dots\dots (4.1.7)$$

where d, A and f are respectively the thickness of the sample, the area of the cell surface and the frequency of the applied electric field. The resultant modulus of the complex dielectric constant is evaluated as follows,

$$\varepsilon^* = \sqrt{(\varepsilon^I)^2 + (\varepsilon^{II})^2} \dots\dots\dots (4.1.8)$$

In order to interpret the influence of plasma power on measured dielectric relaxation of grown PPy films, $\varepsilon^*(f)$ can be described by Havriliak-Nagami function (which is an empirical modification of the Debye relaxation model, accounting for the asymmetry and broadness of the dielectric dispersion curve) with the addition of a conductivity contribution (last term) present at lower frequencies

$$\varepsilon^*(f) = \varepsilon_\infty + \sum_{j=1} \frac{\Delta\varepsilon}{[1+(i(2\pi f)/(2\pi f_j))^\alpha]^\beta} - \frac{i\sigma}{\varepsilon_{0(\omega)}^\xi} \dots\dots\dots (4.1.9)$$

Here, $\Delta\varepsilon = (\varepsilon_S - \varepsilon_\infty)$ indicates dielectric strength, ε_S and ε_∞ are permittivity values at lower and higher frequencies, respectively. f_j is the corresponding relaxation frequency of the medium, ‘ α ’ and ‘ β ’ describe the asymmetry and broadness of the corresponding spectra. ‘ σ ’ is related to conductivity and ‘ ξ ’ is a fitting parameter responsible for the slope of the conductivity [41].

Figure 4.6 illustrates the variation of characteristic dielectric constants ε^I and dielectric loss ε^{II} values of deposited PPy films as a function of applied electric field frequency. At lower frequency region, the dielectric constant (ε^I) values are increased with decrease in applied frequency and this similar behavior is observed for many polymers, it could be due to contribution of ionic conduction which possibly results from the migration of impurities [42]. At higher frequency region, ε^I values are independent of applied frequency. Because at high frequency regions, the excess ions

diffusion along direction of the applied electric field becomes zero due to rapid periodic reversal of the applied electric field. Estimated dielectric constant values of CPP PPy films are decreased with an increase of plasma power. The reason could be that, PPy films grown at lower plasma power (i.e. at 10 W) are predominantly amorphous in nature and the enhancement of plasma power to the higher values (i.e. at 50 W) leads to the increase of number of active impurities in the matrix of grown polymer films and additional crystallization at the expense of the amorphous phase, which reduces the effect of space charge polarization.

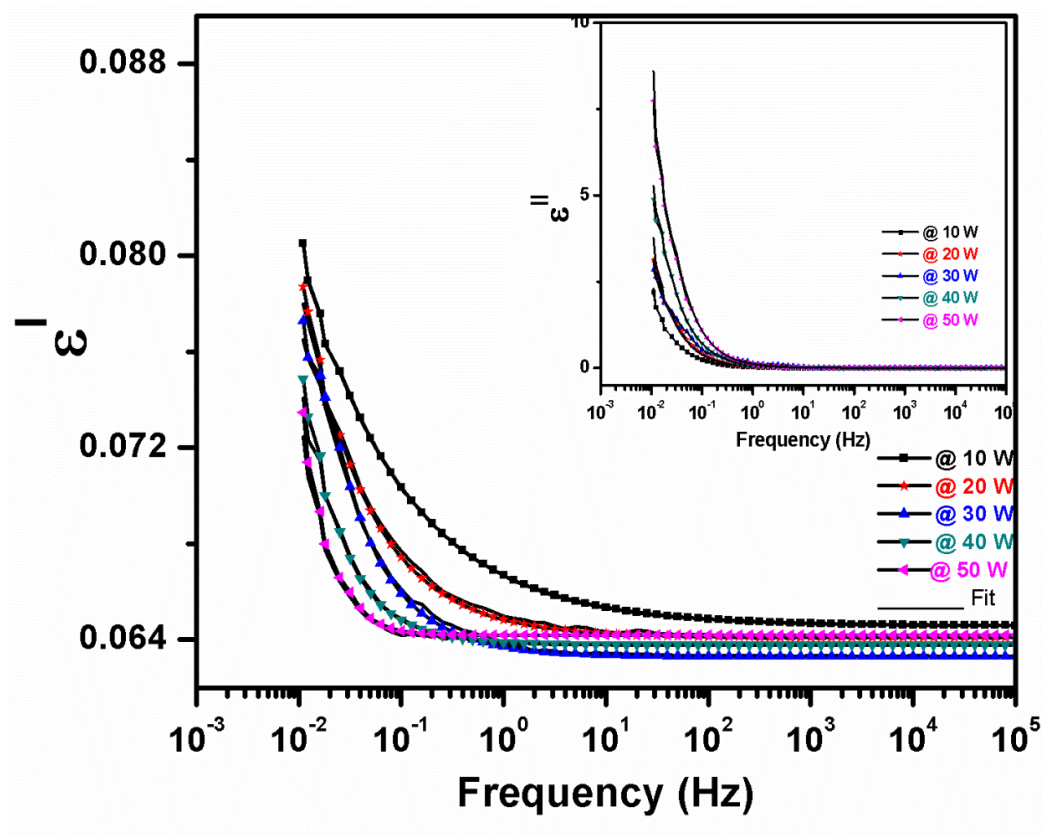


Figure 4.6. Behavior of estimated dielectric constants of grown films as a function of frequency (solid black line represents the fit).

The variation of dielectric loss as a function of frequency for the films grown at various deposition conditions (inset of Figure 4.6). At lower frequency region, dielectric loss values are observed to increase with the decrease of frequency and ϵ'' values are decreased with the increase of plasma power to the higher values. The dielectric strength ' $\Delta\epsilon$ ' provides the information about relaxation strength of polymer matrix, which depends on the volume concentration of the dipole species and their

orientation constrains. The estimated ' $\Delta\varepsilon$ ' values increased slightly with increase of plasma power. At lower plasma power values, the interlinking of activated polymer species show a preferential dipolar orientation in the direction of its polarization. With the increase of plasma power, the activated polymer species oppose to show a preferential dipolar orientation in the direction of polarization and this leads to slight

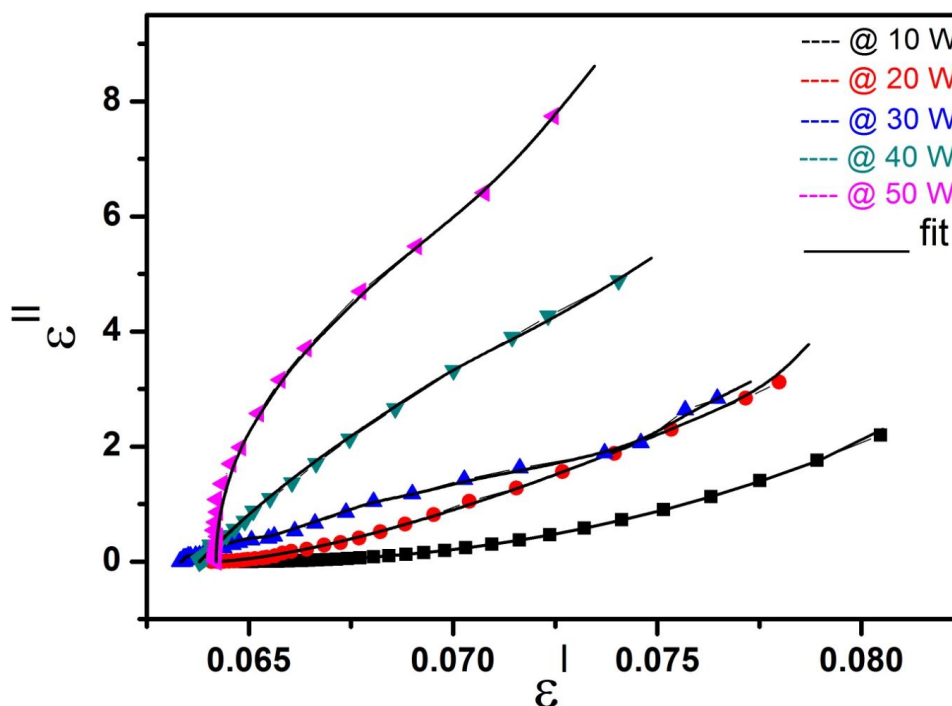


Figure 4.7. Cole – Cole plots for plasma polymerized PPy films.

increase in dielectric strength values. The Cole – Cole plots for grown PPy films are fitted by mathematica curve fitting tool (Figure 4.7) and obtained respective dielectric strength, conductivity values (Table 1). Estimated and fitted conductivity results are in congruent with each other and noticed to be increased appreciably from 1.35×10^{-12} S/m to 6.0×10^{-12} S/m with the increase of plasma powers from 10 W to 50 W, respectively. It reveals the increase of migration of immobile species or defects in the polymer material as a function plasma power.

4.1.4 Conclusions

Cold plasma polymerization technique is a promising plasma assisted physical vapor thin film deposition technique to prepare quality polymer thin films with desired characteristic properties for various applications. Polypyrrole (PPy) has been identified as a potential candidate for opto–electronics, sensors and energy storage device

applications. In the present, we prepared Polypyrrole thin films on ITO coated glass substrates using cold plasma polymerization technique and investigated the influence of plasma power on microstructural, optical and dielectric properties of grown films. All the grown PPy films are observed to be amorphous in nature. In the present study, the FT-IR spectra demonstrated all characteristic peaks of PPy and we did not observe the presence of nitrile group, which represents a loss of functionality due to the pyrrole ring opening. These results authenticate that the cold plasma polymerization is promising technique to produce structurally less defective PPy films by controlling high fragmentation effect during the growth process. We observed significant modifications in surface morphological features of PPy films like grain size & shape, density of clusters and surface roughness as a function of plasma power. The PPy film surface composed of numerous irregular wrinkles of sizes in the range 100–200 nm is modified to vertical spike shaped clusters of sizes in the range 400–500 nm, with an increase of plasma power from 10 W to 50 W. The cold plasma polymerized PPy films demonstrated higher optical absorption and lower optical band gap value of 2.53 eV at higher plasma power of 50 W. The estimated bulk resistance of grown films decreased appreciably with the increase of plasma power and PPy films prepared at higher plasma power of 50 W demonstrated relatively higher conductivity values of 6.0×10^{-12} S/m. The Nyquist plots of PPy films prepared at various plasma powers demonstrated characteristic single semicircles close to origin. Dielectric spectroscopic investigations revealed the significant influence of microstructural properties of grown films on their dielectric responses as a function of frequency and observed slight increase in dielectric strength of matrix of the grown thin films with the increase of plasma power to the higher values.

References

1. H. Yoneyama, K. Wakamoto and H. Tamura, *Journal of Electrochemical Society* 132 (1985) 2414.
2. L. Jiang, H.K. Jun, Y.S. Hoh, J.O. Lim, D.D. Lee and J.S. Hoh, *Sensors and Actuators B* 105 (2005) 132.
3. Jihuai Wu, Qinghua Li, Leqing Fan, Zhang Lan, Pinjiang Li, Jianming Lin and Sanchun Hao, *Journal of Power Sources* 181 (2008) 172.
4. J.H.B. Urroughes, C. A. Jones and R.H. Friend, *Nature* 335 (1988) 137.
5. M.B. Inoue, K.W. Nebesny, Q. Fernando, M.M. Castillo-Ortega, M. Inoue, *Synthetic Materials* 38 (1990) 205.
6. C.T. Kou, T.R. Liou, *Synthetic Materials* 82 (1996) 167.
7. M. Omastova, S. Kosina, J. Pionteck, A. Janke, J. Pavlinec, *Synthetic Materials* 81 (1996) 49.
8. A. Ashery, A.A.M. Farag and M.A. Shenashen, *Synthetic Metals* 162 (2012) 1357.
9. H. Qin, A. Kulkarni, H. Zhang, H. Kim, D. Jiang and T. Kim, *Sensors and Actuators B* 158 (2011) 223.
10. S. Barnoss, H. Shanak, C.C. Bof Bufon and T. Heinzl, *Sensors and Actuators A* 154 (2009) 79.
11. M.F. Mabrook, C. Pearson and M.C. Petty, *Sensors and Actuators B* 115 (2006) 547.
12. J.L. Yagu'e and S. Borro's, *Plasma Processes and Polymers* 9 (2012) 485.
13. X. Li, I. Zhitomirsky, *Journal of Power Sources* 221 (2013) 49.
14. J.S. Shapiro and W.T. Smith, *Polymer* 36 (1995) 1133.
15. D. Kopecky, M. Vrnata, F. Vyslouzil, V. Myslik, P. Fitl, O. Ekrt, P. Matejka, M. Jelinek and T. Kocourek, *Thin Solid Films* 517 (2009) 2083.
16. C.C. Changa,, C.L. Paia, W.C. Chena and S.A. Jenekheb, *Thin Solid Films* 479 (2005) 254.
17. E. P. Landureau, Y.F. Nicolau and M. Delamar, *Synthetic Metals* 72 (1995) 111.

18. C.D. Easton, M.V. Jacob and R.A. Shanks, *Polymer* 50 (2009) 3465.
19. W.J. Yoon, D. Bhattacharyya, R.B. Timmons and P.R. Berger, *Organic Electronics* 11 (2010) 1767.
20. F. Hochart, J. Levalois-Mitjaville and R.D. Jaeger, *Polymer* 41 (2000) 3159.
21. H. Yasuda, Academic Press, New York 1985.
22. J.Y. Ouyang and Y. F. Li, *Polymer* 38 (1997) 3997.
23. S. Saravanan, C. Joseph Mathai, M.R. Anantharaman, S. Venkatachalam, D.K. Avasthi and F. Singh, *Synthetic Metals* 155 (2005) 311.
24. J. L. Yague and S. Borros, *Plasma process and Polymers* 9 (2012) 485.
25. M.A. Leich, N.M. Mackie, K.L. Williams, E.R. Fisher, *Macromolecules* 31 (1998) 7618.
26. L.M.H. Groenewoud, G.H.M. Engbers, J.G.A. Terlingen, H. Wormeester, J. Feijen, *Langmuir* 16 (2000) 6278.
27. L.M. Han, R.B. Timmons, D. Bogdal, J. Pielichowski, *Chemistry of Materials* 10 (1998) 1422.
28. J.G. Wang, K.G. Neoh, E.T. Kang, *Thin Solid Films* 446 (2004) 205.
29. E. Hakansson, T. Lin, H. Wanga and A. Kaynak, *Synthetic Metals* 156 (2006) 1194.
30. G.J. Cruz, J. Morales, R. Olayo, *Thin Solid Films* 342 (1999) 119.
31. H. Yasuda and T. Hirotsu, *Journal Polymer Science: Polymer Chemistry Edition* 16 (1978) 743.
32. J.A. Dean, *Analytical Chemistry Handbook*, McGraw-Hill, 1995.
33. H. Shiigi, M. Kishimoto, H. Yakabe, B. Deore and T. Nagaoka, *Analytical Science* 18 (2002) 41.
34. J. Tauc, R. Grigirovici, A. Vancu, *Physics Status Solid* 15 (1999) 627.
35. A.J. Heeger, S. Kivelson, J.R. Schrieffer, W.P. Su, *Reviews of Modern Physics* 60 (1988) 1781.
36. R. Pariserand, R.G. Parr, *Journal of Chemical Physics* 21 (1953) 767.
37. J.A. Popel, *Trans Faraday Society* 49 (1953) 1375.
38. A. Khan Shamsad, M. Zulfequar, M. Hussain, *Current Applied Physics* 5 (2005) 583.

39. C. Jonda, and Andrea B. R. Maye, *Chemistry of Materials* 11 (1999) 2429.
40. Seong Hyun Kim, Kang-Hoon Choi, Hyang-Mok Lee, Do-Hoon Hwang, Lee-Mi Do, Hye Yong Chu, and Taehyoung Zyung, *Journal Applied Physics* 87 (2000) 882.
41. S. Havriliak and S. Negami, *Polymer* 8 (1967) 161.
42. P.K.C. Pillai, P. Khurana and A. Tripathi, *Journal of material Science Letters* 5 (1986) 629.

4.2 Influence of Silver nanoparticles Inter layer on Optical and Dielectric Properties of PVA Thin films

4.2.1 Introduction

Metal-polymer hybrid nanocomposites (MPHNs) have been recognized as potential candidates for various applications [1-3]. Research on incorporation of metal nanoparticles in polymer matrices has revolutionized in the field of composites as they lead to the achievement of synergistic effects from the organic and inorganic components of the system which led to the expansion of spectrum of applications [4, 5]. Many research groups reported that incorporation of conductive metal nanoparticles into the host polymer matrix has an outstanding influence on its structural, optical and electrical properties making it as a functional material in the field of sensors, storage devices, catalysis, electromagnetic shielding and electrostatic dissipation applications [6-10]. As dielectric material, polymers are most promising host matrices for encapsulation of metal nanoparticles such as gold, nickel, silver, copper, etc as they act as reducing and capping agents with environmental and chemical stability [11, 12]. In addition to this, the presence of metal nanoparticles inside the polymer matrix will also affect the properties of host matrices [13]. The properties of the polymer nanocomposites (PNCs) are depending on the characteristics of the nanoparticles such as high specific surface area, aspect ratio, dispersion and interaction with polymer. The physical properties of the metal nanoparticles (MNPs) can be controlled by their size and shape [14, 15]. Among the various polymers, polyvinyl alcohol (PVA) is a promising material due to its high dielectric strength, film formation, adhesive and the properties of the polymer can be controlled by dopant concentration [16-18]. Further, PVA is highly soluble in water, biologically friendly and the carbon chain backbone with hydroxyl groups has ability to form polymer composite by incorporation of inorganic nanoparticles inside polymer matrix [19, 20]. Coating of nanoparticles to PVA prevents their agglomeration, giving rise to mono-dispersed particles. Adding, silver nanoparticles (AgNPs) are of substantial interest because their characteristic properties which finds in antimicrobial, biosensor materials and electronic applications [21-25].

Previously, Silver doped PVA nanocomposites and thin films were prepared using different physical and chemical methods and studied their microstructural, nonlinear optical, electrical and growth mechanism [26-32]. It is noteworthy to mention that in PNC systems, inclusion of MNP fillers can enhance the effective dielectric constant of polymer matrix. In this case, dielectric matrix serves as a nano dielectric between two MNPs and therefore acts as nanoelectrodes [33]. Moreover, the interface between polymer matrix and MNPs increases due to intrinsic large surface to volume ratio of MNPs. However due to increasing trend and requirement of the miniaturization of electronic devices, we need novel fabrication techniques, to prepare materials using simple methods with enhanced dielectric properties. Substantially, study on the influence AgNPs inter layer as a function of annealing temperature on dielectric and ac conductivity properties of MPHNS is a prerequisite for tuning the properties in view of futuristic circuit component and device fabrication. Hence in the present study, focus was given to prepare 'PVA/AgNPs' thin films onto ITO coated glass substrates using conventional spin coating and cold plasma polymerization (CPP) techniques. In this paper, significantly we focused to investigate the influence of thin inter layer of AgNPs on surface morphological, optical and dielectric properties of 'PVA/AgNPs' thin films as a function of temperature in the range 20 °C to 200 °C.

4.2.2 Experimental

The PVA powder of molecular weight of 89,000 to 98,000 and spherical shaped silver nanoparticles of 100 - 150 nm size were purchased from Sigma Aldrich and Plasma Chem GmbH (Berlin), respectively. In the present study, 5 gr of PVA powder was dissolved in 100 ml of distilled water at 70 °C followed by continuous mechanical stirring for 3 hours to form a viscous solution and 0.09 % concentration of aqueous solution of silver nanoparticles was prepared using deionised water as a solvent. PVA thin films of thickness 10 microns were deposited onto ITO coated glass substrates by spin coating technique at 2000 rpm and followed by deposition of 200 nm thickness of AgNPs over PVA thin films using home built cold plasma polymerization (CPP) technique to prepare 'PVA/AgNPs' thin films.

To study the surface morphological features of the films as a function of temperature, Atomic force microscopic studies were carried out in non-contact mode (AFM, Nano Focus, MOD-1M Plus) with tip size of 10 nm. The optical and dielectric

properties of annealed films were studied using UV-Vis spectrometer and galvanostat - potentiostat/impedentiometers, respectively. The optical absorption spectra were recorded in the wavelength range 300-1000 nm using double beam spectrophotometer (Cary-5E Varian). The resultant, PVA/AgNPs thin films were sandwiched between two ITO electrodes of sheet resistance $10 \Omega/\square$ to make a “PVA/AgNPs/PVA” structured cell (MLTs) and dielectric measurements were carried out using galvanostat-potentiostat/impedentiometer (EG&G 273A) controlled by the impedance software (M398) to acquire the real and imaginary parts of impedance in the frequency range of 10 mHz -10 kHz with a maximum applied voltage of 1.4 V (RMS) and in the absence of external bias. The dielectric measurements have been performed as a function of temperature by placing resultant cell in a CaLCTec FB150 programmable temperature hot stage by varying the temperature in the range $20 \text{ }^\circ\text{C} - 200 \text{ }^\circ\text{C}$. In addition, Havriliak-Negami (H-N) equation is adapted to fit the dielectric spectroscopy data to understand the influence of thin layer of AgNPs as a function of temperature on frequency dependent dielectric parameters such as dielectric strength, relaxation time and conductivity values.

4.2.3 Results and Discussion

Figure 4.8 (a-c) illustrates the modifications in surface morphological features of ‘PVA/AgNPs’ thin films, annealed at different temperatures. Evidently, at low temperature ($20 \text{ }^\circ\text{C}$) formation of denser silver nanoparticle’s clusters is observed over surface of PVA thin films. As evidenced from the optical and dielectric properties, the sizes of the clusters decreased and silver nanoparticles are noticed to be percolating into the PVA host matrix, with increase of temperature till $200 \text{ }^\circ\text{C}$. The evaluated root mean square (rms) roughness of the ‘PVA/AgNPs’ thin films is decreased with an increase in temperature (as shown in Figure 4.8d). The as deposited ‘PVA/AgNPs’ thin films demonstrated higher surface roughness of 48.86 nm and observed to decrease to 14.99 nm with the increase of temperature to the higher value of $200 \text{ }^\circ\text{C}$. At room temperature most of the deposited Ag nanoparticles stick to top surface of PVA thin films and become responsible for higher surface roughness. With the increase of temperature, matrix of PVA becomes more flexible and supports to Ag nanoparticles to percolate into matrix. This process could be predominant at near the glass transition temperature

of PVA, which could be the reason for decreasing of surface roughness at higher annealing temperatures.

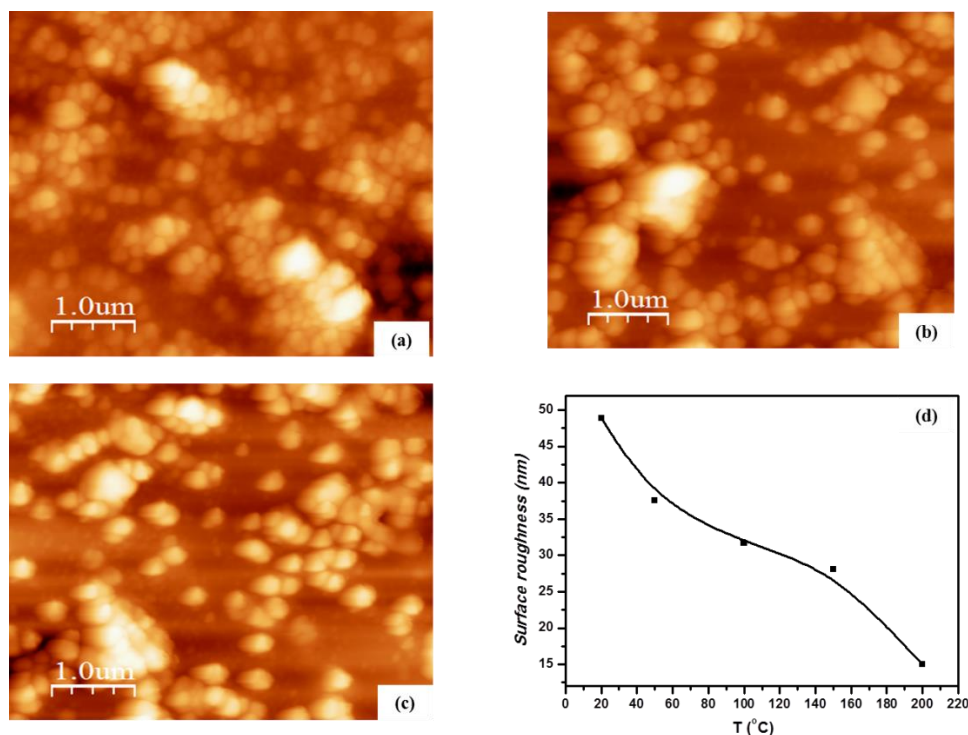


Figure 4.8. Atomic force micrographs for ‘PVA/AgNPs’ thin films various temperatures (a) T = 20 °C (b) T = 100 °C (c) T = 200 °C (d) variation of rms roughness

The optical absorption spectra of ‘PVA/AgNPs’ thin films annealed at different temperatures are shown in Figure 4.9. Pure PVA is a colourless polymer without any considerable absorption in the visible region and sharp increase in absorption below 300 nm is attributed to the bandgap of PVA. A characteristic peak is observed at 478 nm, which represents the signature of silver nanoparticle due to surface Plasmon resonance (SPR). The intensity of the peak increased and found blue shift with increase temperature, this could be due to decrease in size of silver nanoparticles clusters. The most used method for estimation of the bandgap energy from optical measurements is proposed by Tauc, in which the optical bandgap energy of the samples is estimated from the intercept of the extrapolated linear part of the plot of $(\alpha h\nu)^{1/3}$ versus the photon energy E with abscissa. This can be expressed as follows,

$$(\alpha h\nu)^n = B(h\nu - E_g) \dots\dots\dots (4.2.1)$$

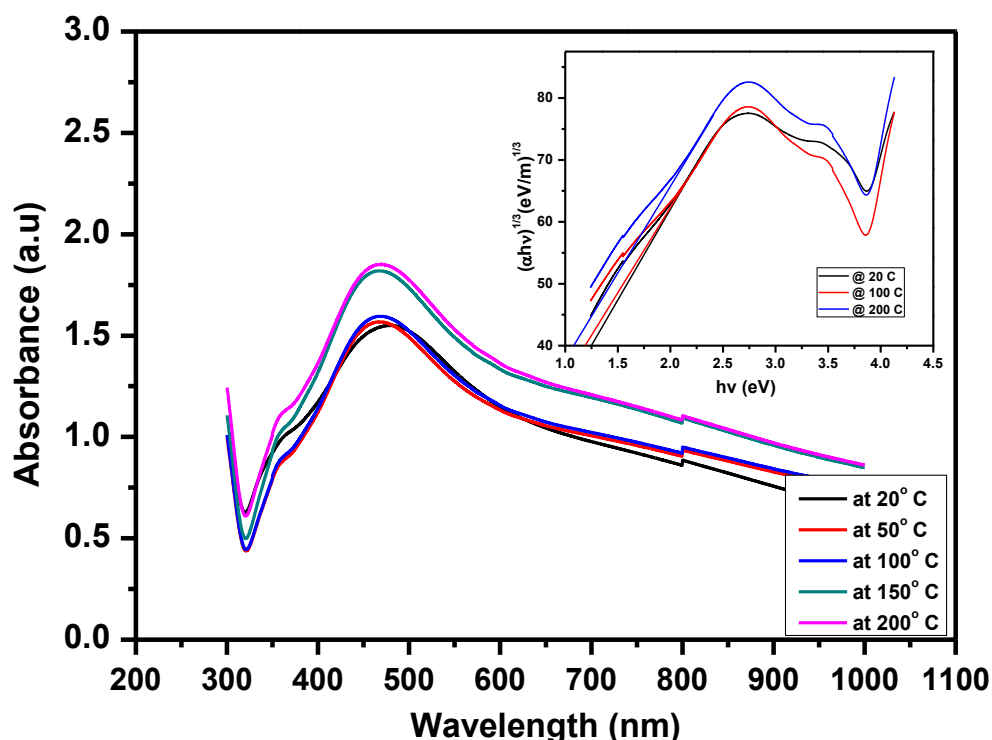


Figure 4.9 Optical absorption spectra for ‘PVA/AgNPs’ thin films at various temperatures in the range 20 °C – 200 °C.

where ‘ α ’ is the absorption coefficient, ‘ $h\nu$ ’ is the energy of the incident photon, B the absorption edge width parameter, E_g the optical band gap and the index ‘ n ’ is connected with the distribution of density of states. The predominant absorption peak at 2.638 eV for AgNPs clusters deposited over surface of PVA thin films indicates the characteristic SPR attributed to AgNPs. The larger absorption observed in UV region is due to energy gap of PVA polymer, which is observed to be decreased slightly with increase in temperature, this could be due to changes in the electron hole in conduction and valence bands.

In the present study, dielectric spectroscopic measurements have been carried out for “PVA/AgNPs/PVA” structured cell (MLTs) to understand the influence of AgNPs layer on dielectric properties of PVA matrix as a function of temperature. The real and imaginary parts of the perpendicular components of complex dielectric permittivity are measured as a function of frequency at different temperatures in the range 20 °C–200 °C. The respective director relaxation can be expressed in terms of complex dielectric permittivity as follows,

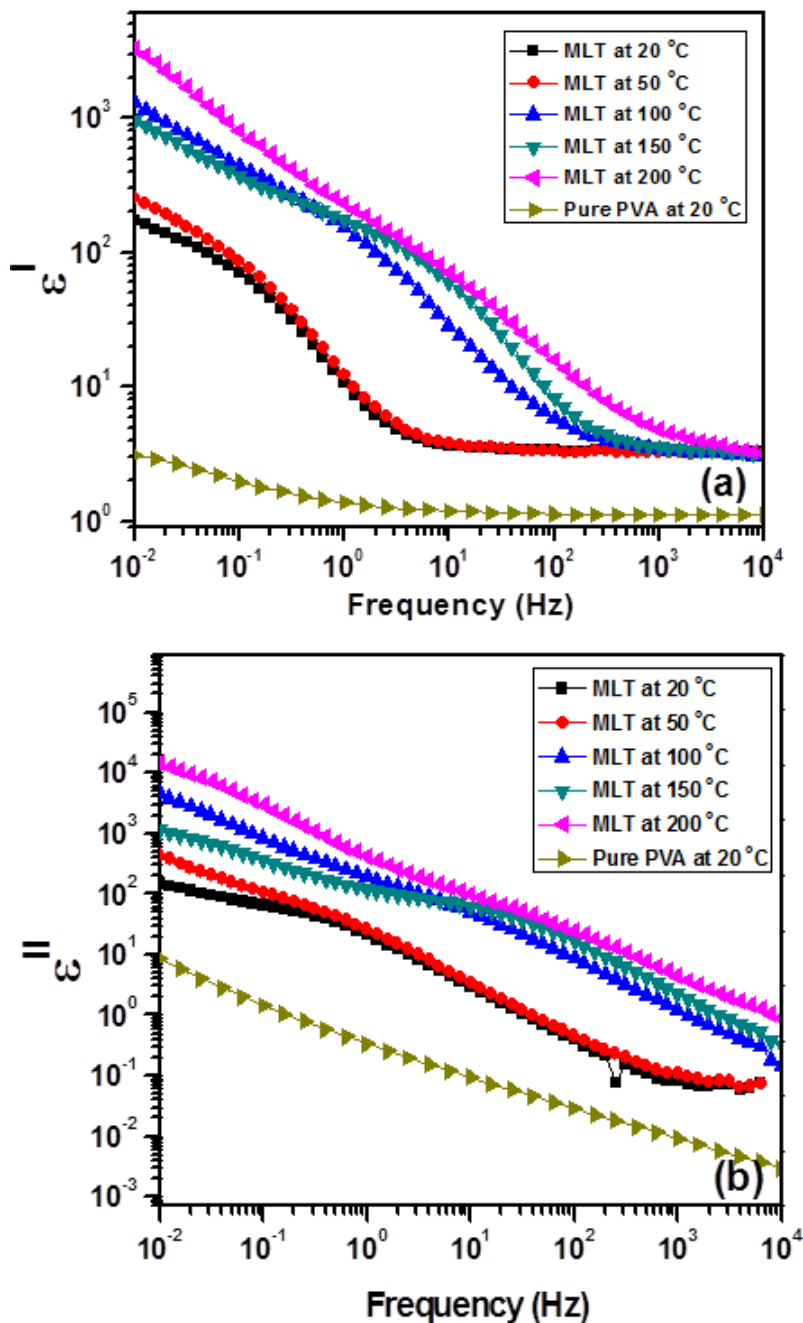


Figure 4.10 Plots of the dielectric permittivity vs. log of frequency (log f) as a function of temperatures for ‘PVA/AgNPs/PVA’ thin films (MLTs).

$$\varepsilon_{\perp}^*(f) = \varepsilon^I(f) - i\varepsilon^{II}(f) \dots\dots\dots (4.2.2)$$

where ε^I represents the real part of dielectric permittivity and its respective spectrum is called dispersion curve. ε^{II} indicates imaginary part of the complex permittivity and its corresponding spectrum was known as dielectric loss curve and f being the frequency of the applied electric field. In order to interpret the influence of AgNPs layer as a

function of temperature on measured dielectric responses of fabricated MLTs, resultant $\varepsilon_{\perp}^*(f)$ can be described by following Havriliak-Nagami (HN) relation [34],

$$\varepsilon_{\perp}^*(f) = \varepsilon_{\infty} + \sum_j \frac{\Delta\varepsilon_j}{[1+(if\tau_j)^{a_j}]^{b_j}} - \frac{i\sigma}{\varepsilon_0(2\pi f)^n} \dots\dots\dots (4.2.3)$$

Here, $\Delta\varepsilon_j = (\varepsilon_S - \varepsilon_{\infty})$ indicates the dielectric strength, ε_S and ε_{∞} are permittivity values at lower and higher frequencies, respectively. $\tau_j = 1/f_{rj}$ is the relaxation time, f_r is the corresponding relaxation frequency, a_j and b_j are shape parameters describing the asymmetry and broadness of the dielectric dispersion curve ranging between 0 and 1, and j is the number of relaxation processes. In the last term, σ is related to conductivity, and n is a fitting parameter responsible for slope of the conductivity. In case of pure insulator, $n = 1$, while the decrease of n , $n < 1$ could be observed if, in addition to the contribution to ε'' from conductivity, there is an influence of electrode polarization. The HN response reduces to Cole-Davidson response when $a = 1$, and to Cole-Cole response when $b = 1$ [35, 36].

Variations of dielectric constant (ε') variation as a function of applied frequency for MLTs is shown in Figure. 4.10a and evidently, in comparison to pure PVA thin films, MLTs are exhibiting enhanced dielectric constant value due to the presence of thin AgNPs layer. It is also observed that dielectric constant increases with an increase in temperature. Relatively, dielectric constant attains higher values at lower frequency region and decreases monotonically with the increase in frequency, indicating the existence of a dielectric relaxation and characteristic nature of polar materials. This can be explained as follows, when high conductive metal nanoparticles are present in insulating PVA matrix, as theory predicts the dielectric permittivity of resultant composite increases with the percolation of metal particle fillers [37, 38]. Due to large conductivity mismatch between the AgNPs and PVA matrix leads to relaxation process, which can be attributed to an interfacial polarization, known as Maxwell-Wagner-Sillar effect [39, 40], a phenomenon appearing in heterogeneous media due to the accumulation of charges at Metal-Polymer interfaces and formation of large dipoles on metal nanoparticles or clusters. This phenomenon contributes to the enhancement of effective permittivity and dielectric losses, and could be the reason for

large dielectric constant values for MLTs at low frequency region and it is observed to be more predominant as a function of temperature.

The formation of localized charge carriers at the charge defect centers (i.e. charged dangling bonds) on the surfaces of AgNPs may be another source for space charges which contributes to the higher dielectric constant values at lower frequency region. At lower frequency regions, both electrode & interfacial effects become predominant to build-up of space charge near electrode/electrolyte interface which partially blocks the charge transport. This can be attributed to the tendency of dipoles in polymeric host matrices to orient them in the direction of applied electric field. Further, polarization effects become dominant and the tendency of orientation of dipoles becomes less according to the field variation at higher frequency regions. This phenomenon leads to decrease in ϵ'' values with the increase of applied frequency to the higher values. In case of MLTs, at higher frequency of 1 KHz and at 20 °C, the dielectric constant value is 3 times higher than the dielectric constant value of pure PVA thin films, and noticed to be increased 16 times with the increase of temperature to the higher value of 200 °C. We believe that, the presence of AgNPs clusters can influence the glass transition temperature of PVA matrix and as a function of temperature AgNPs clusters diffuse into the matrix of PVA. Therefore a gradual increase in dielectric constant occurs with the enhancement of temperature as a result of following two competing mechanisms. As a function of temperature, increase in segmental mobility of the polymer molecules leads to an increase in dielectric constant and due to differential thermal expansion of the polymer and AgNPs clusters clusters disrupts the chains of polymer contacting to clusters, leading to decreases in dielectric constant. However near the glass transition temperature, in the above two mechanisms the segmental mobility of polymer is the dominating factor causing a large increase in the dielectric permittivity.

Figure 4.10b shows the variation of dielectric loss (ϵ'') as a function of applied frequency for MLTs at various temperatures. The dielectric loss values decreased with an increase in frequency. The larger value of the loss factor or dielectric loss at lower frequency region could be due to mobile charges within the polymer matrix. At higher frequencies, periodic field reversal was so fast that there was no excess ion diffusion in

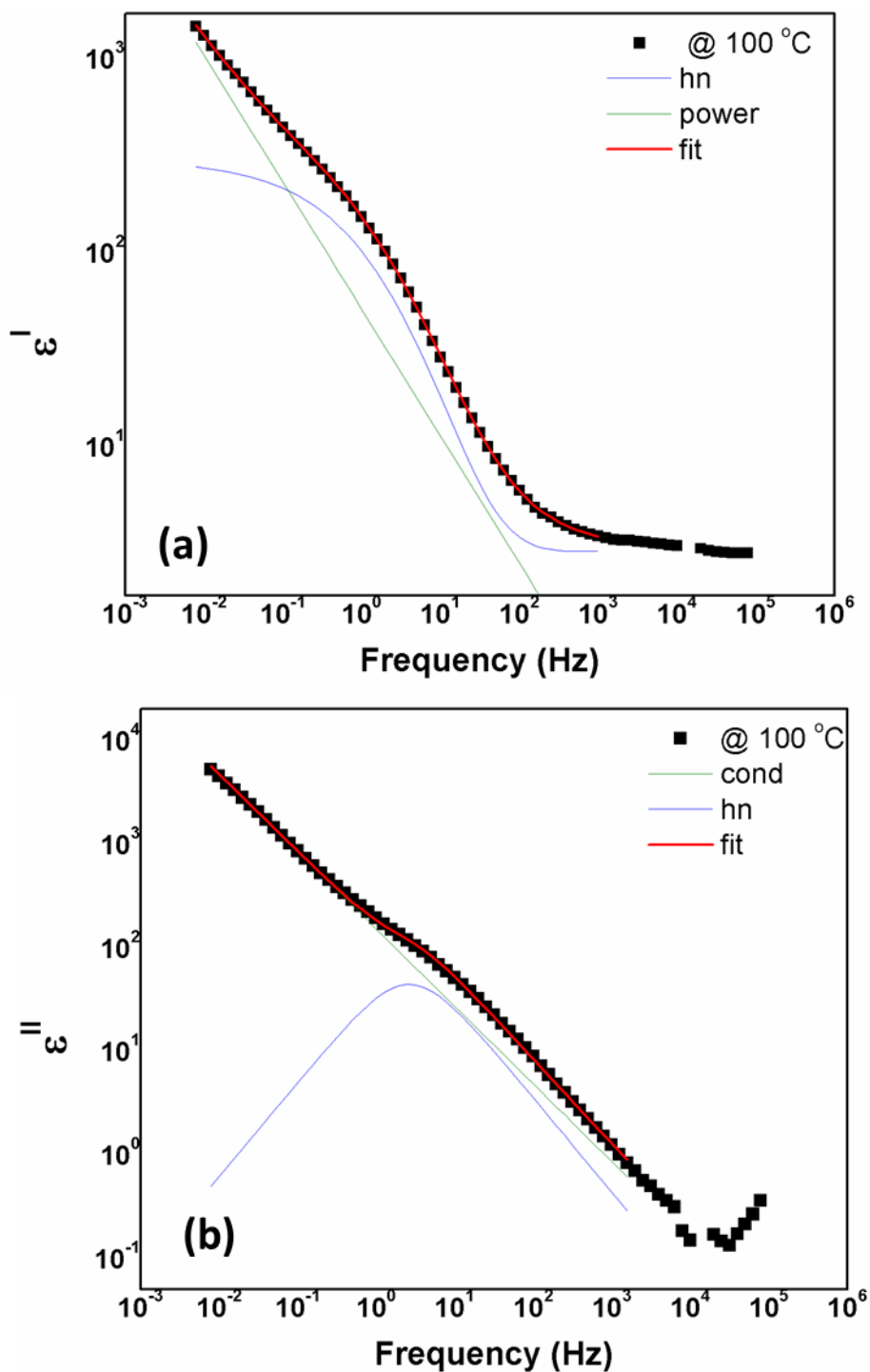


Figure 4.11 Fitting results for dielectric spectrum of 'PVA/AgNPs/PVA' thin films (MLTs) at $T = 100\text{ }^{\circ}\text{C}$: (a) real part, (b) imaginary part.

the direction of electric field and polarization due to charge accumulation decreases, this process leads to decrease in the value of loss factor. The obtained experimental data is fitted for all MLTs maintained at different temperatures by following equation (3) and considering power law as shown in **Figures 4.11 & 4.12** and resultant

distribution parameters (a, b), dielectric strength and evaluated conductivity values are tabulated in **Tables 4.2 & 4.3**.

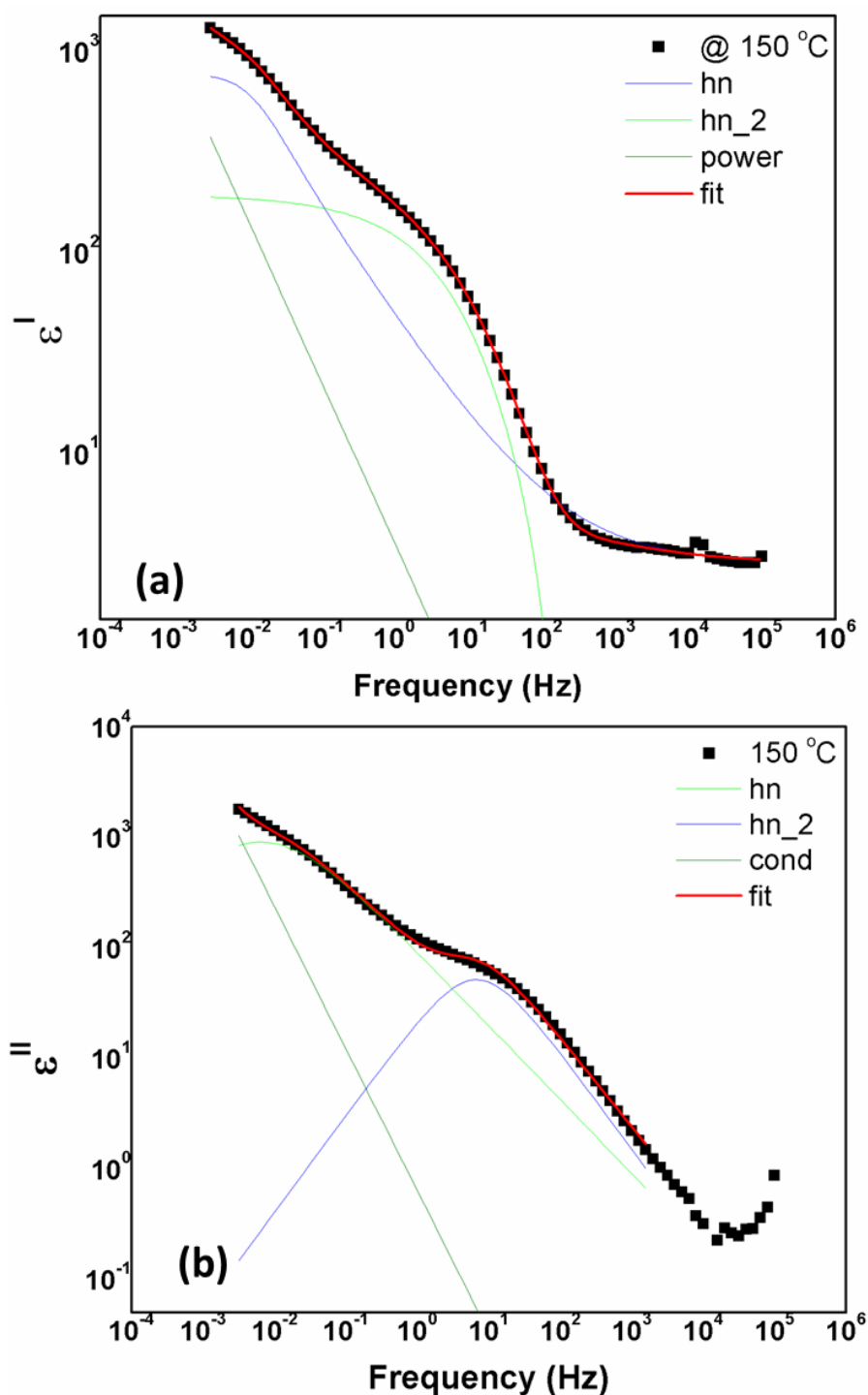


Figure 4.12 Fitting results for dielectric spectrum of 'PVA/AgNPs/PVA' thin films (MLTs) at $T = 150\text{ }^{\circ}\text{C}$: (a) real part, (b) imaginary part.

T (°C)	f _r (Hz)	Δε	a	b	f _{r_err}	Δε_err	a_err	b_err
20	-0.588	130.49	0.60	1	0.021	4.54	0.01	0.073363
50	-0.388	171.93	0.52	0.83	0.114	34.20	0.05	0.437823
100	0.504	303.21	0.47	1	0.062	13.41	0.01	0.137508
150	-1.907	775.86	0.96	0.56	0.226	1567.66	0.54	0.422912
200	0.829	153.27	0.72	1	0.0451	9.64	0	0

Table -4.2: Fitting parameters for relaxation process for ‘PVA/AgNPs/PVA’ structured cell at different temperatures.

T (°C)	log σ (S/cm)	n	log σ_err	n_err
20	-11.72	0.71	0.04	0.022
50	-11.57	0.96	0.461	0.358
100	-10.27	0.74	0.006	0.008
150	-12.22	1.28	3.314	1.7
200	-10.38	0.90	1.498	0.722

Table – 4.3: Fitting parameters for DC conductivity of ‘PVA/AgNPs/PVA’ structured cell at different temperatures.

Variation of the loss tangent ($\tan \delta = \varepsilon''/\varepsilon'$) as a function of frequency for MLTs are illustrated in Figure 4.13. Significant relaxation peaks are noticed at all conditions and it is observed that peak position shifted towards higher frequency side with the increase in temperature. This could be due to more number of charge carriers introduced into PVA matrix by the presence of AgNPs clusters. The analysis of the dielectric behaviour could be explained by using the formulation of dielectric moduli. A complex electric modulus has been used to investigate the conductivity relaxation phenomena, because it suppresses the effects of electrode polarization to give a clear picture of electrical properties inherited in MLTs. Complex electric modulus can be estimated from the impedance data using following expression [41].

$$M^* = (\varepsilon^*)^{-1} = M^l(\omega) + jM^{ll}(\omega) \dots\dots\dots (4.2.4)$$

$$M^I = \varepsilon^I / ((\varepsilon^I)^2 + (\varepsilon^{II})^2) \text{ and } M^{II} = \varepsilon^{II} / ((\varepsilon^I)^2 + (\varepsilon^{II})^2) \dots\dots\dots (4.2.5)$$

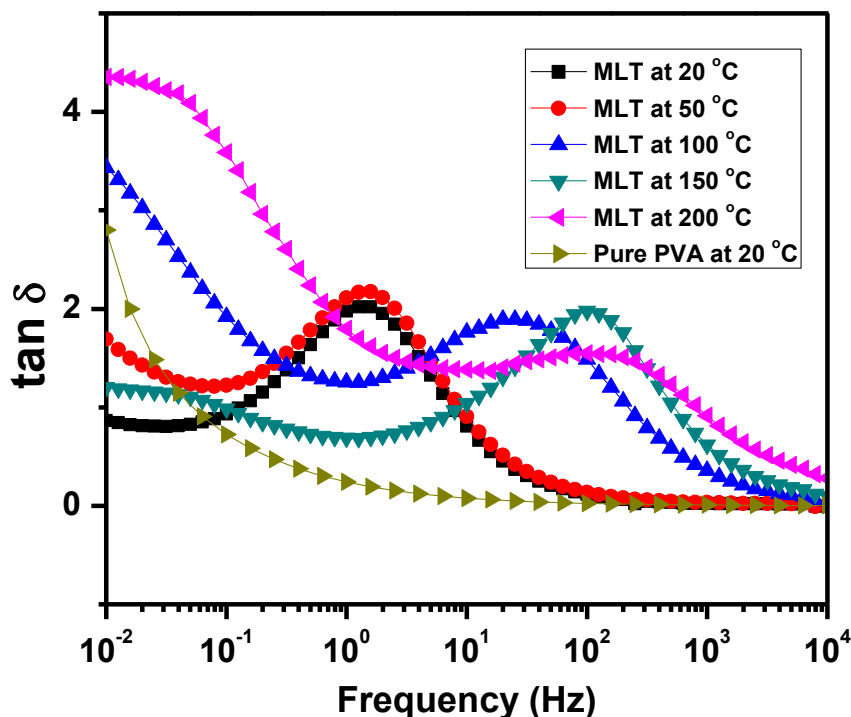


Figure 4.13 The Variation of the loss tangent ($\tan \delta$) with frequency at different temperatures for ‘PVA/AgNPs/PVA’ thin films (MLTs).

In the above expressions M^I , M^{II} and ε^I , ε^{II} are the real and imaginary parts of the electric modulus and dielectric constants, respectively. Figure 4.14a illustrates the variation of M^I with applied frequency at various temperatures and M^I demonstrates a step-like transition and attains a asymptotic value, which indicates the predominant capacitive nature of the samples and also the presence of relaxation processes. These step-like transitions are accompanied by well-defined peaks in the corresponding plots of M^{II} as a function of frequency (Figure 4.14b). Evidently, step-like transition behavior is observed to shift to higher frequency region with the enhancement of temperature. The imaginary part of the electric modulus represents the energy loss under electric field and the variation of the imaginary part of the electric modulus as a function of frequency over a range of temperature, enables us to get an insight into the dielectric and conductivity relaxation processes occurring in the matrix of host polymers. Because, the presence of the conductive particles, dielectric or conductivity relaxations could be observed in the case of interfacial polarization occurred in

heterogeneous systems [42]. As shown in Figure 4.14b, M'' curves exhibit a relaxation peak with significant asymmetry as a function of applied frequency and the respective peak maximum is observed to shift to higher frequency side as a function of temperature. It indicates that the dielectric relaxation is activated thermally and the signature of hopping type conduction [43].

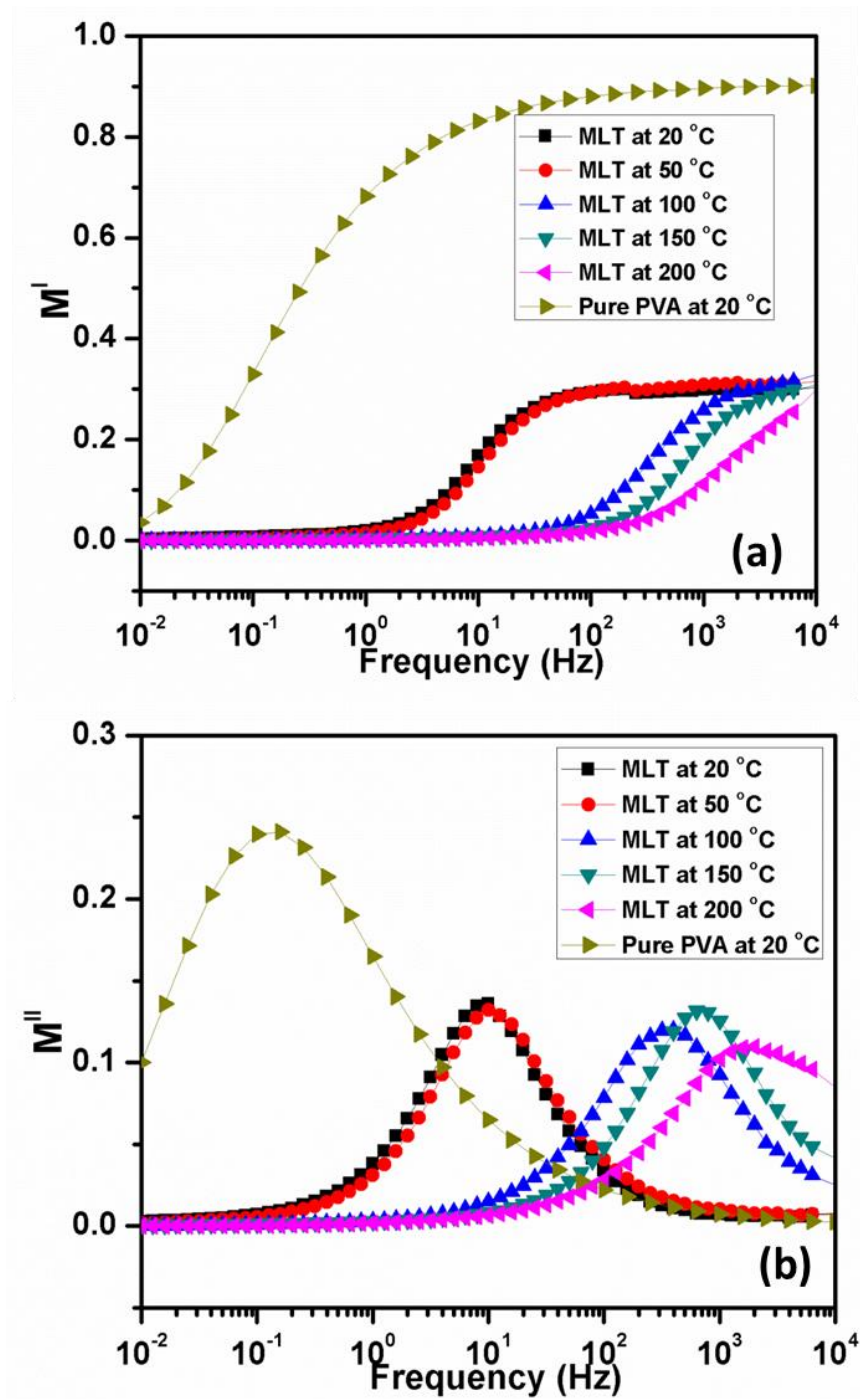


Figure 4.14 The frequency variation of (a) real (M') and (b) imaginary (M'') parts of electric modulus at different measuring temperatures.

4.2.4 Conclusions

In the present report, we made an attempt to understand the influence of interlayer of silver nanoparticles on dielectric properties of intrinsic PVA thin films. We deposited 400 nm thickness of AgNPs interlayer to fabricate “PVA/AgNPs/PVA” structured multi-layered thin films and investigated their frequency dependent dielectric properties as a function of temperature in the 20 °C to 200 °C. The estimated optical bandgap energy of the samples is decreased with increase in temperature. It has been observed that the presence of interlayer has significantly influenced the dielectric relaxation and conductivity properties as a function of temperature. At room temperature, PVA/AgNPs/PVA thin films demonstrated 3 times higher dielectric constant value in comparison to pure PVA at 1 KHz and noticed to increase to 16 with an increase in temperature to the higher value of 200 °C. Inclusion of interlayer enhances the dielectric relaxation frequency, clearly indicating the relaxation of dipoles via multiple channels due to availability of more number of free charge carriers. The peak maximum of imaginary part of electric modulus of multi-layered thin films shifted from 10 Hz to 2000 Hz with the increase of temperatures.

References:

1. G. Neshet, G. Marom, and D. Avnir, *Chemistry of Materials* 20 (2008) 4425. 2008.
2. A. Nimrodh Ananth and S. Umopathy, *Applied Nanoscience* 1 (2011) 87.
3. R. Mukherjee, S. Das, A. Das, S.K. Sharma, A.K. Raychaudhuri and A. Sharma, *ACS Nano* 4 (2010) 3709.
4. S. Prakash, T. Chakrabarty, A.K. Singh and V.K. Shahi, *Biosensors and Bioelectronics* 41 (2-13) 43.
5. W.S Tung, N. Clarke, R.J. Composto and K.I. Winey, *Macromolecules* 46 (2013) 2317.
6. F. Faupel, V. Zaporozhchenko, T. Strunskus and M. Elbahri, *Advanced Engineering Materials* 12 (2010) 1177.
7. R. D. Deshmukh and R.J. Composto, *Langmuir* 23 (2012) 13169.
8. Z. Liu, L. Zhang, S. Poyraz and X. Zhang, *Current Organic Chemistry* 17 (2013) 2256.
9. G. A. Gelves, M. H. A.Saleh and U. Sundararaj, *Journal of Materials Chemistry* 21 (2011) 829.
10. P. Barber, S. Balasubramanian, Y. Anguchamy, S. Gong, A. Wibowo, H. Gao, H. J. Ploehn and H.C Zur Loye, *Materials* 2 (2009) 1697.
11. R. B. Grubbs, *Polymer Reviews* 47 (2007) 197.
12. P. K. Sudeep and T. Emrick, *Polymer Reviews* 47 (2007) 155.
13. B. Susrutha, S. Ram and A.K. Tyagi, *Journal of Nanofluids* 1 (2012) 120.
14. N.T. Nguyen and J.H. Liu, *Journal of the Taiwan Institute of Chemical Engineers* 45 (2014) 2827.
15. D. R. Raj, S. Prasanth, T.V. Vineeshkumar and C. Sudarsanakumar, *Optics Communications* 340 (2015) 86.
16. R.F. Bhajanti, V. Ravindrachary, A. Harisha, G. Ranganathaiah, G.N. Kumaraswamy, *Applied Physics A* 87 (2007) 797.
17. P.K. Khanna, N. Singh, S. Charan, V.V.V.S. Subbarao, R. Gokhale and U.P. Mulik, 93 (2005) 117.
18. S. Mahendia, A.K. Tomar and S. Kumar, *Journal of Alloys and Compounds* 508 (2010) 406.
19. Z.H. Mbhele, M.G. Salemane, C.G.C.E. Sittert, J.M. Nedeljkovic, V. Djokovic and A.S. Luyt, *Chemistry Materials* 15 (2003) 5019.
20. P. B. Bhargav, V.M. Mohan, A.K. Sharma and V.V.R.N. Rao, *Current Applied Physics* 9 (2009) 165.
21. V.K. Sharma, R.A. Yngard and Y. Lin, *Advances in Colloid and Interface Science* 145 (2009) 83.
22. D. R. Monteiro, L. F. Gorup, A. S. Takamiya, A. C.R. Filho, E.R. Camargo and D.B. Barbosa, *International Journal of Antimicrobial Agents* 34 (2009) 103.
23. J.G. Barrasa, J.M. L. Luzuriaga and M. Monge, *Current European Journal of Chemistry* 9 (2011) 7.
24. J. Fabrega, SN. Luoma, CR. Tyler, TS. Galloway and JR. Lead, *Environmental International* 37 (2011) 517.
25. D. Kim, S. Jeong and J. Moon, *Nanotechnology* 17 (2006) 4019.
26. N. Faraji, W.M. Mat Yunus, A. Kharazmi, E. Saion, M. Shahmiri, N. Tamchek, *Journal European optical society Rapid Publication* 7 (2012) 1.
27. R. Gradess, R. Abargues, A. Habbou, J. C. Ferrer, E. Pedrueza, A. Russell, J.L. Valdes and J. P. M. Pastor, *Journal of Materials Chemistry* 19 (2009) 9233.

28. R. Saikia, P. Gogoi and P. Datta, *International Journal of Innovative Research & Development* 1 (2012) 83.
29. I.O. Ali, *Colloids and Surfaces A: Physicochem. Eng. Aspects* 436 (2013) 922.
30. A.S. Roy, S. Gupta, S. Sindhu, A. Parveen and P.C. Ramamurthy, *Composites B* 47 (2013) 314.
31. D. Bhadra, J. Sannigrahi, B. K. Chaudhuri and H. Sakata, *Polymer Composites* 33 (2012) 436.
32. A. Hassen, A. M. E. Sayed, W. M. Morsi and S. E. Sayed, *Journal of Applied Physics* 112 (2012) 1.
33. A.B. Silva, M. Arjmand, U. Sundararaj, R. E.S. Bretas, *Polymer* 55 (2014) 226.
34. S. Havriliak and S. Negami, *Polymer* 8 (1967) 161.
35. D.W. Davidson and R. H. Cole, *Journal of Chemistry Physics* 19 (1951) 1484.
36. K.S. Cole and R.H. Cole, *Journal of Chemistry Physics* 9 (1941) 341.
37. Boettcher CJF, Bordewijk P. Theory of electric polarization, Vol. 2. Amsterdam: Elsevier, 1978. P. 485.
38. Scaife BKP. Principles of dielectrics. Oxford: Oxford Science, 1989. P. 106.
39. Maxwell JC. Electricity and magnetism, Vol. 1. Oxford: Clarendon Press, 1892. P. 452.
40. Sillars RW. The behavior of polar molecules in solid paraffin wax. Proc R Soc Lond 1939; A169: 66 – 82.
41. K.K. Kiran, M. Ravi, Y. Pavani, S. Bhavani, A.K. Sharma, V.V.R. N. Rao, *Journal of Non-Crystalline Solids* 358 (2012) 3205.
42. G M. Tsangaris, G C. Psarras, N. Kouloumbi, *Journal of Material Science* 33 (1998) 2027.
43. G C. Psarras, E. Manolakaki and G M. Tsangaris, *Composites A* 34 (2003) 1187.

Part II. Hyperbolic Metamaterials for Spontaneous Emission enhancement

5.0 Introduction

“Spontaneous emission is known as a quantum effect, which is the responsible for spontaneous decay of excited states of atoms or ions”.

When an atom or laser ion in a gain medium is excited to a higher-lying energy levels (by absorption of a photon), after some time spontaneously return to its ground state, or to some intermediate energy levels, by releasing the energy in the form of a photon, which carries the energy in some random direction as illustrated in **Figure – 5.1**. This process is called *spontaneous emission*. This view is supported by the fact that spontaneous emission can be modified by placing an atom or ion in a microcavity structure, which modifies the mode structure of the optical field.

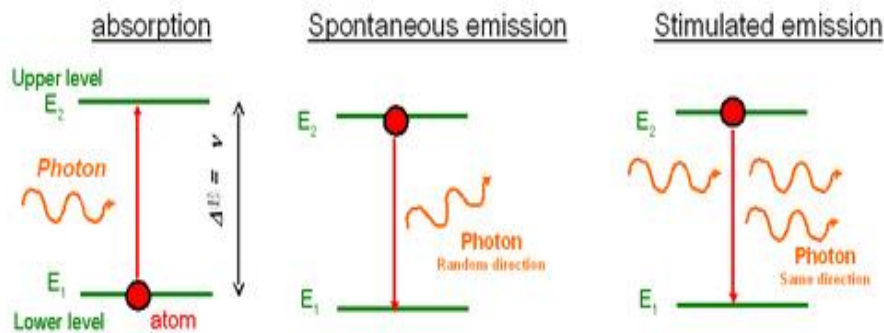


Figure – 5.1: Interaction of a photon with two energy levels of an atom. Left: Absorption moves the atom from the ground state to the excited state. Middle: Spontaneous emission moves the atom from the excited to the ground state. Right: Induced emission of a photon, by a photon interfering with an atom in the excited state.

The rate of spontaneous emission (and thus the lifetime of the excited level) is determined both by the properties of the atom and by the mode structure of the surrounding medium. For an atom in free space (or in a homogeneous medium), transition cross sections can be used for calculating the rate of spontaneous emission events (\rightarrow radiative lifetime). Typical upper-state lifetimes of atoms are a few nanoseconds if there are allowed transitions to lower levels; much longer values can occur for forbidden transitions. Light produced by spontaneous emission is called luminescence. The luminescence emitted by a laser gain medium typically carries a total power which equals around one-tenths to one-third of the laser's output power. The optical spectrum of the luminescent light is essentially governed by transition cross

sections. If the number of light sources in the excited state at time t is given by $N(t)$, the rate at which N decays is:

$$\frac{\partial N(t)}{\partial t} = -A_{21} N(t) \dots\dots\dots (5.1)$$

where A_{21} is the rate of spontaneous emission. In the rate-equation A_{21} is a proportionality constant for this particular transition in this particular light source. The constant is referred to as the Einstein A coefficient, and has units s^{-1} [1]. The above equation can be solved to give:

$$N(t) = N(0)e^{-A_{21}t} = N(0)e^{-\Gamma_{rad}t} \dots\dots\dots (5.2)$$

where $N(0)$ is the initial number of light sources in the excited state, t is the time and Γ_{rad} is the radiative decay rate of the transition. The number of excited states N thus decays exponentially with time, similar to radioactive decay. After one lifetime, the number of excited states decays to 36.8% of its original value ($\frac{1}{e}$ times). The radiative decay rate Γ_{rad} is inversely proportional to the lifetime τ_{21} .

$$A_{21} = \Gamma_{21} = \frac{1}{\tau_{21}} \dots\dots\dots (5.3)$$

Rate of spontaneous emission (i.e., the radiative decay rate) is one of the key factor, this can be described by Fermi's golden rule [2]. The rate of emission depends on two factors: an 'atomic part', which describes the internal structure of the light source and a 'field part', which describes the density of electromagnetic modes of the environment. The atomic part describes the strength of a transition between two states in terms of transition moments. In a homogeneous medium, such as free space, the rate of spontaneous emission in the dipole approximation is given by:

$$\Gamma_{rad}(\omega) = \frac{\omega^3 n |\mu_{12}|^2}{3\pi \epsilon_0 \hbar C^3} = \frac{4\alpha \omega^3 n | \langle 1|r|2 \rangle|^2}{3C^2} \dots (5.4)$$

where ω is the emission frequency, n is the index of refraction, μ_{12} is the transition dipole moment, ϵ_0 is the vacuum permittivity, \hbar is the reduced Planck constant, C is the vacuum speed of light, and α is the fine structure constant. In contrast with atoms, which have a discrete emission spectrum, quantum dots can be tuned continuously by changing their size. This property has been used to check the ω^3 frequency dependence of the spontaneous emission rate as described by Fermi's golden rule [3].

5.1 Radiative and nonradiative decay: the quantum efficiency

In the rate-equation above, it is assumed that decay of the number of excited states N only occurs under emission of light. In this case, radiative decay and this means that the quantum efficiency is 100%. In addition to radiative decay (which occurs under the emission of light) there is a second decay mechanism, known as nonradiative decay. The total decay rate can be expressed as follows,

$$\Gamma_{tot} = \Gamma_{rad} + \Gamma_{nrad} \dots\dots\dots (5.5)$$

where Γ_{tot} is the total decay rate, Γ_{rad} is the radiative decay rate and Γ_{nrad} the nonradiative decay rate. The quantum efficiency (QE) is defined as the fraction of emission processes in which emission of light is involved, which is expressed as follows;

$$Q = \frac{\Gamma_{rad}}{\Gamma_{rad} + \Gamma_{nrad}} \dots\dots\dots (5.6)$$

In nonradiative relaxation, the energy is released as phonons, more commonly known as heat. Nonradiative relaxation occurs when the energy difference between the levels is very small, and these typically occur on a much faster time scale than radiative transitions. For many materials (for instance, semiconductors), electrons move quickly from a high energy level to a meta-stable level via small nonradiative transitions and then make the final move down to the bottom level via an optical or radiative transition. This final transition is the transition over the bandgap in semiconductors. Large nonradiative transitions do not occur frequently because the crystal structure generally cannot support large vibrations without destroying bonds (which generally doesn't happen for relaxation). Meta-stable states form a very important feature that is exploited in the construction of lasers. Specifically, since electrons decay slowly from them, they can be deliberately piled up in this state without too much loss and then stimulated emission can be used to boost an optical signal.

5.2 Purcell Effect

The Purcell effect is the enhancement of a fluorescent molecule's spontaneous emission rate by its environment. In the 1940s Edward Mills Purcell discovered the enhancement of spontaneous emission rates of atoms when they are matched in a

resonant cavity (the Purcell Effect) [4]. The magnitude of the enhancement is given by the Purcell factor,

$$F_P = \frac{3}{4\pi^2} \left(\frac{\lambda_c}{n}\right)^3 \left(\frac{Q}{V}\right) \dots\dots\dots (5.7)$$

where $\left(\frac{\lambda_c}{n}\right)$ is the wavelength within the material, and Q and V are the quality factor and mode volume of the cavity, respectively. One way of seeing why this enhancement arises is by using cavity quantum electrodynamics [5]. Fermi's golden rule dictates that the transition rate for the atom-vacuum (or atom-cavity) system is proportional to the density of final states. In a cavity at resonance, the density of final states is enhanced (though the number of final states may not be). The Purcell factor is then just the ratio of the free space density of states [6].

$$\rho_f = \frac{8\pi n^3 \nu^2}{c^3} \text{ to that of the cavity } \rho_c = \frac{1}{\Delta\nu V}$$

Using $Q = \frac{\nu}{\Delta\nu}$, therefore

$$\rho_c / \rho_f = \frac{1}{8\pi} \left(\frac{\lambda}{n}\right)^3 \cdot \left(\frac{Q}{V}\right), \text{ which is correct upto constant.}$$

It has been predicted theoretically [7,8] that a 'photonic' material environment can control the rate of radiative recombination of an embedded light source. A main research goal is the achievement of a material with a complete photonic bandgap: a range of frequencies in which no electromagnetic modes exist and all propagation directions are forbidden. At the frequencies of the photonic bandgap, spontaneous emission of light is completely inhibited. Fabrication of a material with a complete photonic bandgap is a huge scientific challenge. For this reason photonic materials are being extensively studied. Many different kinds of systems in which the rate of spontaneous emission is modified by the environment are reported, including cavities, two, [9, 10] and three-dimensional [11] photonic bandgap materials. The Purcell effect can also be useful for modeling single-photon sources for quantum cryptography [12]. Controlling the rate of spontaneous emission and thus raising the photon generation efficiency is a key requirement for quantum dot based single-photon sources [13].

Spontaneous emission rates were believed to be an intrinsic property of a material, and that such light could be manipulated only after the photons were emitted.

It was later understood that spontaneous emission also depends strongly on the surrounding environment through the density of states and the local strength of the electromagnetic modes. Spontaneous emission is an essential ingredient in the operation of optoelectronic devices, such as light emitting diodes, or semiconductor lasers. In LEDs, it constitutes the actual output of the device, while in semiconductor lasers it provides the first photon in the ‘laser’ mode that will trigger the coherent stimulated emission that characterizes the laser output. In semiconductor lasers, the portion of spontaneous emission that goes into the lasing mode is only of the order of $\beta = 10^{-5}$, while the rest represents an energy loss that sets a lower limit to the lasing threshold. At the same time, because it takes on average 10^5 photons to be emitted before one photon goes into the right mode, lasers generally display a delay in their turn-on time which limits the speed with which they can be modulated directly to transmit binary information. If we envisage the development of integrated optical circuits with miniature high-speed low-threshold emitters and detectors communicating in the same chip, we would need devices whose spontaneous emission is 4 orders of magnitude lower than that of currently existing semiconductor lasers. At the same time, if we can control spontaneous emission we may be able to increase the efficiency of LEDs and lasers, increase their speed, and reduce their threshold to the point of possibly attaining ‘thresholdless lasing’.

5.3 Optical Microcavities

Optical microcavities, which are resonators with at least one dimension on the order of an optical wavelength, have received much attention with respect to the promising applications for novel types of microlight-emitting diodes and microlasers. Using the optical microcavity structures, one can control emissive behaviors of materials placed inside the cavities [14]. For example, modification of a spatial distribution of radiation power, change of a spectral linewidth, and enhancement and suppression of spontaneous emission are possible [15, 16].

Like acoustic analogue to the tuning fork, the optical micro cavity or micro resonators has a size dependent resonant frequency spectrum. An ideal cavity would confine light indefinitely (i.e., without loss) and would have resonant frequencies at precise values. Deviation from this ideal condition is described by the cavity Q factor (which is

proportional to the confinement time in units of the optical period) [17 – 23]. Q factor and microcavity volume (V) figure prominently in applications of these devices, and a summary of values typical for the devices are presented in Figure – 5.2.


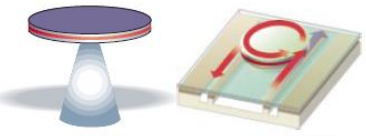
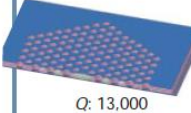
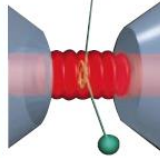
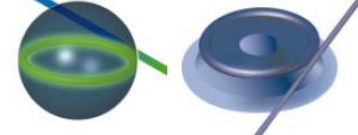
	Fabry-Perot	Whispering gallery	Photonic crystal
High Q	 <p>Q: 2,000 V: $5 (\lambda/n)^3$</p>	 <p>Q: 12,000 V: $6 (\lambda/n)^3$</p> <p>$Q_{\text{H-V}}: 7,000$ $Q_{\text{FDB}}: 1.3 \times 10^5$</p>	 <p>Q: 13,000 V: $1.2 (\lambda/n)^3$</p>
Ultrahigh Q	 <p>F: 4.8×10^5 V: $1,690 \mu\text{m}^3$</p>	 <p>Q: 8×10^9 V: $3,000 \mu\text{m}^3$</p> <p>Q: 10^8</p>	

Figure – 5.2: The microcavities according to the confinement method and by according to high Q and ultrahigh Q.

Since 1946, when it was first proposed that the spontaneous emission from an excited state of an emitter can be significantly altered if it is placed into low-loss wavelength-scale cavity various microcavities designed for efficient control of spontaneous emission [24 – 32].

5.4 Photonic Crystals

Photonic Band Gap materials, also known as photonic crystals (as shown in Figure – 5.3), are materials which have a band gap due to a periodicity in the materials dielectric properties. The band gap in photonic crystals represents the forbidden energy range where wave behaving photons cannot be transmitted through the material. By imitating the periodicity of photonic crystals one can tailor the specific band gap of a structure by defining a pattern with repeating regions, typically holes in a square or hexagonal arrangement, which alternates between materials with high and low dielectric constant. In the one-dimensional case, a PBG structure may be something as well known as the distributed Bragg reflector (DBR). A simple DBR consists of multiple layers of alternating high- and low-index materials arranged periodically. The thickness of each layer is chosen so as to satisfy the Bragg quarter-wave condition, that

$$d = \frac{\lambda_0}{4n} \dots\dots\dots (5.8)$$

where λ_0 is the reference wavelength of the structure, and d and n are the thickness and refractive index of a particular layer, respectively.

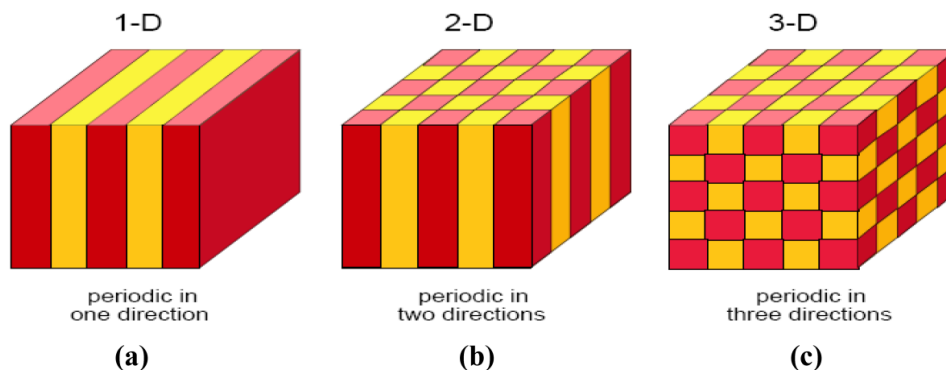


Figure – 5.3: Photonic crystal structures in various directions.

For a typical DBR, there is a range of wavelengths (called the photonic bandgap), centered about the reference wavelength λ_0 , for which the structure is almost totally reflecting (that is, no propagating photon modes are allowed through the structure). Figure – 5.4, shows a typical transmission spectrum for a DBR. The range of wavelengths demarcating the photonic bandgap is shown in the figure. It is important to note that the width of the gap is directly dependent on $\Delta n = n_H - n_L$, the refractive index difference: all other things being equal, the gap will be wider for larger index differences. (Here, n_H and n_L are the high and low refractive indices, respectively.)

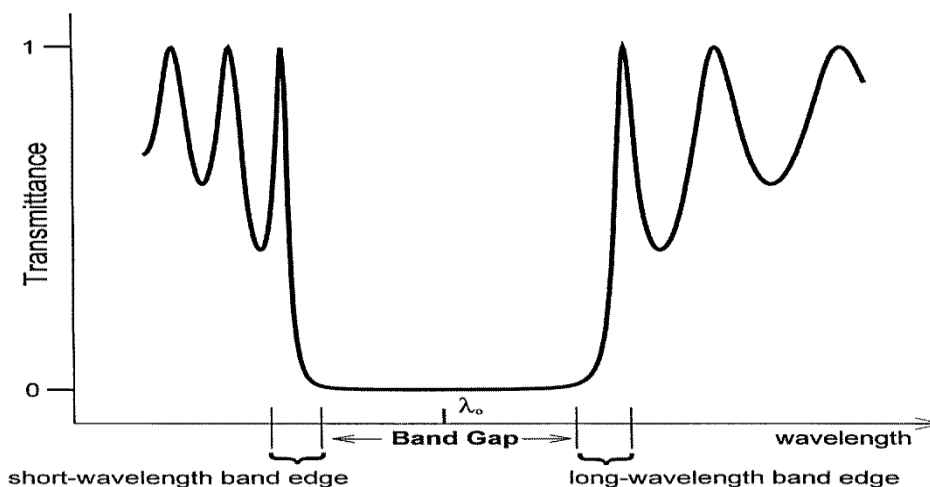


Figure – 5.4: Typical transmission spectra $T(\lambda)$ of a one-dimensional PBG structure.

Photonic crystals, artificially created, multi-dimensionally periodic structures are known for a forbidden electromagnetic bandgap. For that reason, they can be used to *modify spontaneous emission. Initially, it was proposed to use photonic crystals to inhibit spontaneous emission, but they can be employed to enhance it as well.* Therefore in view of enhancement of spontaneous emission previously, closed cavities (microcavities) and open cavities (photonic crystals) have been employed as significant tools to understand cavity quantum electrodynamics and hence for the study of modification of spontaneous emission enhancement by the Purcell effect [33 – 35]. However, the incapability for ‘microcavities’ and ‘photonic crystal’ systems to obtain high quality factor resonance make them unviable for Purcell enhancement. This incompatibility of cavity technologies pushed towards the discovery of novel systems whose exhibit broadband Purcell effect.

In this direction, Metamaterials have been recognized as promising and reliable systems in comparison to conventional cavity approaches due to the existence of a large number of electromagnetic states, which lead to a divergence in the photonic density of states allowing a broadband control. In particular, Metamaterials play a vital role to confine the power emitted by emitters in large spatial wavevector channels. This will open new routes for innovative photonic device applications from broadband single photon sources to strong coupling of emitters and plasmonics.

5.5 Metamaterials

Metamaterials are materials engineered to have properties that have not yet been found in nature. They are made from assemblies of multiple elements fashioned from conventional materials such as metals or plastics. The materials are usually arranged in repeating patterns, often at microscopic or smaller scales that are smaller than the wavelengths of the phenomena they influence. Metamaterials derive their properties not from the properties of the base materials, but from their designed structure. Their precise shape, geometry, size, orientation and arrangement gives them their properties [36 – 40].

5.5.1 About discovery of “Metamaterials”

In 1898, Jagadish Chandra Bose was conducting Microwave experiments on twisted structures, geometries to prove the possibility of existence of man-made artificial chiral elements by today’s terminology [41].

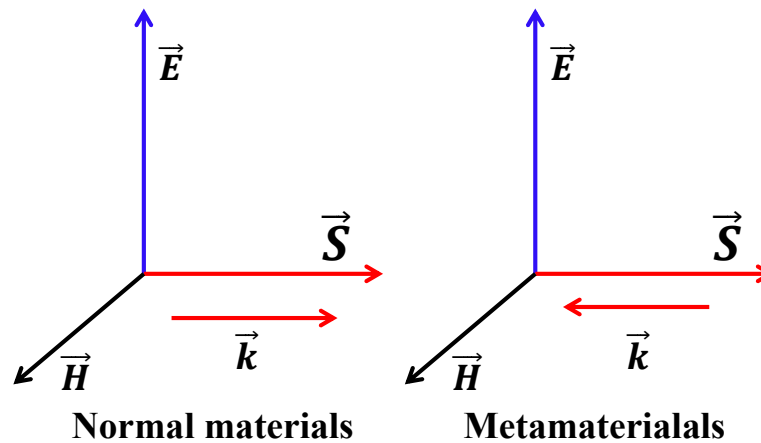


Figure – 5.5 . The pointing Vectors representation of EM waves in left handed and right handed materials.

The significant report on “backward waves associated with reflection directions based on the signs of permittivity and permeability” motivated the researchers community around the Globe, to design and fabricate artificial complex structures [42]. The significant feature of these artificial materials is the negative refraction, so that they recognized as “left handed materials”, which can refract light in contrary to the normal “right handed” rules of electromagnetism. When an electromagnetic wave passes through left handed materials, the electric vector (\vec{E}), the electromagnetic vector (\vec{H}) and wave vector (\vec{k}) do not satisfy the right handed law (as illustrated in Figure – 5.5). Later, Victor Veselago studied on general properties of E. M wave propagation in left handed materials and in his theoretical work, he showed that a plate of material with negative index of refraction can focus light in the same direction, which observed in curved lens made with conventional materials. In 2004, Smith et. al had realized gradient refraction index medium to bend electromagnetic waves. Now, the concept of negative refractive index is widely accepted and the discovery of Metamaterials opened new avenues for the invention and fabrication of “smart devices” for break through applications in current science & technology. In 2001, Rodger coined these artificial complex materials as “Metamaterials” and according to him, Metamaterials are defined as follows: “Man-made macroscopic composites, which are not exist in nature, having

three dimensional and periodic cellular architecture designed to produce an optimized combination of two (or) more responses to a specific excitation". These Metamaterials are artificial periodic structures with lattice constants of size smaller than the wavelength of incident radiation. As an effect of interaction of EM waves, the electric and magnetic properties of the medium can be described in terms of permittivity and permeability. In presence of electric field, permittivity value provides the information about, how much extent a medium changes by absorbing electrical energy. In ordinary materials, both permittivity and permeability values are positive and in case of metamaterials both parameters consist negative values. But still propagation of EM waves through metamaterial is possible because product of respective permittivity and permeability values remains positive.

5.5.2 Theory of Metamaterials

In the word "Metamaterial", Meta is a Greek word, which refers as beyond some something and these Metamaterials can have their EM properties altered to something beyond what we can found nature. These Metamaterials can be characterized by Maxwell equations as follows;

Maxwell equation in time domain:

$$\vec{\nabla} \times \vec{E} = -j\omega\mu\vec{H}; \quad \nabla \cdot \vec{D} = \rho \dots\dots\dots (5.9)$$

$$\vec{\nabla} \times \vec{H} = \vec{J} + j\omega\varepsilon\vec{E}; \quad \nabla \cdot \vec{B} \dots\dots\dots (5.10)$$

In case of plane wave, above equations reduce to

$$\vec{k} \times \vec{E} = \omega\mu\vec{H}; \quad \vec{k} \times \vec{H} = -\omega\varepsilon\vec{E} \dots\dots\dots (5.11)$$

Therefore by considering the above equations, Ziolkowski [43] has classified metamaterials by their constitution parameters as described in Figure – 5.6. The four possible combinations of the signs of both ε and μ are (+,+), (+,-), (-,+), and (-,-). Generally naturally existing materials have positive permittivity and permeability, hence they are known as double – positive (DPS) media. If both ε and μ consist negative values, they called as double – negative (DNG) (or) left handed systems. Materials with one negative parameter are known as single-negative (SNG) and are further classified as ε – negative (ENG) materials, for example naturally exist cold

plasma and silver and μ – negative (MNG) materials like ferromagnetic materials. It is worth to mention that, till to date no material exhibit simultaneous permittivity and permeability has been found in nature, which can design and fabricate artificially.

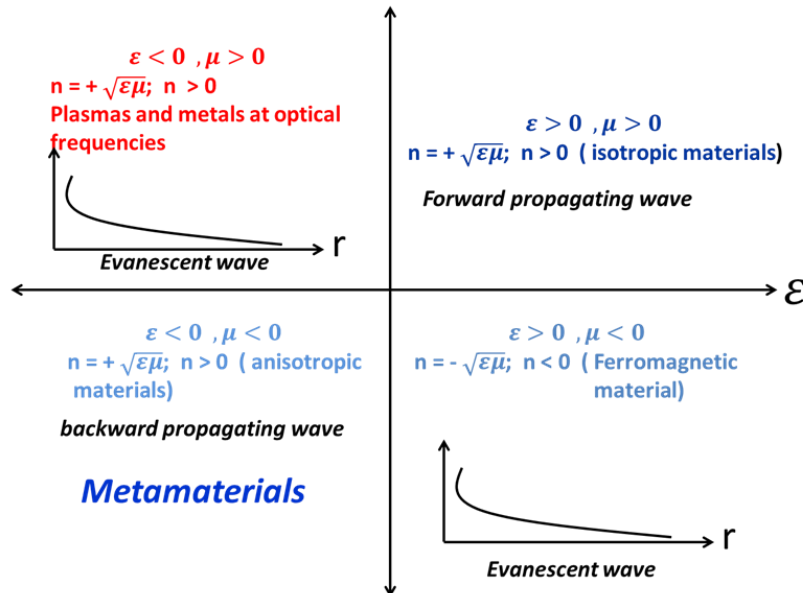


Figure – 5.6. Schematic representation of the possible domains of electromagnetic materials.

In the first quadrant ($\epsilon > 0, \mu > 0$) indicates right handed material (RHM) and wave propagation will occur forward direction. These are commonly used natural material. In this quadrant, the system follows right hand thumb rule for the direction of propagation of wave. The second quadrant ($\epsilon > 0, \mu < 0$) supports for the propagation of evanescent waves, corresponding to MNG and as well as fourth quadrant ($\epsilon < 0, \mu > 0$) system also supports for the propagation for evanescent waves (like electric plasmas), which are called ENG systems. Therefore Metamaterials come under third quadrant ($\epsilon < 0, \mu > 0$), which follows left handed rule and in which propagation of wave takes place in backward direction in this medium. Due to negative μ and negative ϵ the refractive index of the medium is negative, so that these materials are called negative index material. As a result, an incident wave experiences negative refraction at the interface and EM ray bends into inside direction after refracting into medium, which is contrary to positive index materials.

5.6 Hyperbolic Metamaterials

Among the varieties of Metamaterials proposed and fabricated since then, hyperbolic metamaterials (HMMs) have rapidly gained a central role in nanophotonics, due to their unprecedented ability to access and manipulate the near-field [44] of a light emitter or a light scatterer. This feature derives directly from the excitation, inside of HMMs, of coupled surface plasmons (SPs) [45 – 49]. A SP is a collective oscillation of electrons, confined to the surface of a metal in contact with a dielectric. If the metal and the dielectric are shaped as thin layers, their interface is flat, and the metal surface supports propagating surface plasmons (or “surface plasmon polaritons” (SPPs)). If instead the metal has the shape of a nanoparticle or a nanowire, the surface of the metallic domain supports localized surface plasmons. The excitation of these coherent electronic vibrations is accompanied by the generation of an electromagnetic field. The latter decays very fast on both the dielectric and the metallic side, and there by interacts principally with the near-field of the interface.

5.6.1 Surface Plasmons (SPs) and Surface plasmon polaritons (SPPs)

The long-range nature of the coulomb interaction between valence electrons in metals yields collective plasma oscillations similar to the electron-density oscillations observed in electrical discharges in gases. There by explaining the early experiments on the bombardment of thin metallic films by fast electrons. The impact of the film boundaries on the production of collective excitations and found that the boundary effect is to cause the appearance of a new lowered loss due to the excitation of surface collective oscillations, which are known as surface plasmons (as illustrated in Figure – 5.7) [50 – 52]. “Surface plasmons (SPs) are coherent delocalized electron oscillations that exist at the interface between any two materials where the real part of the dielectric function changes sign across the interface (e.g. a metal-dielectric interface, such as a metal sheet in air)”.

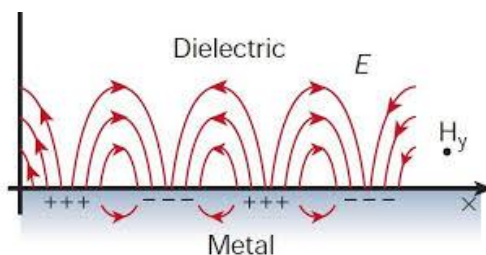


Figure – 5.7: Surface plasmons at interface of Metal and Dielectric films.

Surface plasmon polaritons (SPPs) are electromagnetic waves in infrared (or) visible frequency, which confine and travel along the interface of metal - dielectric (or) metal - air interface. The term surface plasmon polaritons reveals that, the respective electromagnetic wave involves both charge motion in the metal (“**surface plasmon**”) and electromagnetic waves in the dielectric (or) air (“**polaritons**”) as described in the Figure – 5.8.

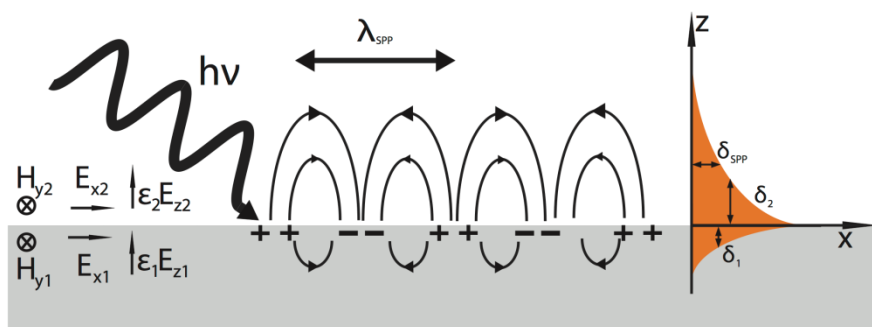


Figure – 5.8: The confined motion of SPPs along metal-dielectric interface.

When electromagnetic radiation interacts with metamaterial, then it is transformed into electromagnetic waves of a different variety [53], namely surface plasmon polaritons (SPPs) [54, 55]. The fundamental plasma frequency can be expressed as

$$\omega_p = \sqrt{\frac{Ne^2}{\epsilon_0 m^*}} \dots\dots\dots (5.12)$$

which is proportional to the density of free carriers N , and effective electron mass m^* . For metals, the plasma frequency falls in the ultraviolet part of the light spectrum, due to the high carrier density. The transverse mode size supported by a plasmonic waveguide is mainly determined by the skin depth in the dielectric [56], which can be calculated as

$$\delta_d = \frac{\lambda_0 \sqrt{-(\epsilon_m + \epsilon_d)}}{2\pi \epsilon_d} \dots\dots\dots (5.13)$$

where λ_0 is the wavelength in vacuum, ϵ_d and ϵ_m are relative permittivity of the dielectric and the metal (metal is treated as a dielectrics with complex-value permittivity), respectively. Near the plasma frequency (in the ultraviolet regime for

most metals), ϵ_m is comparable to ϵ_d , resulting in a small transverse mode size. Recent breakthroughs have produced a wide range of nanoplasmonic devices that generate, guide and detect light [57 – 64]. As the frequency decreases from the near infrared and even down to microwave regime, most metals may be treated as perfect electric conductors (PECs), and the penetration of the EM fields in the dielectric material extends to the distance of the order of many wavelengths and almost completely excluded from the metal surface. The EM waves are weakly localized at the metal-dielectric interface, and the SPPs eventually acquire the characters of Sommerfeld or Zenneck waves [65], which are essentially grazing incidence light fields. This problem can be solved by patterning a metal surface texture (e.g. periodic grooves or holes) with subwavelength features, as shown in Figure – 5.9 (a) and 5.9 (b). This approach can be date back to Goubau [66], Mills and Maradudin [67], who discovered that designed surface textures can result in highly bounded surface waves. In those cases, the EM boundary conditions are altered and strongly localized field radiation can be obtained at longer wavelengths. The dispersion relation of the localized modes obtained by the one-dimensional array of grooves is shown in Figure – 5.9(c), which is similar as the one associated with the SPPs supported by the surfaces of real metals. Therefore, this highly localized EM wave on a textured metal slab is called ‘spoof’ or ‘designer’ surface plasmons [68, 69].

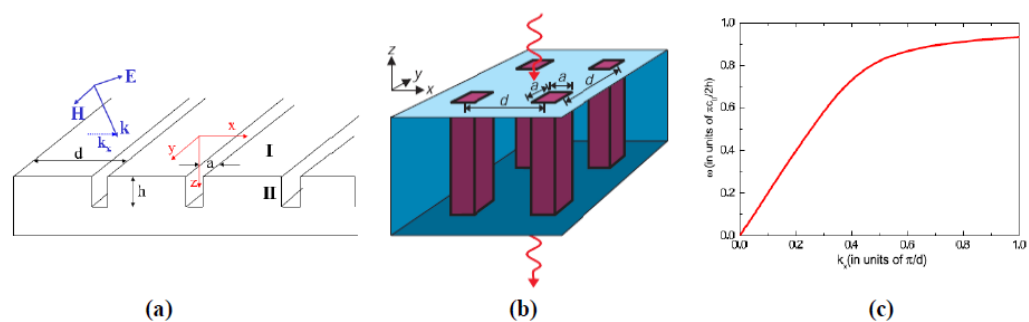


Figure – 5.9: (a) A one-dimensional array of grooves of width a , depth h , and periodicity d . (b) An $a \times a$ square holes arranged on a $d \times d$ lattice are cut into the surface of a perfect conductor, in which localized surface plasmon modes can be induced by the structure. (c) The dispersion relation $[\omega(k_x)]$ of the surface bound states supported by the one-dimensional array of grooves [Fig. 5.9 (a)], with geometrical parameters $a/d=0.2$ and $h/d=1$.

These hyperbolic metamaterials are class of artificial media, which have emerged as one of the most important at optical frequencies. The name is derived from

the isofrequency curve of the medium which is hyperbolic as opposed to circular as in conventional media. The concept of a material with hyperbolic behavior originates from the optics of crystals. In Such media, the constitutive relations connecting the electric displacement D and the magnetic induction B to the electric and magnetic fields E and H can be written as

$$D = \epsilon_0 \bar{\epsilon} E \dots\dots\dots (5.14)$$

$$B = \mu_0 \bar{\mu} H \dots\dots\dots (5.15)$$

where ϵ_0 and μ_0 are, respectively, the vacuum permeability and permittivity, and $\bar{\epsilon}$ and $\bar{\mu}$ are, respectively, the relative permeability and permittivity tensors. For nonmagnetic media, μ simply reduces to the unit tensor. Upon diagonalization, $\bar{\epsilon}$ assumes the form

$$\bar{\epsilon} = \begin{bmatrix} \epsilon_{xx} & 0 & 0 \\ 0 & \epsilon_{yy} & 0 \\ 0 & 0 & \epsilon_{zz} \end{bmatrix} \dots\dots\dots (5.16)$$

in a Cartesian frame of reference oriented along the so-called principal axes of the crystal. The three diagonal components are all positive, and in general depend on the angular frequency ω ; the crystal is termed biaxial when $\epsilon_{xx} \neq \epsilon_{yy} \neq \epsilon_{zz}$, uniaxial when $\epsilon_{xx} = \epsilon_{yy} \neq \epsilon_{zz}$ and becomes isotropic when $\epsilon_{xx} = \epsilon_{yy} = \epsilon_{zz}$. To determine the dispersion relation of light in a medium, consider the following two Maxwell's equations in the absence of sources:

$$\nabla \times E = -\frac{\partial B}{\partial t} \dots\dots\dots (5.17)$$

$$\nabla \times H = \frac{\partial D}{\partial t} \dots\dots\dots (5.18)$$

By considering the above expressions and the plane wave expressions $E = E_0 e^{i(\omega t - k \cdot r)}$ and $H = H_0 e^{i(\omega t - k \cdot r)}$, we obtain

$$k \times E = \omega \mu_0 H \dots\dots\dots (5.19)$$

$$k \times H = -\omega \epsilon_0 \bar{\epsilon} E \dots\dots\dots (5.20)$$

Therefore, the eigen value problem for the electric field E , can be expressed as follows,

$$k \times (k \times E) + \omega^2 \mu_0 \epsilon_0 \bar{\epsilon} E = 0 \dots\dots (5.21),$$

This can be expressed as follows in matrix form,

$$\begin{bmatrix} k_0^2 \varepsilon_{xx} - k_y^2 - k_z^2 & k_x k_y & k_x k_z \\ k_x k_y & k_0^2 \varepsilon_{yy} - k_x^2 - k_z^2 & k_y k_z \\ k_x k_z & k_y k_z & k_0^2 \varepsilon_{zz} - k_x^2 - k_y^2 \end{bmatrix} \begin{bmatrix} E_x \\ E_y \\ E_z \end{bmatrix} = 0,$$

Here $k_0 = \omega/c$, is the magnitude of wavevector and ‘C’ the speed of light in vacuum. In case of uniaxial media, with optical axis oriented along the \hat{z} direction, $\varepsilon_{xx} = \varepsilon_{yy} = \varepsilon_{\perp}$ and $k_{\perp} = \sqrt{k_x^2 + k_y^2}$. Therefore above expression becomes,

$$(k_{\perp}^2 + k_z^2 - \varepsilon_{\perp} k_0^2) \left(\frac{k_{\perp}^2}{\varepsilon_{zz}} + \frac{k_z^2}{\varepsilon_{\perp}} - k_0^2 \right) = 0 \dots\dots\dots (5.22)$$

When set to zero, the two terms above correspond to a spherical and an ellipsoidal isofrequency surface in the k – space; the first describes waves polarized in the xy plane (ordinary or TE waves), the second waves polarized in a plane containing the optical axis (extraordinary or TM waves). The situation changes substantially in case of an extreme anisotropy, namely if one between ε_{\perp} and ε_{zz} is negative. Media with such an optical signature are termed indefinite from the point of view of algebra, since their permittivity tensor represents an indefinite non degenerate quadratic form, and exhibit a number of unconventional properties. Permittivity components with an opposing sign result in a hyperboloidal isofrequency surface for the extraordinary polarization – hence the physical denomination hyperbolic media. As a consequence, waves with arbitrarily large wavevectors retain a propagating nature, while in isotropic materials they become evanescent due to the bounded isofrequency contour [70].

Another unique feature of a hyperbolic environment is the strongly directional light emission. The group velocity $v_g(\omega) = \nabla_k \omega(k)$ and the time-averaged Poynting vector $\hat{S} = \frac{1}{2} \text{Re}\{E \times H\}$ Associated respectively with the directions of propagation and energy flow of light rays, are orthogonal to the isofrequency surfaces [71].

Therefore, the characteristic properties of HMMs can be summarized as follows,

1. These are non-magnetic media and having dielectric tensor which is extremely
2. anisotropic and cannot be found in nature. HMMs have to be fabricate using currently existing nanofabrication technologies by the inclusion of nano structural metamaterials.
3. HMMs are recognized as uniaxial crystals ($\epsilon_{xx} = \epsilon_{yy} \neq \epsilon_{zz}$) and also polaritonic crystal where the coupled states of light and matter give rise to a larger bulk density of electromagnetic states.
4. Amongst all other metamaterials, HMMs exhibit highest figure of merit.
5. Ease of nanofabrication and bulk three dimensional non-resonant response.
6. HMMs are composed of deep subwavelength unit cells and they are tunable across a broad range of wavelengths.

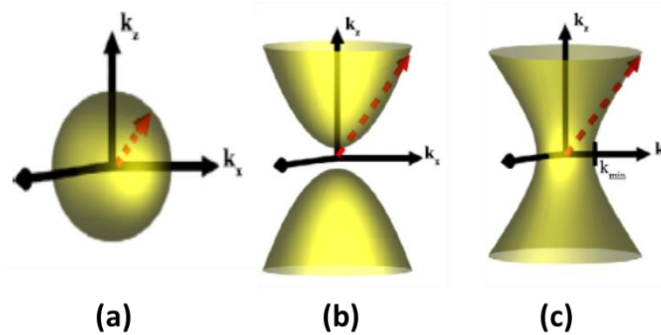


Figure – 5.10: *k*-space topology: The isofrequency contour for (a) an isotropic dielectric is a sphere, (b) extraordinary waves in a uniaxial medium with extreme anisotropy ($\epsilon_{xx} = \epsilon_{yy} > 0$) and $\epsilon_{zz} < 0$, it is a hyperboloid (type I HMM). (c) Hyperboloid of a type II metamaterial when two components of the dielectric tensor are negative ($\epsilon_{xx} = \epsilon_{yy} < 0$) and $\epsilon_{zz} > 0$.

Hyperbolic metamaterials (HMMs) derive their name from the topology of the isofrequency surface. In vacuum, the linear dispersion and isotropic behavior of propagating waves implies a spherical isofrequency surface given by the following equation,

$$k_x^2 + k_y^2 + k_z^2 = \frac{\omega^2}{c^2} \dots\dots\dots (5.23)$$

Here, the wave vector of propagation wave is given by $\vec{k} = [k_x, k_y, k_z]$, ω is the frequency of radiation and ‘c’ is the velocity of light in free space. In case of extraordinary wave (TM polarized) in a uniaxial media, the above expression changes to

$$\frac{k_x^2 + k_y^2}{\epsilon_{zz}} + \frac{k_z^2}{\epsilon_{xx}} = \frac{\omega^2}{c^2} \dots\dots\dots (5.24)$$

In case of uniaxial medium the dielectric tensor ($\vec{\epsilon}$) consists nine components such as ($\vec{\epsilon}$) = [ϵ_{xx} , ϵ_{yy} , ϵ_{zz}]. Here the in-plane isotropic components are $\epsilon_{xx} = \epsilon_{yy} = \epsilon_{\parallel}$ and out-of plane component is $\epsilon_{zz} = \epsilon_{\perp}$. As shown in Figure – 5.10, the spherical isofrequency surface distorts to an ellipsoid by representing the anisotropic nature of medium. But in case of extreme anisotropic media ($\epsilon_{\parallel} * \epsilon_{\perp} < 0$), the respective ellipsoid shaped isofrequency surface opens into an open hyperboloid. To satisfy the condition of extreme anisotropy, the respective material should behave like a metal in one direction and dielectric (insulator) in another. It is worth to mention that, such a materials do not exist in nature at optical frequencies but following currently existing advanced nano fabrication technologies such artificial nanostructured electromagnetic materials can be achieved.

In the designing of HMMs, two possibilities exist depending on which direction metallic nature leading. The HMMs are classified as **Type – I** and **Type –II** based on the number of negative components dielectric tensor. In **Type – I** HMMs one component of the dielectric tensor is negative ($\epsilon_{xx} = \epsilon_{yy} > 0$) and $\epsilon_{zz} < 0$ while **Type – II** HMMs have two components negative ($\epsilon_{xx} = \epsilon_{yy} < 0$) and $\epsilon_{zz} > 0$. Note of course, that if all components are negative, we obtain a metal and if all components are positive we will have a dielectric medium. One striking difference between the **Type – I** and **Type – II** hyperbolic metamaterial is that the hyperboloidal surfaces are two sheeted and single sheeted respectively. The **Type – II** metamaterial is highly reflective since it is more metallic than the Type I counterpart [72]. Significantly, by following two approaches one can achieve the desired hyperbolic isofrequency surface using Metamaterials. In first approach, the metal-dielectric superlattice with subwavelength layer thickness in the order of $\lambda/20$ and respective designed structure should satisfy the effective medium theory conditions (EMT) [73], as shown in Figure – 5.11. The metallic and dielectric layers have permittivities ϵ_m and ϵ_d respectively. Furthermore, we can define the fill fraction of the total thickness of metal in the system to the total thickness of the metamaterial as follows:

$$\rho = \frac{t_m}{t_d + t_m} \dots\dots\dots (5.25)$$

where t_m is the sum of all the thicknesses of metallic layers in the system and t_d is the sum of all the thicknesses of the dielectric layers. The optical phase diagram (Figure – 5.12) for the hyperbolic metamaterial where the effective medium response is plotted with the wavelength and the fill fraction of metal.

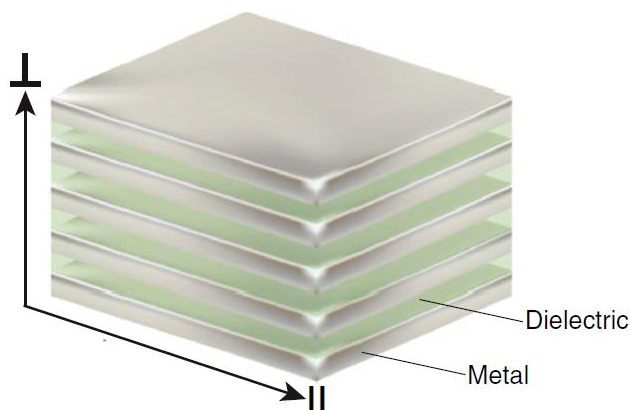


Figure – 5.11: Schematic of anisotropic multilayer composite. The perpendicular direction is defined as parallel to the normal vector from the surface of the metamaterial and the parallel direction is defined as the plane parallel to the metamaterial interface.

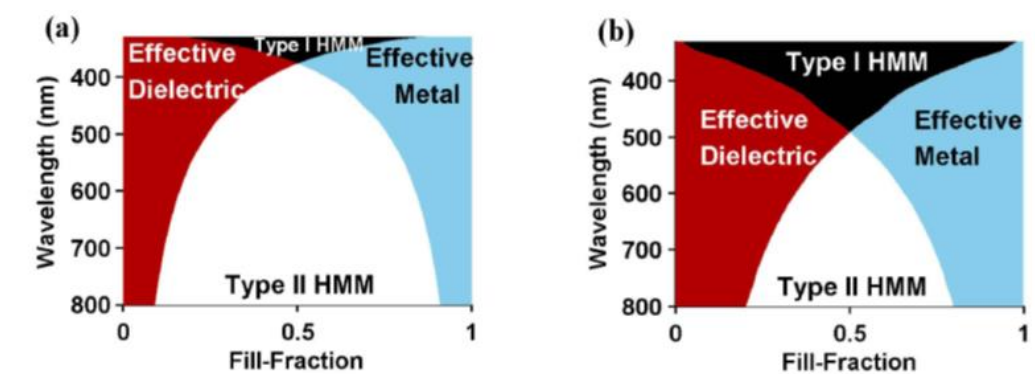


Figure – 5.12: EMT predicts that a metal dielectric composite can behave as an effective dielectric, effective metal, Type I HMM or Type II HMM depending on the wavelength and fill fraction of the metal. Optical phase diagrams for (a) Ag=Al₂O₃ multilayer system (b) Ag=TiO₂ multilayer system.

Another approach to achieving hyperbolic behavior consists of metallic nanowires in a dielectric host (Figure – 5.13). The choice of metals are usually silver and gold grown in a nanoporous alumina template. The major advantage of this design is the low losses, broad bandwidth and high transmission.

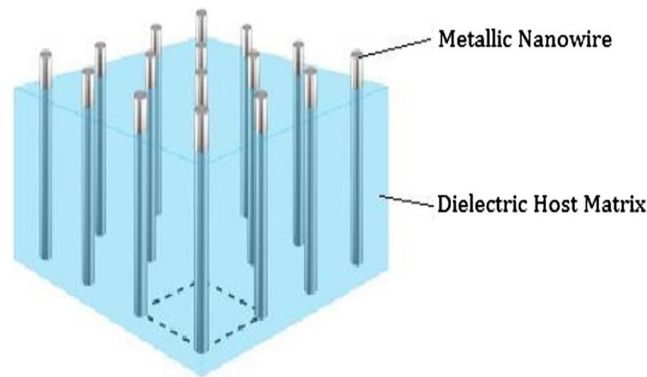


Figure – 5.13: Schematic of an anisotropic nanowire composite. The perpendicular direction is defined along the long axis of the nanowire and the parallel direction is defined as the plane along the short axis of the nanowire.

5.6.2 Effective medium theory (EMT) for Multilayer system

The analytical expressions for the components of permittivity tensor for multilayer system can be achieved by *effective medium theory*. The electric field displacement (D) is proportional to the electric field (E) through the following equation:

$$\vec{D} = \varepsilon_{eff} \vec{E} \dots\dots\dots (5.26)$$

where ε_{eff} is the overall effective permittivity of the medium. In electrostatics the tangential component of the electric field must be continuous across an interface between one medium to another (*i.e.* $E_m^{\parallel} = E_d^{\parallel} = E^{\parallel}$). Here we can take E_m^{\parallel} to be the electric field in the metallic layers, E_d^{\parallel} to be the electric field in the dielectric layers, and E^{\parallel} is the electric field of the subwavelength metamaterial. From the continuity of the dielectric displacement in the parallel direction explained above, the overall displacement by averaging the displacement field contributions from the metallic and dielectric components can be expressed as follows:

$$E_m^{\parallel} = E_d^{\parallel} = E^{\parallel}$$

$$D^{\parallel} = \rho D_m^{\parallel} + (1 - \rho) D_d^{\parallel}$$

$$\varepsilon_{eff}^{\parallel} E^{\parallel} = \rho \varepsilon_m E^{\parallel} + (1 - \rho) \varepsilon_d E^{\parallel}$$

$$\Rightarrow \varepsilon_{\parallel} = \rho \varepsilon_m + (1 - \rho) \varepsilon_d \dots\dots\dots (5.27)$$

It is well acquainted that, the normal component of the electric displacement vector at an interface must be continuous which gives us the expression,

$$D_m^\perp = D_d^\perp = D^\perp$$

The total magnitude of the electric field will be a superposition of the electric field components from the dielectric layers and the metallic layers. Thus, one can define,

$$E^\perp = \rho E_m^\perp + (1 - \rho)E_d^\perp \dots\dots\dots (5.28)$$

By employing above expressions and boundary conditions, the analytic expression for the electric permittivity of the multilayer metamaterial in the perpendicular direction:

$$\varepsilon_\perp = \frac{\varepsilon_m \varepsilon_d}{\rho \varepsilon_d + (1 - \rho) \varepsilon_m} \dots\dots\dots (5.29)$$

Au/Al ₂ O ₃ Ag/Al ₂ O ₃	Au/TiO ₂ Ag/TiO ₂	TiN, ZrN, AZO, GZO, ITO	InGaAs, AlInAs SiC, Graphene
UV	Visible	Near - IR	Mid IR
Plasmonic materials [74]	Plasmonic materials [75]	Alternative plasmonic materials [76]	III-V semiconductor phonon polaritonic materials [77, 78]

Table – 5.1: Selection of Metal and dielectric layers for the fabrication of HMM structures in various Electromagnetic regions.

A wide choice of plasmonic metals and high index dielectrics can give rise to hyperbolic behavior in different wavelength regimes. At ultraviolet (UV) frequencies, Au and Ag along with Al₂O₃ forms the ideal choice for the metamaterial. Close to the plasma frequency of these metals, which is in the UV, their reflectivity decreases and an alternating metal dielectric super-lattice achieves a *Type – I* HMM with high transmission. Table – 5.1, provides the information about selection materials to observe Hyperbolic nature in different wavelength regions, such that the response of the hyperbolic metamaterial can be tuned by the choice of constituent metal and dielectric, and their relative volume ratios.

- **UV and visible:** Silver is the ideal choice of metal due to its low losses. Alumina (Al_2O_3) is a compatible dielectric in the UV range but at higher wavelengths, the large negative real part of the metallic dielectric constant requires a shift to high index dielectrics. Titanium dioxide is an excellent candidate due to its large index, opening the possibility of impedance matching with vacuum [79].
- **Near-IR:** None of the conventional plasmonic metals such as gold or silver are good candidates for hyperbolic metamaterials at near-IR wavelengths. This is because far below the plasma frequency, metals are extremely reflective and lead to high impedance mismatch with surrounding media. The recently developed alternative plasmonic metals based on oxides and nitrides are ideal for applications in hyperbolic metamaterials since their plasma frequency can be tuned to lie in the near-IR [80].
- **Mid-IR:** At mid-infrared wavelengths, doped semiconductors can act as the metallic building block for hyperbolic metamaterials [81]. Another option is the use of phonon-polaritonic metals such as silicon carbide which have their Reststrahlen band in the mid-IR range [82].

5.6.3 Origin of the high-k modes in HMMs

In designed HMMs, due to the metallic building block needed to achieve a negative dielectric constant in one direction, HMMs support bulk plasmon-polaritonic or phonon-polaritonic modes. Thus high-k modes of HMM can be considered as engineered bulk polaritonic modes which owe their large momentum to light-matter coupling. In Figure – 5.14, illustrates contrast of an incident evanescent wave on a conventional dielectric as opposed to a hyperbolic metamaterial. The evanescent wave decays in a simple dielectric but couples to a high-k propagating wave in the hyperbolic metamaterial. The high-k mode is seen to arise due to the coupling between the surface-plasmon-polaritons on each of the interfaces. Thus the high-k modes are in fact the Bloch modes due to the coupled surface plasmon polaritons on the metal-dielectric multilayer superlattice [83].

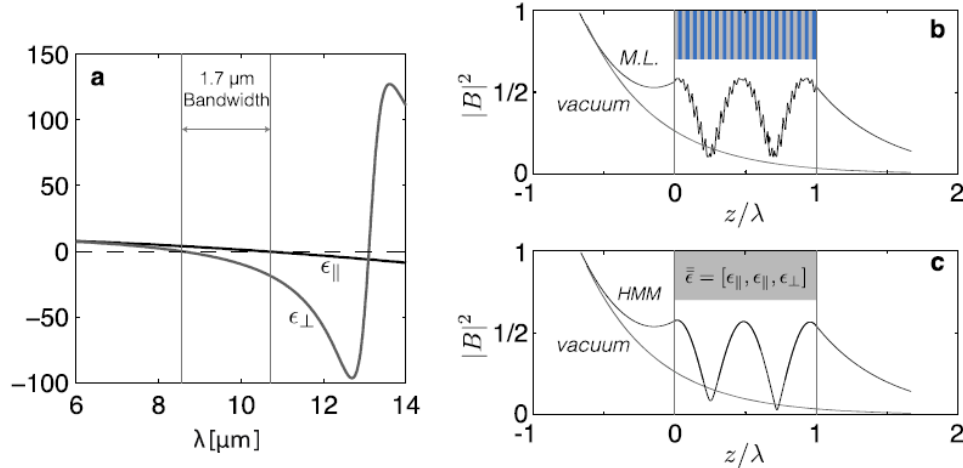


Figure – 5.14: (a) Dispersion of the dielectric constants in a practical multilayer semiconductor realization of the HMM. Note the broadband region in which Type I HMM response is achieved (b) Exact numerical calculation (neglecting loss) in the multilayer structure showing the bloch high- k mode and coupled surface plasmons at the interfaces (c) Evanescent wave incident on an effective medium slab couples to the high- k mode and is transmitted. In contrast, the evanescent wave decays away in vacuum.

5.6.4 Applications of HMMs

(a). **Fluorescence Engineering:** The presence of high- k waves opens a new route into which quantum emitters can decay when placed on an HMM substrate. In the near field of any medium, there are in general three routes of decay corresponding to the types of electromagnetic modes supported by the structure. A quantum emitter or fluorophore can emit into propagating waves of vacuum or bound modes (such as waveguide modes or surface plasmon polaritons), and if the body is absorptive ($\text{Im}(\epsilon) \neq 0$), the third nonradiative route for relaxation is opened up. Fluorescence can be completely quenched due to near-field absorption.

(b). **Super-Planckian Thermal Emission:** The high- k states in HMMs, lead to decrease in radiative spontaneous emission lifetime can also play a key role in thermal conductivity and thermal emission.

(c). **Nano-Imaging:** The hyperlens is an imaging device made of hyperbolic metamaterials which can break the farfield diffraction limit. The subwavelength resolution in the far field arises from the cylindrical (or spherical) nature of the HMM. The device can be fabricated by the same multilayer design principles presented earlier.

In the future, integrating the hyperlens with microfluidic channels can make a significant impact for real-time bioimaging.

(d). Dyakonov Plasmons: Hyperbolic isofrequency curves can also be obtained for two-dimensional surface states. The isofrequency curve for in-plane surface plasmon polaritons on a gold substrate is circular. As opposed to this, when a uniaxial crystal is placed on top of the metal film with different indices along the principle axes, there exists the possibility that plasmons are allowed to propagate in one direction but not in the perpendicular direction. This gives rise to in-plane hyperbolic isofrequency curves for the surface plasmon polaritons. They are a mixed state consisting of both TE and TM polarized light and are called Dyakonov plasmons.

5.6.5 Literature Survey

E. Dulkeith et. al [84] carried out time – resolved fluorescence experiments on “donor – acceptor” system composed of lissamine molecules as donor, which attached to a gold nano particles (acceptor). They maintained constant distance of 1 nm between the lissamine molecule and surface of the nano particle. They discovered that, time constants for the energy transfer on a picosecond time scale which turn out to decrease with increasing nanoparticle size. The radiative rate dyes is reduced by more than an order of magnitude. They reported that, these effects are responsible for the drastic quenching of the fluorescence yield. The estimated radiative rate R_{rad} exhibits a pronounced minimum around $r = 4$ nm. In their reports, concerning the shape of the nano particles, the calculated absolute values for R_{RET} are 2 orders of magnitude larger than the experimentally determined non--radiative rates R_{nonrad} .

In this report, **D.J. Maxwell et. al** [85] showed that biomolecules and nanoparticles can be linked to create a novel nanobiotransducer that is able to recognize and detect target biomolecules in a single step (without washing or separation). At the core is a colloidal gold nanocrystal that is both structurally and functionally integrated with synthetic oligonucleotides (oligos). They have chosen the case of DNA probes labeled with a thiol at one end and a dye at the other. They observed that, the DNA molecules self-organize into a constrained conformation on the nanoparticle surface, and that the fluorophore is completely quenched by the particle. Therefore upon target

binding, the constrained conformation opens and the fluorophore is separated from the particle surface. They concluded that, this structural change generates a fluorescence signal that is highly sensitive and specific to the target DNA. In their investigation, they reported that, an arch-like structure can be assembled on the particle surface and that this structure is not sensitive to temperature, in contrast to the behavior of stem-loop molecular beacons. For relatively large gold particles (10-50 nm diameter), preliminary results demonstrate an efficient long-range energy-transfer effect that is able to quench fluorophores over spatial distances as large as 10 – 20 nm.

In this Communication, **N. Lie et. al** [86] reported on the synthesis and characterization of well-defined hybrid structures that comprise a gold core over coated with a silica shell, followed by a dense monolayer of colloidal CdSe quantum dots (QDs). The idea behind their investigation was “dielectric silica spacer of a controlled thickness provides a simple means for tuning interactions between the QDs and the metal core”. They followed a novel approach, “switching between PL quenching and enhancement by varying the silica shell thickness”, to perform an accurate quantitative analysis of the effect of a metal on the QD PL intensity. The significant result in their observations is that non-uniformity of non-radiative rates across the QD ensemble has a significant effect on both the magnitude and the shell-thickness dependence of the PL intensity.

O.G. Tovmachenko et. al [87] studied the enhancement of fluorescence by nanoparticles consisting of a metal core, a silica- spacer shell of variable thickness, and a dye-labeled shell. They have chosen gold and silver as core metals due to their plasmon-resonance bands are located in the visible range of the spectrum and match the absorption and emission bands of standard dyes. They followed discrete dipole-approximation based calculations to choose spacer thickness, such as close to the theoretical optimal spacer thickness. They used an average dye–metal distances of ~ 25, 24, and 15 nm for the Au-FAM (FAM: carboxyfluorescein), Ag-CYe (CYe: cascade yellow) and Au-CYe particles, respectively.

In case of FAM-Labeled Nanoparticles, the average fluorescence lifetime of FAM in the reference specimen was found to be 4.3 and 3.6 ns at high (490 nm excitation) and low (440 nm excitation) pH, respectively. They reported that, in the

presence of a gold core, the fluorescence lifetime of FAM decreases to 3.1 ns and in this case the pH does not appear to affect the fluorescence lifetime. For CYe-Labeled Nanoparticles, The decays of CYe-labeled, metal-core/silica-shell nanoparticles were significantly shorter than those of reference particles without a metal core. In the case of the silver-core nanoparticles the mean CYe fluorescence decay time went down from 5.1 to 1.95 ns. Reduction of the fluorescence-decay time of CYe in gold-core nanoparticles was stronger; the mean decay time went down to 1.06 ns. They concluded that, dye-labeled, metal-core/silica-shell nanoparticles are an excellent model system to study interactions between fluorescent molecules and metals.

G. Schneider et. al [88] reported on the preparation, characterization, and photo physical study of new fluorescent core/shell nanoparticles fabricated by electrostatic layer-by-layer assembly. They followed layer-by-layer (LBL) depositions of oppositely charged polyelectrolytes onto 13-nm-diameter gold colloids to fabricate metal core-polymer shell capsules in which fluorescent organic dyes fluorescein and lissamine rhodamine B are situated at various distances from the gold core. In this report, the distance between dye and metal core is controlled reliably through LBL assembly, and the fluorescence measurements give a direct access to the effect of the metal core on the radiative rates.

They synthesized Gold nanoparticles using the reduction of tetrachloroauric acid by trisodium citrate. They obtained to Au nanoparticles coated with 2, 10, and 20 layers (Au(PAH/PSS)_n). Fluorescein isothiocyanate (FITC) and lissamine rhodamine B sulfonyl chloride (LISS) were covalently attached to PAH to obtain PAH-FITC and PAH-LISS, respectively. Only a small fraction (approximately 1%) of the available amino groups was labeled. PAH-FITC or PAH-LISS were adsorbed onto the Au(PAH/PSS)_n core-shell particles, followed by the adsorption of a final PSS layer. From their observations, they concluded that, the gold nanocore quenches the fluorescence of the fluorescein and lissamine dyes situated in the outer polymer layers of the core-shell nanoparticles. Even with 20 spacer layers (i.e., 10 pairs of PAH/PSS, corresponding to a dye-nanocore distance of 8 nm).

In this report, **M. Ringler et. al** [89] showed that plasmonic nano resonators composed of two gold nanoparticles change not only the intensity but also the spectral

shape of the emission of fluorescent molecules. They tuned plasmonic resonance frequency by varying the distance between the nanoparticles to favor transitions of a fluorescent molecule to a specific vibrational ground state. The scattering spectroscopy results concerning to the longitudinal plasmon revealed that, the distance between the two nanoparticles decreases, the coupling between their plasmons becomes stronger, leading to an increasing redshift of the longitudinal mode resonance. They concluded that, (i) distance between the mirrors of macroscopic resonators, the distance of two nanoparticles serves to tune the nanoparticle dimer resonator and (ii) the spectral variation of the fluorescence enhancement factor is solely determined by the enhancement factor of the radiative decay rate. They claimed that, this experiment also constitutes the first direct measurement of radiative decay rate enhancement in a single plasmonic nanoresonator.

K.J. et. al [90] demonstrate radiative emission rate enhancements approaching 1000 for emitters coupled to the nanoscale gap between a silver nanowire and a silver substrate. They carried out, a quantitative comparison of obtained results with analytical theory and reported the possibility of enhanced emission rate of gap-mode plasmons nanoscale gap structures can yield high internal quantum efficiency despite the close proximity of metal surfaces. Experimentally, they fabricated six cavity structures with different gap spacings ranging from ~ 5 to ~ 25 nm and these samples contained identical layers of Alq3 (thickness, ~ 2.5 nm) but different thicknesses of Al₂O₃ spacer layer. They investigated the variation of total decay rate (ν_{τ} ns⁻¹) and life time (ps) as a function of Al₂O₃ spacer thickness. They found that, the peak intensity values [from the observation of graph of “total decay rate vs. peak intensity”] increase drastically with total emission rate, which confirms the presence of spontaneous emission enhancement into the gap modes.

A. Rose et. al [91] demonstrated enhancement of both absorption and spontaneous emission as a function of plasmon resonance by hybridizing the optical patch antennas with fluorophores. They reported that, by adapting this type of tunable platform, we achieve fluorescence enhancement factors exceeding 30, 000 of fluorophores coupled to nanopatches resonating close to the excitation wavelength and spontaneous emission rates increased by at least a factor of 74. They designed nanopatch antennas consist of colloiddally synthesized silver nano cubes deposited over

a 50 nm thick silver film and cubes and film are separated by an ~ 5 nm self-assembled polyelectrolyte (PE) spacer layer, coated with a dilute layer of fluorophores (sulfo-cy5 carboxylic acid (Cy5)). They studied, 48 isolated nanopatches with side-lengths ranging from 50 to 100 nm to investigate fluorescence enhancements within the nanopatch system.

They measured fluorescence lifetimes from an ~ 20 μm diameter surface area covered by a higher density ($\sim 5\%$) of uniform nanopatches and a lower density of fluorophores ($1/25\times$ original). They repeated these measurements was for a control sample consisting of glass, spacer layer, and Cy5, as well as another control sample consisting of silver film, spacer layer, and Cy5; both were without silver nanocubes. Lifetimes were compared to the control sample on glass ($\tau_{\text{sp}} = 2.54 \pm 0.04$ ns) and they observed a significant shortening of the Cy5 lifetimes when deposited over the silver film ($\tau_{\text{sp}} = 164 \pm 7$ ps). For Cy5 fluorophores on the nanopatch sample, a biexponential decay is observed with a fast decay component of $\tau_{\text{sp}} = 33 \pm 4$ ps due to fluorophores coupled to the nanopatches, and a slower decay component of $\tau_{\text{sp}} = 157 \pm 5$ ps attributed to uncoupled fluorophores on the silver film.

In this Letter, **P. Goy et. al** [92] reported about their first observation of enhanced atomic spontaneous emission in a resonant cavity. They conducted experiment on Rydberg atoms of Na excited in a niobium superconducting cavity resonant at 340 GHz. Due to very strong electric dipole of Rydberg atoms of Na and of the very good finesse of superconducting resonators, P. Goy et. al observed a cavity-tuning-dependent shortening of the lifetime of atoms crossing, a few at a time, the resonant cavity. In the present study, They employed cavity made up of two spherical niobium mirrors set close to each other and maintained the confocal configuration at a distance $L \approx 25$ mm from each other. By varying of L , the cavity is tuned to resonance frequency by varying the value of L and therefore the transition towards the less excited $22P_{1/2}$, or $22P_{3/2}$. They concluded that, the partial spontaneous emission probability on the $23S$ to $22P$ transition in Na is increased in a high-Q cavity from its free-space value $\Gamma_0 = 150 \text{ s}^{-1}$ upto $\Gamma_{\text{cav}} = 8 \times 10^4 \text{ s}^{-1}$.

The alteration of visible spontaneous emission by atoms coupled to the degenerate modes of a confocal resonator was observed by **D.J. Heinzen et. al** [93]. In their experiment, they maintained two conditions such as (i) resonator linewidth is

greater than the linewidth of the atomic transition and (ii) the atomic sample is of negligible optical thickness, so that the changes in spontaneous emission may easily be understood as an interference effect. They studied Photon counting rate for light transmitted through the cavity mirror, as a function of cavity tuning and observed maximum enhancement factor of $\gamma_{enh}/\gamma_{sp} = 19$ and the maximum inhibition factor $\gamma_{sp}/\gamma_{inh} = 42$. The fluorescence intensity decreases on resonance, corresponding to an increase in the total spontaneous emission rate, from the obtained experimental results they observed total magnitude of the change is $2.2 \pm 0.2\%$.

G.S. Solomon et. al [94] demonstrated a semiconductor analog of a single-atom cavity QED experiment, using a single quantum dot (QD) as the artificial atom, which is positioned in a three-dimensional post microcavity and coupled to a single optical mode. The QDs and planar microcavity were fabricated monolithically using molecular-beam epitaxy. During fabrication steps, a uniform ensemble of QDs with no spatial ordering was formed on the growth surface by depositing the equivalent of 2.5 planar monolayers of InAs, under conditions which give a low QD density of approximately $75 \text{ dots}/\mu\text{m}^2$. In this work, G.S. Solomon et. al demonstrated that the spontaneous emission lifetime from a single QD can be reduced from 1.3 ns to 280 ps by coupling to the modified vacuum field of a three-dimensional microcavity post. A total of 78% of the emission from the QD state is collected in the discrete fundamental cavity mode, which is normal to the sample.

A. Kress et.al [95] demonstrated the ability to control the spontaneous emission dynamics of self-assembled quantum dots via the local density of optical modes in two-dimensional (2D) photonic crystals. They showed that an incomplete 2D photonic band gap is sufficient to significantly lengthen the spontaneous emission lifetime ($> 2 \times$) over a wide bandwidth ($\Delta\lambda \geq 40 \text{ nm}$). For dots that are both spectrally and spatially coupled to strongly localized $\left[V_{modes} \sim 1.5 \left(\frac{\lambda}{n} \right)^3 \right]$, high Q ~ 2700 optical modes, we have directly measured a strong Purcell-enhanced shortening of the emission lifetime $\geq 5.6X$, limited only by our temporal resolution. Analysis of the spectral dependence of the recombination dynamics shows a maximum lifetime shortening of 19 ± 4 . From the directly measured enhancement and suppression we

show that the single-mode coupling efficiency for quantum dots in such structures is at least $\beta = 92\%$ and is estimated to be as large as $\sim 97\%$.

T.B. Hoang et. al [96] examined a mixed approach where a combination of the slow-light effect with cavity enhancement is achieved by embedding semiconductor QDs in short (10–25 μm) photonic crystal waveguide (PhC WGs). In these short PhC WGs, the localization due to disorder is not expected to occur since the PhC WG length becomes smaller than the photon localization length. First they simulated the results of a W1 PhC WG (PhC membrane with one missing air hole row) which is similar to those studied in the optical characterizations. PhC WGs are fabricated such as, a 1.5 μm thick AlGaAs sacrificial layer and a 320 nm thick GaAs slab were grown on a GaAs substrate by molecular beam epitaxy. The slab contains an InAs QD layer (a few QDs/ μm^2) emitting near 1300 nm. In parallel, the PhC hole pattern was defined by electron beam lithography and transferred from the resist into an underlying SiO₂ layer by CHF₃/Ar reactive ion etching. In PL results, they noticed several FP modes together with narrower (multi) excitonic lines, some of which are resonant with a FP mode. From life time measurements, T.B. Hoang et. al noticed that, the decay time decreases from 1.6 ns, when the QD emission is away from resonance, down to ~ 0.8 ns as the emission energy approaches the band-edge.

M. Patterson et. al [97] introduced the concept and theory for a photonic-crystal ridge waveguide in high index semiconductors that can be used to tailor the single-photon emission of an embedded quantum dot. The design exploits a band structure with a large bandwidth of slow light. By tuning the device geometry, the group velocity of the fundamental waveguide mode and the Purcell factor enhanced spontaneous emission can be uniquely controlled. The vertical asymmetry naturally creates a broadband region of slow-light propagation that is ideal for enhancing emission from embedded QDs and channeling the light into the waveguide. We provide two reference designs with Purcell factors of at least 10 and 43 over bandwidths of 435 and 51 GHz (~ 1.8 and 0.21 meV), respectively.

G. Strangi et. al [98] experimentally demonstrated the control of spontaneous emission enhancement in multilayered Au/Al₂O₃ hyperbolic metamaterials (HMMs). They employed effective medium theory to confirm hyperbolic dispersion of fabricated

Au/Al₂O₃ multilayers at optical frequencies. The modification of spontaneous emission enhancement is observed when the emission wavelengths of different chromophores deposited on top of the multilayer are tuned from the elliptical to hyperbolic spectral region of the HMM. From photoluminescence studies, they noticed a reduction in photoluminescence intensity from 10 bilayers (HMM) compared to the reference sample, and this large reduction is due to the preferential emission into high-k metamaterial states. They carried out life time measurements of dye molecules placed on top of HMM and observed a large variation in spontaneous emission lifetime of dye onto the 10 bilayers HMM structure compared to the reference sample. G. Strangi et. al attributed these results to the existence of high-k modes as well as non-radiative and surface plasmon polariton (SPP) modes present in designed HMM.

In the present paper, **H.N.S. Krishnamoorthy et. al** [99] demonstrated the modification of spontaneous light emission from quantum dots placed near the surface of the metamaterial undergoing the topological Lifshitz transition, and present the theoretical description of the effect. To observe the signature of the predicted topological transition manifested through enhancement in spontaneous emission rate, they investigated a metamaterial structure that consist of alternating subwavelength layers of metal (silver) and dielectric (TiO₂), with multiple quantum dot emitters positioned on its top surface. They carried out time resolved PL measurements for metamaterial sample, the control sample and the glass substrate at a wavelength of 621 nm, which is very close to the topological transition wavelength. They observed large change in the spontaneous emission lifetime of the quantum dots between metamaterial and the glass substrate and attributed this result to the excitation of the metamaterial states. The spontaneous emission rate shows an enhancement by a factor of ~ 3 in the metamaterial when compared to the control sample which is attributed solely due to the metamaterial states. The overall reduction in the lifetime of the quantum dots when compared to those on a glass substrate is ~ 11.

J.M. Gerard et. al [100] conducted cavity quantum electrodynamic experiments by adapting Semiconductor quantum boxes (QB's) because of their sharp emission. They carried out time-resolved photoluminescence measurements on InAs QB's placed in the core of small-volume and high-finesse GaAsyAlAs pillar microresonators. They designed and fabricated micropillars of circular cross section, a

core diameter in the 40–70 nm range, which have been processed through the reactive ion etching (RIE) of a GaAs/AlAs planar microcavity grown by molecular beam epitaxy. A spontaneous emission rate enhancement by a factor of up to 5 is selectively observed for the QB's which were on resonance with one-cavity mode. They explained its magnitude by considering the Purcell figure of merit of the micropillars and the effect of the random spatial and spectral distributions of the QB's.

Z. Jacob et. al [101] demonstrated theoretically that metamaterials with hyperbolic dispersion support a large number of electromagnetic states that can couple to quantum emitters leading to a broadband Purcell effect. They considered radiative decay engineering using a substrate which interacts with an emitter placed above it and classical dipole radiation theory to understand the Purcell effect. They engineered the patterning scale “a” of the metamaterial and found that for distances, $d \ll a$ the effective medium approximation is not valid for a dipole in the near field since the interaction is dominated by waves with wavenumbers $k > (1/a)$. They concluded that, in the present study proposed device based on hyperbolic metamaterials is compatible with a wide variety of sources and capable of room temperature operation due to the broad bandwidth enhancement of spontaneous emission and directional photon emission.

H. Yokoyama et. al [102] observed Enhanced spontaneous emission with wavelength-sized monolithic Fabry Perot cavities containing GaAs quantum wells. In the present investigation, they fabricated microcavity by the epitaxial growth of both multi quantum well light-emitting active layers and multilayer reflectors on a GaAs substrate. This structure is basically a very short planar Fabry-Perot cavity structure, but with distributed feedback reflectors. With an on-resonance cavity structure, the photoluminescence intensity increases in the cavity axis direction, and the spontaneous emission lifetime is experimentally found to decrease. They noticed important things in their experiments to distinguish between stimulated and spontaneous emission. They reported that, when the carrier density is less than 10^{18} cm^{-3} , net stimulated emission (stimulated emission rate $>$ stimulated absorption rate) may not occur around the PL peak wavelengths. In this direction, they estimated the carrier density to be $\sim 10^{18} \text{ cm}^{-3}$, and concluded that, the light emission observed in the present experiment is due to spontaneous emission.

S. Ogawa et. al [103] fabricated three-dimensional (3D) photonic crystals (PCs) containing artificial point defects have been fabricated to emit light at optical communications wavelengths. They constructed PCs by stacking 0.7-micrometer-period gallium arsenide striped layers, resulting in a 3D “woodpile” photonic crystal. Indium–gallium arsenide–phosphide quantum-well layers emitting at a wavelength of 1.55 micrometers were incorporated in the center of the crystal. Samples having up to nine stacked layers were constructed, and artificial point-defect cavities of different sizes were formed in the light-emitting layer. In their studies, when a 3D PC is constructed with more than 17 layers, including a light emitting layer, linewidths of less than 0.5 nm are expected, equivalent to a Q factor of more than 3000. They performed micro-PL (μ PL) mapping to know the direct information on the PBG effect and the localization of emitted light and conclude that, Light emission was suppressed in the photonic crystal regions, whereas cavity modes were successfully observed at the point defects and were size dependent.

K. Aoki et al [104] reported on the first demonstration of the coupling of fully confined electrons and photons using a combination of three dimensional photonic crystal nanocavities and quantum dots. In their approach, the 3D structure was broken up into simple building blocks. Planar components were designed so that the rods of adjacent layers crossed each other orthogonally, and those of the next-nearest neighboring layers were aligned parallel but with a half-period to form a so-called woodpile structure. The three dimensional photonic crystals were assembled by stacking planar components using a sophisticated micromanipulation technique. In addition, Point defects, containing embedded quantum dots, were introduced into the photonic crystals as active sites. By measuring the photoluminescence spectra of the assembly, the process by which light emitted from the quantum dots is coupled to the defect modes of a three dimensional photonic crystal was demonstrated for the first time. The characteristics of the sharp emission peaks agreed well with numerical simulations, and these were confirmed to be resonant modes by polarization measurements. They reported highest quality factor (Q-factor) value of 2,300 for three dimensional photonic crystals.

M.A. Noginov et. al [105] experimentally studied the effect of the hyperbolic super singularity on the spontaneous emission lifetime of dye deposited on a hyperbolic metamaterial. They fabricated Alumina membranes with the dimensions

1 cm × 1 cm × 51 μm and consist 35 nm channels (voids) extending through the whole thickness of the membrane perpendicular to its surface. They maintained surface filling factor of the voids was ~15% and respective membranes were filled with silver. The film of polymethyl methacrylate (PMMA) doped with IR-140 laser dye at concentration 0:013 M was deposited over top of the silver-filled membrane. During emission kinetic measurements for dye-doped film deposited onto the unfilled membrane, they noticed nearly single exponential with the decay-time equal to 760 ps.

Z. Jacob et al [106] showed that, nanostructured metamaterials with hyperbolic dispersion can dramatically enhance the photonic density of states paving the way for metamaterial-based PDOS engineering. In this direction, they placed dye molecules in the near field of a hyperbolic metamaterial spontaneously excite unique electromagnetic states in the metamaterial medium responsible for the enhanced PDOS leading to a decrease in the lifetime of emitters. They designed and fabricated HMM structure made up of Sixteen alternating subwavelength layers of alumina and gold (thickness 19 nm) are deposited using an electron beam evaporation technique with careful control of the individual layer thicknesses. They employed Rhodamine 800 and deposited over designed HMM to operate at the wavelength of emission of the dye. They performed lifetime measurements using fluorescence lifetime imaging and respective dye is excited using a pump laser ($\lambda_{\text{pump}} = 635 \text{ nm}$) with 88 ps pulses. They did simulation work on Lifetime measurements of molecules on the metamaterial using a semi classical approach based on a many dipole model give a factor of 1.7 decrease as compared to the dielectric. This is in agreement with the experimentally measured lifetimes of 2 ns for the dielectric and 1.1 ns for the HMM with a spacer of 21 nm. Similar results are obtained for a spacer layer of 29 nm as well. In the current report, they probed the available local density of states in the near field of the metamaterial using spontaneous emission of dyes. They demonstrated decrease in the lifetime of emitters, which demonstrates the spontaneous excitation of unique electromagnetic states in the metamaterial.

5.6.6 Scope of the work

In view of the unprecedented characteristics of hyperbolic metamaterials (HMMs) and by virtue of their ability to break the classical limitations of optics, the current investigations are intended to work on these artificial HMM materials for the application of “Enhancement of spontaneous emission of a chromophores due to the Purcell effect”. The incompatibility of preexisting cavity and photonic crystal technologies triggered for the discovery of HMM structures due to the existence of a large number of electromagnetic states, which lead to a divergence in the photonic density of states allowing a broadband control.

It is worth to mentioned that, the rapid developments of nano fabrication techniques opened the possibilities for designing and fabrication of subwavelength sized hyperbolic metamaterials, to exhibit properties unattainable with conventional media. These exotic properties of HMM structures opened new avenues for their potential applications in quantum nanophotonics, such as enhanced-light interactions, subwavelength imaging, negative refraction and low-loss fiber cladding. As illustrated in literature survey, various research communities have been reported about their excellency to utilize different HMM structures in Microwave to Optical wavelength regions by choosing appropriate metal, dielectric materials for fabrication of HMM structures and by employing Effective medium theory (EMT). In our approach, we proposed new grating coupled hyperbolic metamaterial (GCHMM) configuration for the enhancement of spontaneous emission rate of dye molecules by exploiting the unique property of a hypergrating to outcouple and extract the non-radiative plasmonic modes.

Therefore in the present investigation, two different lamellar HMM structures are designed and fabricated by employing Silver (Ag) as metal layer and Al₂O₃, SiO₂, dye doped PMMA as dielectric layers. They deposited at optimized thin film growth conditions by thermal, electron beam physical vapour deposition techniques and spin coating techniques, respectively. The Coumarin – 500 and DCM dye molecules are employed as chromophores to observe their spontaneous emission rates, by introducing them in the vicinity and embedded inside the HMM structures.

5.6.7 Objectivities of the present work

The main objectives of the present investigations are

- ✓ Optimizing the thicknesses of metal (Ag) and dielectric (Al_2O_3 , SiO_2 , dye doped PMMA) thin layers by employing stylus profilometer and ellipsometer.
- ✓ Designing and Fabrication of lamellar ‘metal – dielectric HMM’ structures and investigating their hyperbolic nature by estimating their parallel and perpendicular component values of permittivity values from reflection measurements recorded at various wavelengths by ellipsometer.
- ✓ Depositing dye embedded PMMA layers over pre-deposited spacer layer on surface of fabricated HMM structures.
- ✓ Investigating the optical absorption and photoluminescence (PL) quenching phenomenon by carrying out PL studies to get evidence for the presence of high – k modes.
- ✓ Conducting Time-Correlated Single Photon Counting (TCSPC) experiments at various emission wavelengths corresponding to selected dyes for the study.
- ✓ Evaluating the life times of dye molecules at various emission wavelengths and estimating the respective spontaneous decay rates.
- ✓ Making 2D metal (Ag) grating over (dye+HMM) structures by following standard protocols and conducting TCSPC experiments to know the influence of metal grating on spontaneous decay rates of the respective dye molecules.

References

- 1.R. Loudon, *The Quantum Theory of Light*, 3rd ed. (Oxford University Press Inc., New York, 2001).
- 2.B. Henderson and G. Imbusch, *Optical Spectroscopy of Inorganic Solids* (Clarendon Press, Oxford, UK, 1989).
- 3.A. F. van Driel, G. Allan, C. Delerue, P. Lodahl, W. L. Vos and D. Vanmaekelbergh, *Physical Review Letters* 95 (2005) 236804.
- 4.E. M. Purcell, *Phys. Rev.* 69, 681 (1946).
- 5.S. Haroche, D. Kleppner (1989). "Cavity Quantum Dynamics". *Physics Today*: 24–30.
- 6.D. Kleppner, *Physical Review Letters* 47 (1981) 233–236.
- 7.V. P. Bykov, *Soviet Journal of Quantum Electronics* 4 (1975) 861.
- 8.E. Yablonovitch, *Physical Review Letters* 58 (1987) 2059.
- 9.A. Kress, F. Hofbauer, N. Reinelt, M. Kaniber, H. J. Krenner, R. Meyer, G. Bohm, and J. J. Finley, *Physical Review B* 71 (2005) 241304.
- 10.D. Englund, D. Fattal, E. Waks, G. Solomon, B. Zhang, T. Nakaoka, Y. Arakawa, Y. Yamamoto, J. Vuckovic, *Physical Review Letters* 95 (2005) 013904.
- 11.P. Lodahl, A. F. van Driel, I. S. Nikolaev, A. Irman, K. Overgaag, D. Vanmaekelbergh and W. L. Vos, *Nature* 430 (2004) 654.
- 12.M. C. Münnix, A. Lochmann, D. Bimberg, V. A. Haisler, *IEEE Journal of Quantum Electronics* 45 (2009) 1084.
- 13.D. Bimberg, E. Stock; A. Lochmann; A. Schliwa, J. A. Tofflinger; W. Unrau. M. C. Münnix, S. Rodt, V. A. Haisler, A. I. Toropov, A. Bakarov, *IEEE Photonics Journal* 1 (2009) 58.
- 14.T. Tsutsui, N. Takada and S. Saito, *Synthetic Metals* 71 (1995) 2001.
- 15.Y. Yokoyama, *Science* 256 (1992) 66.
- 16.Y. Yamamoto, R. E. Slusher, *Physics Today*, p. 66, June (1993).
- 17.J.M. Gerard, *Applied Physics Letters* 69 (1996) 449.
- 18.G.S. Solomon, M. Pelton, *Phys. Status Solidi* 178 (2000) 341.
- 19.J.L. Jewell, *Applied Physics Letters* 54 (1989) 1400.
- 20.Chang, R. K. (ed.) *Optical Processes in Microcavities* (World Scientific, Singapore, 1996).
- 21.Rayleigh, L. in *Scientific Papers* 617–620 (Cambridge Univ., Cambridge, 1912).
- 22.D.K. Armani, T.J. Kippenberg, *Nature* 421 (2003) 925.

23. O. Painter, *Science* 284 (1999) 1819.
24. A.F. Levi, R.E. Slusher, *Applied Physics Letters* 62 (1993) 561.
25. T. Baba, *IEEE J. Select. Topics Quantum Electron.* 3(3) (1997) 808.
26. S.A. Backes, J.R.A. Cleaver, *Applied Physics Letters* 74 (1997) 176.
27. S.I. Shopova, G. Farca, *Applied Physics Letters* 85(2004) 6101.
28. M. Pelton, J. Vuckovic, G.S. Solomon, *IEEE J. Quantum. Electron.* 38(202)170.
29. G.S. Solomon, M. Pelton and Y. Yamamoto, *Physics Review Letters* 86 (2001) 3903.
30. O.J. Painter, A. Husain, A. Scherer, *Journal of Lightwave Technology* 17(1999)2082.
31. M. Boroditsky, R. Vrijen, *Journal of Lightwave Technology* 17(1999) 2096.
32. B. Gayral, J.M. Gerard, *Applied Physics Letters* 75(1999) 1908.
33. P. Lodahl, *Nature* 430 (2004) 654.
34. B. Lounis, *Report Progress Physisc* 68 (2005) 1129.
35. S. Hughes, *Optics Letters* 29 (2004) 2659.
36. Engheta, Nader; Richard W. Ziolkowski (June 2006). *Metamaterials: Physics and Engineering Explorations*. Wiley & Sons. pp. xv, 3–30, 37, 143–150, 215–234, 240–256. ISBN 978-0-471-76102-0.
37. Zouhdi, Saïd; Ari Sihvola; Alexey P. Vinogradov (December 2008). *Metamaterials and Plasmonics: Fundamentals, Modelling, Applications*. New York: Springer-Verlag. pp. 3–10, Chap. 3, 106. ISBN 978-1-4020-9406-4.
38. R.A. Shelby, D.R. Smith, *Science* 292 (2001) 77.
39. B. John, (2004). "Negative Refraction" *Contemporary Physics (Princeton University Press)* 45 (3): 191–202.
40. V.G. Veselago, *Soviet Physics Uspekhi* 10 (1968) 509.
41. J.C. Bose, "On the rotation of plane of polarization of electric waves by a twisted structure", *Proceedings of Royal Society of London*, 63 (1898) 146.
42. H. Lamp, "On Group-Velocity", *Proc. London Math. Sco.*, 1 (1904) 473.
43. N. Engheta, and R.W. Ziolkowski, "Electromagnetic Metamaterials: Physics and Engineering Explorations" 1st edition, *Willey – IEEE Press*, 2006.
44. Y. Liu, X. Zhang, *Chem.Soc.Rev.* 40(2011)2494–2507.
45. H. Raether, *Surface Plasmonson Smooth and Rough Surfaces and on Gratings*, Springer Tracts in Modern Physics, vol. 111, *Springer, Berlin, Heidelberg*, 1988.

- 46.S.Maier,
Plasmonics:FundamentalsandApplications:FundamentalsandApplications,*Springer*,
NewYork,2007.
- 47.W.L. Barnes, A. Dereux, T.W. Ebbesen, *Nature* 424(2003)824–830.
- 48.S.A. Maier, H.A. Atwater, *Journal of Applied Physics* 98(2005) 011101.
- 49.J.M. Pitarke, *Reports Progressive Physics* 70 (2007) 1.
- 50.R.H. Ritchie, *Physics Review* 106 (1957) 874.
- 51.W. Lang, *Optik* 3 (1948) 233.
- 52.E.A. Stern, *Physics Review* 120 (1960) 130.
- 53.Plasmonic Metamaterials. http://en.wikipedia.org/wiki/Plasmonic_metamaterials.
- 54.H. Atwater, *A. Sci. Am.* 296, 56(2007).
- 55.W. L. Barnes, *Nature* 424 (2003) 824-830.
- 56.G. Goubau, *Journal of Applied Physics* 21 (1950)1119.
- 57.J. R. Krenn, *Physics Review Letters* 82 (1999) 2590.
- 58.L. Yin, V. K. Vlasko-Vlasov, *Nano Letters* 5 (2005) 1399.
- 59.S. I. Bozhevolnyi, V. S. Volkov, *Physics Review Letters* 95 (2005) 046802.
- 60.D. M. Koller, A. Hohenau, *Nat. Photonics* 2 (2008) 684.
- 61.S. I. Bozhevolnyi, V. S. Volkov, *Nature* 440 (2006) 508.
- 62.L. Tang, S. E. Kocabas, *Nat. Photonics* 2, 226(2008).
- 63.E. Berhagen, M. Spasenovic, *Physics Review Letters* 102 (2009) 203904.
- 64.F. De Angelis, G. Das, *Nat. Nanotechnol.* 5 (2010) 67.
- 65.D. L. Mills, and A. A. Maradudin, *Physics Review B Condensed Matter* 39
(1989) 1569.
- 66.F. J. Garcia-Vidal, L. Martín-Moreno, and J. B. Pendry, *Journal of Optics A,
Pure Applied Optics* 7 (2005) S97.
- 67.J. B. Pendry, L. Martín-Moreno, *Science* 305 (2004) 847.
- 68.F. J. de Abajo, *Physics Review Letters* 95 (2005) 233901.
- 69.D.R. Smith, D. Schurig, *Phys.Rev.Lett.*90(2003)077405.
- 70.L. Novotny, B.Hecht, Principles of Nano-Optics, Principles of Nano-optics,
Cambridge University Press, New York, 2012.
- 71.B. zaleh, M.Teich, Fundamentals of Photonics, *Wiley Series in Pure and Applied
Optics, Wiley, Hoboken,2007*.
- 72.D Korobkin, B Neuner III, *Optics Express* 18 (2010) 22734.
- 73.P. A. Belov, C. R. Simovski, *Physical Review B* 71 (2005) 19.

- 74.GV Naik, J Kim, A Boltasseva, *Optical Material Express* 1 (2011) 1090.
- 75.D Lu, Z Liu, *Nature Communications* 3 (2012) 1205.
- 76.GV Naik, A Boltasseva, *Physics Status Solidi (RRL)* 4(010) 295.
- 77.AJ Hoffman, L Alekseyev, *Nature Materials* 6(2007) 946.
- 78.A Boltasseva, *Science* 331(2011) 290.
- 79.Y. Xiong, Z. Liu, C. Sun, and X. Zhang, *Nano Letters* 7 (2007) 3360.
- 80.G. V. Naik, J. Kim, and A. Boltasseva, *Optical Materials Express* 1(2011) 1090.
- 81.A. J. Hoffman, L. Alekseyev, *Nature Materials* 6 (2007) 946.
- 82.D. Korobkin, B. Neuner III, *Optics Express* 18 (2010) 22734.
- 83.J. Elser, V. A. Podolskiy, *Applied Physics Letters* 90 (2007) 191109.
- 84.E. Dulkeith, *Physics Review Letters* 89 (2002) 203002.
- 85.D. J. Maxwell, J. R. Taylor and S. Nie, *Journal of American Chemical Society* 124 (2002) 9606.
- 86.N. Liu, B.S. Prall and V.I. Klimov, *Journal of American Chemical Society* 128 (2006) 15362.
- 87.O.G. Tovmachenko, C. Graf, D.J. van den Heuvel, A. van Blaaderen and H.C. Gerritsen, *Advanced Materials* 18 (2006) 91.
- 88.G. Schneider, *Nano Letters* 6 (2006) 530.
- 89.M. Ringler, A. Schwemer, M. Wunderlich, A. Nichtl, K. Kürzinger, T. A. Klar and J. Feldmann, *Physics Review Letter* 100 (2008) 203002.
- 90.K. J. Russel, T-L. Liu, S. Cui and E.L. Hu, *Nature Photonics* 6 (2012) 459.
- 91.A. Rose, T. B. Hoang, F. McGuire, J. J. Mock, C. Ciraci, D. R. Smith, and M. H. Mikkelsen, *Nano Letters* 14 (2014) 4797.
- 92.P. Goy, J.M. Raimond, M. Gross and S. Haroche, *Physics Review Letters* 50 (1983) 1903.
- 93.D.J. Heinzen, J.J. Childs, J.E. Thomas and M.S. Feld, *Physics Review Letters* 58 (1987) 1320.
- 94.G.S. Solomon, M. Pelton and Y. Yamamoto, *Physics Review Letters* 86 (2001) 3903.
- 95.A. Kress, F. Hofbauer, N. Reinelt, M. Kaniber, H. J. Krenner, R. Meyer, G. Böhm, and J. J. Finley, *Physics Review B* 71 (2005) 241304.
- 96.T. B. Hoang, J. Beetz, L. Midolo, M. Skacel, M. Lermer, M. Kamp and Andrea Fiore, *APPLIED PHYSICS LETTERS* 100, 061122 (2012).
- 97.M. Patterson and S. Hughes, *PHYSICAL REVIEW B* 80 (2009) 125307.

98. K. V. Sreekanth, T. Biaglow and G. Strangi, *Journal of Applied Physics* 114 (2013) 134306.
99. H.N.S. Krishnamoorthy, Z. Jacob, E. Narimanov, I. Kretzschmar, V.M. Menon *Science* 336 (2012) 205.
100. J. M. Gérard, B. Sermage, B. Gayral, B. Legrand, E. Costard and V. Thierry-Mieg, *PHYSICAL REVIEW LETTERS* 81 (1998) 1110.
101. Z. Jacob, I. I. Smolyaninov and E. E. Narimanov, *APPLIED PHYSICS LETTERS* 100 (2012) 181105.
102. H. Yokoyama, K. Nishi, T. Anan, H. Yamada, S. D. Brorson, and E. P. Ippen, *Applied Physics Letters* 57 (1990) 2814.
103. S. Ogawa, M. Imada, S. Yoshimoto, M. Okano, S. Noda, *Optics Letters* 305 (2004) 227.
104. K. Aoki, D. Guimard, M. Nishiokai, M. Nomura, S. Iwamoto and Y. Arakawa, *Nature photonics* 2 (2008) 688.
105. M. A. Noginov, H. Li, Yu. A. Barnakov, D. Dryden, G. Nataraj, G. Zhu, C. E. Bonner, M. Mayy, Z. Jacob and E. E. Narimanov, *Optics Letters* 35 (2010) 1863.
106. Z. Jacob, J.-Y. Kim, G.V. Naik, A. Boltasseva, E.E. Narimanov, V.M. Shalaev, *Applied Physics B* 100 (2010) 215.

**HMM structures fabrication
&
characterization techniques**

6.0 Thin films growth and characterization techniques

The thin film technology activity is represented by a relatively new research area, called “SURFACE ENGINEERING”. Surface Engineering has been one of the most expanding scientific areas includes the design and processing of surface layers and coatings, internal interfaces and their characterization. This Surface Engineering is directed by the demands of thin film and surface characteristics of materials. These thin film systems necessitate direct control of materials on the molecular and atomic scale, including surface modifications, deposition and structuring. Many these techniques were accountable for remarkable advances in the fundamental understanding of the physics and chemistry of thin films, their microstructural evolution and their properties. This progress has led to the development of novel materials, expanded applications and new designs of devices and functional thin film systems. It is noteworthy that, the quality of thin films, their microstructural and basic characteristics in a device level mainly depend upon type of thin film deposition techniques. There exists a variety of several physical/chemical vapor thin film deposition techniques/technologies originate from purely physical or purely chemical processes. In this regard various thin film deposition techniques were illustrated and discussed about their respective working principles and limitations in comparison to the other film processing techniques.

The detailed depiction of the techniques employed for the fabrication of HMM structures, is presented in *Section - A* of this chapter. The characterization techniques and their basic principles, used in the characterization of HMM structures for the determination of film thickness, optical absorption & reflection measurements, PL studies, and TCSPC measurements are presented in the *section – B*.

Section - A

6.1 Thermal evaporation

Thermal evaporation is one of the Physical Vapor Deposition (PVD). Thermal Evaporation involves heating a solid material inside a high vacuum chamber, taking it to a temperature which produces some vapor pressure. Inside the vacuum, even a relatively low vapor pressure is sufficient to raise a vapor cloud inside the chamber. This evaporated material now constitutes a vapor stream, which traverses the chamber and hits the substrate, sticking to it as a coating or film. The material is heated to its

melting point and is liquid, it is usually located in the bottom of the chamber, often in some sort of upright crucible. The vapor then rises above this bottom source, and the substrates are held inverted in appropriate fixtures at the top of the chamber. The surfaces intended to be coated are thus facing down toward the heated source material to receive their coating [1,2].

There are two primary means of heating the source material. One method, often referred to as Filament Evaporation, is a simple electrical resistive heat element, or filament. There are numerous different physical configurations of these filaments, including many known as "boats" - essentially thin sheet metal pieces of suitable high temperature metals (such as tungsten) with formed indentations or troughs into which the material is placed. The filament source offers the safety of low voltage, although very high current is required, usually several hundred amps.

In the present investigation, we employed *Angstrom thermal evaporation* system to deposit thin films of silver thin films on glass substrates.

6.2 Electron beam evaporation

Electron beam deposition is a method of using electron beams generated from an electron source in a vacuum to irradiate an evaporant material, and heating and evaporating it so that the evaporated material forms a thin film on a substance, such as a substrate or a lens. The deflection type electron source that is installed in a vacuum device is used in a wide range of fields and it is known as electron beam physical vapor deposition (EBPVD) [3,4]. In an EBPVD system, the deposition chamber must be evacuated to a pressure of at least 7.5×10^{-5} Torr (10^{-2} Pa) to allow passage of electrons from the electron gun to the evaporation material which can be in the form of an ingot or rod. Multiple types of evaporation materials and electron guns can be used simultaneously in a single EBPVD system, each having a power from tens to hundreds of kW. Electron beams can be generated by thermionic emission, field electron emission or the anodic arc method. The generated electron beam is accelerated to a high kinetic energy and directed towards the evaporation material. Upon striking the evaporation material, the electrons will lose their energy very rapidly. The kinetic energy of the electrons is converted into other forms of energy through interactions with the evaporation material. The thermal energy that is produced heats up the evaporation material causing it to melt or sublime. Once temperature and vacuum

level are sufficiently high, vapor will result from the melt or solid. The resulting vapor can then be used to coat surfaces. Accelerating voltages can be between 3 kV – 40 kV. When the accelerating voltage is between 20 kV – 25 kV and the beam current is a few amperes, 85% of the electron's kinetic energy can be converted into thermal energy. Some of the incident electron energy is lost through the production of X-rays and secondary electron emission. There are three main EBPVD configurations, electromagnetic alignment, electromagnetic focusing and the pendant drop configuration. Electromagnetic alignment and electromagnetic focusing use evaporation material that is in the form of an ingot while the pendant drop configuration uses a rod. Ingots will be enclosed in a copper crucible or hearth[4] while a rod will be mounted at one end in a socket. Both the crucible and socket must be cooled. This is typically done by water circulation. In the case of ingots, molten liquid can form on its surface which can be kept constant by vertical displacement of the ingot. The evaporation rate may be on the order of 10^{-2} g/cm² sec.

In the present investigation, we employed Angstrom electron beam evaporation system to deposit thin films of Al₂O₃ and SiO₂ thin films on glass substrates.

6.3 Electron beam lithography

Electron Beam Lithography is a specialized technique for creating extremely fine patterns (~ 50 nm). Derived from the early scanning electron microscopes, the technique in brief consists of scanning a beam of electrons across a surface covered with a resist film sensitive to those electrons, thus depositing energy in the desired pattern in the resist film. The main attributes of the technology are: 1) it is capable of very high resolution; 2) it is a flexible technique that can work with a variety of materials; 3) it is slow, being one or more orders of magnitude slower than optical lithography and 4) it is expensive and complicated – electron beam lithography tools can cost many millions of dollars and require frequent service to stay properly maintained [5 – 7].

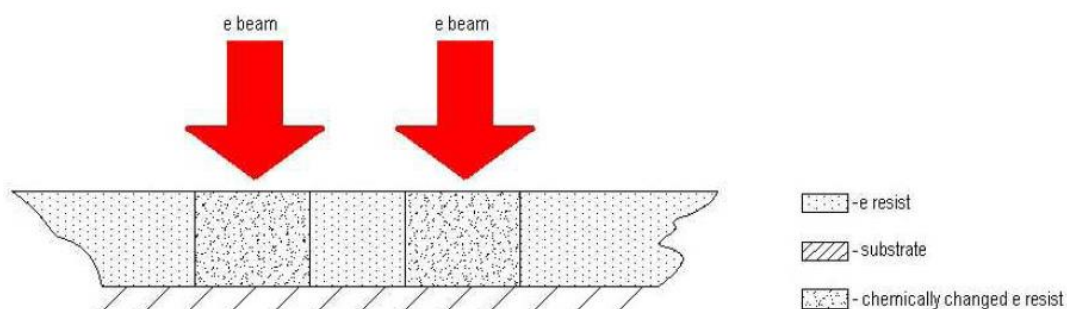


Figure – 6.3.1: E resist cross-section: The electron beam causes chemical changes in the exposed areas.

The basic idea behind electron beam lithography is identical to optical or any other lithographies. The substrate is coated with a thin layer of resist (in analogy with photoresist we use the word e resist), which is chemically changed under exposure to the electron beam (Figure – 6.3.1), so that the exposed (non-exposed) areas can be dissolved in a specific solvent (positive (negative) lithography). This process is called development (in analogy with development of photographic films, Figure – 6.3.2).

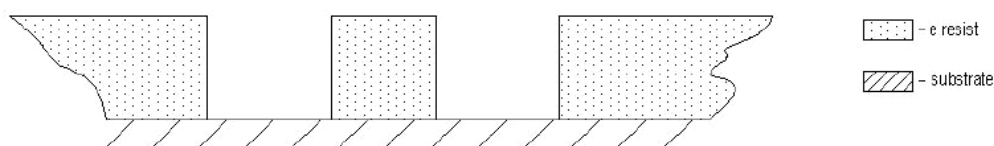


Figure – 6.3.2: E resist cross-section: Only the chemically changed e resist can be dissolved in a specific solvent (positive lithography).

After the removal of the exposed resist a thin metallic layer is deposited on the substrate. On the areas exposed to the electron beam the deposited metal sticks to the substrate, while on the unexposed areas the metal sticks to the resist surface (Figure – 6.3.3).

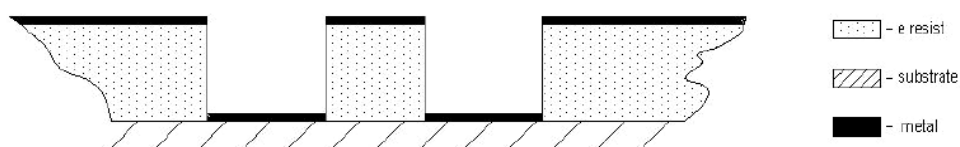


Figure – 6.3.3: E resist cross-section after metal deposition.

After metal deposition the remaining (unexposed) E resist is dissolved in an aggressive solvent (lift off). The metal sticking to the resist loses “footing” and so only the metal

sticking to the substrate remains. In the present investigation, we employed Electron beam lithographic technique (Tescan Vega) to fabricate two dimensional PMMA grating patterns over HMM substrates.

Section - B

6.4 Ellipsometry

Ellipsometry is generally a non-invasive, non-destructive measurement technique to obtain optical properties of a sample material by means of the reflected light waves. The technique measures a relative change in polarization and is therefore not dependent on absolute intensity as long as the absolute intensity is sufficient. This makes ellipsometric measurement very precise and reproducible. Ellipsometry uses the fact that linearly polarized light at an oblique incidence to a surface changes polarization state when it is reflected. It becomes elliptically polarized, thereby the name "ellipsometry". In some cases elliptically polarized light is used as the incident light wave. The idea of ellipsometry is shown in general in Figure – 6.4.1.

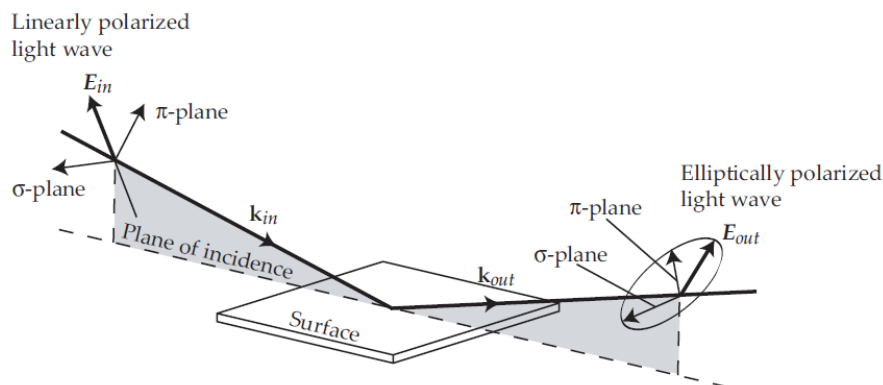


Figure – 6.4.1: The general principle in ellipsometry.

When a monochromatic, plane light wave is directed at a surface at oblique incidence, the plane of incidence is defined as a plane perpendicular to the surface and containing the vector which points in the direction of propagation of the light wave. This vector is called the wavevector k_{in} . Perpendicular to k_{in} are the two mutually perpendicular vectors for the electric field E and the magnetic field B of the light wave. The E -vector is chosen as the vector defining the polarization of the light wave and is therefore the only one shown in Figure – 6.4.1. The E -vector is decomposed into two components, which are mutually perpendicular and perpendicular to k_{in} . The two components of E

are respectively parallel and perpendicular to the plane of incidence as seen in Figure – 6.4.1. The vectors are named from their German names, “Parallel” and “Senkrecht”, and are from this given the corresponding Greek letters π and σ , respectively [8 – 10].

The incident light wave is linearly polarized. Polarization will be described in depth later, but for now the π - and σ -component of E can be seen as oscillating with an amplitude and mutual phase causing the endpoint of E to move in a straight line in the plane of the π - and σ -components. When the light wave reflects off the surface, the polarization changes to elliptical polarization. This means that the amplitude and mutual phase of the π - and σ -component of E are changed causing the endpoint of E to move in an ellipse. The form of the ellipse can be measured by a detector and data processing can relate this to the ellipsometric parameters ψ and Δ . The ellipsometric parameters can be related to the reflection coefficients of the light polarized parallel and perpendicular to the plane of incidence ρ_π and ρ_σ , respectively. The relation is the basic equation in ellipsometry and is given by the complex ratio ρ of the two reflection coefficients,

$$\rho = \frac{\rho_\pi}{\rho_\sigma} = \tan(\Psi)e^{j\Delta} \dots\dots\dots (6.1)$$

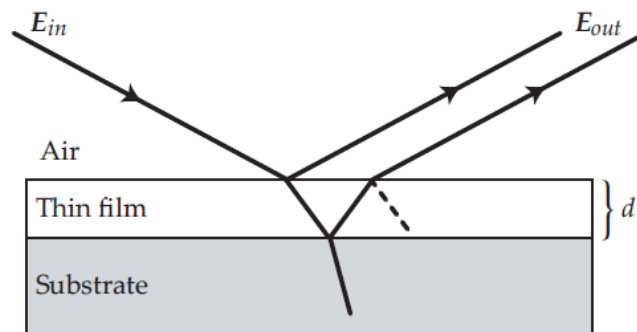


Figure – 6.4.2: Illustration of a thin film on top of a substrate.

The ellipsometric parameters ψ and Δ are given by a measurement with an ellipsometer and the two reflection coefficients are functions of the complex refractive index of the material. Ellipsometry is often used to measure the thickness of thin films on top of a substrate. A simplified model of this is shown in Figure – 6.4.2 where an incident light wave is reflected off and transmitted through the surface of a thin film. If the refractive indexes of the film and the substrate are known, it is possible to calculate

the thickness d of the thin film by ellipsometry. This application of ellipsometry is widely used to investigate materials and surfaces.

6.5 Stylus Profilometry

Stylus profilometer is one of the common tools to measure surface film characteristics. Stylus profiling technology for surface metrology dates back to the late 1960's with the introduction of Dektak® I stylus profiler. Stylus profilers are versatile measurement tools for studying surface topography. Their primary function is to measure film thickness by scanning step heights and trench depths. They are also useful for measuring surface planarity and thin film stress, as well as surface roughness and waviness measurements [11, 12].

The stylus profilers rely on a small-diameter stylus moving along a surface either by movement of the stylus or movement of the surface of interest. A true stylus profiler moves linearly to obtain the measurement. As the stylus encounters surface features, the stylus moves vertically to measure various surface features, such as deposited film, irregularities, or finish. Stylus profilers have become the standard for monitoring thin film deposition and etch processes. Consequently, stylus profilers are also widely used for measuring MEMS, compound semiconductor devices, flat panel displays, optoelectronics, optical thin films, optics, solar cells, ceramic, paper, surface finish, coatings, and much more, addressing a broad range of applications in semiconductor, data storage, opto-telecommunications, and R&D/industrial.

True stylus profilers employ a stylus, which is mounted on an arm, coupled to a linear variable differential transformer (LVDT). However, not all stylus profilers utilize LVDT in their sensors, as other sensor types have been developed over the years. The stylus is composed typically of metal with a diamond tip, and in changes from plus to minus as a function of core displacement, corresponding to the mechanical changes that occur whenever the stylus moves up and down over the features on the surface. The varying DC signal is then digitized and stored to represent the surface profile of the sample. In the present investigation, we employed Stylus Profilometer (KLA-Tencor P-6) to measure the thicknesses of deposited dielectric and metal thin films.

6.6 Photoluminescence Spectroscopy

Photoluminescence is divided into two categories: fluorescence and phosphorescence. A pair of electrons occupying the same electronic ground state have opposite spins and are said to be in a singlet spin state (Figure – 6.6.1a). When an analyte absorbs an ultraviolet or visible photon, one of its valence electrons moves from the ground state to an excited state with a conservation of the electron's spin (Figure – 6.6.1b). Emission of a photon from the singlet excited state to the singlet ground state—or between any two energy levels with the same spin—is called fluorescence. The probability of fluorescence is very high and the average lifetime of an electron in the excited state is only $10^{-5} - 10^{-8}$ s. Fluorescence, therefore, decays rapidly once the source of excitation is removed [13 – 15].

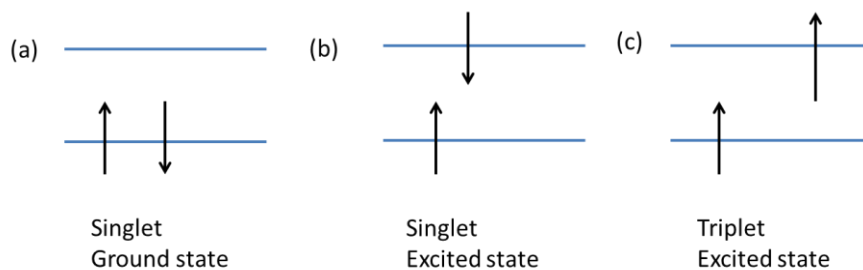


Figure – 6.6.1: Electron configurations for (a) a singlet ground state; (b) a singlet excited state; and (c) a triplet excited state.

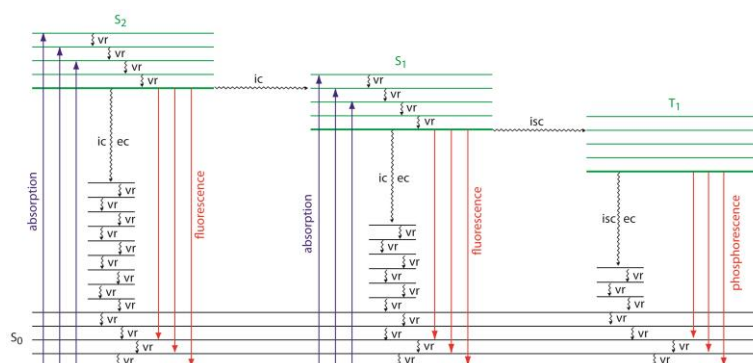


Figure – 6.6.2: Energy level diagram for a molecule showing pathways for the deactivation of an excited state: vr is vibrational relaxation; ic is internal conversion; ec is external conversion; and isc is an intersystem crossing. The lowest vibrational energy for each electronic state is indicated by the thicker line. The electronic ground state is shown in black and the three electronic excited states are shown in green. The absorption, fluorescence, and phosphorescence of photons also are shown.

In some cases an electron in a singlet excited state is transformed to a triplet excited state (Figure – 6.6.1c) in which its spin is no longer paired with the ground state. Emission between a triplet excited state and a singlet ground state—or between any two energy levels that differ in their respective spin states—is called phosphorescence. Because the average lifetime for phosphorescence ranges from 10^{-4} – 10^4 s, phosphorescence may continue for some time after removing the excitation source. To appreciate the origin of fluorescence and phosphorescence we must consider what happens to a molecule following the absorption of a photon. When the molecule initially occupies the lowest vibrational energy level of its electronic ground state, which is a singlet state labeled S_0 in Figure – 6.6.2. Absorption of a photon excites the molecule to one of several vibrational energy levels in the first excited electronic state (S_1), or the second electronic excited state (S_2), both of which are singlet states. Relaxation to the ground state occurs by a number of mechanisms, some involving the emission of photons and others occurring without emitting photons. These relaxation mechanisms are shown in Figure – 6.6.2. The most likely relaxation pathway is the one with the shortest lifetime for the excited state.

Photoluminescence spectra are recorded by measuring the intensity of emitted radiation as a function of either the excitation wavelength or the emission wavelength. An excitation spectrum is obtained by monitoring emission at a fixed wavelength while varying the excitation wavelength. When corrected for variations in the source's intensity and the detector's response, a sample's excitation spectrum is nearly identical to its absorbance spectrum. The excitation spectrum provides a convenient means for selecting the best excitation wavelength for a quantitative or qualitative analysis.

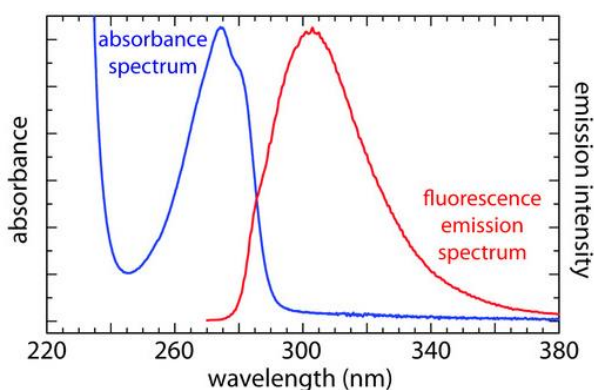


Figure – 6.6.3: Absorbance spectrum and fluorescence emission spectrum for tyrosine in a p^H 7, 0.1 M phosphate buffer.

In an emission spectrum a fixed wavelength is used to excite the sample and the intensity of emitted radiation is monitored as function of wavelength. Although a molecule has only a single excitation spectrum, it has two emission spectra, one for fluorescence and one for phosphorescence. For an example, Figure – 6.6.3 shows the UV absorption spectrum and the UV fluorescence emission spectrum for tyrosine. In the present study, we conducted steady-state photoluminescence measurements using a spectrofluorometer to verify the coupling of dye emission into the metamaterial states. The detection method was based on a reflection geometry in which dyes were excited using a mercury lamp and the emitted signals were detected using a last generation multichannel photomultiplier tube. Steady-state emission spectra were recorded on a HORIBA Jobin-Yvon Fluorolog-3 FL3-211 spectrometer (Figure – 6.6.4) equipped with a 450W xenon arc lamp (L), double-grating excitation (M_{ex}) and single-grating emission (M_{em}) monochromators (2.1nm/mm dispersion; 1200 grooves/mm), and a Hamamatsu R928 photomultiplier tube (PM) or a TBX-04-D single photon-counting detector (D_{TCSPC}) or a InGaAs liquid nitrogen-cooled solid-state detector (D_{InGaAs}). Emission and excitation spectra were corrected for source intensity (lamp and grating) and emission spectral response (detector and grating) by standard correction curves.

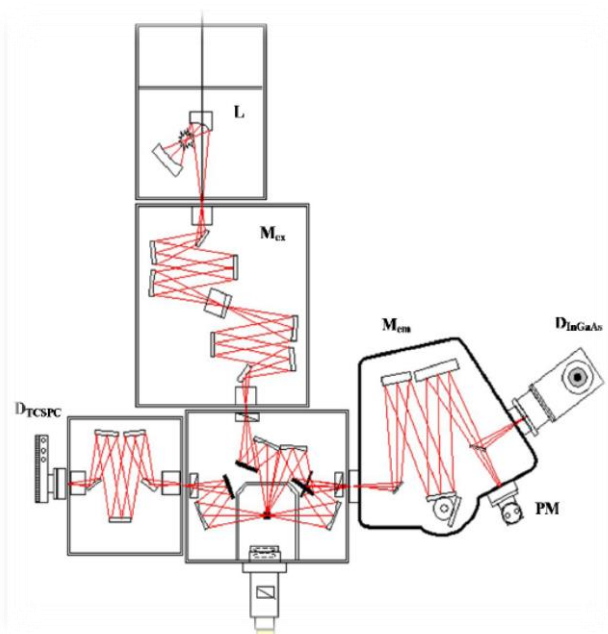


Figure – 6.6.4: FluoroLog3-2iHRI-TCSPC-IGA, optical configuration.

6.7 Time-Correlated Single Photon Counting Technique

Since the principle operation of acquiring the fluorescence lifetime in time-domain for both HORIBA Jobin-Yvon spectrofluorometer and Edinburgh FLS980 Series fluorescence lifetime spectrometer is based on the Time-correlated single-photon counting (TCSPC) data, therefore before describing the characteristics of the mentioned instruments, this method of lifetime measurement is described. Time-correlated single-photon counting (TCSPC) is a digital technique, in which counting of time-correlated photons is related to excitation pulse. To collect TCSPC data the sample is excited periodically with a fast source. Excitation frequency is determined respect to the optical behavior of the sample. This provides the possibility to extend the data collection over multiple cycles and reconstruct the decay profile from single photon events collected over many cycles. The expected exponential shape of lifetime waveform would be observed if many fluorophores are excited and numerous photons are detected.

However, for acquiring TCSPC data, due to conditions of measurement, less than one photon is detected per laser pulse. In fact, typically in every 100 excitation pulses just one photon is detected. This drawback comes from the dead time of electronics that they are not enough fast to measure multiple photons per pulse. The principle of TCSPC used in both spectrofluorometers can be understood by provided scheme in Figure – 6.7.1. The experiment starts with exciting the sample by repetitive pulses of a light source such as laser or flash-lamp. Simultaneously, the light source sends a signal to a constant function discriminator (CFD), which accurately measures the arrival time of the pulse. The output signal of CFD block is applied to time-to-amplitude converter (TAC) block, in order to trigger a voltage ramp, which can increase linearly with time on the nanosecond timescale. A second channel identifies the pulse from the single detected photon. As a single photon sensitive detector a Photomultiplier Tube (PMT), Micro Channel Plate (MCP) or a Single Photon Avalanche Diode (SPAD) can be used. As the emission pulse is arrived to CFD, this block sends a signal to TAC to stop the voltage ramp. Now TAC provide an output pulse which the difference between start and stop points of that, is proportional to time delay between the excitation and emission signals. The output signal of TAC is amplified by a programmable gain amplifier (PGA). Finally a multichannel analyzer converts the output signal of PGA to a numerical value by using an analog-to-digital converter (ADC). The electronic circuits embedded in window discriminator (WD)

block are responsible to minimize false readings of signal by restricting the acquired signal to determined range of voltages. The obtained digital signal is stored as a single event with the measured time delay. In order to complete the decay histogram this process needs to be repeated with a pulsed-light source, until one has collected more than 10000 counts in the peak channel.

As shown in Figure – 6.7.1, an ultrafast optical set up has been used to measure the lifetimes of the samples. The optical set up consists of a Ti: Sapphire tunable femtosecond laser (Chameleon Ultra II from Coherent), Pulse Picker (by Coherent), Second Harmonic Generator (by Coherent), and a spectrofluorometer for time-correlated single photon counting (TCSPC) instrument (by Edinburgh instruments). The time resolution of the TCSPC instrument is ≤ 5 ps. In the experiments, the Coumarin 500 dye was excited by using a pulsed laser at 400 nm with a pulse width of about 120 fs and a repetition rate of 4 MHz. Here the emission wavelengths were varied using a monochromator that belongs to the TCSPC instrument.

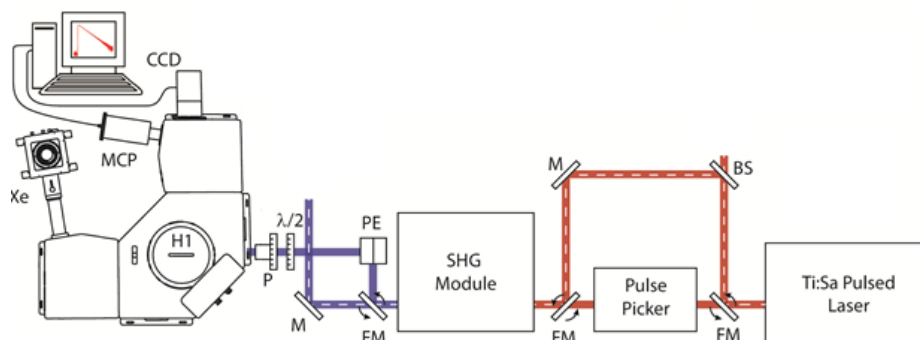


Figure – 6.7.1: Experimental set up used for the lifetime photoluminescence measurements.

References:

1. G. Gerlach, W. Dotzel, Introduction to Microsystem Technology: A Guide for Students. Hobken, NJ: John Wiley and Sons, 2008.
2. B. Streetman and S. Banerjee, Solid State Electronic Devices. New Jersey: Pearson Education, 2006.
3. Harsha, K.S.S, "Principles of Physical Vapor Deposition of Thin Films", Elsevier, Great Britain (2006), p.400.
4. George, J., "Preparation of thin films", Marcel Dekker, Inc., New York (1992), p.13.
5. McCord MA, Rooks M. Electron beam lithography. In: Rai-Choudury P, editor. Handbook of microlithography, micromachining and microfabrication, vol. 1. Bellingham: SPIE; 1997. ISBN 978-081-942-378-8.
6. Nabity J, Compbell LA, Zhu M, Zhou W. E-beam nanolithography integrated with scanning electron microscope. In: Zhou W, Wang ZhL, editors. Scanning microscopy for nanotechnology: techniques and applications. 1st ed. New York: Springer; 2006. ISBN 978-144-192-209-0.
7. Wu CS, Makiuchi Y, Chen CD, In: Wang M, editors. Lithography. High-energy electron beam lithography for nanoscale fabrication. Croatia: InTech; 2010, ISBN 978-953-307-064-3.
8. H. G. Tompkins and W. A. McGahan, Spectroscopic Ellipsometry and Reflectometry, John Wiley & Sons Inc (1999) ISBN 0-471-18172-2.
9. H. Fujiwara, Spectroscopic Ellipsometry: Principles and Applications, John Wiley & Sons Inc (2007), ISBN 0-470-01608-6.
10. M. Losurdo and K. Hingerl (Editors), Ellipsometry at the Nanoscale, Springer (2013), ISBN 978-3-642-33955-4.
11. W J Walecki, F Szondy and M M Hilali, "Fast in-line surface topography metrology enabling stress calculation for solar cell manufacturing for throughput in excess of 2000 wafers per hour" 2008 Meas. Sci. Technol. 19 025302 (6pp) doi:10.1088/0957-0233/19/2/025302.
12. Stout, K. J.; Blunt, Liam (2000). Three-Dimensional Surface Topography (2nd ed.). Penton Press. p. 22. ISBN 978-1-85718-026-8.
13. Haug, H.; Koch, S. W. (2009). Quantum Theory of the Optical and Electronic Properties of Semiconductors (5th ed.). World Scientific. p. 216. ISBN 9812838848.

14. Kimble, H. J.; Dagenais, M.; Mandel, L. (1977). "Photon Antibunching in Resonance Fluorescence". *Physical Review Letters* 39 (11): 691–695. doi:10.1103/PhysRevLett.39.691.
15. Kira, M.; Koch, S. W. (2011). *Semiconductor Quantum Optics*. Cambridge University Press. ISBN 978-0521875097.

7.0 Spontaneous Emission rate enhancement using Hyperbolic metamaterials

7.1 Introduction

In view of cutting-edge scientific advances in the field of nanophotonics, unique multi-scale metamaterials have been recognized as versatile engineered structures to mitigate classical limitations of optics and enable numerous challenging applications. The central guiding principle in all the metamaterials consists of fabricating a medium composed of unit cells far below the size of the wavelength. The unique resonances of the unit cell based on its structure and material composition as well as coupling between the cells lead to a designed macroscopic electromagnetic response. In contrast to existing optical metamaterials in the visible and near-infrared wavelength regions, *hyperbolic metamaterials (HMMs) or indefinite media* are distinguished as promising class of metamaterials owing to their characteristic features like hyperbolic form of the iso-frequency dispersion curve and the directional nature of light propagation [1]. The artificial HMMs can be analogous to uniaxial metacrystals with an extremely anisotropic dielectric tensor, $\epsilon = \text{diag}[\epsilon_{xx}, \epsilon_{yy}, \epsilon_{zz}]$ such that $\epsilon_{xx} = \epsilon_{yy}$ and $\epsilon_{zz} * \epsilon_{xx} < 0$, which leads to a hyperbolic dispersion exhibiting dielectric properties ($\epsilon > 0$) in one direction and metallic nature in another direction ($\epsilon < 0$). The reason for their widespread interest is due to the relative ease of nanofabrication, broadband nonresonant response, wavelength tunability, bulk three-dimensional response, and high figure of merit [2].

This distinctive physical consequence of dispersion relation enables the propagation of waves with very high wavevectors, known as high-k waves, showing a broadband singularity in the density of photonic states [3]. These interesting properties of HMMs promise a spectrum of substantial futuristic applications such as spontaneous emission enhancement [4 – 9], nanoimaging [10 – 12], negative refraction [13 – 15], super-planckian thermal emission [16] and biosensing [17]. The hyperbolic dispersion of HMMs leads to the existence of high photonic density of states, which can be investigated by understanding the modifications in spontaneous emission of emitters placed in the vicinity of HMM [4].

In cavity quantum electrodynamics, microcavities and photonics crystals (which are characterized by spectrally narrow resonances) have been employed as

significant tools to understand cavity quantum electrodynamics and hence for the study of modification of spontaneous emission enhancement by the Purcell effect [18 – 20]. However, the incapability for ‘microcavities’ and ‘photonic crystal’ systems to obtain high quality factor resonance make them unviable for Purcell enhancement. This incompatibility of cavity technologies pushed towards the discovery of novel systems whose exhibit broadband Purcell effect. Hyperbolic metamaterials are promising and reliable systems in comparison to conventional cavity approaches due to the existence of a large number of electromagnetic states, which lead to a divergence in the photonic density of states allowing a broadband control. The photonic density of states for a hyperbolic metamaterial has contributions from the large wavevector HMM states up to the wavevector $k_{max} \gg k_0$ and is given by equation – 4.1 [21]. In particular, HMMs play a vital role to confine the power emitted by emitters in large spatial wavevector channels. This will open new routes for innovative photonic device applications from broadband single photon sources to strong coupling of emitters and plasmonics.

$$\rho(\omega) \sim k_{max}^3 \dots\dots\dots (7.1)$$

Previously, many research groups have explored about modifications in the spontaneous emission rates of organic dyes and quantum dots positioned in the close vicinity of the surface of a metamaterial with hyperbolic dispersion. However, the Purcell enhancement of HMM is limited at the far-field due to the non-radiative behavior of plasmonic modes in HMM. Recently, nanopatterned hyperbolic metamaterials have been proposed for outcoupling the non-radiative plasmonic modes and to enhance the spontaneous emission of fluorescent molecules [22, 23]. Here we propose another novel approach, which is based on a grating coupled HMM (GCHMM) configuration to further improve the spontaneous emission rate of emitters placed nearby HMM, by exploiting the unique property of a hypergrating to outcouple and extract the non-radiative plasmonic modes. We have recently demonstrated that a grating coupled HMM geometry (hypergrating geometry) can be used to excite both surface and bulk plasmon modes from a HMM system [24].

Therefore, In the present work, experimentally we designed & fabricated ‘hyperbolic metamaterial (HMM)’ and ‘Metal grating coupled hyperbolic metamaterial (GCHMM)’ configurations to investigate the enhancement of spontaneous emission rate enhancement of fluorescent molecules.

7.2 Designing and fabrication of Hyperbolic metamaterials

7.2a Substrates Selection and Cleaning procedures:

In the present investigation, all metal and dielectric thin layers are deposited on glass substrates (Micro slides from Corning) for the fabrication of HMM structures. A thoroughly cleaned substrate is a prerequisite for the preparation of thin films with reproducible properties. The following sequential steps have been followed for cleaning the corning glass substrates.

1. The substrates were properly washed in running water and distilled water.
2. The substrates were kept in a glass container containing ethanol solution for about 15 minutes.
3. Later, they were cleaned with detergent solution followed by distilled water.
4. The substrates were subjected to ultrasonic agitation in detergent solution, distilled water and in acetone in that order of 10 minutes in each liquid.
5. Then substrates were subjected to vapor degreasing with isopropyl alcohol to increase the rate of surface contaminant removal. After that the substrates were kept in an oven (80°C) for 30 minutes for drying.

7.2b Deposition of Multilayered Metal and Dielectric films:

There are two practical approaches to achieve the hyperbolic dispersion, which are (i) A thin film multilayer (super-lattice) consisting of alternating layers of metal and dielectric gives rise to the desired extreme anisotropy and (ii). Metallic nanowires in a dielectric host. The fact that hyperbolicity requires metallic behavior in one direction and insulating behavior in the other leads to the requirement that both metals and dielectrics must be used as building blocks. In the present investigation, we fabricated multilayered lamellar thin film structures, in which we have chosen silver (Ag) as a metal layer and alumina (Al_2O_3) as a dielectric layer. Therefore, we maintained metal fill fraction value of 34% in all fabricated HMM structures. In the present investigation, Ag and Al_2O_3 pellets (supplied by Kurt J. Lesker company) are used as a source materials to deposit them in thin film form by using thermal and electron beam evaporation physical vapor thin film deposition techniques (Angstrom Thin films deposition systems) at deposition rate of 0.3 Å/s, respectively. The as deposited Ag and Al_2O_3 thin films are characterized by Variable Angle Spectroscopic Ellipsometry (J. A. Woollam Co., Inc, V-VASE) to obtain their thicknesses and optical

constants. The resultant spectroscopic measurement data was fitted with preexisting models and respective Ag and Al₂O₃ film thicknesses are found to be 12 nm and 25 nm, respectively.

First, we fabricated control sample consisting of single period of alternate Al₂O₃ at ≈ 25 nm thickness and Ag at ≈ 12 nm, as shown schematically in Figure – 4.2.1. In the fabricated control sample structure, a single period is defined as a unit cell of ‘Al₂O₃/Ag’ layers. A metal-dielectric stack can be validly approximated by a homogenous anisotropic medium when the unit cell thickness is smaller than $\lambda/10$ and if it consists of at least 4 periods. Hence, as illustrated in Figure – 7.2.1, we continued to deposited three and six periods of ‘Al₂O₃/Ag’ stacks to check Hyperbolicity nature of the deposited metal-dielectric stacks. The dielectric constants of thin films of Ag and Al₂O₃ are experimentally determined using spectroscopic ellipsometry. The real (red line) and imaginary (blue line) permittivity values of Ag as well as dielectric constants (black line) of Al₂O₃ are shown in Figure – 7.2.2a. It is clearly evident that real permittivity values of Ag show a well-known decreasing trend towards strongly negative values. This is due to the Drude-type response of free electrons in metals at higher wavelengths [25]. In the fabricated HMM structure, the individual metal and dielectric layers dimensions are satisfying the criteria of effective medium theory (EMT) to achieve homogeneity. Therefore the uniaxial dielectric tensor components of an anisotropic medium of HMM are evaluated using EMT. In the calculation, the optical constants of Ag and Al₂O₃ are taken from experimentally obtained values (Figure – 7.2.2a). Therefore by following EMT approximations, parallel (\parallel) and perpendicular (\perp) permittivities of the medium with respect to the layers can be expressed as follows[26],

$$\varepsilon_{\parallel} = \rho\varepsilon_m + (1 - \rho)\varepsilon_d \dots\dots\dots (7.2)$$

$$\varepsilon_{\perp} = \frac{\varepsilon_m\varepsilon_d}{\rho\varepsilon_d + (1 - \rho)\varepsilon_m} \dots\dots\dots (7.3)$$

In the above expressions, ρ represents fill fraction of the metal, $\rho = \frac{t_m}{t_m + t_d}$, in this present investigation it value if found to be 32 % and ε_m & ε_d indicate permittivity values of metal and dielectric layers, respectively. The evaluated dielectric permittivity tensor components of the fabricated HMM consists of six periods ($\varepsilon_{\parallel}(\varepsilon_{xx} = \varepsilon_{yy}) < 0$) and

$\epsilon_{\perp}(\epsilon_z) > 0$ imply a hyperbolic dispersion above the wavelength of 430 nm, at which transition occurs from elliptical to hyperbolic dispersion as shown in Figure – 7.2.2b.



(a) Single period



(b) Three periods



(c) Six periods

Figure – 7.2.1: Schematic representation of fabricating steps for HMM structure: (a) Control sample composed of single period of ‘Ag/Al₂O₃’ layers (b) Three periods of ‘Ag/Al₂O₃’ layers (c) Six periods of ‘Ag/Al₂O₃’ layers.

An organic dye (Coumarin 500) is selected to investigate the influence of designed HMM on spontaneous emission. For this, Coumarin 500 dye (from Exciton) is initially dissolved in ethanol (0.3% by wt.) solution and in the next step resultant solution is dissolved in Poly(methyl methacrylate) (PMMA) resist (950PMMA C2 Resist from MICROCHEM). As illustrated in Figure – 7.2.3b , prepared dye doped

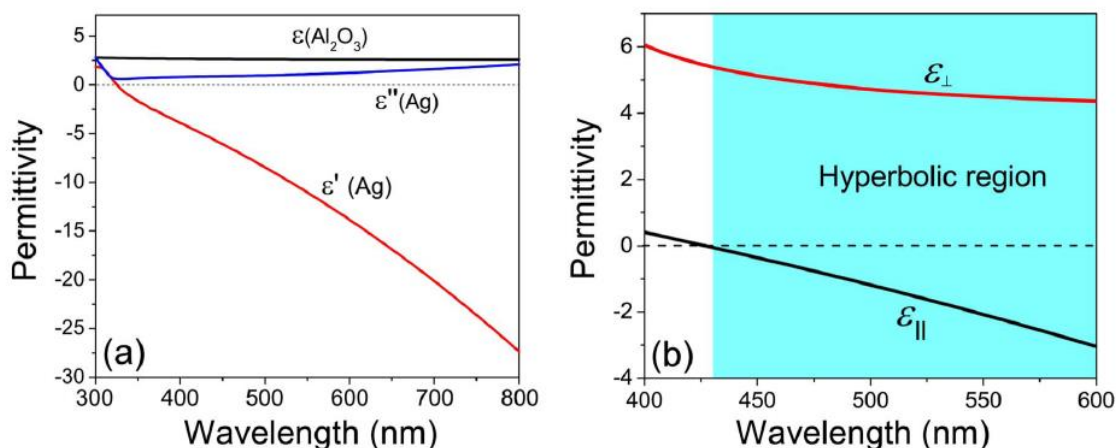


Figure – 7.2.2: Characterization of HMM: (a) Experimentally determined permittivity values of Ag and Al_2O_3 thin films. The red and blue lines represent the real and imaginary permittivity values of Ag, respectively and black line represents the permittivity values of Al_2O_3 . (b) Real parts of effective permittivity of $\text{Ag}/\text{Al}_2\text{O}_3$ HMM determined with effective media theory. The $\text{Ag}/\text{Al}_2\text{O}_3$ HMM shows hyperbolic dispersion at $\lambda \geq 430$ nm.

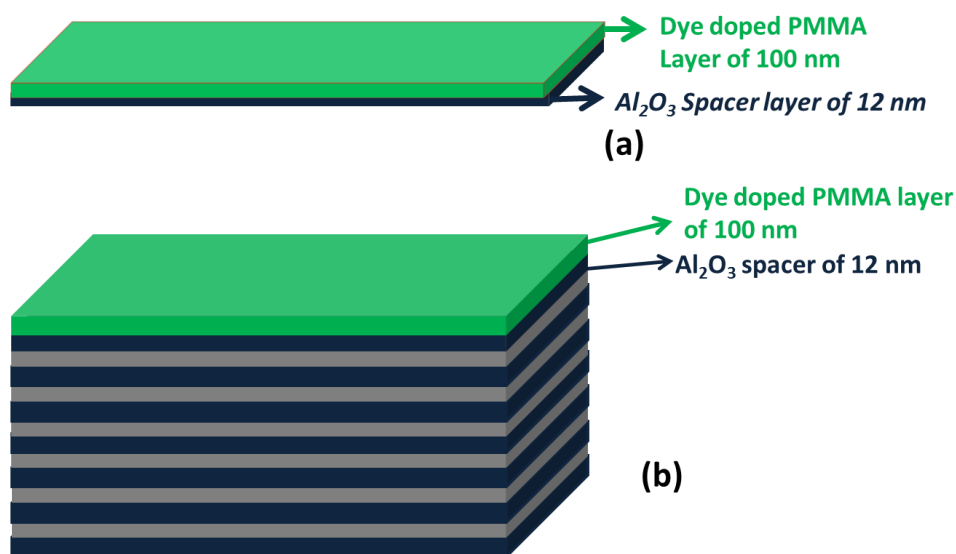


Figure – 7.2.3: (a) Reference sample and (b) dye doped PMMA layer deposited over fabricated HMM structures.

PMMA solution was spin coated at 5000 rpm, in order to get a thickness of around 100 nm on Al_2O_3 spacer layer, which is pre-deposited over HMM sample. The thickness was measured using a Stylus Profilometer (KLA-Tencor P-6). For comparative analysis, a reference sample is fabricated by spin coating a layer of dye-doped PMMA

over a pre-deposited Al_2O_3 spacer (same thickness of 12 nm) over glass substrates (as shown in Figure – 7.2.3a).

The optical absorption measurements have been carried for reference sample, using UV – Vis spectrophotometer to get the information about maximum absorption of Coumarin 500 (C 500), as evidenced from Figure – 7.2.4a, it is observed at 380 nm wavelength. To verify the coupling of C 500 dye emission into the metamaterial states, we conducted steady state photoluminescence measurements are conducted for reference sample using spectrofluorometer. The detection method was based on a reflection geometry in which dyes were excited using a mercury lamp and the emitted signals were detected using a last generation multichannel photomultiplier tube. For 400 nm excitation wavelength, the maximum emission wavelength of Coumarin 500 dye dissolved PMMA is observed at 480 nm wavelength (Figure – 7.2.4b).

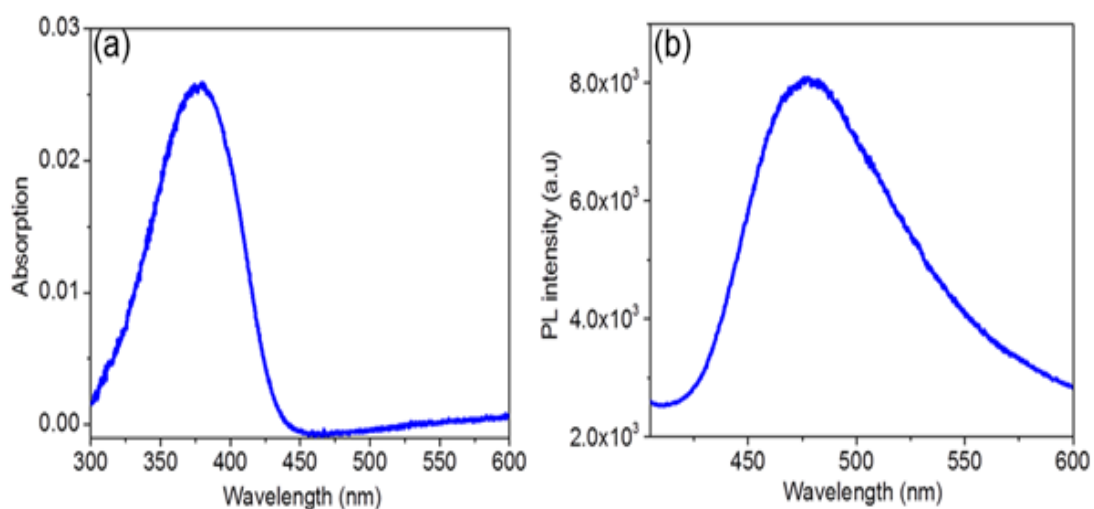


Figure – 7.2.4: (a) Absorption spectrum of dye dissolved PMMA (for reference sample). (b) Steady-state photoluminescence measurements of dye on reference sample.

Increasing the photonic density of states (PDOS) is the key to enhancing the spontaneous emission from emitters which have a low quantum yield [27].

In this direction, Metamaterials with hyperbolic dispersion, are demonstrate a unique broadband singularity in the photonic density of states, unlike any other conventional photonic system. The HMM allows propagating high wavevector spatial modes which decay exponentially in an isotropic medium (eg: vacuum) and these modes contribute to the density of states causing a divergence [28]. The spontaneous

emission is enhanced in the vicinity of hyperbolic metamaterial due to the larger photonic density of states compared to vacuum, causing a decrease in the radiative lifetime of emitters such as quantum dots or molecules.

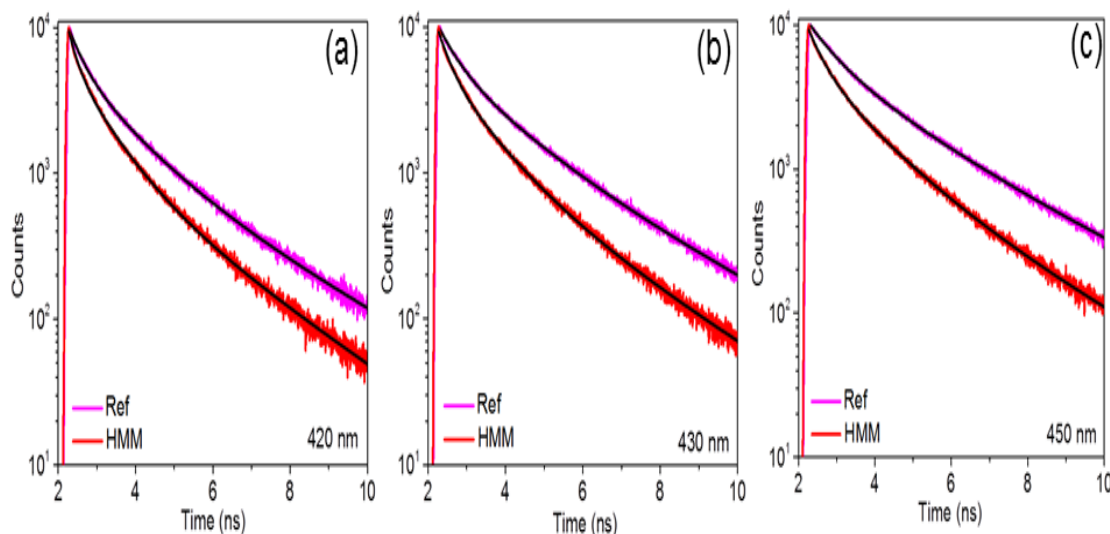


Figure – 7.2.5. Time-resolved photoluminescence measurements of Coumarin dye on Ref and HMM samples. (a) in elliptical region ($\lambda_e=420$ nm), (b) at critical wavelength ($\lambda_c=430$ nm), and (c) in hyperbolic region ($\lambda_e=450$ nm).

Therefore to understand the influence of HMM on spontaneous emission of C 500 dye molecules, Time-resolved photoluminescence measurements are performed to study the decay rates of both reference and HMM samples. An ultrafast optical set up has been used to measure the lifetimes of the samples. The optical set up consists of a Ti: Sapphire tunable femtosecond laser (Chameleon Ultra II from Coherent), Pulse Picker (by Coherent), Second Harmonic Generator (by Coherent), and a spectrofluorometer for time-correlated single photon counting (TCSPC) instrument (by Edinburgh instruments). The time resolution of the TCSPC instrument is ≤ 5 ps. The time decay curves of Reference and HMM samples for three different emission wavelengths are shown in Figure – 7.2.5. The transition from elliptical to hyperbolic dispersion is very clear from the figures that there is a large variation in time decay for HMM compared to reference sample when the emission wavelength is increased from 420 nm to 450 nm. The resultant decay curves of three samples have been fitted using three exponential functions $R(t) = B_1 e^{-t/\tau_1} + B_2 e^{-t/\tau_2} + B_3 e^{-t/\tau_3}$; instead of single exponential function because the detected signals arise from the collective response of molecules randomly distributed in PMMA. Here τ_3 represents longer decay time, which

is attributed to dye molecules away from the HMM and τ_1 and τ_2 indicate shorter decay times, which can be attributed to strong coupling of dye molecules with HMM.

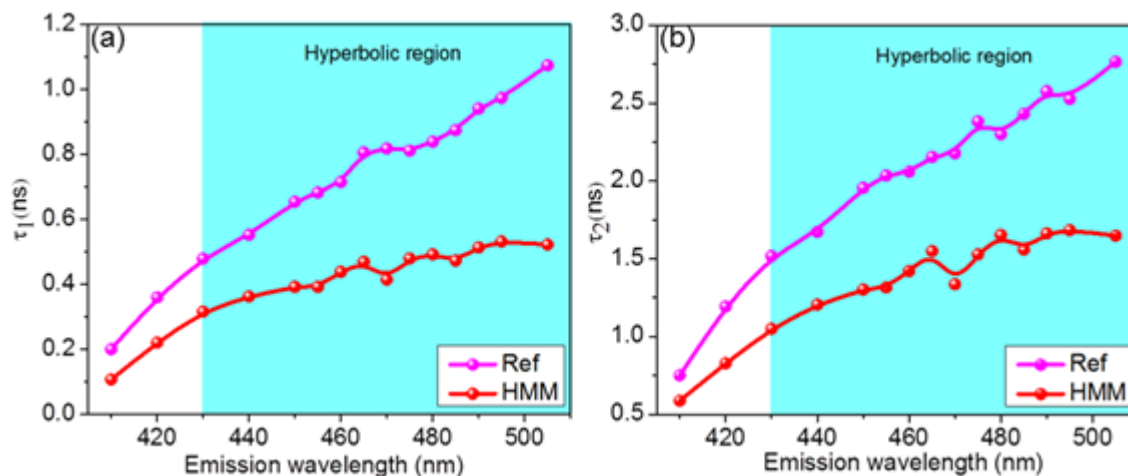


Figure – 7.2.6: Variation of spontaneous emission lifetimes of the Coumarin dye on Ref and HMM samples, as a function of emission wavelength. (a) first decay time and (b) second decay time.

The obtained three lifetimes of Ref and HMM samples as a function of emission wavelengths are shown in Figure – 7.2.6. A large variation in spontaneous emission lifetime of dye onto the HMM compared to reference sample is observed. In addition, the second and third lifetimes of HMM are very small compared to reference sample, particularly for some wavelengths in the hyperbolic spectral region of HMM (above 430 nm). These results reveal the hyperbolic dispersion in designed HMM samples and rate of enhancement of high – k metamaterial states. The decay rate enhancement is defined as inverse of decay time and in the present investigation significantly first and second decay times (τ_1, τ_2) are considered for comparative study. It is well acquainted that, HMM supports the propagation of surface plasmon polaritons (SPPs) and highly confined bulk plasmon polaritons (BPPs). However it is a difficult task to excite both SPPs and BPPs modes at optical frequencies due to momentum mismatch between incident light and the guided modes. This can be achieved in two ways, such as prism and metal grating coupling techniques.

7.3 Prism Coupling technique

There are two methods of prism coupling light to surface plasmon polaritons (SPPs), which are known as Otto and the Kretschmann-Raether geometries, both of which take place on smooth surfaces [Figure – 7.3.1]. Here, the basic principle is the

phenomena of total internal reflection in a highindex prism that has been brought near to a metal interface [29, 30].

$$k = n_p \sin\theta(\omega/c) \dots\dots\dots (7.4)$$

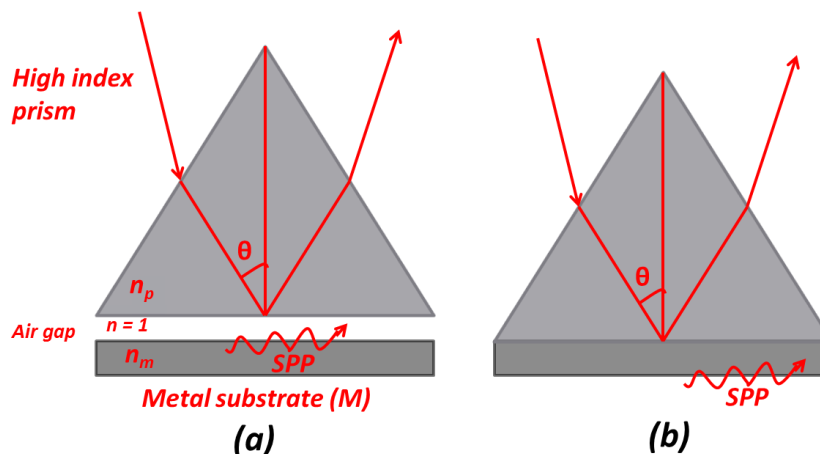


Figure – 7.3.1: Two methods of prism-coupling radiation to SPPs; (a) Otto configuration, and (b) Kretschmann-Raether configuration.

The SPP is excited optically via the enhanced momentum of an evanescent wave that will penetrate into the rare medium. When electromagnetic radiation is allowed to pass through dielectric medium and incident on metal – dielectric interface at an angle θ , then a wave of surface charges will be induced with wavevector $n \sin\theta(\omega/c)$, which is always less than $n(\omega/c)$ for all the values of θ . Here n is the refractive index of dielectric. But the SPP contains wavevector greater than $n(\omega/c)$, and it is this discrepancy that prevents the SPP from being directly excited. However, a spacer layer with refractive index n_s may be employed between a metal M and a prism (P) [Figure – 7.3.1a]. Medium P has refractive index $n_p > n_s$ and hence the component of momentum along the interface between the media can be increased: If the angle of incidence, θ , at the prism/dielectric(air) interface is greater than the critical angle, such that only an evanescent field penetrates into the spacer layer, the electromagnetic field will be able to couple to the SPP at the metal interface if the increased momentum of the evanescent field is equal to k_{SPP} . This is an attenuated total reflection (ATR) technique and was first utilized by Otto. The coupling strength is determined by the width of the air gap and optimum coupling is achieved for a gap width of the order of the incident wavelength. This is difficult to achieve for experiments at visible wavelengths since the dimensions of dust particles are much larger than the width of the spacer layer.

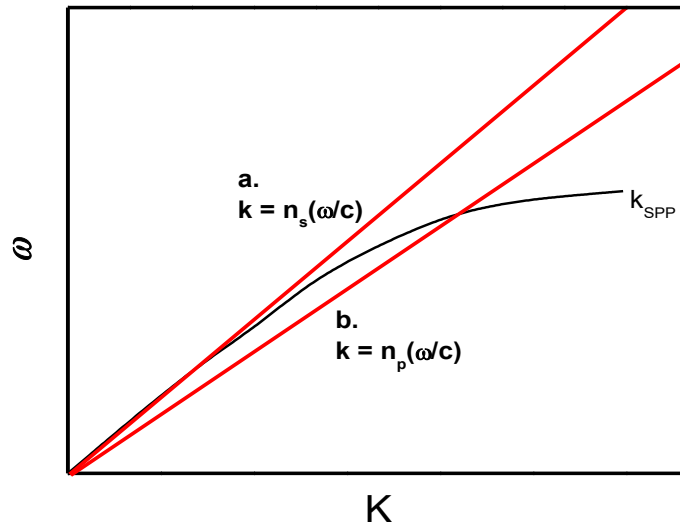


Figure – 7.3.2: Dispersion of a SPP at a metal-dielectric interface (schematic). Lines (a) and (b) illustrate the dispersion of plane waves in the spacer layer (S) and the high index prism (P) respectively where n is the refractive index of the medium. Only photons (polaritons) with momenta that lie between lines (a) and (b) may couple to SPPs.

The configuration shown in Figure – 473.1b was first demonstrated by Kretschmann and Raether, they involved metal thin metal film directly on to the surface of the prism. The low index gap is now provided by the metal layer itself. The evanescent fields pass through the film and excite a SPP on the bottom surface of the metal. Since the metal has a much higher optical impedance than air, optimum coupling at visible wavelengths may be achieved for a film thickness of approximately 45 nm. Coupling to the SPP via the ATR technique is therefore only possible in the frequency region that lie between lines (a) and (b) in Figure – 7.3.2.

7.4 Grating Coupling technique

The surface plasmon polaritons (SPPs) are known as non-radiative. So, the coupling between surface and bulk polaritons can take place when the surface is rough. Because a rough surface corresponds to a superposition of a number of different gratings, the physics underlying the coupling of SPPs to bulk polaritons at a rough interface is essentially the same as that via a single corrugation. In the year 1902, Wood proposed grating configuration to observe coupling of SPPs [31].

$$k_{SPP} = n_1 k_0 \sin\theta \pm N k_g \dots\dots\dots (7.5)$$

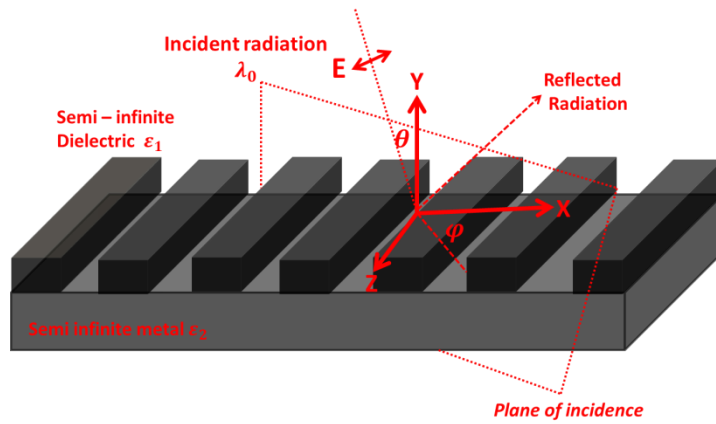


Figure – 7.4.1: Grating geometry and coordinate system used throughout this thesis. The direction of the electric field vector (E) is illustrated for the situation when p-polarised (TM) radiation is incident.

In this method, when incident radiation at an angle θ with respect to the normal of the average plane of the surface can scatter from the grating, increasing or decreasing the component of its wave vector by integer multiples of the grating wave vector $k_g \left(= \frac{2\pi}{\lambda_g} \right)$. This gives rise to diffracted orders. When a diffracted order has a wave vector greater than that of the incident grazing radiation in first medium $n_1 k_0 = \sqrt{\epsilon_1}(\omega/c)$ it will not propagate and will become evanescent. It is the enhanced momentum of these evanescent fields that may couple radiation to the SPP according to the coupling condition.

$$k_{SPP} = n_1 k_0 \sin\theta \pm N k_g \dots\dots\dots (7.6)$$

If the azimuthal angle, φ defined as the angle between the plane of incidence and the grating wave vector, is not equal to zero, then k_{SPP}, k_0 and k_g are no longer collinear and the scalar equivalent of Equation 4.6 (above) becomes,

$$k_{SPP}^2 = n_1^2 k_0^2 \sin^2\theta + N^2 k_g^2 \pm 2n_1 k_g k_0 \sin\theta \cos\varphi \dots\dots\dots (7.7)$$

The coordinate system used throughout this thesis to describe the orientation of the grating is illustrated in Figure – 7.4.1. The polar angle, θ , is used to describe the angle of incidence measured from the normal to the average plane of the grating; the azimuthal angle, φ , describes the rotation of the plane of incidence from the positive X - axis. The Y-axis runs perpendicularly to the direction of the grating grooves (parallel to the grating wave vector), and φ is measured in the X-Z plane.

Recently, nanopatterned hyperbolic metamaterials have been proposed for out coupling the non-radiative plasmonic modes and to enhance the spontaneous emission rates of fluorescent molecules. Therefore in the present study, we proposed grating coupled HMM (GCHMM) configuration to further improve the spontaneous emission rate of emitters placed nearby HMM, by exploiting the unique property of a hypergrating to outcouple and extract the non-radiative plasmonic modes. Two-dimensional diffraction grating on top of the dye dissolved PMMA was fabricated using Electron-beam lithography (Tescan Vega) by following steps mentioned given below (as shown in Figure – 7.4.2).

1. Initially, MMA resist (8.5MMAEL 11 from MICROCHEM) was spin coated on the sample at 4000 rpm and baked at $180\mu\text{C}$ for 2 min.
2. After some time, PMMA resist (950PMMA C2 Resist from MICROCHEM) was spin coated at 5000 rpm and baked at $180\mu\text{C}$ for 3 min.
3. As prepared sample was patterned using E-beam lithography with dosage 200 mC/cm^2 and beam intensity 8.
4. The exposed samples were developed using MIBK: IPA solution for 90 s and IPA for 30 s.
5. The developed samples were imaged using scanning electron microscope (SEM by Tescan Vega), confirming that the periodic holes were exactly fitting the design.
6. After that an Ag layer of 20 nm thickness was deposited directly on top of the sample using thermal evaporation of Ag pellets (from Kurt J. Lesker Company).

A grating coupling technique is employed to excite plasmonic modes associated with HMM. By following the electron-beam lithographic technique, a 2D diffraction grating is patterned above the dye mixed PMMA layer deposited over the HMM structure, followed by deposition of an Ag layer of thickness 20 nm. The fabricated grating has an average period of 500 nm and average hole diameter of 160 nm. The total area of patterned grating structure over HMM is around 5 mm X 5 mm.

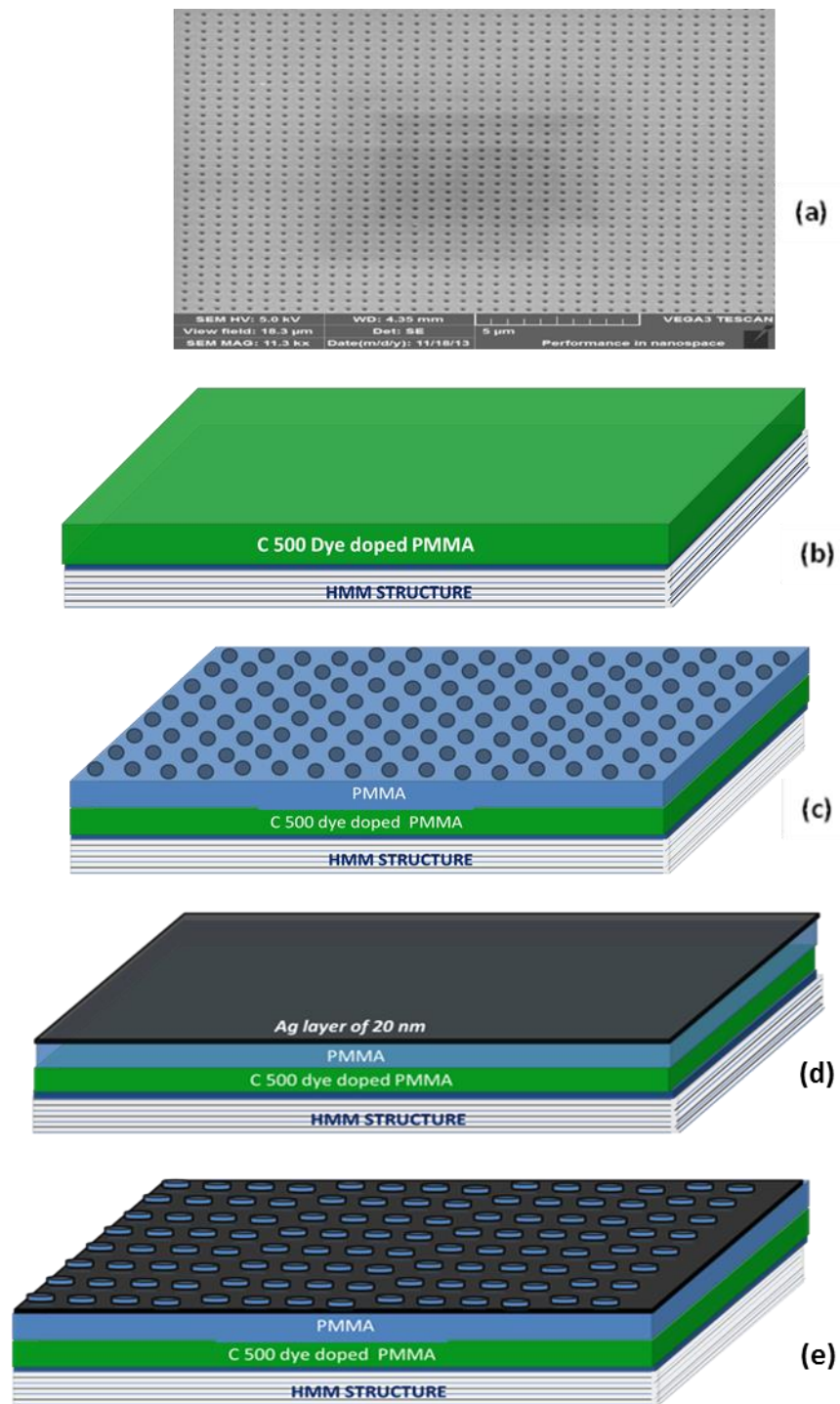


Figure – 7.4.2: Fabrication steps for GCHMM: (a) SEM image of designed 2D grating structure over PMMA substrates (b) Dye deposited over HMM (c) Electron beam exposed PMMA layer over dye posited HMM (d) Ag layer (20 nm) deposited over Electron beam exposed PMMA layer over dye posited HMM (e) Ag grating over HMM structure.

The SEM image of patterned 2D Ag diffraction grating is shown in Figure – 7.4.2a. During the diffraction grating fabrication, Ag film of thickness 20 nm is directly deposited on the PMMA diffraction grating, but not directly on the dye mixed PMMA layer. Note that a thin PMMA spacer layer is at the interface between Ag film and dye mixed PMMA layer because a thin layer of PMMA resist always left during the resist development (etching) process (see Figure – 7.4.2d). Hence this thin spacer layer can avoid the nonradiative contribution due to quenching at the Ag-Dye mixed PMMA interface.

According to grating coupling principle, the surface plasmon modes can be excited when the wavevector of the grating diffraction orders are greater than the incident light. Under this condition, diffraction orders are no longer propagating waves, but evanescent field, and the enhanced wavevector of evanescent field is responsible for the coupling of incident light to surface plasmon modes by following the condition $k_{SPP} = n_0 k_0 \sin\theta \pm m k_{gx} \pm n k_{gy}$. Being θ the incident grazing angle, n_0 is the refractive index of incident medium, $k_0 = 2\pi/\lambda$, is the vacuum wavevector, m and n are the grating diffraction orders and $k_g = 2\pi/\Lambda$, is the grating wavevector with Λ being the grating period. On the other hand, by introducing a diffraction grating on top of the HMM, it is possible to diffract light and produce a wide range of wave vectors into the HMM. Due to the existence of impedance mismatch at the various openings, the generated wave vectors can couple through the surface modes [32]. It should be noted that the large thickness (around 100 nm) of dye dissolved PMMA layer can decrease the coupling efficiency of the proposed structure. Nonetheless, unintentional scatterers are common in dye dissolved PMMA layer and these scatterers also enable the excitation of surface plasmon modes through the coupling of incident light to the surface plasmon polaritons (SPPs) [33, 34]. These two phenomena contribute to the excitation of high-k modes inside the HMM. Since the emitter is placed inside the GCHMM, it is a challenging operation to couple the incident radiation to the emitter because of the impedance mismatch between air and HMM. However, the grating coupling helps to outcouple the highly confined modes from the structure to the far field.

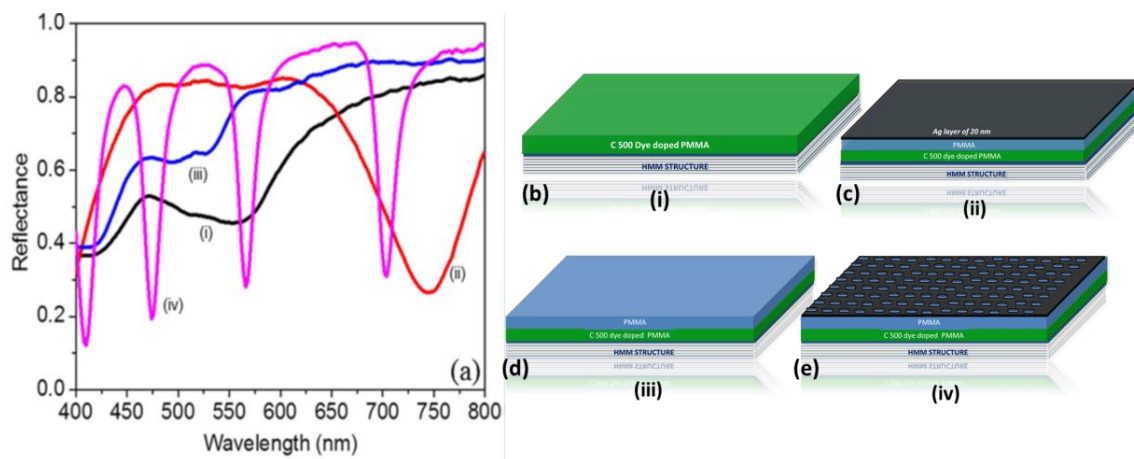


Figure – 7.4.3: Reflectance spectra as a function of excitation wavelength: (a) Reflectance spectrum of various samples obtained at incident grazing angle of 50° . The studied samples are shown in Figs. (b) to (e). The GCHMM sample (iv) shows four prominent reflectance dips corresponding to the excited plasmonic modes (both surface and bulk plasmon polaritons) from the geometry.

In order to show the excited plasmonic modes from GCHMM, the reflectance spectrum of different samples for p-polarization is obtained and shown in Figure – 7.4.3a. It is clearly evident that, in comparison to all the samples GCHMM demonstrated pronounced reflection maxima, that correspond to expected plasmonic modes (both surface and bulk plasmon modes). Here incident grazing angle is set to be 50° . The transmission measurement of GCHMM at normal incidence is carried out and shown in Figure – 7.4.4. It is evident from the figure that the resonant transmission peaks are located around the same positions of the reflectance minima. The obtained transmission plot also shows the existence of plasmonic modes in GCHMM. The bulk modes of HMM can be experimentally probed by studying the reflectance spectra as a function of incident angle at a particular wavelength. The excitation of bulk plasmon modes at different excitation wavelengths are shown in Figure – 7.4.5. It should be noted that the investigated wavelength spectral region supports the bulk plasmon modes. As reported before, the number of dielectric layers in the multilayer decides the total number of bulk modes. Here, we observed only one bulk mode for both 430 nm and 450 nm excitation wavelength that represents the fundamental mode. However, two bulk modes are present for 480 nm excitation wavelength that represent the fundamental and first order mode, respectively. Note that the higher order bulk modes are absent in the reflectance spectra because of the coupling issue due to large modal indices of the higher order guided modes. In addition, Ag film deposited HMM shows a

broad reflectance minimum at higher wavelength (750 nm), which is due to the presence of Ag scatterers intermixed at the interface.

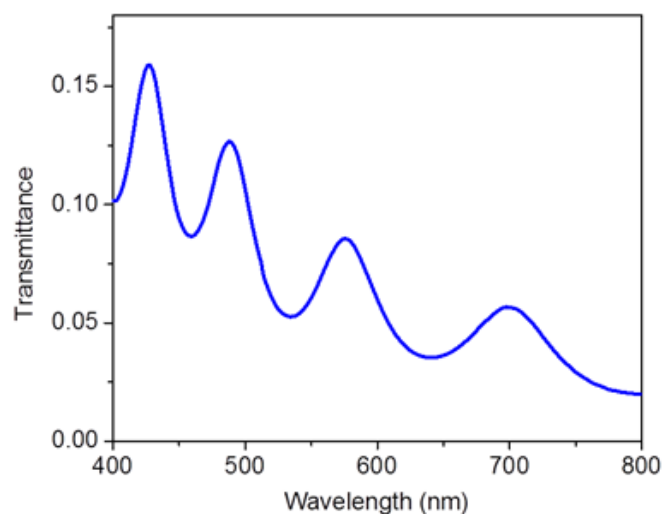


Figure – 7.4.4. Transmittance spectrum of GCHMM at normal incidence. The obtained four prominent transmission maximum correspond to the excitation of plasmonic modes from GCHMM.

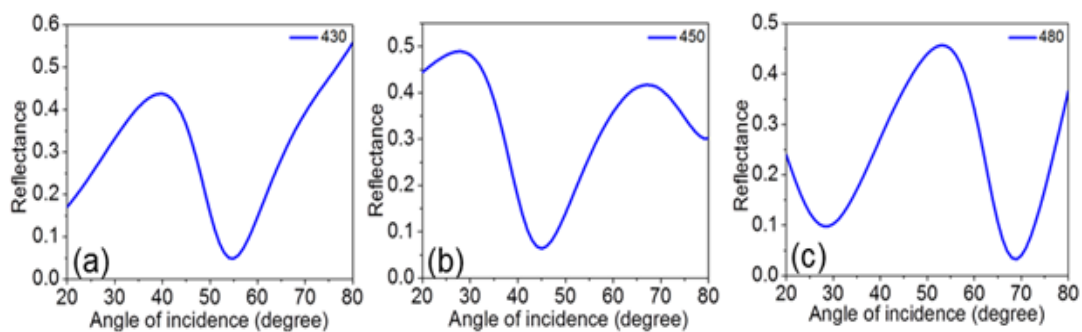


Figure – 7.4.5. Reflectance spectra of GCHMM as a function of incident angle. (a) 430 nm, (b) 450 nm and (c) 480 nm.

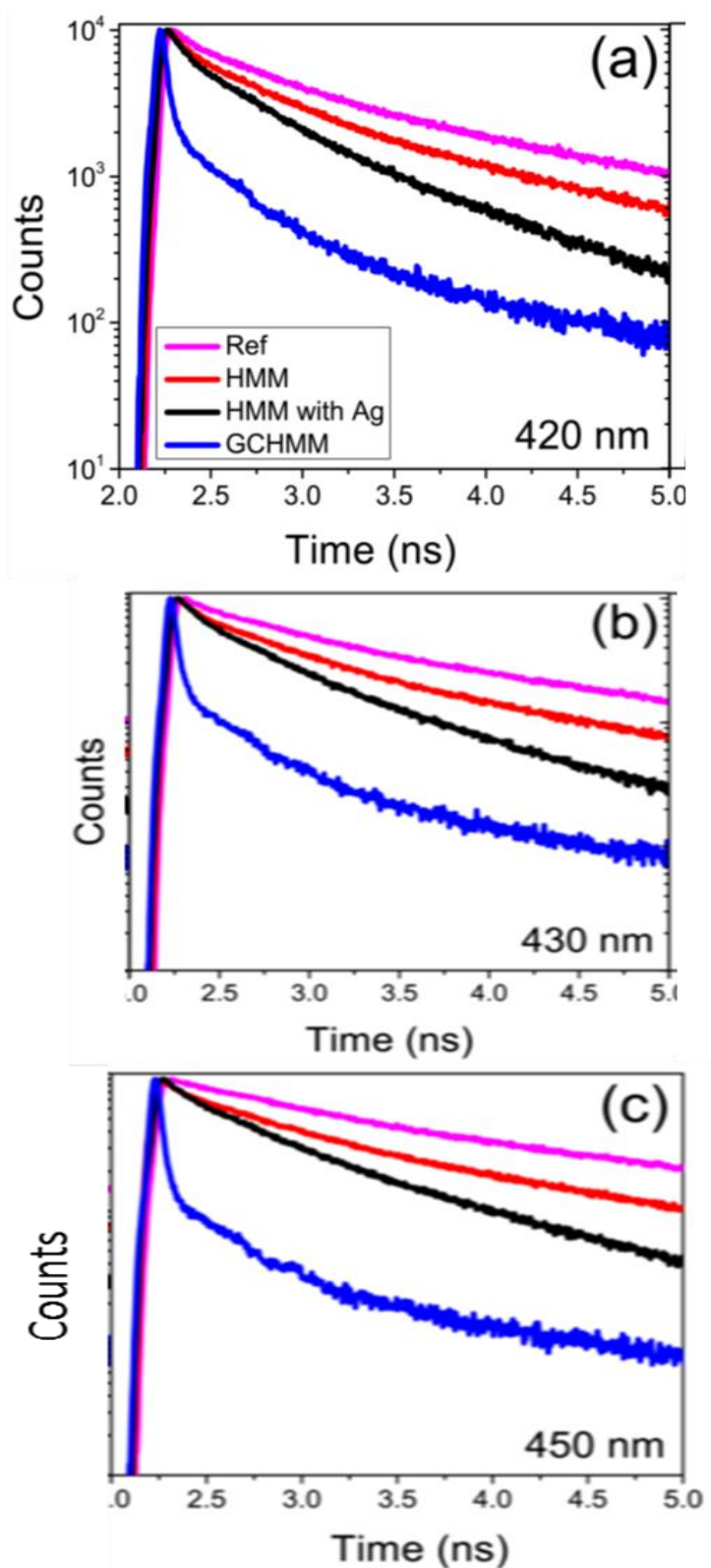


Figure – 7.4.6: Time-resolved photoluminescence measurements of Coumarin dye on various samples, Ref (pink), HMM (red), HMM with Ag (black), and GCHMM (blue)) with emission wavelength: (a) in elliptical region ($\lambda_e = 420$ nm), (b) at critical wavelength ($\lambda_c = 430$ nm), and (c) in hyperbolic region ($\lambda_e = 450$ nm).

To verify the large decay rate enhancement of proposed configuration, the GCHMM sample is compared with HMM and Ag film deposited HMM samples. Throughout the wavelength spectral range of the HMM, one can see that the GCHMM (blue curve) shows a large decay rate variation with respect to HMM (red curve) and Ag film deposited HMM (black curve) (as evidenced from Figure – 7.4.6). In addition, the decay rate variation increases when the emission wavelength is varied from the elliptical to hyperbolic spectral region of the HMM. The maximum decay rate is obtained for GCHMM for all wavelengths, which are $1/0.035 \text{ ns}^{-1}$, $1/0.030 \text{ ns}^{-1}$, and $1/0.031 \text{ ns}^{-1}$ for 420 nm, 480 nm and 510 nm, respectively. The corresponding decay rates at the respective wavelengths are $1/0.220 \text{ ns}^{-1}$, $1/0.491 \text{ ns}^{-1}$, and $1/0.575 \text{ ns}^{-1}$ for HMM and $1/0.071 \text{ ns}^{-1}$, $1/0.353 \text{ ns}^{-1}$ and $1/0.534 \text{ ns}^{-1}$ for Ag film deposited HMM. Note that the first decay time (t_1) is considered here for comparison. This large decay rate of GCHMM is attributed to the strong coupling of emitters to HMM via metallic diffraction grating. Specifically, the metallic grating excites the plasmonic Bloch modes (high-k modes) as well as surface plasmon polaritons of HMM and there is a strong overlap between these modes with the quantum emitters, which leads to a broadband enhancement of photonic density of states (PDOS). In addition, 2D diffraction grating scatters the high-k modes of HMM into well-defined free space modes. The sub-wavelength confinement of the emitter inside the GCHMM structure also enhances the decay rate. Furthermore, improved decay rate is observed for Ag film deposited HMM at certain emission wavelengths as compared to HMM. It is attributed to the presence of Ag scatterers intermixed at the interface with dye Doped PMMA layer and nonradiative contribution due to quenching at the Ag-dye doped PMMA interface. In order to emphasize the improved plasmon-exciton coupling in GCHMM, normalized lifetimes of GCHMM and Ag film deposited HMM are compared (the fitting curves are Figure – 7.4.7). The first (t_1) and second (t_2) decay times of both samples, normalized with respect to HMM as a function of emission wavelength, are shown in Figure – 7.4.8 (a) and (b), respectively. It is evident from those figures that same decay rate variation is obtained for both decay times. For GCHMM, lifetime values are higher in elliptical region and smaller in hyperbolic region. This behavior represents the preferential emission of high-k modes from GCHMM. However, the lifetimes of Ag film deposited HMM are randomly varying along the spectral range showing that the presence of Ag film does not support the preferential emission of high-k modes.. The smaller life-time values of GCHMM in hyperbolic region

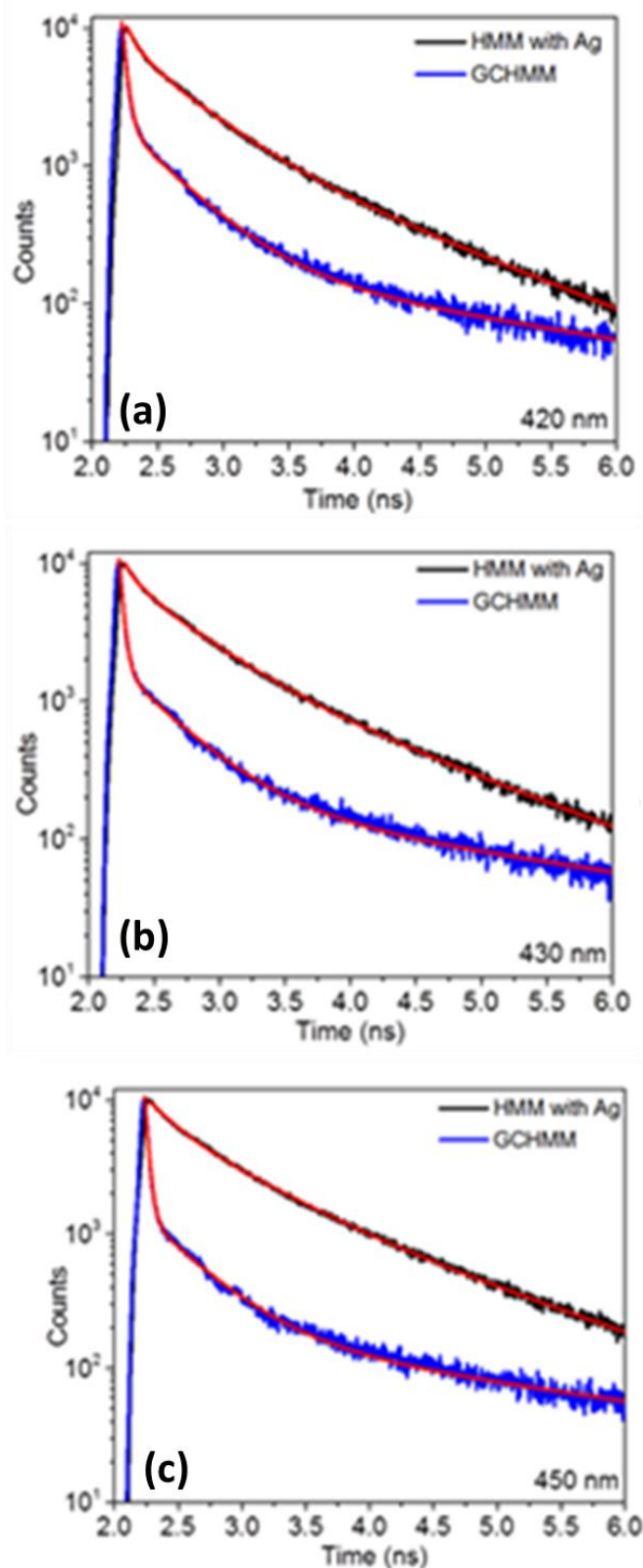


Figure – 7.4.7: Time-resolved photoluminescence measurements of Coumarin dye on HMM with Ag and GCHMM samples. (a) in elliptical region ($\lambda_e=420 \text{ nm}$), (b) at critical wavelength ($\lambda_c=430 \text{ nm}$), and (c) in hyperbolic region ($\lambda_e=450 \text{ nm}$). Red lines represent the corresponding fit.

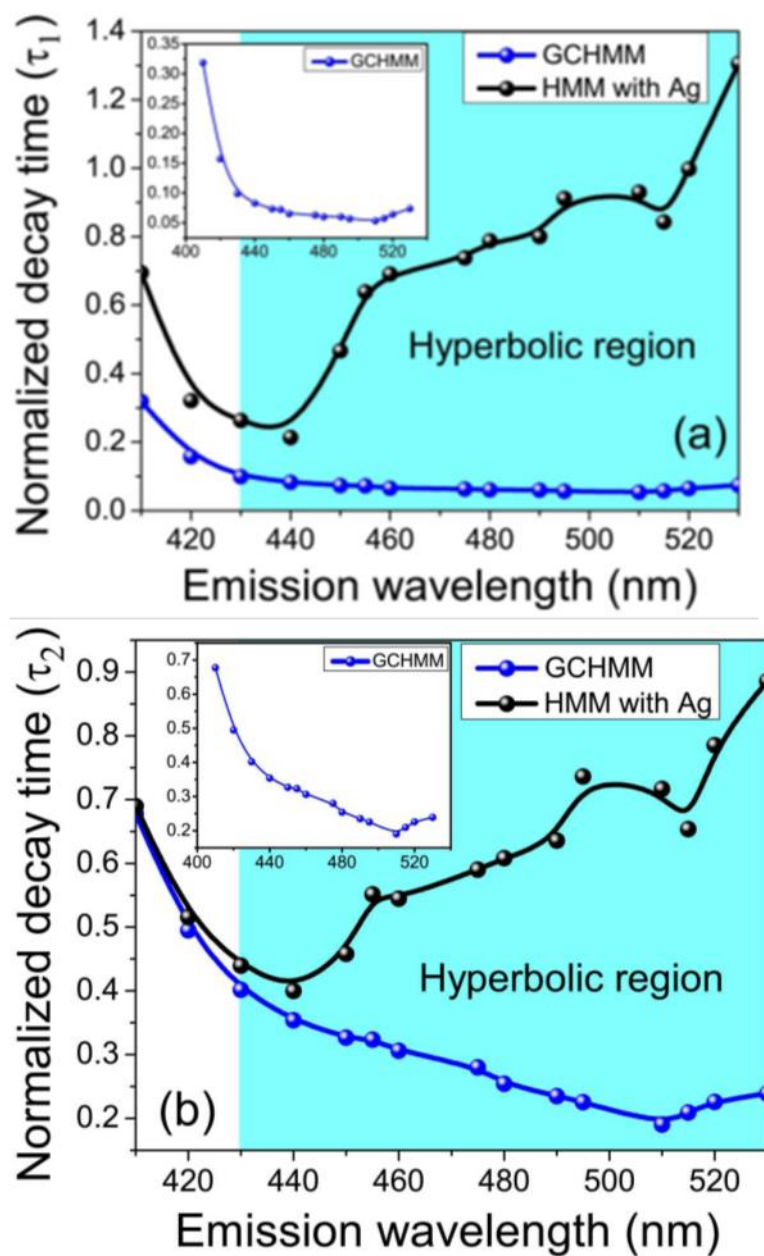


Figure – 7.4.8: Lifetimes of dye on GCHMM and Ag film deposited HMM normalized with respect to HMM sample: for (a) first decay time (t_1) and (b) second decay time (t_2). The solid lines are for eye guide. Enlarged plot of normalized decay time of GCHMM is shown in the inset of (a) and (b). Normalized lifetime is studied as a function of emission wavelength from elliptical to hyperbolic dispersion. In the case of GCHMM, a maximum decay rate is observed at 510 nm for both decay times.

are due to the hyperbolic dispersion. It should be noted that the lifetime values of GCHMM behave non-monotonically as function of the wavelength, they decrease by reaching a minimum value at 510 nm, then in the same hyperbolic region show a change of slope towards higher lifetime values. The observed behavior is a clear signature of the outcoupling ability of GCHMM. According to t_1 , a maximum of 18-fold decay rate enhancement is obtained for GCHMM at 510 nm emission wavelength,

whereas 5-fold decay rate enhancement is obtained for t_2 . In comparison to Ag film deposited HMM, the maximum decay rate enhancement for GCHMM is observed at 510 nm, which is around 17 times and 4 times higher for t_1 and t_2 , respectively. The observed large spontaneous emission rate enhancement of GCHMM is mainly due to radiative recombination rate, whereas non-radiative recombination rate is negligible in GCHMM. Thus the observed behavior of GCHMM strongly supports the influence of diffraction grating on the spontaneous emission rate enhancement. The main advantage of GCHMM compared to the other two samples is the ability to outcouple the high wavevector plasmonic modes from HMM to far-field, by the detection of fast-decaying signals from emitters strongly coupled to the multilayer structure. In the case of HMM, the field inside the multilayer is highly confined and it is unable to be detected at far field due to the evanescent nature of field at the top surface of HMM. However, the grating coupler helps to translate the evanescent field to a propagating field for far-field detection. This is evident from the time-resolved photoluminescence measurements.

8.0 Augmentation of Spontaneous emission in dye embedded hyperbolic metamaterial associated with grating coupled technique

8.1 Introduction

In the present report, our investigations are aimed to carry out a comparative study on modification of spontaneous emission of a fluorescent dye molecules placed in the vicinity of HMM structure and dye molecules embedded HMM (DEHMM) structure, in which fluorescent dye molecules are not directly in contact with thin silver layers. In extension to this, we fabricated silver grating coupled HMM structures and observed substantial enhancement in spontaneous emission in case of grating coupled DEHMM (GCDEHMM) configuration. Figure – 8.1.1 illustrates schematic representation of two different lamellar “Ag/pure polymer” and “SiO₂/dye impregnated polymer/SiO₂/Ag” nanopatterned multilayered HMM structures, which are fabricated by following sequential depositions of alternative layers of Silver, pure Poly methyl Methacrylate (PMMA) polymer, silica (SiO₂) and PMMA impregnated with DCM laser dye. In this study, Ag pellets, SiO₂, PMMA and DCM dye doped PMMA polymer are used as source materials to fabricate above mentioned HMMs, by their sequential depositions over Micro glass slide substrates, by using thermal, electron beam and spin coating thin films deposition techniques, respectively. The thickness measurements of

grown films were carried out by ellipsometry and WVASE32 fitting software is employed to fit the experimental results.

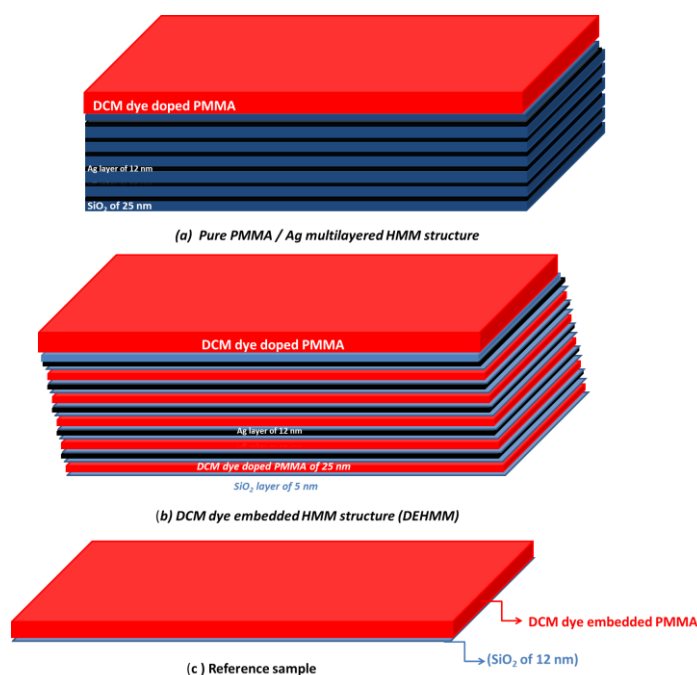


Figure – 8.1.1: Designed two different HMM structures: (a) 5 stacks of Pure PMMA (25 nm) and Ag (12 nm) multilayered HMM structure (b) 5 stacks of “SiO₂/DCM dye doped PMMA/SiO₂”(25 nm) and Ag (12 nm) lamellar DEHMM structure (c) Reference sample.

The dye on top of HMM is fabricated by depositing 5 stacks of Ag and SiO₂ layers of thicknesses of 12 nm and 25 nm (shown systematically in Figure – 5.2.1a), respectively. On top layer of Ag, a SiO₂ spacer layer of thickness 12 nm and followed by DCM laser dye dissolved PMMA layer of thickness 100 nm are deposited. In this HMM structure, the evaluated fill fraction of Ag is set to be 32 %. The DCM laser dye embedded HMM (DEHMM) structure is fabricated by depositing 5 stacks of “SiO₂ (5 nm)/dye doped PMMA (15 nm)/SiO₂ (5 nm)” and Ag layer of thickness 12 nm, as shown in Figure – 8.2.1b. In this process, the DCM laser dye is initially dissolved in ethanol (0.3 % by wt.) solution and in the next step resultant solution is dissolved in PMMA resist (950PMMA Resist from MICROCHEM). In DEHMM, the evaluated metal fill fraction value is found to be 32 %. To investigate the influence of designed DEHMM on spontaneous emission enhancement; the DCM dye dissolved PMMA layer of thickness 100 nm is spin coated over pre-deposited SiO₂ spacer of thickness 12 nm on top Ag layer of DEHMM structure. For comparative analysis, a reference sample is

fabricated by spin coating of DCM dye dissolved PMMA of thickness 100 nm over pre-deposited SiO₂ spacer (12 nm thickness) on glass substrates (Figure – 8.2.1c). In the current study, the individual metal and dielectric layers dimensions are satisfying the criteria of effective medium theory (EMT) to achieve homogeneity. In this present investigation it value if found to be 32 % and ϵ_m & ϵ_d indicate permittivity values of metal and dielectric layers, respectively. Based on EMT numerical calculations, we evaluated real parts of parallel and horizontal components of dielectric permittivity values as a function of wavelength and fabricated HMMs are observed to exhibiting hyperbolic dispersion (as evidenced from Figure – 8.2.2) at above 375 nm.

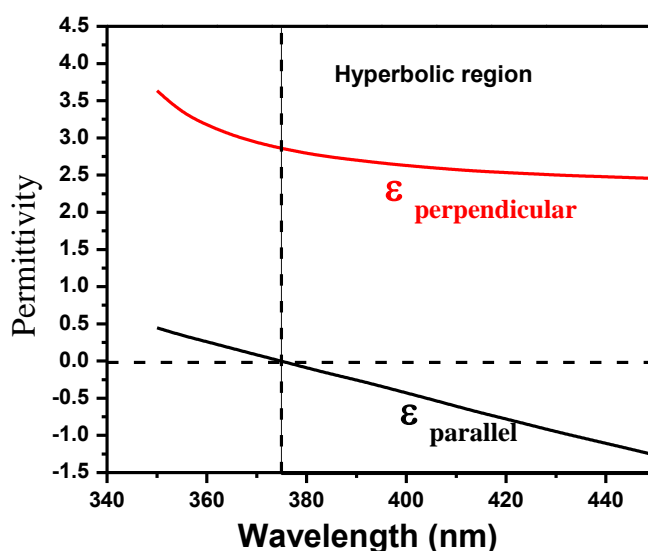


Figure – 8.2.2: Real parts of permittivity tensor components HMM evaluated in accordance with effective medium theory.

8.2 Results and Discussion

The steady-state photoluminescence (PL) measurements have been carried out using a spectrofluorometer setup to record emission spectra (at excitation wavelength of 450 nm) to understand the coupling of dye emission into the HMM states. In this setup, detection method was based on a reflection geometry in which dyes were excited using a mercury lamp and the emitted signals were detected using a last generation multichannel photomultiplier tube. With reference sample the observed PL intensities are reduced to large extent for the dye embedded (DEHMM) and dye placed on top of HMM samples (as evidenced from Figure – 8.2.3). This could be attributed to enhancement of preferential emission into existing high-k metamaterial states and increase of quenching in emission of dye molecules due to existence of large number plasmonic Bloch modes inside the HMM structures.

Time-resolved photoluminescence measurements are performed as a function of emission wavelengths to investigate the decay rate enhancement of dye molecules placed in the vicinity of various samples. An ultrafast optical setup has been used for time-correlated single photon counting (TCSPC) measurements using Edinburgh instruments and this setup consists of a Ti: Sapphire tunable femtosecond laser (Chameleon Ultra II from Coherent), a Pulse Picker, a Second Harmonic Generator and a spectrofluorometer.

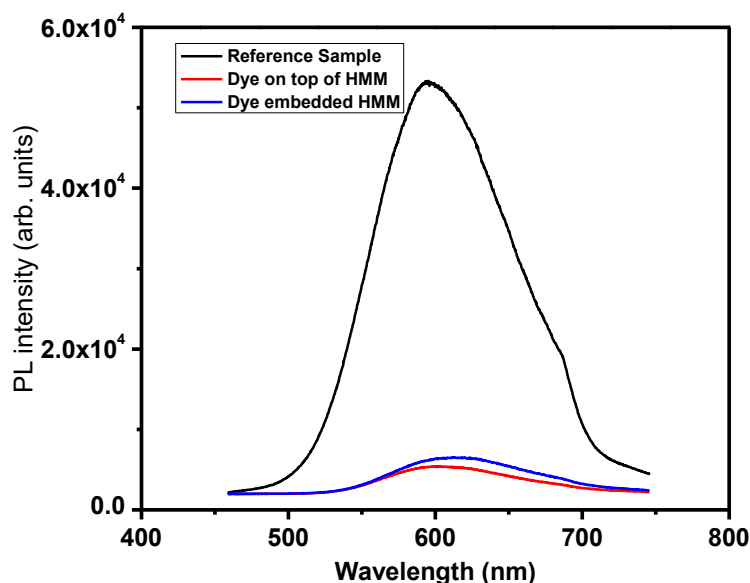


Figure – 8.2.3: Steady – state photoluminescence measurements for reference, dye on top HMM and DEHMM samples.

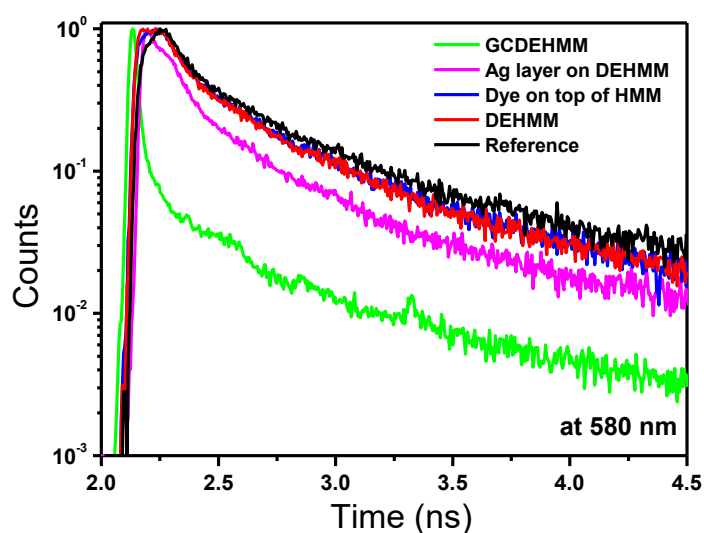


Figure – 8.2.4: Emission kinetics of dye molecules on various samples as a function of emission wavelength at 580 nm.

The time resolution of the TCSPC instrument is ≤ 5 ps. The DCM dye molecules are excited by using a pulsed laser at 450 nm with a pulse width of about 120 fs and a repetition rate of 4 MHz. The emission kinematics of fluorescent DCM dye molecules are studied at different emission wavelengths, by placing them on variety of samples. Figure – 8.2.4, represents Time-resolved photoluminescence measurements for the samples at emission wavelength of 580 nm and evidently in comparison to reference (Black curve) sample, both the dye placed on top of HMM (blue curve) and DEHMM (Red curve) samples demonstrated considerable shorter decay curves. Significantly, DEHMM sample demonstrated considerable shorter decay curve than dye placed on top of HMM sample. The resultant decay curves of three samples have been fitted using three exponential functions $R(t) = B_1 e^{-t/\tau_1} + B_2 e^{-t/\tau_2} + B_3 e^{-t/\tau_3}$; instead of single exponential function because the detected signals arise from the collective response of molecules randomly distributed in PMMA. Here τ_3 represents longer decay

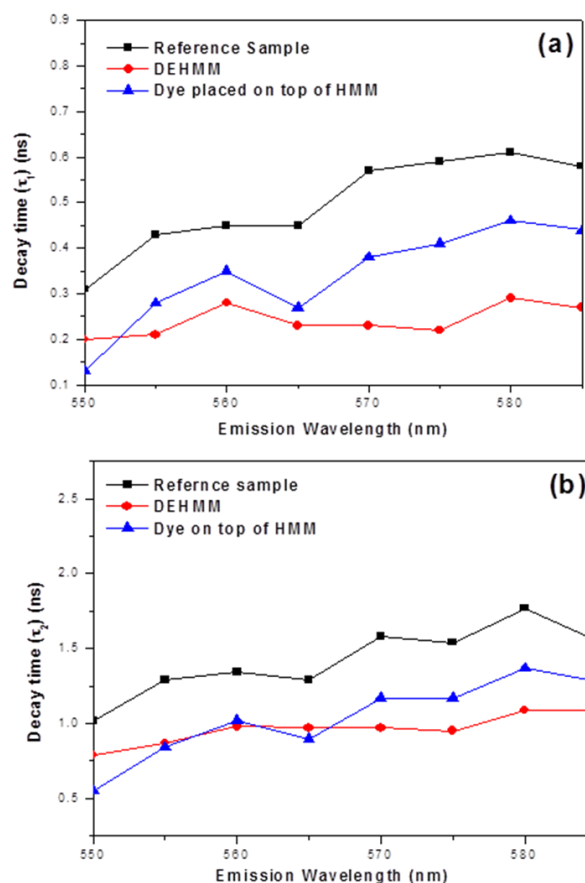


Figure – 8.2.5. Variation of (a) first decay time (τ_1) and (b) second decay times (τ_2) for reference, dye placed on top of HMM and DEHMM samples, as a function of emission wavelengths.

time, which is attributed to dye molecules away from the HMM and τ_1 and τ_2 indicate shorter decay times, which can be attributed to strong coupling of dye molecules with HMM. The evaluated shorter decay times (τ_1 , τ_2) as a function of emission wavelengths (as represented in Figure – 8.2.5) are noticed to be less for HMM and DEHMM samples than the reference sample.

These results reveal the hyperbolic dispersion in deigned HMM samples and rate of enhancement of high – k metamaterial states. The decay rate enhancement is defined as inverse of decay time and in the present investigation first decay time (τ_1) is considered for comparative study. At emission wavelength of 580 nm, the estimated decay rates are observed to be $1/0.61 \text{ ns}^{-1}$, $1/0.46 \text{ ns}^{-1}$ and $1/0.29 \text{ ns}^{-1}$ for reference, dye placed on top of HMM and DEHMM samples, respectively. With respect to reference and dye on top of HMM samples, DEHMM sample demonstrated 2 - fold and 1.6 - fold decay rate enhancements, respectively at emission wavelength of 580 nm (as evidenced from Figure – 8.2.5). Therefore, these results reveal that, -decay rate enhancement is more when dye molecules are embedded inside the HMM.

It is well acquaint that, HMM supports the propagation of surface plasmon polaritons (SPPs) and highly confined bulk plasmon polaritons (BPPs). However it is a difficult task to excite both SPPs and BPPs modes at optical frequencies due to momentum mismatch between incident light and the guided modes. This can be achieved by prism coupling method, in which high index prism has been brought near to a metal surface and the respective guided modes are excited optically via the enhanced momentum of an evanescent wave. In practical, prism coupling method is difficult due to requirement of high index prism to achieve momentum matching between incident photon and guided modes. Hence in the present investigation, we adapted novel hyper grating configuration to fabricate optical HMMs and the respective SPP and BPPs guided modes are excited efficiently at optical frequencies by 2D metal grating coupling technique. Therefore in this context, hypergrating refers as a collective architecture of both Ag metallic diffraction grating and HMM. To fabricate hypergrating structure, two dimensional Ag grating was made on top of the HMM and DEHMM samples using electron beam lithography (Tescan Vega). In this process, first MMA resist (8.5 MMA EL 11 from MICROCHEM) was spin coated on the sample at 4000 rpm and baked at 1800C for 5 min. In the second step PMMA resist (950 PMMA

C2 Resist from MICROCHEM) was spin coated at 5000 rpm and baked at 1800C for 8 min. As prepared samples were patterned using e-beam lithography with dosage 150 $\mu\text{C}/\text{cm}^2$ and beam intensity 6. The as exposed samples were developed using MIBK: IPA solution and IPA for 90 s and 30 s, respectively. After that an Ag layer of 20 nm thickness was deposited directly on top of the sample using thermal evaporation of Ag pellets.

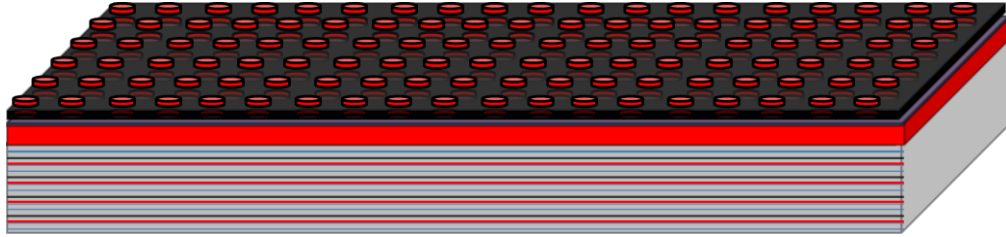


Figure – 8.2.6: Grating coupled DEHMM (GCDEHMM) sample structure

As described above, the grating coupling (GC) technique is adapted to excite surface plasmon modes associated to DEHMM samples and to observe the enhancement of spontaneous emission of dye molecules (as illustrated in Figure – 8.2.6). In accordance with GC technique, the surface plasmon modes can be excited when the wavevector of the grating diffraction orders are greater than the incident light one. With the effect of this condition, diffraction orders do not exist as longer propagating waves and become evanescent field with enhanced wavevector. This enables the coupling of incident light to surface plasmon modes by satisfying the condition $k_{SPP} = n_0 k_0 \sin \theta \pm m k_{gx} \pm n k_{gy}$. Here θ , n_0 and k_0 represent the incident grazing angle, refractive index of incident medium and vacuum wavevector, respectively. In the above expression, m and n are the grating diffraction orders and $k_g = 2\pi/\Lambda$ is the grating wavevector with Λ being the grating period. By diffracting light, a wide range of wavevectors can produce into the HMM by introducing a diffraction grating on top of the HMM. Resultantly, the generated wave vectors can couple through the surface modes due to the existence of impedance mismatch at the various openings,.

A comparative investigation has performed on DEHMM and grating coupled DEHMM (GCDEHMM) samples to observe the influence of GC technique on enhancement of spontaneous emission of dye molecules. At all spectral emission

wavelengths, GCDEHMM sample demonstrated higher decay rate variation with respect to the reference and DEHMM samples. The respective decay curves at emission

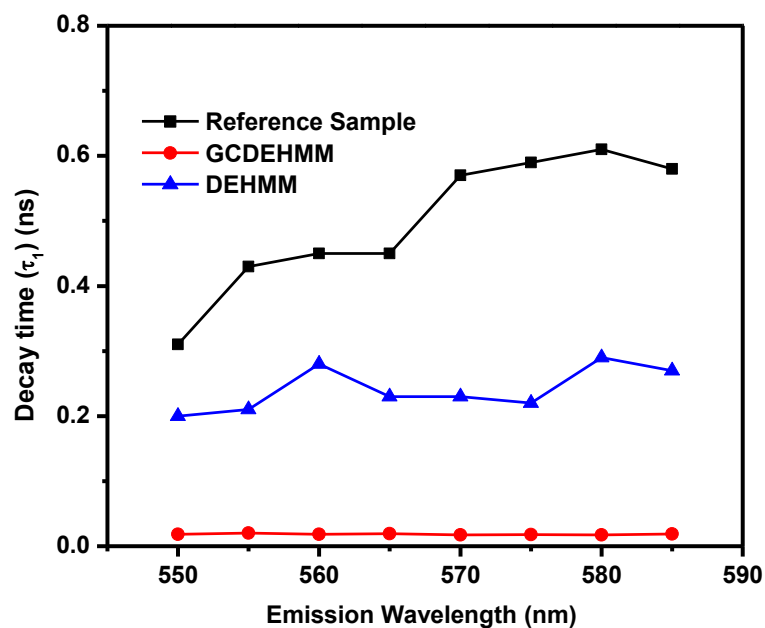


Figure – 8.2.7: Variation of first decay time (τ_1) as a function of emission wavelengths, for reference, DEHMM and GCDEHMM samples.

wavelength of 580 nm for GCDEHMM (Green curve), DEHMM (Red curve) and Ag layer on top of DEHMM (Magenta curve) samples are shown in Figure – 8.2.4. By following three exponential functions data fitting procedures, the evaluated short decay times (τ_1 , τ_2) are noticed to be varying randomly with respect to emission wavelengths for all the samples. Significantly, the evaluated decay times for GCDEHMM sample are much shorter than reference & DEHMM samples and constant throughout the spectral wavelengths as shown in in Figure – 8.2.7. The observed decay rate enhancement values at emission wavelength of 580 nm for GCDEHMM, DEHMM and reference samples are found to be $1/0.01744 \text{ ns}^{-1}$, $1/0.29 \text{ ns}^{-1}$ and $1/0.61 \text{ ns}^{-1}$, respectively. Therefore, in comparison reference to reference sample the GCDEHMM sample is demonstrated a maximum of 35-fold decay rate enhancement at emission wavelength of 580 nm.

8.3 Conclusions:

Nanostructured Metamaterials have been extensively used to manipulate the spontaneous light emission rate of molecules and their radiative efficiency. Because molecules near a metallic surface experience a different environment than in free space, their spontaneous radiative emission rate is generally enhanced. Such enhancement, measured by means of the Purcell factor, arises as a consequence of the overlap between the surface plasmon mode frequency and the emission spectrum of the molecule. However, such overlap is available only for a few narrow bands of frequency due to the limited plasmonic materials existing in nature. Although this limitation can be overcome by using hyperbolic metamaterials (HMMs)—a type of nanoscale artificial material with hyperbolic dispersion relations—the Purcell factor and the radiative power have remained relatively low.

we fabricated multilayered lamellar thin film structures, in which we have chosen silver (Ag) as a metal layer and alumina (Al₂O₃) as a dielectric layer. Therefore, we maintained metal fill fraction value of 34% in all fabricated HMM structures. An organic dye (Coumarin 500) is selected to investigate the influence of designed HMM on spontaneous emission. The evaluated dielectric permittivity tensor components of the fabricated HMM consists of six periods ($\epsilon_{\parallel}(\epsilon_{xx} = \epsilon_{yy}) < 0$) and $\epsilon_{\perp}(\epsilon_z) > 0$ imply a hyperbolic dispersion above the wavelength of 430 nm, at which transition occurs from elliptical to hyperbolic dispersion. As evidenced from Time-resolved photoluminescence measurements, the maximum decay rate is obtained for GCHMM for all wavelengths, which are 1/0.035 ns⁻¹, 1/0.030 ns⁻¹, and 1/0.031 ns⁻¹ for 420 nm, 480 nm and 510 nm, respectively. A maximum of 18-fold decay rate enhancement is obtained for GCHMM at 510 nm emission wavelength.

A grating coupled dye-embedded hyperbolic metamaterial geometry has been designed and fabricated for improving the spontaneous emission rate enhancement of quantum emitters. In comparison to a reference sample, about 35-fold spontaneous emission decay rate enhancement of dye molecules is obtained using a 2D silver diffraction grating coupled with DEHMM. We further demonstrated a comparative study on modification of spontaneous emission of fluorescent dye molecules placed in the vicinity of HMM structure and dye molecules embedded HMM structure. A semi-classical numerical approach has been used to compare the decay rate enhancement of HMM and DEHMM.

Acknowledgements:

We acknowledge support of the Ohio Third Frontier Project “Research Cluster on Surfaces in Advanced Materials (RC-SAM) at Case Western Reserve University”.

Authors Contribution:

K.V. Sreekanth and G. Strangi conceived the idea and designed the research. K.V. Sreekanth fabricated and characterized the samples, carried out ellipsometry and ultrafast optical experiments, and performed simulations and numerical modeling, and wrote the manuscript. K.H. Krishna fabricated the samples and performed the experiments. K.V. Sreekanth, A.D. Luca and G. Strangi analyzed the data. All authors discussed the results and commended on the manuscript.

References

1. A. Poddubny, I. Iorsh, P. Belov, Y. Kivshar, *Nature Photonics* 7 (2013) 948.
2. A. J. Hoffman, L. Alekseyev, *Nature Materials* 6 (2007) 946.
3. J.B. Pendry, *Science* 306 (2004)1353.
4. Krishnamoorthy, H. N. S., Jacob, Z., Narimanov, E., Kretzschmar, I. & Menon, V. M., *Science* 336 (2012) 205.
5. Z. Jacob, *Applied Physics B* 100 (2012) 215.
6. Z. Jacob, I.I. Smolyaninov, &E.E. Narimanov, *Applied Physics Letters* 100 (2012) 181105.
7. W.D. Newman, C.L. Cortes, & Z. Jacob, *J. Opt. Soc. Am. B* 30 (2013) 766.
8. M.A. Noginov, *Optics Letters* 35 (2010) 1863.
9. K.V. Sreekanth, T. Biaglow, & G. Strangi, *Journal of Applied Physics* 114, (2013) 134306.
10. A. Ono, J.-I Kato & S. Kawata, *Physics Review Letters* 95 (2005) 267407.
11. A. Salandrino & N. Engheta, *Physics Review B*. 74 (2006) 075103.
12. Z. Liu, H. Lee, Y. Xiong, C. Sun & X. Zhang, *Science* 315 (2007) 1686.
13. A.J. Hoffman, *Nature Materials* 6 (2007) 946.
14. M. Scalora, *Opt. Exp.* 15 (2007) 508.
15. D.R. Smith, P. Kolinko & D. Schurig, *J. Opt. Soc. Am. B* 21 (2004) 1032.
16. Y. Guo, C.L. Cortes, S. Molesky & Z. Jacob, *Applied Physics Letters* 101 (2012) 131106.
17. A.V. Kabashin, *Nature Materials* 8 (2009) 867.
18. P. Lodahl, *Nature* 430 (2004) 654.
19. B. Lounis & M. Orrit, *Rep. Prog. Phys.* 68 (2005) 1129.
20. S. Hughes, *Opt. Lett.* 29 (2004) 2659.
21. Z. Jacob, I.I. Smolyaninov, E.E. Narimanov, IPDB2, CLEO-IQEC (2009).
22. D. Lu, J.J. Kan, E.E Fullerton & Z. Liu, *Nature Nanotechnology* 9 (2014) 48.
23. L. Ferrari, D. Lu, D. Lepage & Z. Liu, *Opt. Exp.* 22 (2014) 4301.
24. K.V. Sreekanth, A. De Luca & G. Strangi, *Scientific Reports* 3 (2013) 3291.
25. R. Maas, J. Parsons, N. Engheta & A. Polman, *Nature Photonics* 7 (2013) 907.
26. K.V. Sreekanth, A. De Luca & G. Strangi, *Appl. Phys. Lett.* 103 (2013) 023107.
27. B. Lounis and M. Orrit, *Rep. Prog. Phys.*, 68 (2005)1129
28. Z. Jacob, L. V. Alekseyev and E. Narimanov, *Opt. Express* 14 (2006) 8247.
29. A. Otto, *Z. Physics* 216 (1968) 398.

30. E. Kretschmann and H. Raether, *Z. Naturf A* 23 (1968) 2135.
31. R.W. Wood, *Phil. Mag.* 4 (1902) 396.
32. W. Yan, L. Shen, L. Ran, & J.A. Kong, *J. Opt. Soc. Am. A* 24 (2007) 530.
33. M.A. Noginov, *Physics Review Letters* 101 (2008) 226806.
34. Noginov, M. A. *Solis-sate random lasers*. New York: Springer (2005).